UNIVERSITY OF SOUTHAMPTON

FACULTY OF PHYSICAL AND APPLIED SCIENCES

Electronics and Computer Science

Quadrature Error Cancellation for Micro-Machined Vibratory Gyroscope Embedded in High Order Electromechanical Sigma Delta Modulator

by

Pejwaak Salimi

Thesis for the degree of Doctor of Philosophy

March 2013

Abstract

Vibratory micro-machined gyroscopes utilize Coriolis force to detect the rotation rate. Recently it has been proved that embedding the gyroscope in an electromechanical ΣΔ modulator (EMSDM), results in increased linearity, rate detection range, and immunity to fabrication variations. In addition, this architecture can be deployed as a ΣΔ modulator (SDM) analogue to digital converter (ADC), providing a digital bit stream that can be used directly by any digital signal processing system (e.g. micro-processors). Furthermore, recent research has proved that higher order EMSDMs proved to deliver better performance in terms of signal to noise ratio while retaining linearity, dynamic range, fabrication tolerance and bandwidth advantages. Furthermore, in the view of ADC performance, higher order SDMs achieve higher resolution performance which is a desired feature for an ADC. Considering all these advantages, there have been attempts to deploy this approach in designing micro-machined gyroscopes interface in form of low-pass and band-pass EMSDM in order to achieve detection of high angular rate motions and angular motions with faster variation (which requires higher band width). However, the fabrication process of vibratory micro machined gyroscopes just like any other micro fabrication process is prone to flaws and inaccuracies. One of these flaws in the case of vibratory gyroscopes is the root cause of a mechanical coupling that occurs between the excitation direction and detection direction. This coupling results in appearance of an error signal in the detection direction which is known as quadrature error. Existence of this mechanical error results in reduction of performance in this type of gyroscopes and most importantly it limits the dynamic range of the sensor. In this work, a novel interface is proposed that eliminates the quadrature error while retaining the advantages of EMSDM for micro-machined gyroscopes system. The approach is a combination of quadrature amplitude modulation technique which is quite mature in communication systems, time division modulation in digital systems and the fundamental theory of EMSDM. A system level model of the novel architecture has been developed by using Matlab and Simulink. The system level simulation of the novel interface indicates that attenuation of -80dB can be achieved for the quadrature error signal. Furthermore, circuit level simulation model has been developed using Orcad/Pspice, in order to verify the consistency of the system level simulation. Finally a prototype PCB has been built characterized to evaluate the practical system performance. The measurement results on the hardware implementation show that the quadrature error power spectral density is attenuated by -70dB. In another words, the quadrature error is attenuated by about 3 orders of magnitude in the hardware implementation prototype.

Contents

List of figures ..... *vi*

List of tables ..... *xiii*

Acknowledgements ..... *xiv*

Chapter 1 Introduction *1*

1.1. Introduction 1

1.2. Motivation 2

1.3. Thesis structure 2

Chapter 2 Fundamental theory *4*

2.1. Operation theory of micro-machined gyroscopes 4

2.1.1. Mechanical structure and equations 4

2.1.2. Micro-machined gyroscope figures of performance 9

2.2. Principles of sigma delta modulator 11

2.2.1. Introduction 11

2.2.2. Principle of SDM 11

2.2.3. Quantization noise 12

2.2.4. High order sigma delta modulator 15

2.2.5. Band-pass SDM 16

2.3. Electromechanical sigma delta modulator 19

2.3.1. Introduction 19

2.3.2. Structure of electromechanical delta sigma modulators 19

2.3.3. Electromechanical sigma delta modulator design methods 21

2.4. Quadrature error 28

2.4.1. Introduction 28

2.4.2. Sources of quadrature error 28

2.5. Quadrature amplitude modulation 32

2.5.1. Introduction 32

2.5.2. Quadrature amplitude modulation principle 32

2.6. Summary 34

Chapter 3 Literature review *35*

3.1. Introduction 35

3.2. Open loop gyroscopes 35

3.3. High order closed loop control for a micro-machined gyroscope....39
3.4. Read-out circuits for sensing element....42
3.5. Quadrature error cancellation techniques....44
3.6. Discussion and conclusion....49

Chapter 4 Quadrature error cancellation method for band-pass EMSDM 52

4.1. Introduction....52
4.2. Automated design method for EMSDM....52
4.2.1. Introduction....52
4.2.2. Matlab genetic algorithm optimization....52
4.2.3. Automatic EMSDM optimizer....53
4.2.4. Verifying the automatically designed system by a linear model....57
4.3. System design theory....58
4.4. Simulation results....65
4.4.1. Sensing elements....65
4.4.2. System design for the low Q factor sensing element....66
4.5. Linear analysis....68
4.5.1. Linear system approximation for the novel system....69
4.5.2. Calculating the signal to noise ratio by the linear transfer function....72
4.6. System design for micro-gyroscopes with a high quality factor....73
4.7. Removal of excess loop delay compensation....76
4.8. Summary....77

Chapter 5 Circuit level simulation 78

5.1. Introduction....78
5.2. Circuit simulation model of the sub-system blocks....78
5.3. Circuit simulation results....87
5.4. Conclusion....91

Chapter 6 Experiment results....93

6.1. Introduction....93
6.2. Sub-circuits deployed in the implementation of the novel system....93
6.3. Experiment results....98
6.4. Conclusion....106

Chapter 7 Conclusion and future work 107

7.1. Conclusion....107

7.2. Future works 107
7.2.1. Deploying MESH technique in the novel system 107
7.3. Deploying a 4th order complex SDM 108
7.4. Extending GA design automation to hardware implementation 109
Appendix A ***110***
Appendix B ***117***
Appendix C ***118***
Appendix D ***124***
References ***131***

List of figures

Figure 2.1: Micro-machined accelerometer (a) mechanical structure and (b) Mechanical lumped model of an mass-damper-spring system (here accelerometer) 4
Figure 2.2: Demonstration on how an observer perceives Coriolis force for a floating particle travelling along y-axis [4]. 5
Figure 2.3: A tuning fork (a) in steady state and both branch are parallel. (b) An angular motion is present and the two branches are bent away due two effect of Coriolis force. 6
Figure 2.4: Systematic diagram of a basic Vibratory Gyroscope. kx,bx and ky,by are spring constant and damping factor for drive mode and sense mode respectively (reproduced from [12]). 6
Figure 2.5: Realization diagram of a vibratory micro-gyroscope. This figure presents a schematic drawing of a planar vibrating gyroscope [14] 9
Figure 2.6: Conceptual schematic of a first order SDM with a quantizer which acts as a low resolution ADC (reproduced from [18]. 12
Figure 2.7: Converting the quantizer block to a linear combination. K_q is the equivalent variable gain of a quantizer and N_q is the equivalent noise source for quantization noise. This conversion is also known as quasi model (reproduced from [20]). 14
Figure 2.8: A first order low-pass SDM is transformed to its linear model in by replacing the quantizer with a noise source. 14
Figure 2.9: Theoretical inbound noise for single stage SDM. In this figure L=0 means that input signal is sampled but there is no feedback loop (reproduced from [18]). 16
Figure 2.10: Structure of a single loop second order band-pass SDM modulator. As it is shown the integrator of an low-pass SDM is replaced by a resonator. 17
Figure 2.11: Replacement of poles and zeros of a loop filter by converting a low-pass SDM to a band-pass type (reproduced from [18]) 17
Figure 2.12: Conversion of an SDM from low-pass to band-pass changes the bode diagram characters. Left low-pass, right band-pass (reproduced from [18]). 18
Figure 2.13: Structure of an 6^{th} order band-pass SDM. This modulator is obtained by replacing the integrators in an 3^{rd} order low-pass SDM with resonators. 18
Figure 2.14: Power spectral density (PSD) of an output bit stream of a 6^{th} order delta sigma modulator for a signal with the central frequency of around 4 KHz. 18
Figure 2.15:A second order EMSDM for an accelerometer. The interface is formed by a micro-machined accelerometer, read-out circuit, compensation circuit, a quantizer coupled with a quantizer to form a second order electromechanical delta sigma modulator. Eventually the loop is closed by a voltage to electrostatic for converter. 19
Figure 2.16: An accelerometer coupled with an analogue electronic filter and a quantizer to form a high order EMSDM. The loop consists some type of digital to analogue converter and voltage to electrostatic force converter for closing the loop. 20
Figure 2.17: Comparisons between power spectral density of a second-order and fifth-order accelerometer closed-loop system (reproduces from [29]). 21

Figure 2.18: Design flow for a high order closed-loop electromechanical sigma delta modulator (adopted from [32]). 22
Figure 2.19: Convertion of a 4th order low-pass pure electronic SDM to a 5th order EMSDM for an inertial sensor (reproduced from [32]) 23
Figure 2.20: Linear model of the 5th order closed loop EMSDM for micro-machined accelerometer. In this model In1 is the input acceleration and input electronic noise and input quantization noise are presented (reproduced from [29]) 24
Figure 2.21: Magnitude bode diagram of a 5th order EMSDM for a sample accelerometer. In this diagram STF, QNTF and ENTF are presented and the diagram does co-respond to the expected behaviour of a real life EMSDM for an accelerometer (reproduced from [29]). 25
Figure 2.22: Linear approximation model of an 8th order EMSDM interface for a micro-machined gyroscope (reproduced from [25]). 26
Figure 2.23: Bode plot of the linear model of an 8th order band-pass EMSDM system for a micro-gyroscope. In this plot STF, QNTF and ENTF are presented. As expected this system demonstrates significantly high attenuation for quantization noise around central (sensing element resonant) frequency. 27
Figure 2.24: Power spectral density of a 6th order band-pass EMSDM for a sample micro-gyroscope. The co-efficient are the same as the ones in linear approximation QNTF. 27
Figure 2.25: Lumped-element model of a single axis vibrating gyroscope. Axis x, y and z are the coordinate with respect to a (non-inertial) reference system fixed with the sensor frame (reproduced from [38]. 28
Figure 2.26: Cross section of non-parallel sidewall in a comb finger structure (reproduced from [37]). 30
Figure 2.27: Sense mode representation. Black boxes represent fixed comb fingers and gray shapes represent the mass and moving comb fingers. Ɛ is the angle between the ideal drive mode axis and the actual drive mode axis. (a) Motion caused by quadrature error and (b) Motion caused by Coriolis force (reproduced from [39]). 30
Figure 2.28: Power spectral density of the output bit stream of a 6th order band-pass micro-gyroscope sigma delta modulator for input angular rate of 300º/s with quadrature error for drive axis deviation of Ɛ=0.0005. 31
Figure 2.29: Amplitude modulation and demodulation system diagram for x(t) as an information signal with the carrier frequency of f_c (reproduced from [40]). 32
Figure 2.30: Quadrature amplitude modulator and demodulator system schematic. In this figure xi(t) and xq(t) are two signals both are modulated at the same frequency with the 90 degrees phase difference (reproduced from [40]). 33
Figure 3.1: Tuning-fork differential gyro element anodically bonded on glass which was originally designed by Draper Lab (reproduced from [46]). 35
Figure 3.2: Structure of a Vibrating Ring Gyroscope (left). The new vibrating ring gyroscope utilizing polysilicon to form the thick, high aspect ratio ring, and p++ microstructures for sense/drive electrodes (right) (reproduced from [49]). 36

Figure 3.3: Decoupled frame structure for drive mode and sense mode used in Berkeley sensor & actuators centre micro-gyroscope 2002 (reproduced from [50]). 37
Figure 3.4: Structural schematic of the proposed gyroscope architecture with levered anti-phase drive-mode and linearly coupled anti-phase sense-mode for maximising the Q-factor of sense mode (reproduced from [52]). 38
Figure 3.5: Low-pass EMSDM architecture for secondary (sense) of a gyroscope sensing element. This systems uses feed forward arrangement of low-pass filters for noise shaping (reproduced from [56]). 39
Figure 3.6: Complete read-out and control system for a bulk micro-machined gyroscope. Band-pass SDM architecture is used to control both primary (drive) and secondary (sense) mode. The secondary mode output bit-stream is used to dynamically compensate the quadrature error (reproduced from [57]) 40
Figure 3.7: Control loop for sense mode of a micro-machined gyroscope sensing element. In this interface the sense mode is embed in a 6^{th} order band-pass EMSDM by replacing the first second order loop filter with the sense mode of a sensing element (reproduced from [25]). 40
Figure 3.8: Force feedback loop using low-pass modulator. Also quadrature error compensation is presented (reproduced from [60]) 41
Figure 3.9: Sixth order band-pass EMSDM interface circuit that is implemented on a PCB (reproduced from [61]). 42
Figure 3.10: a readout circuit for capacitive accelerometers based on switching capacitors. The main clock phases are ϕ_p: pre-charge; ϕ_1: readout phase; ϕ_2: Offset sampling for CDS; ϕ_f : Feedback phase for closed-loop operation mode; ϕ_{sw}: Sense electrode in readout & feedback phases. Reset phase (reset) and ϕ_2 are the same (reproduced from [64]). 43
Figure 3.11: capacity to voltage convertor circuit based on concepts of ac-bridge and amplitude modulation and demodulation (adopted from [63]). 43
Figure 3.12: The figure on the left shows the displacement of the proof mass due to the presence of quadrature error and the figure on the right shows the movement after the effect of quadrature error is eliminated by applying an asymmetric DC bias to sense fingers (reproduced from [39]).44
Figure 3.13: Quadrature error compensation is applied as a voltage which is produced from a 7 bit data that is generated produce by coherent demodulation in digital domain of the interface (reproduced from [57]) 45
Figure 3.14: Schematic of the closed-loop feedback control with quadrature error. The two compensation signals are extracted by a phase sensitive demodulation method and the equivalent magnitude of both errors are fed back to the sensing element as electrostatic forces (reproduced from [65]). 45
Figure 3.15: Conceptual schematic of the offset & quadrature error compensation signal injection (reproduced from [60]). 46
Figure 3.16: Circuit diagram presenting the deployment of quadrature error compensation capacitors (C_{c+},C_{c-})(reproduced from [38]). 47

Figure 3.17: Schematic of (a) passive and (b) active quadrature error compensation by re-injecting drive charges in sense channel (reproduced from [66]). 48
Figure 3.18: Implementation of mechanical structure for quadrature error compensation (a) simplified structure (b) SEM photograph (reproduced from [67]) 48
Figure 4.1: Simulink model of a 6th order band-pass micro-machined gyroscope closed-loop control system that is used in GA system (reproduced from [73]) 54
Figure 4.2: Screen-shot of series of possible solutions generated by GA-optimization fitness function. As shown for each solution a SNR and displacement are calculated. Negative SNR denotes that the system is stable. 55
Figure 4.3: Power spectral density for a sample 6th order band-pass closed-loop micro-gyroscope system generated by GA optimization system with parameters in table 1. The sampling frequency of this system is F_s=32768Hz and oversampling ratio (OSR) is 256. 56
Figure 4.4: Linear approximation model of the Simulink model of the closed-loop 6th order band-pass gyroscope which was shown in Fig. 4.1. In this figure "In1" is used to extract quantization noise transfer function in relation to "Out1". "In2" is used to extract electronic noise transfer function in relation to "Out1" and "In3" is used to extract signal transfer function in relation to "Out1". 57
Figure 4.5: Frequency responses of STF, ENTF, QNTF for the 6th order band-pass gyroscope linear model shown in Fig. 4.4 operating around the drive mode frequency (ω_d). 58
Figure 4.6: System diagram of the method for separating the angular rate information and quadrature error and reconstructing them at the sensing element drive mode resonance frequency. 60
Figure 4.7: A conceptual diagram of the novel gyroscope sense mode closed loop interface with quadrature error elimination system. As is shown each components of the read-out signal is separately fed into two sets of electronics loop filter and the output of the two quantizers are sent to a multiplexer. Ultimately, the multiplexer output is converted to electrostatic force and is applied to feedback electrodes 61
Figure 4.8: Linear approximation model for Coriolis force part of the system. 63
Figure 4.9: Linear approximation model for the quadrature error part of the system. 63
Figure 4.10: System level structure of the novel micro-machined gyroscope system with quadrature error elimination capability. 64
Figure 4.11: Bode plot (magnitude) of a sense mode (of a sample sensing element) transfer function with a low Q (quality factor) of 100. 66
Figure 4.12: Power spectral density of the output bit-stream of the novel system architecture for a low Q factor (~100) sensing element. As shown, the power spectral density of the quadrature error is significantly attenuated (by around 8 orders of magnitude) in comparison to its predecessor. ... 67
Figure 4.13: Proof mass displacement comparison between the closed-loop (blue) and open-loop (red) system. 68
Figure 4.14: SNR vs. angular rate diagram for estimating the minimum detectable angular rate. As is shown the minimum detectable rate is around 0.17°/s. 68

Figure 4.15: Diagram of the noise transfer function at information channel shown in Fig. 4.8.The bode diagram indicates that the system is stable within the simulated band-width. 70
Figure 4.16: Bode diagram of the signal transfer function at the information channel shown in Fig. 4.8. The bode diagram indicates that the system is stable within the simulated band-width in the Simulink model. 71
Figure 4.17: A root-locus diagram for the quantization noise transfer function (QNTF). As is shown the system is stable for a limited magnitude of gain; this determines the dynamic range of the system. 72
Figure 4.18: Bode plot of a sense mode transfer function with high a Q (quality factor) of about 10000..... 73
Figure 4.19: Power spectral density for the novel gyroscope system with high quality factor. Attenuation of more than 70dB (for quadrature error) is achieved in this simulation model..... 74
Figure 4.20: Comparison between the displacement of the proof mass in a high Q sense mode of the sample sensing element. It shows the displacement in open loop condition (red) and closed loop condition (blue). 75
Figure 4.21: Comparison between the signal to noise ratio versus the angular rate frequency for an open-loop system and the novel closed- loop system for a sample sensing element with high quality factor for both sense mode and drive. 76
Figure 4.22: Removal of excess delay compensation for the band-pass EMSDM by removing the return-zero(RZ) and the half return-zero (HRZ) in (a) and changing it two the arrangement that is in (b)..... 77
Figure 5.1: Behavioral model of sense mode of a sample micro-gyroscope. 78
Figure 5.2: Sub-circuit for conversion the voltage (projected displacement) variation to capacitance variation. The input to this circuit is the output of transfer function block shown in Fig. 5.1. 79
Figure 5.3: Capacitance to voltage convertor circuit. This circuit uses ac-bridge and AM demodulation (reproduced from [82]). The output of sense mode of the sensing element is differential which is a contributory factor in improving accuracy and removing common input noise. 80
Figure 5.4: The differential output of the instrumentation amplifier. As shown, the output of each side of the sense mode (in the sensing element) is complementary to the other. 80
Figure 5.5: The output of the instrumentation amplifier for a sample angular rate of 300 °/s at 64Hz. 81
Figure 5.6: Compensation transfer function block in the Simulink model with zero z and pole p. To make this transfer function a phase lag compensation, zero in this circuit must be smaller than the pole in this circuit. 81
Figure 5.7: Realization of the compensation transfer function. The function is realized as an all pass/phase shift circuit. Amp_out+ and Amp_out- denote the differential input of the circuit from the instrumentation amplifier while Cmp+ and Cmp- denote the differential output from the circuit.82
Figure 5.8: Input (black) and output (red) signals of the phase compensation circuit shown in Fig. 5.7. 82
Figure 5.9: Demodulator and modulator block for the separation of the information signal from quadrature error. Cmp+ and Cmp- nodes denote the inputs from the compensation circuit, RES+ and RES- denote the outputs to the information electronic loop filter and QRES+ and QRES- denote the outputs to the quadrature error electronic loop filter..... 83

Figure 5.10: The output signal from the two outputs of the sub-circuit block shown in Fig. 5.9. The red signal is the quadrature error and the blue signal is the information signal at 300°/s at 64Hz. ... 83
Figure 5.11: Circuit model of the resonator element in the band-pass loop filter..... 84
Figure 5.12: Fast Fourier transform (FFT) for the output of the resonator shown in Fig. 5.11. For this resonator, the resonance frequency was about 4.10KHz. 85
Figure 5.13: Pspice circuit model for the quantizer. An analogue comparator switches between a positive DC voltage and a negative DC voltage. This quantized signal is then transformed into a digitally compatible format by using a D-flip flop. 85
Figure 5.14: The output of the D type flip flop. The variation in the width of each pulse, denotes the pulse density modulation which is deployed by each EMSDM stage in the novel system. 86
Figure 5.15: Time division multiplexer block for multiplexing the information signal bit-stream and the quadrature error bit-stream. The multiplexer chip switches between the channels at a frequency which is twice the sampling frequency. 86
Figure 5.16: Circuit model for an analogue switch with SPDT configuration. 87
Figure 5.17: FFT of the information channel bit-stream. As shown, the quadrature error is attenuated by about two orders of magnitude. 88
Figure 5.18: FFT of the quadrature error channel bit-stream. As shown, the quadrature error is extracted and fed through this channel..... 89
Figure 5.19: Two sense mode transfer function blocks. One is in the control loop and one is in open-loop mode. The one in the control loop recieves the feedback signal via the "To_Sensor" node..... 89
Figure 5.20: Comparison between proof mass displacement (readout circuit output) in open-loop (green) and closed-loop (red) modes. The feedback voltage is set to 5V..... 90
Figure 5.21: Comparison between proof mass displacement (readout circuit output) in open-loop (green) and closed-loop (red) modes. The feedback voltage is set to 8V..... 90
Figure 5.22: Comparison between proof mass displacement (readout circuit output) in open-loop (green) and closed-loop (red) modes. The feedback voltage is set to 9V..... 91
Figure 6.1: (a) Diagram of the packaged and wire bonded MEMS gyroscope; (b) a SEM view of the sensing and feedback electrodes (reproduced from [61]). 93
Figure 6.2: Placement of the passive high-pass filter, in order to filter the coupled voltage from the drive mode. The cut-off frequency for this filter is set to 1.4MHz. 94
Figure 6.3: Instrumentation amplifier with its output converted from single ended to differential output. This arrangement contributes towards conserving space and lowering power. 95
Figure 6.4: The two outputs of the quadrature demodulator against a zero angular rate input. One output extracts quadrature error (green) and the other one extracts angular rate (yellow)..... 96
Figure 6.5: The output signals from the quadrature demodulator again a non-zero angular rate input. One output extracts quadrature error (green) and the other one extracts angular rate (yellow). 96
Figure 6.6: The frequency response spectrum for the 4^{th} order pure electronic SDM output bit-stream for zero-input. As shown, the quantization noise is shaped away around 4.1KHz which is the resonant frequency of the sense mode in the sensing element. 97

Figure 6.7: The complete circuit for a 6th order band-pass EMDSM with the capability of eliminating quadrature error..... 98
Figure 6.8: Power spectrum for the bit-stream from the quadrature error channel in open loop mode. 99
Figure 6.9: Power spectrum for the output bit-stream from the quadrature error channel when feedback voltage was increased to greater than 1V..... 100
Figure 6.10: Power spectrum from the quadrature error channel bit-stream when the feedback voltage was set at 5V. 100
Figure 6.11: Power spectral density of the bit-stream from the quadrature error channel after adjustments where mad to maximize the quadrature error power in the channel. 101
Figure 6.12: Power spectral density of the bit-stream from the angular rate channel after adjustments were made to minimize the quadrature error power in the channel. 101
Figure 6.13: The output from the instrumentation amplifier for a feedback voltage of 0V. This diagram projects the displacement of the proof mass. 102
Figure 6.14: Power spectral density of the information (angular rate) channel at a zero angular rate with 3V feedback voltage. There is some cross talk from the quadrature error channel into this channel.102
Figure 6.15: Power spectral density of the bit-stream from the quadrature error channel at a feedback voltage of 3V. In contrast to the one with a feedback voltage of 0V the power has decreased by about 5dB..... 103
Figure 6.16: The displacement of the proof mass (amplifier output) at a feedback voltage of 3V..... 103
Figure 6.17: The displacement of the proof mass (amplifier output) at a feedback voltage of 5V..... 104
Figure 6.18: Power spectral density of the information (angular rate) channel at a zero angular rate with a 5V feedback voltage. There is some cross talk from the quadrature error channel into this channel. There is about a 5dB decrease in the amount of cross talk in comparison to the one with a feedback voltage of 3V. 104
Figure 6.19: Power spectral density of the bit-stream from the quadrature error channel at a feedback voltage of 5V. In comparison with the one with a feedback voltage of 0V the power has decreased by about 7dB. 105
Figure 7.1: Electromechanical 4th order MASH22 SDM. The sensing element is embedded within the first loop, whereas the second loop is purely electronic SDM. The output bit-streams of the two loops are combined by digital filters (reproduced from [88]). 107
Figure 7.2: Creating a z-plane complex pole: (a) complex signal flow graph, (b) two-path signal flow graph, and (c) single-ended circuit realization.(reproduced from [89]). 108
Figure 7.3: A conceptual flow graph of deploying a complex pure electronic SDM in implementation of the novel gyroscope system. 108
Figure 7.4: Conceptual presentation of deploying GA system for direct hardware implementation. In this method a network of digital potentiometers change some circuit parameters to reach an optimum hardware design. 109

List of tables

Table 2.1: Performance requirements for different grades of gyroscopes..... 11
Table 2.2: Parameters for a sample accelerometer sensing element. 23
Table 2.3: Parameters for a sample gyroscope sensing element. 24
Table 3.1: Experimental demonstration of zero rare output improvement with the quadrature error cancellation (reproduced from [67])..... 48
Table 3.2: Experimental demonstration of bias stability improvement with the quadrature error cancellation (reproduced from [67])..... 49
Table 3.3: Experimental demonstration of angel random walk improvement with the quadrature error cancellation (reproduced from [67]). 49
Table 3.4: Summary of contribution and achievements of quadrature error compensation. 50
Table 4.1: Parameters of running the Simulink model in GA process 53
Table 4.2: Comparison of different orders of band-pass EMSDM systems..... 62
Table 4.3: Sensing element specification for the low Q factor type..... 65
Table 4.4: Sensing element specification for the high Q factor type..... 65
Table 4.5: Simulation parameters for the sense mode of the gyroscope 66
Table 4.6: Parameters for the linear approximation models..... 69
Table 4.7: Conditions and results of SNR calculation..... 72
Table 4.8: Parameters for the sense mode of the gyroscope used in this example..... 73
Table 4.9: Summary of achievements of the novel system for a high Q sensing element 75
Table 5.1: Circuit level simulation parameter for the novel gyroscope system 87
Table 5.2: RMS of proof mass displacement versus feedback voltage 91
Table 6.1: Specifications for the sample gyroscope sensing element 98
Table 6.2: Feedback voltage versus root mean square of proof mass displacement**Error! Bookmark not defined.**

Acknowledgements

I would like to thank my supervisor, Professor Michael Kraft for his incredible support during these years. This work would not have been possible without his perfect guidance and help.

Also, special thanks to Dr. Reuben Wilcock for his great support and help with designing the hardware and his assistance during the implementation of the circuit.

I would also like to thank Mr. Feng Chen for his helpful ideas, which were quite helpful through out the project.

I would acknowledge with gratitude the useful discussion and collaboration with the friendly PhD fellows in of Mountbatten Building: Dr. Rob Mounder, Dr. Ioannis Zeimpekis, Dr. Hossein Nili, Mr. Bader A. Almutairi, Mr. Ali A. Alshehri and Dr. Haitao Ding.

Finally, I thank the wonderful group secretaries, Glenys Howe, Lucia Hewett who always gave me generous and kind help.

This work was fully supported by Engineering & Physical Sciences Research Council (EPSRC) and Thales UK Research and Technology.

Chapter 1 Introduction

1.1. Introduction

Micro-system technologies (MSTs) and micro electro-mechanical systems (MEMS) have opened new horizons for a large variety of applications in different sectors of science and commerce. In addition, this rapidly advancing technology has resulted in innovative solutions to many existing problems and challenges in medical, automotive and aviation fields. It is now possible to design and implement applications such as pressure sensing, motion detection and biomedical applications in micro scale dimensions. The capability of batch fabrication and integration of these with some electronics interfaces on a single chip, are considered as the advantages of MEMS sensors. These advantages result in reduced costs and an improvement in the utilization and accuracy that this technology can deliver [1] [2] [3] [4]. It is intriguing to know that these instruments have been deployed even in order to assist the film and cinema industry by improving the camera movement control [5] [6].

Moreover, the aviation and automotive industries in both the military and commercial sectors, have found many areas for deploying MEMS sensors. One type of sensor which has drawn a lot of interest is MEMS gyroscope. The design of these sensors is based on the principle of the Coriolis force which results from the angular motions of a resonating object. Gyroscope sensors are usually used to monitor the angular velocity of an object (e.g. airplane, car, missile …) and assist the control system to keep the balance of the structure while travelling [7]. Also, these types of sensors are used for different aspects of controlling a car such as roll-over and cruise control systems and the development and deployment of such sensors promises to deliver even safer and more comfortable vehicles [8].

Just like any other new technology, some imperfections come along with all the advantages. For example, DRIE (Deep Reactive Ion Etching) is a fabrication technology which is used to fabricate micro accelerometers. Fabricated accelerometers suffer from issues such as nonparallel comb fingers in its sensing mass due to imperfections in this process [9] [10]. Such problems make research and development in the field of micro scale inertial sensors even more challenging for reaching performance levels which are crucial for applications such as airplane cruise control.

In this work, the focus is on rectifying an effect of fabrication imperfection, on the performance of closed-loop micro-machined vibratory gyroscopes. In simple terms, in this type of gyroscope a mechanical structure of the micro-gyroscopes (sensing element) is embedded in an electromechanical sigma delta modulator (EMSDM) to form a closed-loop vibratory micro-gyroscope. The gyroscope system measures the rate of an angular motion of the object which the system is attached to. The in-depth and scientific explanation of closed-loop vibratory micro-gyroscope operations will be presented in chapter 2. In this report the micro-machined mechanical

structure of the gyroscope is referred as the sensing element and the complete closed-loop system is referred as the micro-gyroscope.

1.2. Motivation

One of the researches on improving the performance has been on deploying the concept of EMSDM as mentioned in section 1.1. These works have made further progress in delivering higher order EMSDM for micro-machined gyroscopes, in the view of improving performance figures such as resolution, linearity, bandwidth, tolerance to fabrication imperfection, etc. However, there is one defect which limits the performance of any gyroscope system, regardless of its operating mode (open-loop or closed loop). This error is known as quadrature error which in the absence of a compensation mechanism can cause significant performance deterioration such as limiting the dynamic range. The effect of this error is even more limiting when a sensing element has got quite high sensitivity. It can limit the dynamic range of such gyroscopes down to a rate as low as 100 deg/s. Therefore it is quite crucial to deploy a quadrature error compensation method to prevent such problems and enable a gyroscope system to sustain its performance in spite of the effect of this error.

As stated in the previous section the focus of this project is on higher order EMSDM for micro-machined gyroscopes. The goal is to design a new gyroscope system which will retain the advantages of higher order EMSDM and compensates the quadrature error effect simultaneously. Also it is desirable to design the system in a way that a large number of sensing elements from different vendors can be incorporated. This approach in the design strategy makes the new system highly versatile in terms of applicability.

1.3. Thesis structure

In chapter 2, the fundamental principle of a micro-machined gyroscope is described by explaining the physical significance of the underlying phenomena, which is from the bases of vibratory gyroscope operations and determine the performance figures for any gyroscope system. Then mathematical equations and transfer functions which rule the operation of the mechanical structure is presented. Then, the theory of sigma-delta modulator (SDM) for low-pass and band-pass architectures is presented and quantization noise and signal to noise ratio (SNR) in SDM systems are explained. Afterwards, the idea of embedding the sensing element in a SDM structure to form an EMSDM is explained. In addition, the performance figures and linear equations for signal transfer function (STF), electronic noise transfer function (ENTF) and quantization noise transfer function (QNTF) are presented. By using these transfer functions, a system can be assessed from linear control theory point of view. Also in chapter 2, quadrature error in micro-vibratory gyroscopes is described and the sources of this error and its effect are introduced and explained.

In chapter 3, a review of previous works on improving the performance of micro-machined gyroscopes (on both sensing element and closed-loop gyroscope system) is presented. In addition, as one of the objectives of this project is to implement the system in hardware, a review on different methods of implementing the read-out circuit for capacitive variation (in this case the gyroscope) is added to the literature review. Then the focus of the review moves on to different quadrature error cancellation methods which have been proposed so far. At the end of the chapter a critical a brief review is presented along with tables of comparisons to support the new idea.

In chapter 4, first a new design method based on the MATLAB programming language and SIMULINK, is introduced and the design of an existing architecture with the new design system is analyzed. Then this simulation model is used to introduce the effect of quadrature error on performance of the band-pass EMSDM for micro-machined gyroscopes in terms of dynamic range. Afterwards, the idea of the novel design for cancelling quadrature error in band-pass EMSDM is presented. Then the SIMULINK system-level model of the novel design is presented and it is shown that how the new MATLAB tool assists to calculate all the coefficients for the new design. Ultimately, some performance figures are presented to show how the novel system has eliminated the effect of quadrature error at system level.

In chapter 5, the novel system architecture is designed in circuit level simulation environment by using PSPICE equivalent models of the electronic components. In this model the behavioral model of the sensing element is embedded in an electronic circuit which is formed based on the PSPICE models of commercial components. The chapter ends by presenting the behavior of the novel system in eliminating the effect of quadrature error. Also, a comparison between system- and circuit-level simulation results is presented.

In chapter 6, the hardware implementation of the system is presented including a description on practical circuit issues which were encountered during the implementation of the system. Also, some performance figures including quadrature error attenuation, signal to noise ratio and bias stability are presented. In addition, a comparison between the hardware implementation and simulation results at system level (SIMULINK) and circuit level (PSPICE) is delivered. The chapter ends with a conclusion on the achievements towards the objective of this project.

In chapter 7, some ideas on how the proposed system can be further improved, are discussed. In this regard, the possibility of incorporating digital (microcontroller) system to automate some aspects of system operation is assessed. Also, using some alternative architecture for this system with the aim of simplifying the design is brought to attention.

Chapter 2 Fundamental theory

2.1. Operation theory of micro-machined gyroscopes

2.1.1. Mechanical structure and equations

Before describing the structure and operations of micro-machined gyroscopes, it is useful to describe the simpler structure of a micro-machined accelerometer as its theory of operation is similar in terms of external excitation and proof mass movement.

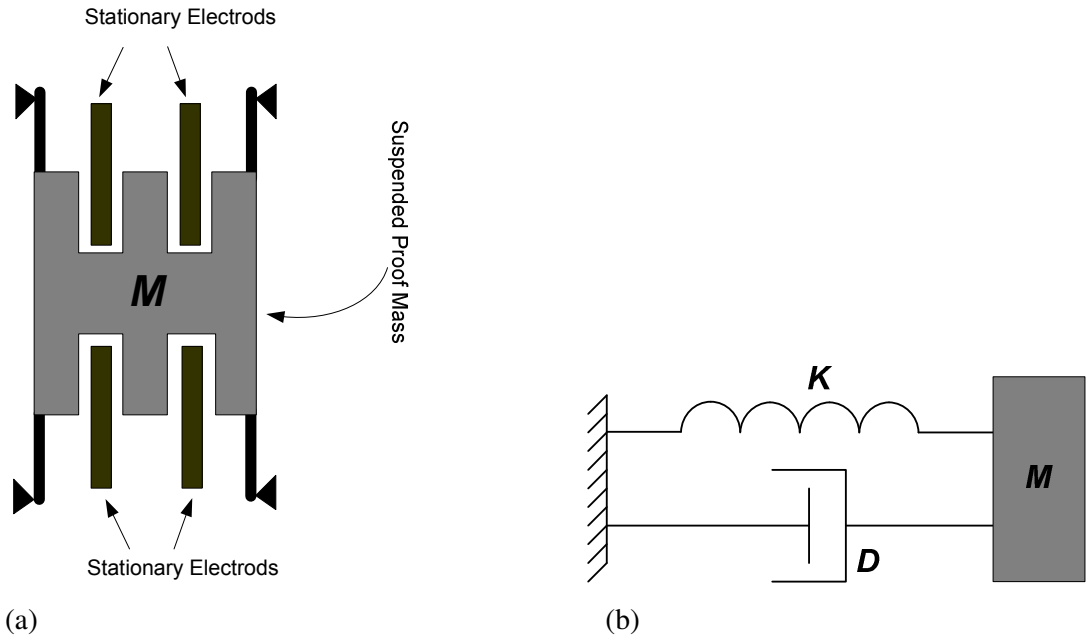

Figure 2.1: A micro-machined accelerometer (a) mechanical structure and (b)mechanical lumped model of an mass-damper-spring system (representing an accelerometer)

As shown in Figure 2.1a, an accelerometer consists of a proof mass suspended by compliant beams anchored to a fixed frame. The proof mass has a mass of M, the suspension beams have an effective spring constant of K, and there is a damping factor (D) affecting the dynamic movement of the mass. As shown in fig 2.1b, the accelerometer can be modeled by a second-order mass-damper-spring system. When an external acceleration is posed, the support frame is displaced relative to the proof mass, which in turn changes the internal stress in the suspension spring. Both this relative displacement and the suspension-beam stress can be used as a measure of the external acceleration. By using Newton's second law and the accelerometer model, the mechanical transfer function between the acceleration and the displacement of the proof mass can be obtained as follow [4]:

$$H(s) = \frac{x(s)}{a(s)} = \frac{1}{s^2 + \frac{D}{M}s + \frac{K}{M}} = \frac{1}{s^2 + \frac{\omega_r}{Q}s + {\omega_r}^2} \tag{2.1}$$

In this equation, a is the external acceleration, x is the proof mass displacement, $\omega_{r=}\sqrt{K/M}$ is the natural resonance frequency, and $Q = \sqrt{KM}/D$ is the quality factor.

Based on its definition, the resonance frequency of the structure can be increased by increasing the spring constant and decreasing the proof mass, while the quality factor of the device can be increased by reducing damping and by increasing proof mass and spring constant. Lastly, the static response of the device can be improved by reducing its resonant frequency [4] [11]. In addition to understanding the mass-damper-spring mechanical model, it is also essential to understand the Coriolis force, as in micro-machined gyroscopes; the external acceleration is replaced with the Coriolis force, which is generated by angular motion velocity posed to the mass in the mechanical model.

To understand the Coriolis Effect, a particle can be imagined to be travelling in space with a velocity vector V. It can be assumed that an observer sitting on the x-axis of the xyz coordinate system, as shown in Figure 2.2 is watching this particle. If the coordinate system along with the observer starts rotating around the z-axis with an angular velocity, the observer would see the particle changing its trajectory toward the x-axis with an acceleration equals to:

$$a_{coriolis} = 2\vec{V} \times \vec{\Omega} \tag{2.2}$$

The force resulting from this acceleration is given by:

$$F_{coriolis} = 2 \times m \times \vec{V} \times \vec{\Omega} \tag{2.3}$$

In the above two equations, ***m*** is the mass of the travelling particle, ***V*** is the linear velocity of the particle and **Ω** is the rate of angular motion that is posed to the particle. It must be noted that although no real force has been exerted on the particle, to an observer who is attached to the rotating reference frame; an apparent force has resulted that is directly proportional to the rate of rotation as given by equation

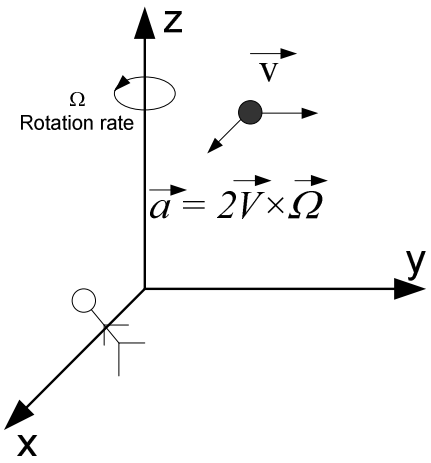

Figure 2.2: Demonstration on how an observer perceives the Coriolis force for a floating particle travelling along the y-axis [4].

Alternatively the Coriolis Effect can be demonstrated through its effect on branches of a rotating tuning fork as shown in Figure 2.3. As depicted, the two branches start to bend apart at the presence of an angular motion due to the presence of a Coriolis force.

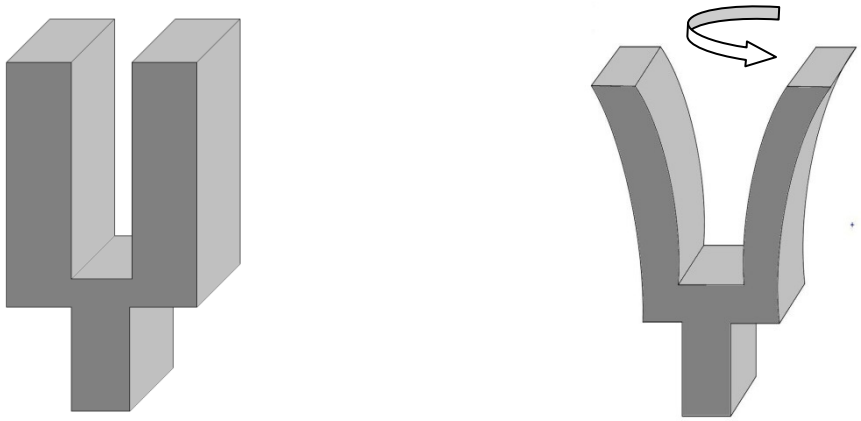

(a) (b)

Figure 2.3: A tuning fork (a) in steady state with the two branches being parallel. (b) in angular motion with the two branches bent away due to the effect of Coriolis force.

So far in this chapter, the Coriolis force has been described and the principle of micro-machined mass, damper, spring system has been presented. As these are the two fundamental components in the structure and operating principle of micro-machined gyroscopes, the next step will be to describe the operations of micro-machined gyroscope (sensing element).

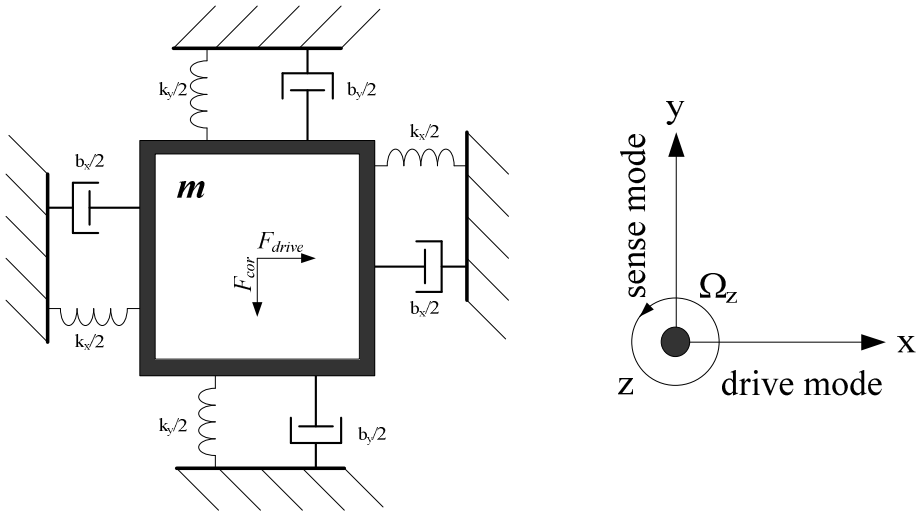

Figure 2.4: Systematic diagram of a basic Vibratory Gyroscope. kx,bx and ky,by are spring constant and damping factor for drive and sense modes respectively (reproduced from [12]).

As shown in the mechanical lumped model of a micro-gyroscope in Figure 2.4, while the proof mass is driven by a regulated force (i.e. electrostatic force) along the drive mode axis at the resonance frequency, in the absence of any rotational motion around the Z axis, the only movement is the oscillation along the drive mode (along x axis). Once the sensing element starts rotating around the z-axis the proof mass starts to oscillate along the sense mode at the natural resonant frequency of the drive mode. In other word, the mass can be imagined as the particle in Figure 2.2 and its oscillation along the drive mode can be considered its travel along the y-axis. Hence, the oscillation of the mass along the sense mode due to the Coriolis force resembles the movement of the particle along the x-axis. It must be noted that the drive mode of the sensing element in a micro-gyroscope, is driven and controlled by an electronic circuit which generates sine wave drive signals that are subsequently fed to drive mode nodes of the sensing element [13].

Moreover, the operation of sensing element can be described mathematically, by extracting the equations for the drive mode oscillation of the proof mass, generation of the Coriolis force and oscillation of the sense mode.

The proof mass is driven along X-axis; its vibration amplitude is given by:

$$x = A_x \cos(\omega_x t) \tag{2.4}$$

In this equation, A_x is the amplitude of the proof mass oscillation in drive mode and ω_x is the frequency of oscillation of the drive mode. Assuming the system is then rotated around the z-axis with an angular velocity $\vec{\Omega}$ with respect to an inertial system, the Coriolis force acting upon the proof mass can be calculated as follows:

$$\overrightarrow{F_{Coriolis}} = 2mV_x\overrightarrow{e_x} \times \vec{\Omega} \tag{2.5}$$

$$\overrightarrow{F_{Coriolis}} = -2mA_x\omega_x\Omega_z \sin(\omega_x t)\overrightarrow{e_y} \tag{2.6}$$

where m is the weight of proof mass (kg), V_x is velocity of oscillation (m/s), ω_x is the frequency of drive signal (rad/sec) and A_x is the amplitude of the oscillation of the proof mass in drive mode. In equation (***2.6***), $F_{Coriolis}$ can be replaced by the equivalent relation to proof mass to derive the displacement of the sense mode:

$$m\frac{d^2y}{dt^2} + b_y\frac{dy}{dt} + k_y y = -2mA_x\omega_x\Omega_z \sin(\omega_x t) \tag{2.7}$$

From this differential equation, the displacement in the y-axis is derived as:

$$y = -A_y \sin(\omega_x t - \varphi) \tag{2.8}$$

In (***2.8***) A_y is the magnitude of the proof mass displacement in the sense mode of the sensing element. This displacement can be calculated as follows:

$$A_y = \frac{2A_x\omega_x\Omega_z}{\omega_y^2\sqrt{\left(1-\frac{\omega_x^2}{\omega_y^2}\right)^2 + 4\xi_y^2\frac{\omega_x^2}{\omega_y^2}}} \tag{2.9}$$

where A_x is drive mode amplitude, ω_x is the drive resonant frequency; Ω_z is the rate of angular motion around the Z-axis (shown in Figure 2.4), ω_y is the sense frequency, and ξ_y is the damping ratio of the sense mode in the sensing element. This parameter can be calculated as:

$$\xi_y = \frac{b_y}{2m\omega_y} \tag{2.10}$$

and the phase lag between drive and sense modes is calculated as follows:

$$\varphi = arctan\frac{2\xi_y\omega_x\omega_y}{\omega_y^2 - \omega_x^2} \tag{2.11}$$

From equations (***2.5***) and (***2.6***) can be concluded that the angular motion rate is mechanically modulated at the resonance frequency of the drive mode. This phenomenon is used in signal recovery and later in this work for elimination of an error signal. As in further parts of this report the gyroscope shall be modeled in the S-domain (frequency domain) it is beneficial to mention the s-domain behavioral equation of sense and drive modes. This function is a transfer function that takes Coriolis force (for sense mode) or electrostatic force (for drive mode) as an input and the displacement of proof mass as an output. This function is written as below:

$$H_s(s) = \frac{1/m}{S^2 + \frac{\omega_s}{Q}s + \omega_s} \tag{2.12}$$

In this function, ω_s is the natural resonance frequency of drive or sense mode, Q is the quality factor and m is the mass of the proof mass of the drive and sense mode. Figure 2.5 shows a realization diagram of planar vibratory gyroscope based on theorems which are described above. It depicts a schematic of the vibrating micro-gyroscope consisting of two vibrating masses, eight

folded springs, a pair of sensing electrodes, an electrostatic comb electrode, and a displacement-monitoring electrode.

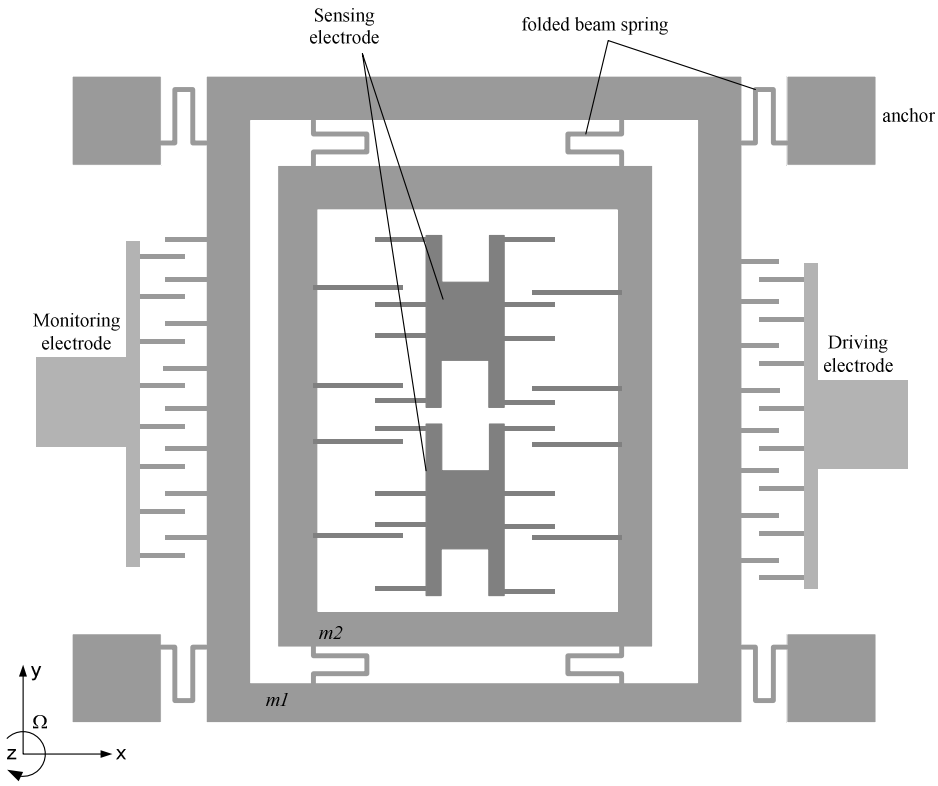

Figure 2.5: Realization diagram of a vibratory micro-gyroscope. This figure presents a schematic drawing of a planar vibrating gyroscope [14] .

Vibrating masses m_1 and m_2 are excited in the *X* direction by applying input voltages to the driving electrodes. Four folded springs and anchors guide m_1 to move in the *X* direction, where as the other four folded springs enable m_2 to move in the *Y* direction relative to m_1. Another comb electrode is located in the opposite side of the driving electrode to monitor the vibration driven by the comb actuator [14].

So far in this section, the structure and operation of the gyroscope sensing element has been provided. In all micro-gyroscope (open-loop and closed loop) systems that are discussed and presented in this work, the sensing element operates according to these equations. The information presented thus far in the section will also be used in later chapters of this work where as it will be shown how the parameters of a sample sensing element and the describing equations are used for designing a micro-gyroscope system.

2.1.2. Micro-machined gyroscope figures of performance

As in other fabricated devices such as transistors and op-amp there are a number of figures and parameters that demonstrate the performance level of micro-machined gyroscopes.

Categorically, there is three different grades for gyroscopes: gyroscopes can be: rate grade, tactical grade or inertial grade. In order to determine the grade of a sample gyroscope, the following performance figures are assessed [4] [15] [16] [17]:

- Angle random walk: The output of a MEMS gyro will be perturbed by some thermo-mechanical noise. As a result the measurements obtained from the sensor are perturbed by a white noise sequence, which is simply a sequence of zero-mean uncorrelated random variables. In this case each random variable is identically distributed and has a finite variance. The unit for this parameter is °/√h. 0.2 °/√h, for a sample gyroscope means that after 1 hour the standard deviation of the orientation error will be 0.2°.
- Bias drift: The bias of a MEMS gyroscope varies over time due to flicker noise in the electronics and in other components susceptible to random flickering. Flicker noise is noise with a 1/f spectrum, the effects of which are usually observed at low frequencies in electronic components. A bias stability measurement describes how the bias of a device may change over a specified period of time. The unit for bias stability is °/h.
- Scale factor accuracy: Measurement of an angular motion produces a corresponding voltage level in the output of the gyroscope. The ratio between the angular motion rate and the voltage level at the output of the system is known as scale factor. The consistency of the scale factor (linearity) is referred to as scale factor accuracy.
- Full scale range: The performance of any sample gyroscope is limited by the maximum angular motion rate. In other words, if the gyroscope is subject to an angular motion above this limit, the output will no longer be proportional to the input angular rate. This limit is known as full scale range with the units of °/s.
- Max shock in 1 millisecond (msec): Typically, the gyroscope system is attached to a mobile system ; e.g. car, airplane, etc. It is crucial for the gyroscope to retains its performance while the bearing object is subject to acceleration. The max shock denotes the maximum limit of this shock in the form of acceleration and its unit is g.
- Bandwidth: It is very rare to find a situation where the angular rate of an object is constant. Normally the angular motion rate changes continuously at different frequencies. It is important to specify the a sample gyroscope can follow up to a certain frequency of changes in the angular motion rate of the bearing object. This parameter is called bandwidth and its unit is Hz.

The following table demonstrates the required performance figures for each of the three grades [4]:

Parameter	Rate grade	Tactical grade	Inertial grade
Angle random walk ($°/\sqrt{h}$)	>0.5	0.5-0.05	<0.001
Bias Drift ($°/h$)	10-1000	0.1-10	<0.01
Scale Factor accuracy, %	0.1-1	0.01-0.1	<0.001
Full scale range ($°/sec$)	50-1000	>500	>400
Max. Shock in 1msec. g's	10^3	10^3-10^4	10^3
Bandwidth, Hz	>70	~100	~100

Table 2.1: Performance requirements for different grades of gyroscopes.

Currently, the focus of attempts towards overcoming challenges is on improving the performance of micro-gyroscopes (in both open-loop and closed-loop) to achieve tactical grade and inertial grade. In the literature review (chapter 3), contributions made in different aspects of micro-gyroscope systems, will be presented and discussed.

2.2. Principles of sigma delta modulator

2.2.1. Introduction

The sigma delta modulator (SDM) structure plays a crucial role in designing the closed loop control system for this work as this part of the system provides quantization noise shaping. Therefore, it is useful to have a brief introduction to its principles and design theory. In this section, the principle, design process and low-pass and band-pass modulator structure are presented and explained.

2.2.2. Principle of SDM

The performance of digital signal processing and communication systems is generally limited by the precision of the digital input signal achieved at the interface between analogue and digital information. Sigma delta modulation based analogue-to-digital conversion (ADC) technology is a cost effective alternative for high resolution (greater than 12 bits) converters and can be integrated on digital signal processor chips. In contrast to the delta modulator and Nyquist conversion, SDM has higher efficiency in oversampling quantization. Therefore higher resolution digital output can be obtained. Moreover, SDM can access larger analogue inputs compare to alternative oversampling ADC (e.g. delta modulator). As a result, SDM can be considered to have a larger dynamic range.

As shown in Figure 2.6 the structure of SDM is a feedback loop that contains a loop filter, low resolution ADC and a digital to analogue converter (DAC). In this architecture the loop filter is in the forward path [18].

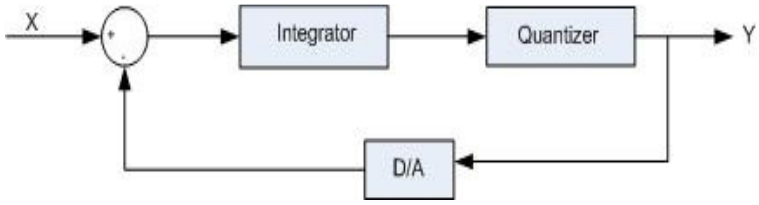

Figure 2.6: Conceptual schematic of a first order SDM with a quantizer that acts as a low resolution ADC (reproduced from [18].

The input and output in the above system are related through the following equation:

$$y(n) = x(n-1) + e(n) - e(n-1) \tag{2.13}$$

As the equation shows, the digital output contains a delayed, but otherwise unchanged replica of the analogue input signal *x*, and a differential version of the quantization error *e*. Since the signal is not changed by the modulation process, the modulation operation does not need an integrator as was the case for the delta modulator. Hence, the amplification of in-band noise and distortion at the receiver does not occur. Moreover, if the loop-filter has a high gain in the signal band, the in-band quantization noise is strongly attenuated. The process of attenuating this noise is commonly called noise shaping [18].

In addition, the relationship between the input and output can be explained as a mechanism in which the feedback, forces the average value of the quantized signal to track the average of the input signal. Any persistent difference between the input and the output is accumulated in the integrator and eventually corrects itself. This view on the operation of SDM is the foundation of deploying the architecture in EMSDM (as will be discussed in chapter 3).

2.2.3. Quantization noise

The process of converting an analogue signal (which has infinite resolution by definition) into a finite range number system (quantization) introduces an error signal that depends on how the signal is being approximated. This quantization error is on the order of one least-significant-bit (LSB) in amplitude, and is relatively small compared to full-amplitude signals. However, as the input signal gets smaller, the quantization error constitutes a larger portion of the total signal [19]. Accordingly, one of the primary objectives in designing SDM is to limit or shape the quantization error. It must be noted that the error is independent from the input signal. Further, it is equally

probable to lie anywhere in the range of $\pm\Delta/2$ (where Δ is the difference between the two level of quantizer output). its mean square value is given by:

$$e_{rms}^2 = \frac{1}{\Delta}\int_{-\Delta/2}^{\Delta/2} e^2\, de = \frac{\Delta^2}{12} \tag{2.14}$$

In addition, in oversampling modulators, the power of a signal that is sampled at f_s spreads into the frequency band of $0 \le f \le f_s/2$. Considering that the quantization noise is white, the power spectral density of the quantization noise is given by:

$$E(f) = e_{rms}\sqrt{\frac{2}{f_s}} \tag{2.15}$$

In addition, the ratio between the oversampling frequency f_s and Nyquist frequency f_0 for the sampling function is called the oversampling ratio and is given by:

$$OSR = \frac{f_s}{2f_0} \tag{2.16}$$

The quantization noise power that falls into the signal band is calculated as follow:

$$n_0^2 = \int_0^{f_0} e^2(f)df = e_{rms}^2\left(\frac{2f_0}{f_s}\right) = \frac{e_{rms}^2}{OSR} \tag{2.17}$$

In summary, the following assumptions are made for the quantization noise in order to be able to develop linear models (i.e. in Matlab) and subsequently transfer functions:

- The quantization error sequence e[n] is statistically independent of the input signal.
- The probability density function (PDF) of e[n] is uniform over the range of the bin (error range) width.
- The random variables of the error process are uncorrelated [20].

In conclusion, it is shown by (2.17) that oversampling reduces the in-band noise. Later in this section, where we use equation (2.17) to analyze the behavior of first order and higher order SDM in order to investigate the frequency response of SDM, a linear model must be produced to project the modulator as an LTI system. Extracting the behavior of a sample SDM requires the conversion

(or replacement) of the non-linear component in the system to/with a linear equivalent. This is achieved by replacing the quantizer with a noise source and gain block, as shown in Figure 2.7.

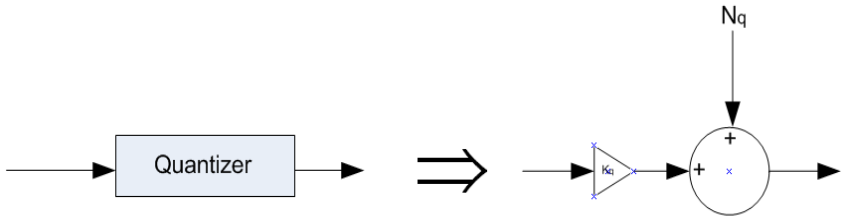

Figure 2.7: Converting the quantizer block to a linear combination. K_q is the equivalent variable gain of a quantizer and N_q is the equivalent noise source for quantization noise. This conversion is also known as quasi model (reproduced from [20]).

In this model, K_q is quantizer gain and for each system it can be calculated as the ratio of the output to input and N_q is the quantization noise which can be estimated as shown in (2.17). However, the gain can be neglected from the system and only be used to determine the maximum signal level that reaches the input of the quantizer before the modulator becomes unstable. This method is used by Motorola in analysis of SDM [19].

One method for predicting the behaviour of a SDM design is to extract three transfer functions which are derived by considering different point of inputs. The first function is the signal transfer function (STF). As the name denotes, it determines the behaviour of a sample SDM against input signal. The second function is the quantization noise transfer function (QNTF). This function determines how the sample SDM shapes the quantization noise within the desired band-width. The third function is the electronic noise transfer function (ENTF). This function helps the designer to determine how much electronic noise can be suppressed for the specific design and hence how much freedom or tolerance in terms of noise level is available in designing the circuit.

To clarify the method of extracting the linear transfer function, it is useful to apply the method to a simple first order SDM. In Figure 2.8 it is shown that how the sample SDM is transformed into its linear equivalent.

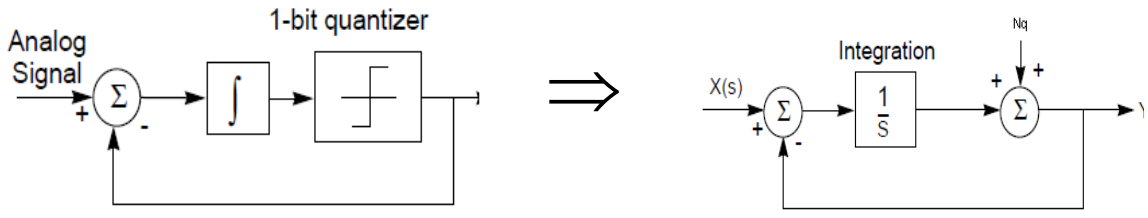

Figure 2.8: A first order low-pass SDM is transformed to its linear model by replacing the quantizer with a noise source.

Now from the linear model the two functions STF and QNTF can be derived. As shown in Figure 2.8, x(s) represents in input signal, y(s) represents the output signal and N_q represents the quantization noise source in the Laplace domain.

$$\frac{Y(s)}{X(s)} = \frac{\frac{1}{s}}{1+\frac{1}{s}} = \frac{1}{s+1} \tag{2.18}$$

$$\frac{Y(s)}{N_q(s)} = \frac{1}{1+\frac{1}{s}} = \frac{s}{s+1} \tag{2.19}$$

It can be seen from equations (2.18) and (2.19) that for the input signal x, the sample SDM acts as a low-pass filter and for quantization noise N_q, it functions as a high-pass filter. This means that quantization noise will be shaped away from the signal band. Hence, the further quantization noise is shaped away, the better signal to noise ratio is obtained. In further sections and in chapter 4 this method is used to determine the behaviour of EMSDM. More details on linear modelling of SDMs can be found in [21].

2.2.4. High order sigma delta modulator

The root mean square for in band quantization noise n_0 for a second order SDM can be calculated as follows:

$$n_0 \approx e_{rms}\frac{\pi^2}{\sqrt{3}}(2f_0T)^{3/2} = e_{rms}\frac{\pi^2}{\sqrt{3}}\,OSR^{-3/2} \qquad f_s^2 \gg f_0^2 \tag{2.20}$$

In this equation, e_{rms} is the quantization noise density, f_0 is the input signal frequency and T is the sampling period. From this equation, it is concluded that for every doubling of sampling frequency, the inbound noise will fall by 15 dB, giving 2.5 additional bits to the SDM resolution. The technique can be extended to provide prediction of noise for higher order SDMs which are formed by adding more feedback loops to the circuit. In general, when a modulator has L loop and is not over-loaded, it can be shown that the spectral density of the modulation noise n_0 is:

$$n_0 = e_{rms}\frac{\pi^L}{\sqrt{2L+1}}(2f_0T)^{L+1/2} \tag{2.21}$$

In equation (2.21), L is the order of the SDM also known as number of the feedback loops, f_0 is the signal frequency band and T is the sampling period. The relation between SDM order, sampling period and reduction in inbound noise is shown in Figure 2.9.

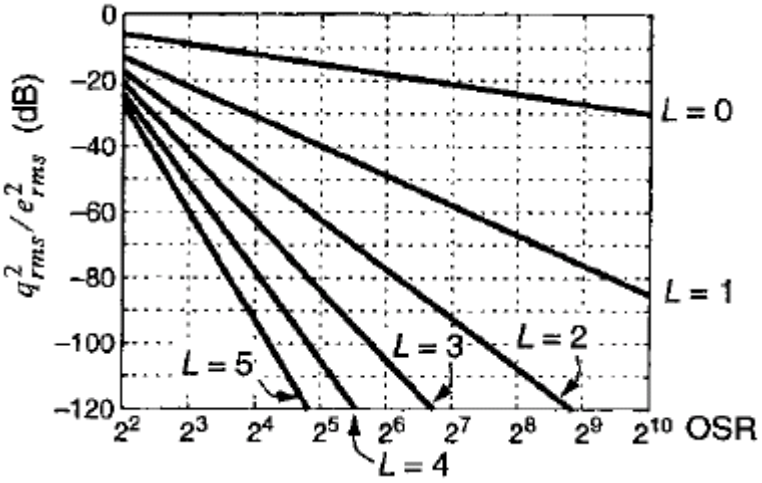

Figure 2.9: Theoretical inbound noise for single stage SDM. In this figure L=0 means that the input signal is sampled but there is no feedback loop. q is the quantization noise and e is electronic noise (reproduced from [18]).

The inbound noise drops 3(2L-1) dB for every doubling of the oversampling rate which results in achieving higher sampling resolutions. Although as proved it is crucial to use higher order SDMs and higher sampling rates in order to achieve better analogue to digital conversion performance, it must be noted that such strategies brings their own challenges. These challenges include compensating the additional electronic noise due to adding new stages or maintaining the loop stability as the sampling frequency increases.

2.2.5. Band-pass SDM

Up to now, in low-pass SDMs it was assumed that the signal energy was concentrated in a narrow band at low frequencies, centered at DC. In applications such as RF communication systems, the signal has a narrow bandwidth and is centered at a non-zero frequency. In this case SDM is still effective but the QNTF need be band-stop rather a high-pass filter. The main advantage of band-pass SDMs is that for obtaining good resolution the sampling rate does not need to be much higher that the base band. Such advantage makes this type of SDM a suitable choice for systems where the signal is centered at a non-zero frequency. Band-pass SDMs operate in much the same way as conventional (Low-pass) modulators and retain many of their advantage over Nyquist-rate converters. These advantages include inherent linearity (for single-bit systems), reduced Anti-Alias filter complexity, and a robust analogue implementation. The primary motivation for the development of band-pass converters is the simplicity imparted to systems

dealing with narrow-band signals. Such systems include radio frequency communication system, spectrum analyzers, and special-purpose instrumentation for narrow-band sources.

Similar to a low-pass SDM, a band-pass SDM can be constructed by placing a resonator (instead of a low-pass filter) and quantiser in a loop, as shown in Figure 2.10. The resonator may be implemented as a discrete-time filter using, for example, switch-capacitor or switched-current technology or maybe implemented as a continuous-time filter using, for example, LC tank resonator, Gm-C resonator or active RC resonator [18].

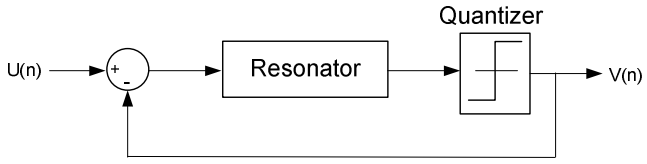

Figure 2.10: Structure of a single loop second order band-pass SDM modulator. As shown, the integrator of a low-pass SDM is replaced by a resonator.

One method to design the transfer function for a band-pass modulator is to begin with designing a low-pass SDM and then apply a low-pass to band-pass transformation known as Pseudo transform. The low-pass prototype must be designed to reach the desired SNR that is a function of both the oversampling ratio of the band-pass modulator and the low-pass to band-pass transformation procedure employed. For example, if one were to apply the transformation $z \rightarrow -z^2$ to a low-pass SDM prototype, the zeros of loop filter would be mapped from dc to $\pm\pi/2$ as shown in Figure 2.11. This would place two zeros exactly at a quarter of the sampling rate [22] [23]. Also, this transform moves the centre of frequency from dc to f_0 (central frequency of the input signal) as shown in Figure 2.12. This transformation places the centre frequency at $\omega_0 = \pi/2$, and thus for a fixed centre frequency the sampling frequency is dictated by the relation $f_s = 4f_0$ where f_s is sampling frequency and f_0 is the central frequency. Also, since this transformation preserves the oversampling ratio, the oversampling ratio of the SDM is again determined by the signal parameters: $R = 2f_0/B$ where R is oversampling ratio, B is the bandwidth around central signal and f_0 is the central frequency.

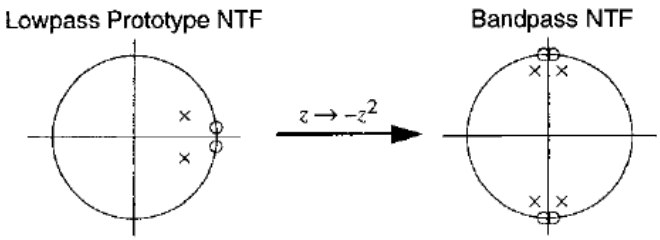

Figure 2.11: Replacement of poles and zeros of a loop filter by converting a low-pass SDM to a band-pass type (reproduced from [18]).

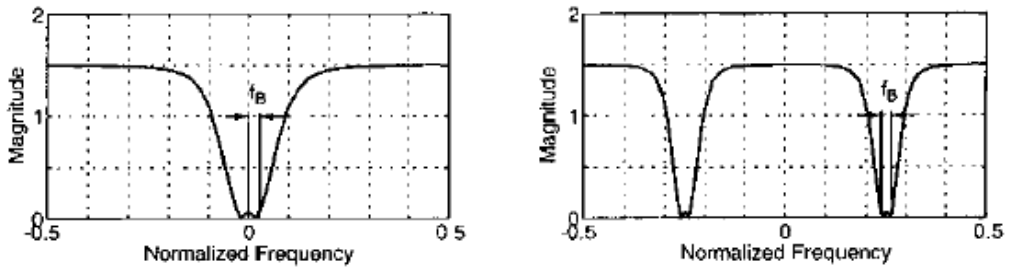

Figure 2.12: Conversion of an SDM from low-pass to band-pass changes the bode diagram characters. Left low-pass, right band-pass (reproduced from [18]).

From a system structure point of view the integrators will be replaced with resonators in a sample SDM. For example as shown in Figure 2.13by replacing the three integrators in the 3rd order low-pass SDM with three resonators, a 6th order band-pass SDM is built. Figure 2.14 presents verification of the functioning of this architecture as a band-pass SDM.

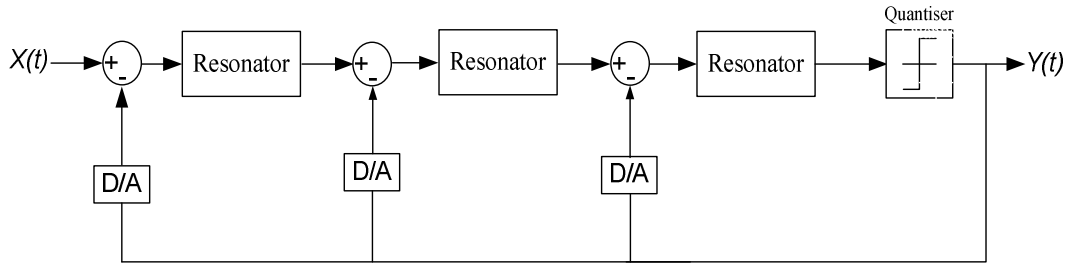

Figure 2.13: Structure of a 6th order band-pass SDM. This modulator is obtained by replacing the integrators in a 3rd order low-pass SDM with resonators.

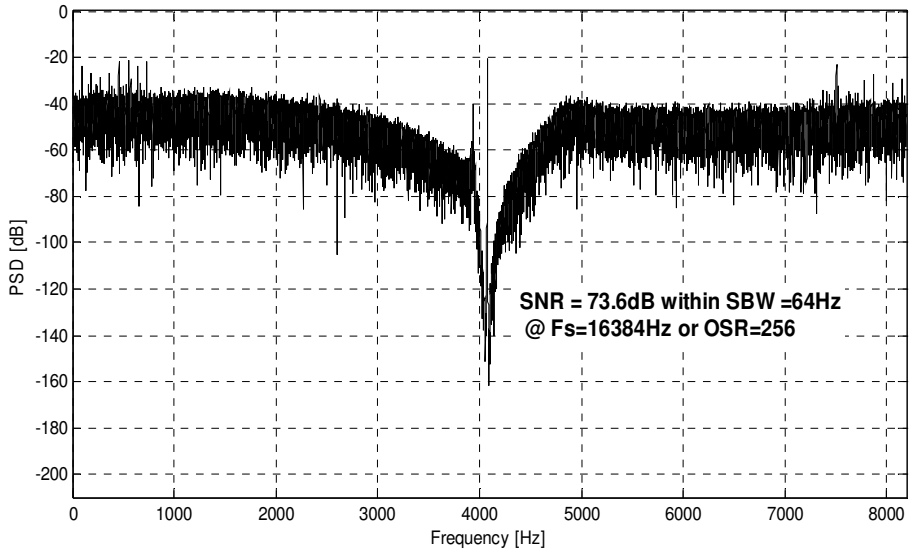

Figure 2.14: Power spectral density (PSD) of an output bit stream of a 6th order delta sigma modulator for a signal with the central frequency of around 4 KHz.

As shown in the power Spectral density graph in Figure 2.14, the input signal is reproduced at the output of the SDM with quantization noise being attenuated around the central frequency to below -120dB. This simulation also verifies the prediction of band-pass SDM, which was produced by linear transfer functions as shown in Figure 2.12.

2.3. Electromechanical sigma delta modulator

2.3.1. Introduction

As stated in Chapter 1, the advantages of closed-loop control for MEMS devices, has opened new fields of research in designing new interfaces for micro-machined accelerometers and gyroscopes [24]. In this section the principles of EMSDM – as one of the closed-loop control systems for inertial sensors – are presented. Although electromechanical modulators will be discussed in the literature review, because the novel micro-gyroscope is based on EMSDM, it is beneficial to introduce the fundamental theory of designing EMSDM.

2.3.2. Structure of electromechanical delta sigma modulators

The SDM interface is attractive for micro-machined inertial sensors since they combine the benefits of feedback control systems and analogue-to-digital data conversion at a relatively modest circuit cost. EMSDM is a name mostly used for a system where the structure is quite similar to pure electronic SDMs. Simplest structure of an interface is a closed-loop circuit that comprising of only an analogue front-end, a quantizer and a digital to analogue converter as shown in Figure 2.15.

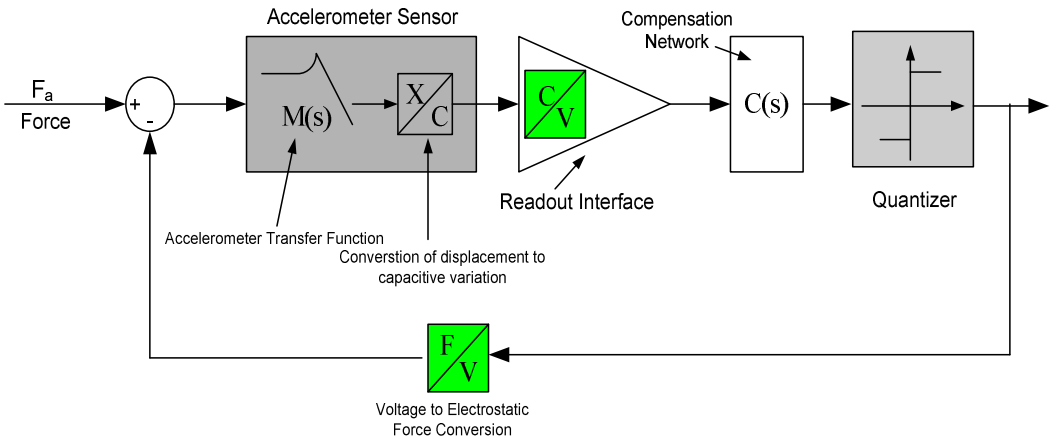

Figure 2.15:A second order EMSDM for an accelerometer. The interface is formed from a micro-machined accelerometer, read-out circuit, compensation circuit, coupled with a quantizer to form a second order electromechanical delta sigma modulator. Eventually the loop is closed by a voltage to electrostatic for converter.

The feedback signal is converted to a constant value electrostatic force that is generated according to the following formula:

$$K_{fb} = sgn(D_{out}) \frac{\varepsilon_0 A_{fb} V_{fb}^2}{2(d_0 + sgn(D_{out}).x)^2} \quad (2.22)$$

where ε_0 is the dielectric constant, A_{fb} is the area of the feedback electrode, V_{fb} is feedback voltage, d_0 is the nominal gap between the proof mass and the electrodes to either side, x is the deflection of proof mass from its rest position and D_{out} is the quantizer output bit stream [25]. However as stated in section 2.2.3, the operation of quantization introduces quantization error which is perceived as an additional noise source. The main goal of applying the sigma delta concept to inertial sensors is to achieve the benefits of feedback and digitization without compromising the resolution of the analogue front-end. Therefore, the interface should be designed such that the quantization error adds a negligible noise penalty. In addition, when an additional loop is used to suppress the noise from quantization the loop must be appropriately compensated to ensure stability. There are two options on how an EMSDM is formed:

- To couple an inertial sensor (accelerometer or micro-gyroscope) with a quantizer and form a feedback path from the quantizer output to the sensor as shown in Figure 2.15. This combination forms second order EMSDM [26] [27].
- To replace one of the integrators or resonators (depending on the type of modulator) with an inertial sensor (e.g. accelerometer) as shown in Figure 2.16. Using, this method, EMSDMs with orders higher than 2 can be achieved.

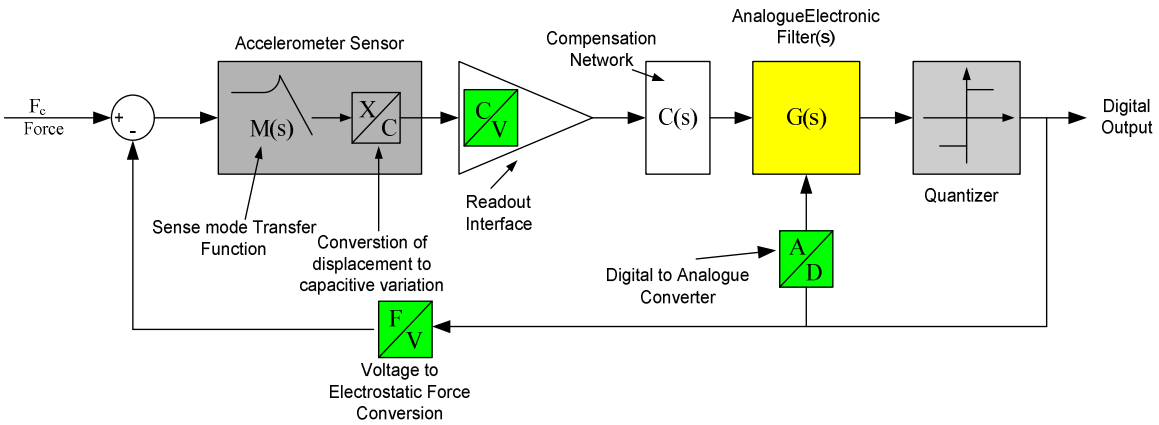

Figure 2.16: An accelerometer coupled with an analogue electronic filter and a quantizer to form a high order EMSDM. The loop includes some type of digital to analogue converter and voltage to electrostatic force converter for closing the loop.

The resolution of the high-order (order>2) modulator is within fractions of a decibel of that of the underlying open-loop system, which consists only of the mechanical sensor and the interface front-end. Furthermore, the high-order sigma delta modulator can achieve high resolution at lower sampling rates compared to that resolution in a second order electromechanical sigma delta modulator. Therefore it is concluded that high-order electromechanical modulation enables micro-machined inertial sensors to operate in a feedback configuration with inherent digitization without incurring a resolution penalty from quantization error. The technique also overcomes the trade-off between resolution and phase compensation, which forces second-order systems to operate with a reduced phase margin [28].

Y. Dong et al proposed a fifth order closed-loop accelerometer and as shown in Figure 2.17, there is about 80 dB attenuation of quantization noise in comparison to the second order system. Such achievement practically proves that increasing the order of an EMSDM will decrease the quantization noise penalty on resolution [29].

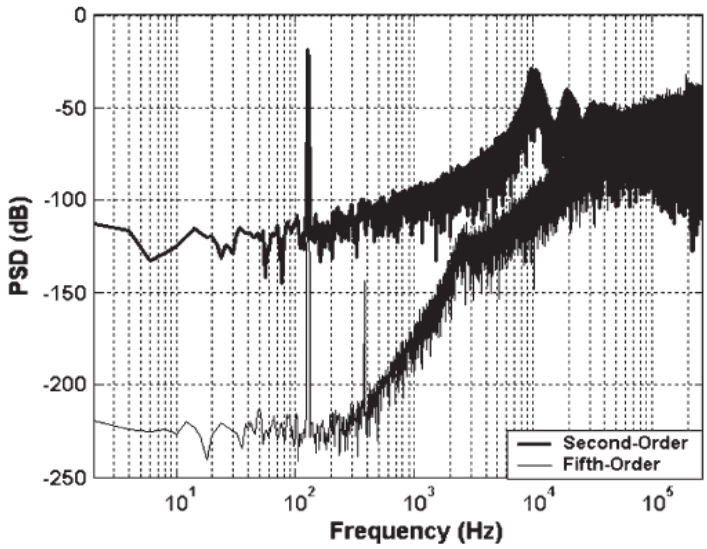

Figure 2.17: Comparisons between the power spectral densities of second-order and fifth-order accelerometer closed-loop system (reproduces from [29]).

This achievement on higher order EMSDM has been used in several researches and projects to build low-pass/band-pass closed loop micro-machined accelerometer and gyroscope systems [30] [31]. The deployment of such architecture as a contribution to designing new gyroscope systems will be discussed in detail in the literature review section.

2.3.3. Electromechanical sigma delta modulator design methods

As stated in section 2.1.1, the mechanical behavior (displacement of proof mass) of accelerometer and sense mode and drive mode of a gyroscope sensing element can be described by

a second-order mechanical transfer function. For the design of a high-order EMSDM, the loop includes the second-order transfer function with additional electronic integrators (or resonator in case of a band-pass system) to obtain better quantization noise shaping. In addition, the mechanical input node which is at the input of the mechanical transfer function cannot be connected to the electronic integrators to form feed-forward paths or feedback from the front end electronic integrators as it is a mechanical effect as opposed to an electronic signal encountered in pure electronic modulators [32]. Therefore, the design methodology of high-order EMSDM is different from conventional SDM based A/D converters. However, as the design of high-order electronic SDM is reasonably improved and advanced, the design of a high-order EMSDM should take advantage of these techniques. Interpolative topologies with multi-feedback or feed-forward loops, which have been proven as very successful approaches to implement high-order EMSDM [18], [33] can be modified, adopted and applied to EMSDM. For example, a high-order SDM A/D converter is designed using existing methods such as mapping the QNTF to an analogue Butterworth or Inverse-Chebeyshev filter [18]. Exploiting this method in the EMSDM domain leads to a design method for high-order (>2) SDMs with the sensing element embedded in them to form a high-order EMSDM as presented in Figure 2.18 [32].

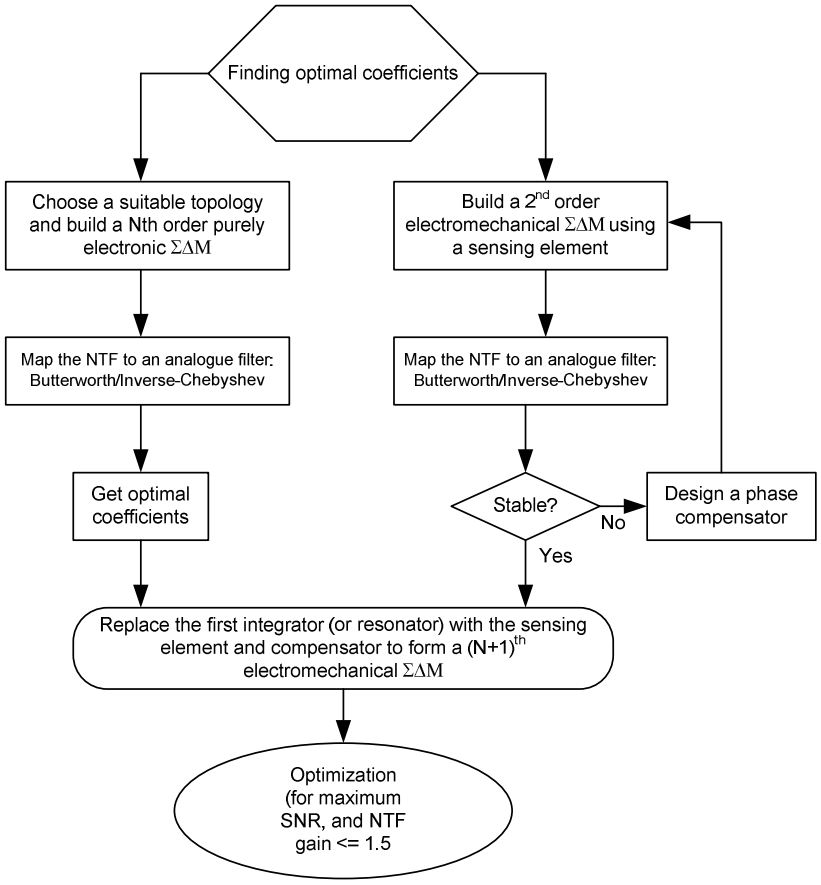

Figure 2.18: Design flow for a high order closed-loop electromechanical sigma delta modulator (adopted from [32]).

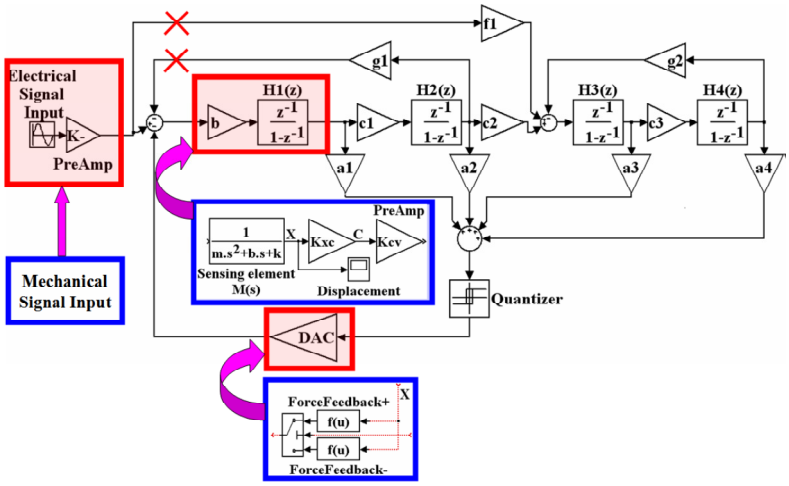

Figure 2.19: Conversion of a 4th order low-pass pure electronic SDM to a 5th order EMSDM for an inertial sensor (reproduced from [32]) .

As an example, in Figure 2.19 a pure electronic fourth order CIFF (Cascaded Integrator Feed Forward) SDM is depicted. According to the design flow, after designing a stable electronic SDM, the first integrator is replaced with the second order sensing element. In addition, the DAC is replaced with a force feedback element and this (electrostatic) force is fed to the sensing element. It must be noted that the dynamic range of the sensing element is defined by the magnitude of the feedback force (as it was by DAC in electronic SDM). An electrostatic feedback force is generated on the proof mass, by applying a voltage to the electrodes of the sensing element. For a given sensing element in a closed-loop control system, the dynamic range is determined by the electrostatic force which can be set by the feedback voltage mentioned earlier in section 2.3.2. In order to verify the validity of this method, a linear model of a sample 5th order low-pass EMSDM for accelerometer and a linear model of a sample 8th order band-pass EMSDM are discussed. In order to verify this method, a linear approximation model of a sample 5th order low-pass EMSDM for an accelerometer sensing element in Figure 2.20 and a linear model of a sample 8th order band-pass EMSDM for a micro-gyroscope sensing element in Figure 2.22 are presented. In these two models the sample accelerometer and the sample micro-gyroscope have the specifications given in Table 2.2 and Table 2.3, respectively.

Proof mass	m = 1.2e-6kg
Damping coefficient	b = 0.006 N/m/s
Spring stiffness	k=5 N/m
Resonant frequency	325Hz
Quality factor	0.408
Number of comb fingers	1800

Table 2.2: Parameters for a sample accelerometer sensing element.

Mass of proof mass	m = 2e-9kg
Drive mode frequency (Hz)	$f_x=2^{14}$ (Hz)
Drive mode frequency (rad/s)	$\omega_x=2\pi f_x$(rad/s)
Sense mode frequency (rad/s)	$\omega_y=2\pi f_y$(rad/s)
Q_x	100
Q_y	100
K_{fb}	3.15×10^{-9}(N/V)

Table 2.3: Parameters for a sample gyroscope sensing element.

An advantage of generating a linear system is that it provides the opportunity to have an approximate prediction of the frequency responses of a system. Figure 2.20 shows a linear model approximation of a low-pass 5th order architecture. The quantizer is replaced with a gain and an adder and a noise source as explained in section 2.2.3. For each system transfer function, STF, ENTF and QNTF are generated using automatic flow-graph generator [34] [29]. In these two examples all three sources are shown and the transfer functions are presented.

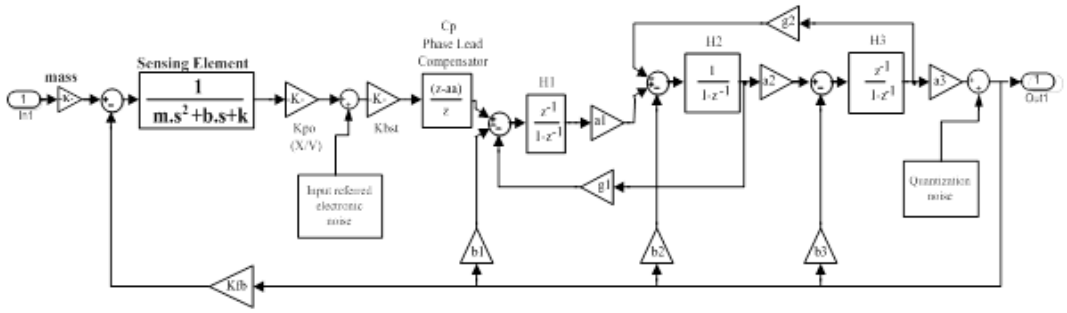

Figure 2.20: Linear model of the 5th order closed loop EMSDM for micro-machined accelerometer. In this model In1 is the input acceleration and input electronic noise and input quantization noise are presented (reproduced from [29]) .

The transfer functions are written as follows:

$$\mathrm{STF}_1(\mathrm{z}) = \frac{\mathrm{k_m(z)K_q}\prod_{\mathrm{i=1}}^{3}\mathrm{H_i(z)a_i/K_{fb}}}{\mathrm{L_1(z)}} \tag{2.23}$$

$$ENTF_1(z) = \frac{k_m(z)K_q\prod_{i=3}^{3}H_{i(z)}a_i/(K_{fb}M_m(z)K_{po})}{L_1(z)} \tag{2.24}$$

$$QNTF_1(z) = \frac{1+\sum_{i=1}^{2}H_i(z)a_iH_{i+1}(z)g_i}{L_1(z)} \tag{2.25}$$

In these transfer functions $L_1(z)$ is:

$$L_1(z) = 1 + k_m(z)\prod_{i=1}^{3} H_i(z)a_i + K_q\sum_{i=1}^{3} b_i \prod_{j=1}^{3} H_j(z)\, a_j + \sum_{i=1}^{2} a_i g_i \prod_{j=i}^{i+1} H_j(z) + H_1(z)a_1 H_2(z) g_1 a_3 H_3(z) b_3 K_q$$

In these equations $k_m(z)=K_{fb}M_m(z)K_{po}K_{bst}C_p(z)$ where K_{fb} is the force feedback coefficient (in Newton per Volt), Mm(z) is the sensing element transfer function, K_{po} the pick-off circuit gain to convert displacement to voltage and K_{bst} is the gain of the boost circuit. The following bode diagram is produced from the above STF, QNTF and ENTF. As shown in Figure 2.21, the behavior of the linear model does correspond to the excepted behavior of a 5th orders EMSDM. For instance, around the resonant frequency of the sensing element, the model shows great amplification for signal and great attenuation for quantization noise.

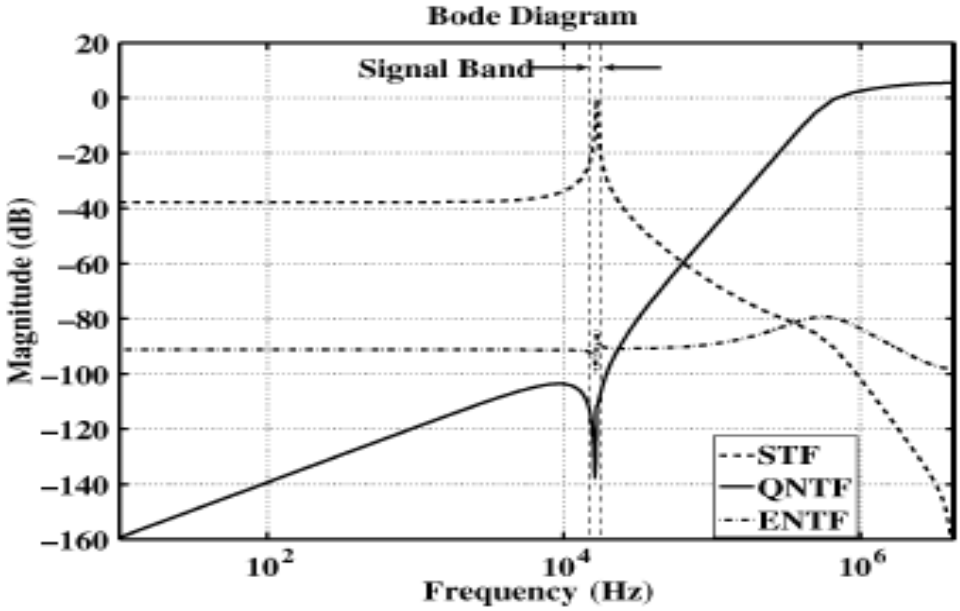

Figure 2.21: Magnitude bode diagram of a 5th order EMSDM for a sample accelerometer. In this diagram STF, QNTF and ENTF are presented and the diagram does correspond to the expected behaviour of a real life EMSDM for an accelerometer (reproduced from [29]).

It should be noted that the bode plots in Figure 2.21 are not a direct result of the three transfer functions. Both electronic and quantization noise are translated to an angular rate error. In other word, the sources of both noises are moved to the input of the system, where the angular rate is fed to the sensing element and for both electronic noise and quantization noise, their angular rate

equivalents are taken into account.The other example is a linear approximation model of an 8th order band-pass EMSDM for a sample micro-machined gyroscope which is shown in Figure 2.22.

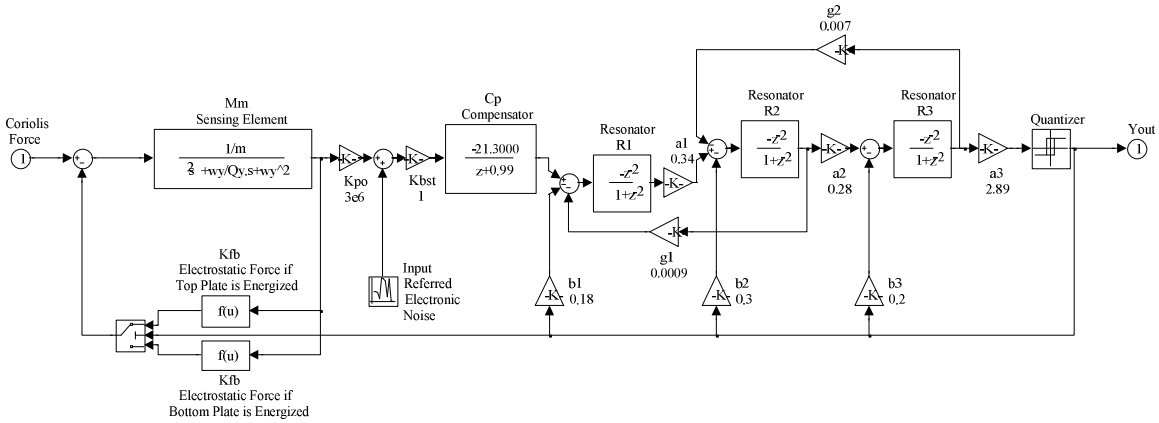

Figure 2.22: Linear approximation model of an 8th order EMSDM interface for a micro-machined gyroscope (reproduced from [25]).

The linear transfer functions STF, ENTF and QNTF for the system shown above can be written as follows:

$$\mathrm{STF}_2(z) = \frac{k_m K_q \prod_{i=1}^{3} R_i(z) a_i / K_{fb}}{L_2(z)} \tag{2.26}$$

$$\boldsymbol{ENTF_2(z) = \frac{k_m(z) K_q \prod_{i=1}^{3} R_i(z)\, a_i / (K_{fb} M_m(z) K_{po})}{L_2(z)}} \tag{2.27}$$

$$\mathrm{QNTF}_2(z) = \frac{1 + \sum_{i=1}^{2} R_i(z) a_i R_{i+1}(z) g_i}{L_2(z)} \tag{2.28}$$

where L2(z) is:

$$\mathrm{L}_2(\mathrm{z}) = 1 + k_m(z) K_q \prod_{i=1}^{3} R_i(z) a_i + K_q \sum_{i=1}^{3} b_i \prod_{j=i}^{3} R_j(z) a_j + \sum_{i=1}^{2} a_i g_i \prod_{j=i}^{i+1} R_j(z) + R_1(z) a_1 R_2(z) g_1 a_3 R_3(z)\, b_3 K_q$$

As shown in the bode diagram in Figure 2.23, such an architecture promises good quantization noise shaping around the central frequency (which in this case should match the sense mode resonant frequency). It also promises significant attenuation in the magnitude of electronics noise and this can also mean that this architecture is a suitable choice for low-noise systems. Hence it can be concluded that this system will perform as expected for a sample EMSDM gyroscope [25].

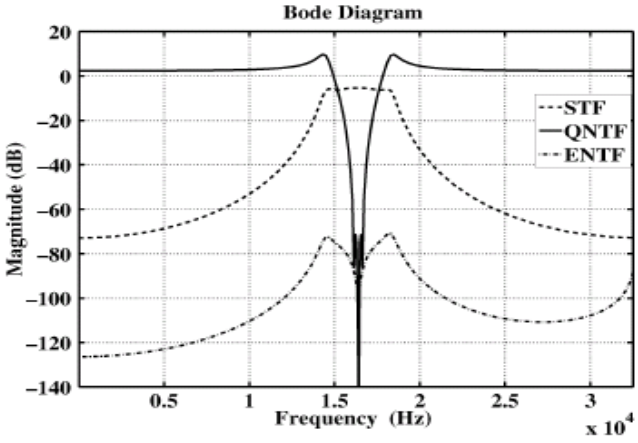

Figure 2.23: Bode plot of the linear model of an 8th order band-pass EMSDM system for a micro-gyroscope. In this plot STF, QNTF and ENTF are presented. As expected this system demonstrates significantly high attenuation for quantization noise around central (sensing element resonant) frequency.

Further more, this prediction is verified by running a simulation process on a Simulink model of the sample 6th order EMSDM. The simulation output is projected as the power spectral density of the output bit-stream as shown in Figure 2.24.

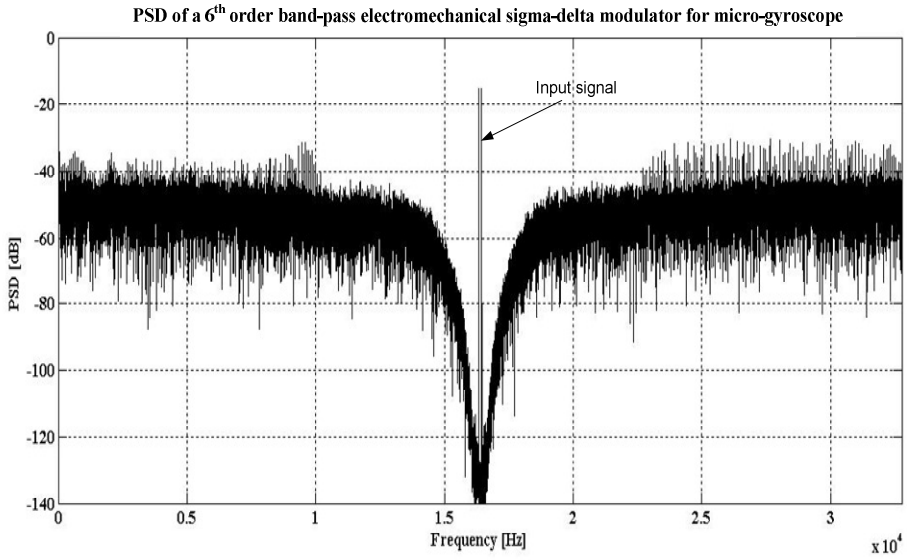

Figure 2.24: Power spectral density of a 6th order band-pass EMSDM for a sample micro-gyroscope. The co-efficient are the same as those in linear approximation QNTF.

The design method introduced in Figure 2.18 and Figure 2.19 suffers from a technical flaw. From a mathematical point of view, in transforming from pure electronic SDM to an EMSDM a structural change is occurred by replacing the first filter component by the sensing element. Hence, the optimized coefficients for the electronic SDM will not be optimized for the new system. As a

matter of fact to optimize the EMSDM a manual change of coefficients is required which can be time consuming and sometimes cannot reach the best performance. Therefore, an alternative method has been invented and used for several micro-machined accelerometer and gyroscope closed-loop systems which will be demonstrated in chapter 4.

One last but important note on designing the band-pass EMSDM for micro-machined gyroscopes is that in cases that drive and sense mode resonant frequencies are not perfectly matched, the central frequency of resonators must be matched to the drive mode resonant frequency and not sense mode resonant frequency [35] [36].

2.4. Quadrature error

2.4.1. Introduction

For any electronic/MEMS device, the output is expected to be zero for zero input. However, in real world this is not the case. For example, operational amplifiers have an offset voltage at their output node. MEMS sensors are not an exception from this phenomenon. As explained previously, the measured quantity in micro-gyroscopes is the Coriolis acceleration. There is an off-axis oscillation of the proof mass in the drive mode that generates false Coriolis acceleration and this motion is 90° out of phase with the measured angular motion. Due to this phase difference this false angular motion is called Quadrature error. This error is commonly encountered in vibratory-gyroscope [35] [37].

2.4.2. Sources of quadrature error

The imperfections and tolerances that occur in the micro fabrication of sensing elements are the source of quadrature error. This error is produced via off drive mode oscillation at the absence of angular rate and is rooted in the asymmetry between the springs of the mass-damper-spring structure. To demonstrate the effect of asymmetric spring constants, a lump model of the sensing element is used - as shown in Figure 2.25

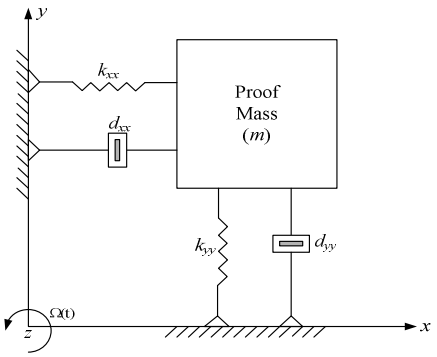

Figure 2.25: Lumped-element model of a single axis vibrating gyroscope. Axes x, y and z are the coordinates with respect to a (non-inertial) reference system fixed with the sensor frame (reproduced from [38].

Consider a reference system fixed with the sensor frame, whose x and y axes are aligned with the two orthogonal directions of vibration of the proof mass. The in-plane equations of motion of the proof mass in the sensor-fixed frame can be written as:

$$\mathrm{M}\ddot{\mathrm{q}}(t) + \mathrm{D}\dot{\mathrm{q}}(t) + \mathrm{Kq}(t) = \mathrm{F}(t) + 2\Omega(t)\mathrm{MS}\dot{\mathrm{q}}(t) \tag{2.29}$$

where *q(t)* is the in-plane displacement vector, *F(t)* is the vector of external actuating forces and *Ω(t)* represents the sensor angular velocity along the *z*-axis (orthogonal to the $x - y$ plane). The 2x2 real, positive definite matrices are:

$$\mathrm{M} = \begin{bmatrix} \mathrm{mx} & 0 \\ 0 & \mathrm{my} \end{bmatrix} \quad \mathrm{D} = \begin{bmatrix} \mathrm{dxx} & \mathrm{dxy} \\ \mathrm{dyx} & \mathrm{dyy} \end{bmatrix} \quad \mathrm{K} = \begin{bmatrix} \mathrm{kxx} & \mathrm{kxy} \\ \mathrm{kyx} & \mathrm{kyy} \end{bmatrix}$$

M, *D* and *K* denote the mass, damping and stiffness matrices respectively. The off diagonal terms d_{xy}, d_{yx} in the damping matrix *D* and k_{xy}, k_{yx} in the stiffness matrix *K* represent non-proportional viscous damping and anisoelasticity effects. In the following, only anisoelasticity effects are considered, while non-proportional damping is neglected. Also, *S* is the skew-symmetric matrix:

$$\mathrm{S} = \begin{bmatrix} 0 & 1 \\ -1 & 0 \end{bmatrix}$$

This metrics explains how the Coriolis acceleration couples the dynamics of the two modes of vibration. The conventional mode of operation consists of driving the proof mass into a controlled harmonic motion along the direction of a first mode of vibration (drive mode), and then detecting the motion arising along the direction of the remaining mode (sense mode) whenever the sensing element is subjected to an angular motion. In Figure 2.25, if x and y axes denote the directions of the drive and sense modes, respectively, then the equations of motion for proof mass in sense mode during the normal mode of operation can be rewritten as follows:

$$\mathrm{x}(\mathrm{t}) = -\mathrm{X}_0 \sin\omega_{\mathrm{x}}\mathrm{t} \tag{2.30}$$

$$\ddot{\mathrm{y}}(\mathrm{t}) + \frac{\omega_{\mathrm{y}}}{\mathrm{Q}_{\mathrm{y}}}\dot{\mathrm{y}}(\mathrm{t}) + \omega_{\mathrm{y}}^2\mathrm{y}(\mathrm{t}) = -2\Omega(\mathrm{t})\dot{\mathrm{x}}(\mathrm{t}) - \omega_{\mathrm{yx}}\mathrm{x}(\mathrm{t}) \tag{2.31}$$

where ω_x and ω_y are the natural frequencies of, the drive and sense mode, respectively. Also, ω_{xy} is the coefficient of coupling between the two modes. Considering the two terms on the right hand side of equation (2.31) while taking equation (2.30) into account, it can be seen that the

coupling acceleration and the Coriolis acceleration are in quadrature. Therefore, it can be concluded that springs stiffness asymmetry contributes to the quadrature error [38].

In addition, surface and bulk micro-machining can results in fabrication of an imperfect micro structure. Such imperfection can also lead to making non-parallel/non-abrupt sensing and driving structure walls of their comb finger as shown in Figure 2.26.

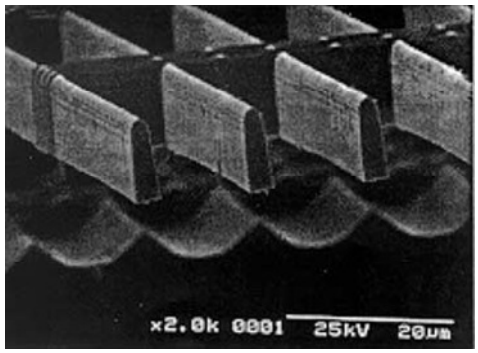

Figure 2.26: Cross section of non-parallel sidewall in a comb finger structure (reproduced from [37]).

This fabrication imperfection results in motions in the drive mode that are not exactly parallel to the drive mode axis. Hence, some motion is projected into the sense mode. The existence of this error can also be modeled as shown in Figure 2.27. In other words, an off x-axis movement exists while there is no angular motion due to the side walls being non-parallel.

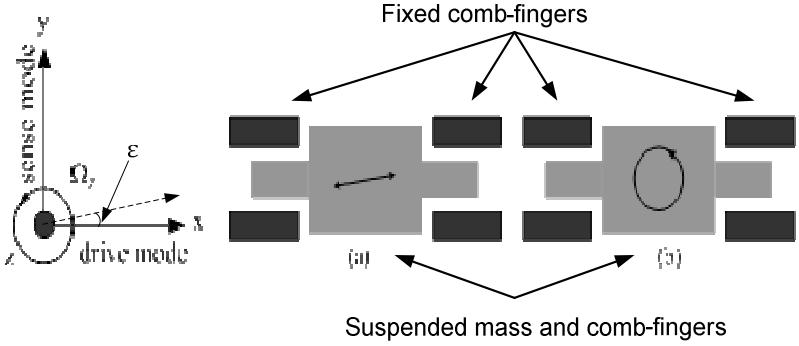

Figure 2.27: Sense mode representation. Black boxes represent fixed comb fingers and gray shapes represent the mass and moving comb fingers. ε is the angle between the ideal drive mode axis and the actual drive mode axis. (a) Motion caused by quadrature error and (b) Motion caused by Coriolis force (reproduced from [39]).

In mathematical terms, the quadrature error can be presented as follows; Assuming *x(t)* is motion in the drive mode, then $y_{Quadrature}$ is derived as follows:

$$x(t) = X_0 \sin(\omega_x t) \tag{2.32}$$

$$\boldsymbol{y_{Quadrature} = -\varepsilon . x(t)} \tag{2.33}$$

$$\boldsymbol{\ddot{y}_{Quadrature} = \varepsilon . X_0 . \omega_x^2 . sin(\omega_x t)} \tag{2.34}$$

Where $y_{Quadrature}$ is the displacement of sense mode due to the quadrature error and Ɛ is the coefficient between drive and sense mode movements, whose value can be expressed as a sine function of the angle between the x-axis (ideal drive mode direction) and the actual drive movement direction Ɛ (shown in Figure 2.27). In addition, the effect of the quadrature error can be presented as the existence of a signal in the power spectral density (PSD) of the output of the band-pass gyroscope as shown in Figure 2.28. In this figure, the quadrature error appears as a signal in the middle of two other spikes (which represent an angular motion input of 300 °/s). This signal power is produced by Ɛ=0.0005°. As it is shown, such small deviation can result in a huge amount of quadrature error. Moreover, the calculation of SNR for this figure shows that the signal to noise ration is -6.6dB. It must be noted that in this particular case, this negative number does not signify the existence of a huge amount of noise. To find out why a negative SNR is obtained for this figure, the calculation of the parameter must be explored.

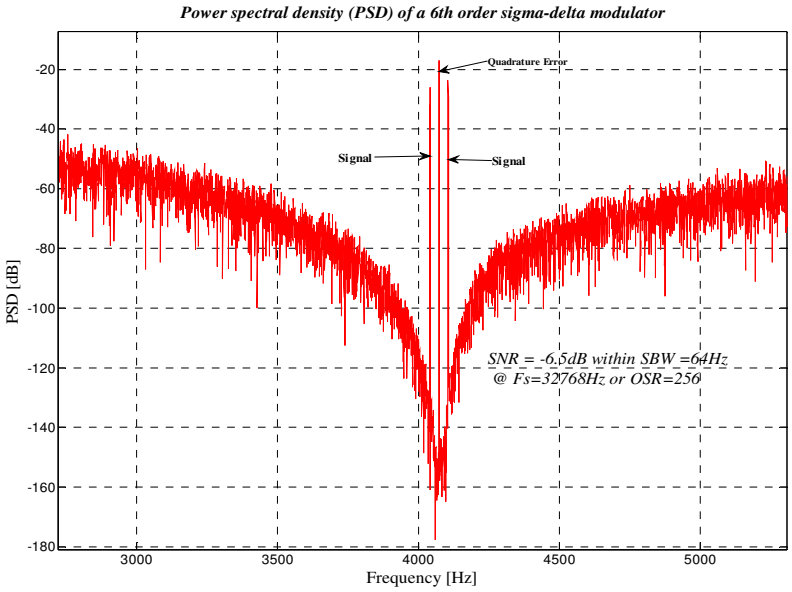

Figure 2.28: Power spectral density of the output bit stream of a 6th order band-pass micro-gyroscope sigma delta modulator for an input angular rate of 300°/s with quadrature error for drive axis deviation of Ɛ=0.0005.

The algorithm for calculation of SNR extracts the requested signal (in this case, angular rate of 300 °/s at 64Hz) from a given output signal. Then it calculates the power of all alternative signals (including quadrature error) as power of noise. Since the power of quadrature error is greater that

the power of the input signal, the resultant SNR becomes negative (here -6.5 dB). This calculation once more signifies that a small deviation from the ideal drive axis can give rise to substantial quadrature error.

2.5. Quadrature amplitude modulation

2.5.1. Introduction

Quadrature amplitude modulation (QAM) is a well-established technique that has been deployed in many communication systems for a long while. Since a part of the novel interface design uses QAM theory in its design and implementation, it is beneficial to review the theory of QAM in communication systems.

2.5.2. Quadrature amplitude modulation principle

In an amplitude modulation system, an information signal (e.g. audio) is modulated at a higher frequency with a carrier signal [40] [41]. In other words, the modulated signal has the amplitude that follows the magnitude of the information signal and its frequency is that of the carrier signal. A diagram of the operation of this type of modulation is shown in Figure 2.29.

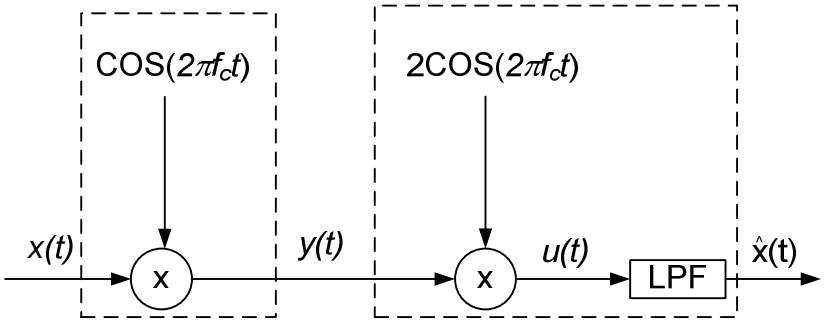

Figure 2.29: Amplitude modulation and demodulation system diagram for x(t) as an information signal with the carrier frequency of f_c (reproduced from [40]).

In Figure 2.29, x(t) is the information signal and is used to vary the amplitude of the carrier signal. In this case, the carrier is a sinusoidal signal $cos(2\pi f_c t)$, where f_c is usually considerably higher than the highest frequency in the message. The mathematical analysis of amplitude modulation and demodulation is as follows:

$$y(t) = x(t)\cos(2\pi f_c t) \tag{2.35}$$

$$u(t) = 2x(t)\cos(2\pi f_c t)\cos(2\pi f_c t) \tag{2.36}$$

where *y(t)* is the output signal from the modulator and u(t) is the product to be fed into the low-pass filter (LPF). Using the trigonometric identity $2\cos(\theta) = 1 + \cos(2\theta)$, the following equations are derived:

$$u(t) = x(t)(1 + \cos(4\pi f_c t)) \tag{2.37}$$

$$u(t) = x(t) + x(t)\cos(4\pi f_c t) \tag{2.38}$$

The signal u(t) contains both low- and high-frequency components and once the signal is passed through LPF, only the x(t) term (information signal) remains. So far, only a cosine carrier wave has been considered. Very similar results would be obtained with a carrier wave. This is due to the fact that the sine and cosine functions differ only by a phase shift of π/2 radians. This regulation indicates that the cosine and sine functions are orthogonal to each other, meaning that a signal $x_i(t)$ that is amplitude modulated onto a cosine carrier wave will not interfere with another signal $x_q(t)$ that is modulated onto a sine carrier wave having the same frequency f_c. In this way, we can transmit two signals at once, which is useful for stereo audio transmission for example. These signals are referred to as the in-phase signal $x_i(t)$ and the quadrature-phase signal $x_q(t)$. The additional presence of the quadrature-phase signal gives quadrature amplitude modulation (QAM) its name. A schematic for QAM in a communication system is shown in Figure 2.30

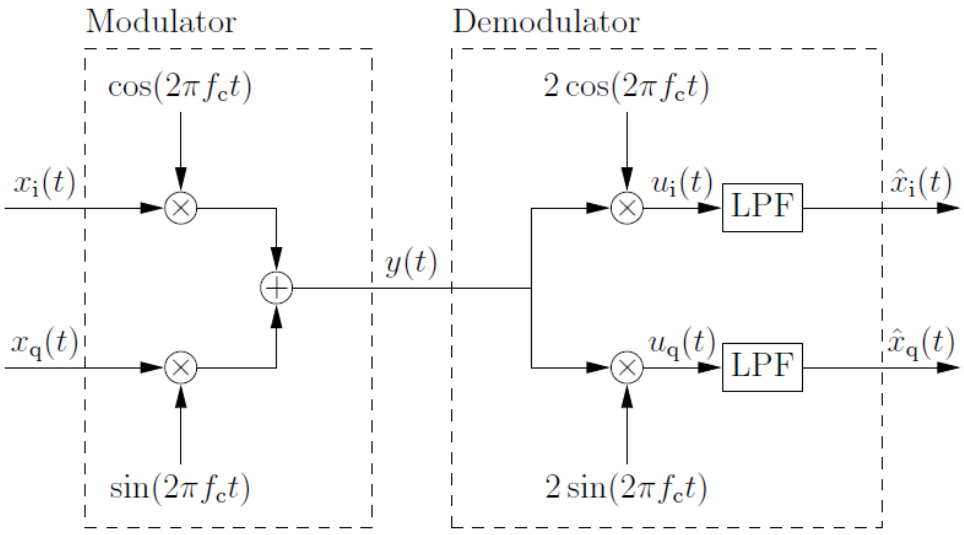

Figure 2.30: Quadrature amplitude modulator and demodulator system schematic. In this figure $x_i(t)$ and $x_q(t)$ are two signals that are both modulated at the same frequency with the 90 degrees phase difference (reproduced from [40]).

As shown in Figure 2.30, *y(t)* (the modulation combination) is produced as follows:

$$y(t) = x_i(t)\cos(2\pi f_c t) + x_q(t)\sin(2\pi f_c t) \tag{2.39}$$

$$u_i(t) = 2x_i(t)\cos(2\pi f_c t)\cos(2\pi f_c t) + 2x_q \sin(2\pi f_c t)\sin(2\pi f_c t) \quad (2.40)$$

$$u_q(t) = 2x_q(t)\sin(2\pi f_c t)\sin(2\pi f_c t) + 2x_i \cos(2\pi f_c t)\cos(2\pi f_c t) \quad (2.41)$$

According to trigonometric rules the following equations hold valid as identities:

$$2\cos(\theta)\cos(\theta) = 1 + \cos(2\theta) \quad (2.42)$$

$$2\sin(\theta)\sin(\theta) = 1 - \cos(2\theta) \quad (2.43)$$

Using (2.42) and (2.43) in equations (2.40) and (2.41) results in the following equations:

$$u_i(t) = x_i(t) + x_i(t)\cos(4\pi f_c t) + x_q(t)\sin(4\pi f_c t) \quad (2.44)$$

$$\boldsymbol{u_q(t) = x_q(t) - x_q(t)\cos(4\pi f_c t) + x_i(t)\sin(4\pi f_c t)} \quad (2.45)$$

After applying LPF on $u_i(t)$ and $u_q(t)$ as shown in Figure 2.30, information signals are obtained as shown below:

$$\hat{x}_i(t) = x_i(t) \quad (2.46)$$

$$\hat{x}_q(t) = x_q(t) \quad (2.47)$$

As it is proved, from a mixture of two signals that have the same frequency but are in quadrature, the two original signals can be extracted using the above technique [42] [43].

2.6. Summary

In this chapter the fundamental theory of micro-machined vibratory gyroscopes was presented. Then the root cause of quadrature error was described and explored. Further more, the theory and technique of quadrature modulation and demodulation was introduced and discussed. It will be shown in chapter 4 how this technique is used in the novel gyroscope system.

Chapter 3 Literature review

3.1. Introduction

In this chapter previous contributions towards improvement of performance of both open-loop and closed loop gyroscopes are discussed. First, the improvements at device (sensing element) fabrication level are presented. Then, different architecture of closed-loop gyroscopes are presented and discussed. Moreover, as the design of a read-out circuit is essential for circuit implementation in this project, a review is presented of a number of proposed capacitive sensor read-out circuits. Ultimately, the focus of the review is set on research about reducing and compensating the effect of quadrature error for systems of different variety (in architecture). Discussions will include quadrature error compensation methods at sensing element fabrication level and circuit implementation level. After an in-depth review, a brief overview of all research around this subject (quadrature error compensation) is presented in a table of figures, followed by conclusions.

3.2. Open loop gyroscopes

In 1991, the Charles Stark Draper laboratory demonstrated one of the first silicon-micro-machined rate gyroscopes at a resolution of 4 °/s [4] [44]. This bulk silicon device was a double gimballed vibratory gyroscope supported by flexures with the vibrating mechanical element made of silicon. Draper later reported a further improved silicon on-glass tuning fork gyroscope fabricated by the dissolved wafer process in 1993 [45]. One of the sensing element designs originally designed by the Draper Laboratory and later used by Honeywell is shown in Figure 3.1 . The gyro element size is 1.5mm×1.1mm including stators and bond pads. The gyro element is made of boron-doped silicon using the deep reactive ion etching (DRIE) process [46].

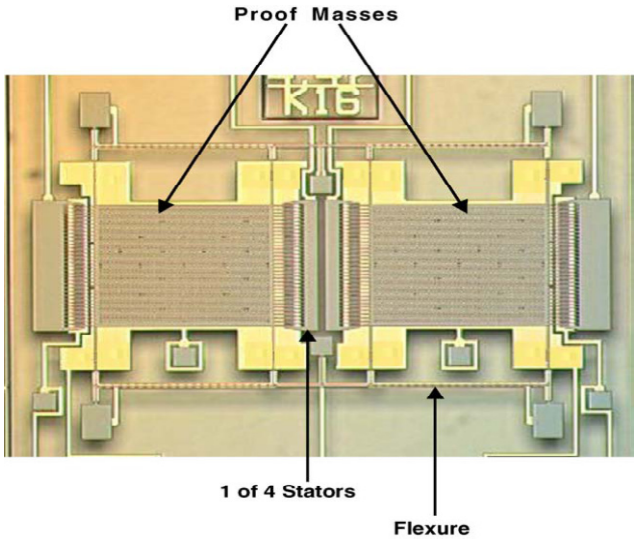

Figure 3.1: Tuning-fork differential gyro element anodically bonded on glass the device was originally designed by the Draper Lab (reproduced from [46]).

In 1995, Tanaka et. al. at the Yokohama research & development centre, introduced their surface micro-machined vibrating gyroscope which delivered a resolution of 7 °/s. Despite the relatively low resolution it was proved that ion beam milling helps to reduce the mismatch between the frequencies of drive and sense modes. Moreover, vacuum packaging was deployed in the fabrication process of this gyroscope and Q factors of 2,800 and 16,000 were obtained for drive and sense modes respectively. It was shown that deploying both techniques (ion beam milling and vacuum packaging) contributes towards increasing the mechanical sensitivity of a gyroscope sensing element [47].

There have been other attempts in order to design and fabricate micro-machined gyroscope based on comb-fingers structures. In 1999, Francis E. H. Tay et al. attempted to fabricate a gyroscope sensing element and they produced a device which had a sensitivity of 35 °/s at a resonant frequency of 3.3 kHz [48].

In 1998,Farrokh Ayazi designed the first of the poly-silicon vibrating ring gyroscope using combined bulk and surface micromachining technology as shown in Figure 3.2. The advantage of this design was a lower noise floor which was measured at 0.8×10^{-3} °/s/√Hz. Another advantage, from a fabrication standpoint, of this gyroscope sensing element is the ability to avoid the process complications normally associated with fabricating a surface machined or bulk machined gyroscopes. However the notable disadvantage of such a micro-gyroscope is that over time it is prone to wear at the rotor shaft area [49]. Therefore the majority of works have focused on tuning fork vibratory gyroscopes.

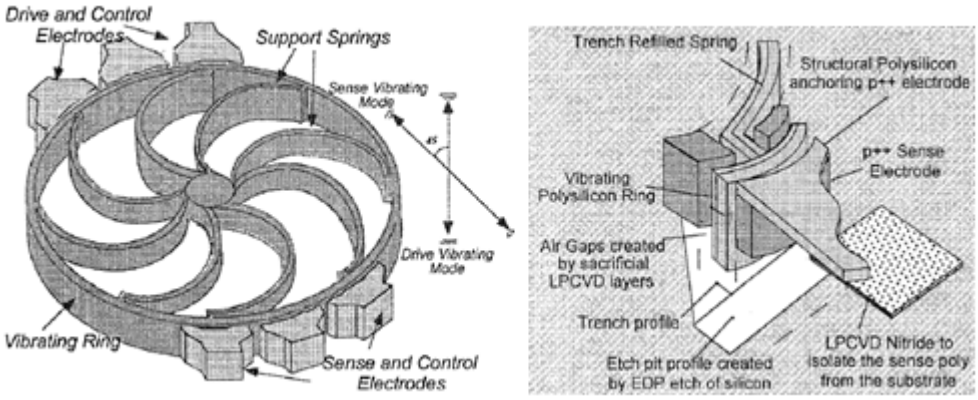

Figure 3.2: Structure of a Vibrating Ring Gyroscope (left). The new vibrating ring gyroscope utilizing polysilicon to form the thick, high aspect ratio ring, and p++ microstructures for sense/drive electrodes (right) (reproduced from [49]).

Further progress was achieved in 2002 by M. Palaniapan et al. at the Berkeley sensor & actuator centre, University of California. They introduced an integrated surface-micro-machined z-axis frame micro-gyroscope which was fabricated by using a modular-MEMS process using 6μm thick poly-silicon as the structural material and 5V 0.8μm CMOS process. This gyroscope would

work at vacuum pressure and matched mode in order to maximize the quality factor, hence maximising the displacement at sense mode. Also, in order to avoid unstable operations due to matching of modes a decoupled drive and sense mode structure is used. The design of the decoupled frame is shown in Figure 3.3. The experimental results showed 0.33 mV/º/s/√Hz sensitivity and 0.05 º/s/√Hz noise floor for this gyroscope sensing element [50].

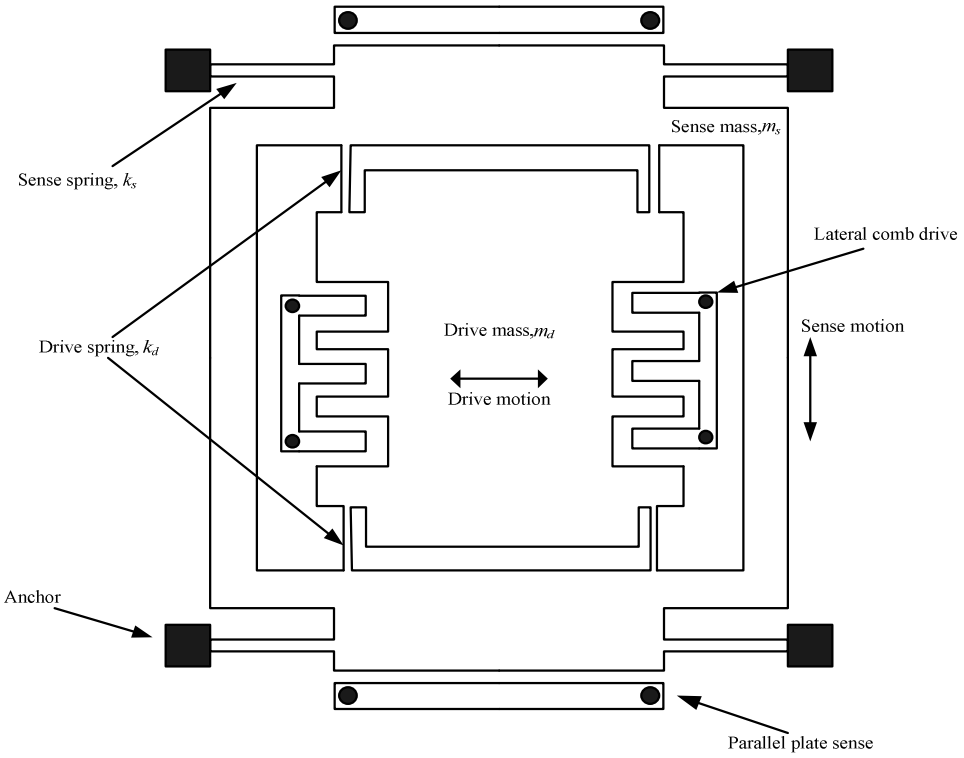

Figure 3.3: Decoupled frame structure for drive mode and sense mode used in Berkeley sensor & actuators centre micro-gyroscope 2002 (reproduced from [50]).

Further, in 2006, the MEMS centre of Harbin institute of technology presented a low noise bulk micro-machined gyroscope with a symmetrical and decoupled structure fabricated using DRIE (deep reactive ion-etch) process and silicon-glass anodic bonding. This gyroscope sensing element achieved the noise floor of 3.33×10^{-5} º/s/√Hz at atmospheric pressure [51]. Moreover, in 2008 Zaman et al. reported the design and fabrication of an in-plane mode-matched tuning fork gyroscope (M^2-TG) sensing element. This sensing element uses two high-quality-factor (Q) resonant flexural modes of a single crystalline silicon microstructure to detect angular rate about the z axis. It is reported that this sensing element achieved zero hertz split frequency between drive and sense modes. This achievement resulted in quality factor amplification in angular rate sensitivity and also improved overall noise floor and bias stability of the sensing element. For this device bias instability of 0.15 º/h and 83 mV/ º/s was achieved. Furthermore, in 2009 A. Truson et al. at MicroSystems laboratory reported, for the first time, on the development of a gyroscope sensing element architecture with structurally forced anti-phase drive-mode and linearly coupled,

dynamically balanced anti-phase sense-mode. The new design utilizes two symmetrically-decoupled tines with drive- and sense-mode synchronization mechanisms, and prioritizes the sense-mode quality factor as shown in Fig. 3.4. The levered drive mode mechanism structurally forces the anti-phase drive mode motion and eliminates the lower frequency spurious modes. The linearly coupled, dynamically balanced anti-phase sense-mode design minimizes substrate energy dissipation. The results are based on SOI prototypes characterized in vacuum that demonstrated a drive-mode quality factor of 67,000 and an ultra-high sense-mode quality factor of 125,000, yielding a mechanical scale factor of 0.4 nm/(°/h) for mode-matched operation [52].

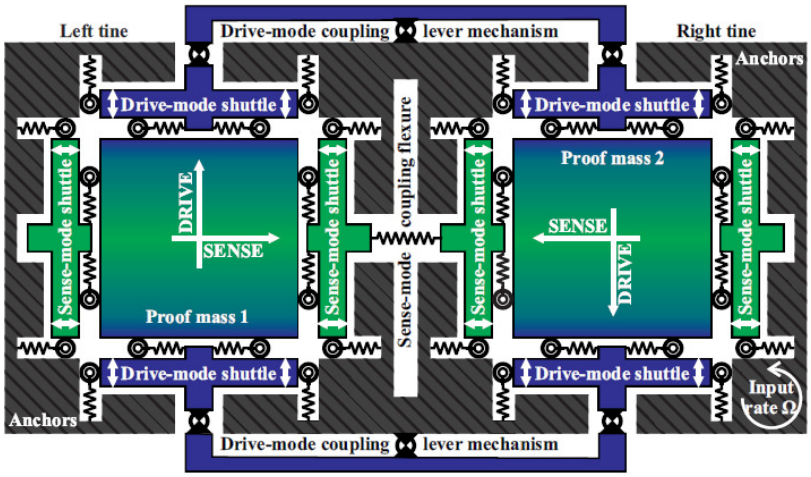

Figure 3.4: Structural schematic of the proposed gyroscope architecture with levered anti-phase drive-mode and linearly coupled anti-phase sense-mode for maximising the Q-factor of the sense mode (reproduced from [52]).

In 2010 H. Ding et al. reported on the fabrication of a high-resolution silicon-on-glass z-axis gyroscope operating at atmospheric pressure. The mechanical structure was designed in such a way that it exhibited low cross coupling between drive and sense modes namely less than 1.35%, as verified by experimental measurements. Also, due to a symmetrically designed structure, the specified bandwidth can be maintained in spite of fabrication imperfections. The fabrication process flow for this gyroscope was based on a combination of silicon on glass bonding and deep reactive ion etching which, resulting in a large proof mass and capacitances. Using area-varying capacitors, large quality factors of 217 and 97 for drive and sense modes, respectively, were achieved while operating at atmospheric pressure. This achievement in structure of this gyroscope leads to obtaining 0.0015 °/s/√Hz in a 50 Hz bandwidth and a sensitivity of 10.2 mV/°/s for a dynamic range of ±300°/s [53].

Over the past few years, the number of academic groups the attempted towards improving the performance of micro-machined gyroscopes by improving the mechanical structure of the sensing element. However, some characteristics (e.g. linearity and dynamic range) can be improved by

deploying other mechanisms and solutions where the sensing element is a sub system and is surrounded by some other mechanisms to improve the performance of the gyroscope system.

3.3. High order closed loop control for a micro-machined gyroscope

As was briefly discussed in 2.3, the advantages of closed loop EMSDM have made it an attractive option for designing control systems for inertial sensing systems. Early attempts were made by designing low order (i.e. second order) EMSDMs [54] [55] and later on some higher order inertial systems have been reported, proving that while the advantages on lower order systems are retained, quantization noise can be significantly improved and as a result better resolution is achievable [25] [29].

In 2006, J. Raman et al. at Ghent university, presented a 5th order closed-loop sigma-delta force-feedback architecture that was proposed as a gyroscope system. This system is based on low-pass SDM architecture as shown in Figure 3.5.

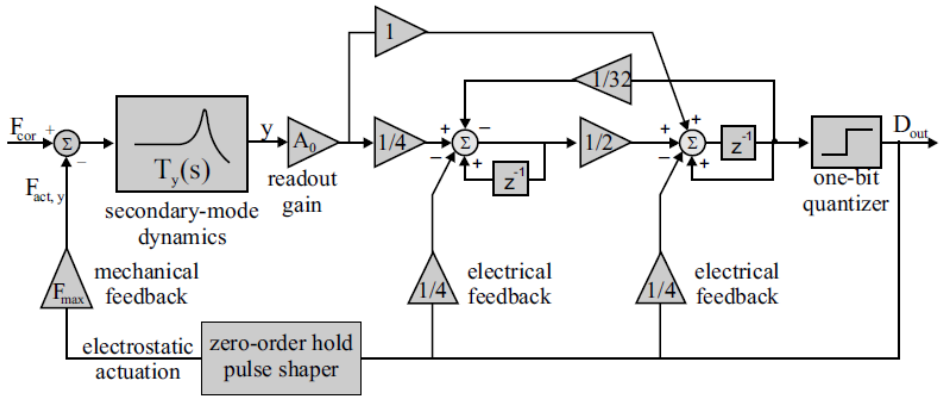

Figure 3.5: Low-pass EMSDM architecture for secondary (sense) of a gyroscope sensing element. This systems uses feed forward arrangement of low-pass filters for noise shaping (reproduced from [56]).

This architecture showed a significant improvement in dynamic range and delivered the resolution of about 0.055 °/s/√Hz. Also, it was proved that a stable interface can be designed without an explicit compensation filter as this filter could affect noise-shaping [56].

In 2006, Mikko Saukoski et al. reported the fabrication of an application specified integrated circuit (ASIC) for read-out and closed-loop system (all in one chip) along with FPGA implementation of digital signal processing. This interface deploys a band-pass electronics SDM sub-system and a DSP (digital signal processing) block for both primary (drive mode) mode and secondary (sense) mode. In the sense mode (as shown Figure 3.6), after the output is converted to a digital bit-stream, the quadrature error portion of the output is fed to a high voltage digital to analogue converter in order to generate quadrature error compensation electrostatic force. It is also

using the closed-loop architecture to control the primary mode by controlling the drive frequency and amplitude. This prototype achieved 0.053 °/s/√Hz with 49.9 dB signal-to-noise ratio frequency of 36 Hz [57]. Later in 2008, the implementation of this interface was revised and improved and a noise floor of 0.042 °/s/√Hz was measured over 40 Hz, and a signal to noise ratio of 51.6 dB against a 100°/s input angular rate was achieved [58].

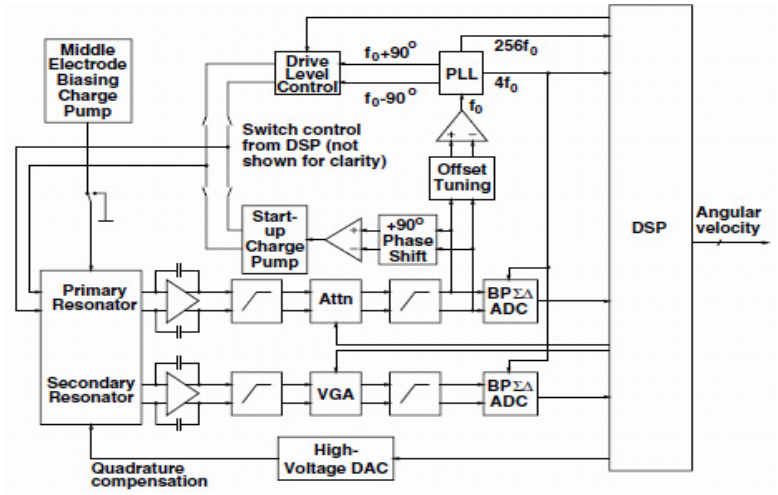

Figure 3.6: Complete read-out and control system for a bulk micro-machined gyroscope. A band-pass SDM architecture is used to control both primary (drive) and secondary (sense) modes. The secondary mode output bit-stream is used to dynamically compensate the quadrature error (reproduced from [57]).

In 2007, Y. Dong et al. presented the first EMSDM which used band-pass electronic loop filter for noise shaping. As shown in Figure 3.7 this system was built by coupling the sensing element (in this case the sense mode of the sensing element) to a pure electronic band-pass SDM. Effectively this arrangement uses a band-pass form of noise-shaping for eliminating the quantization noise around the resonant frequency at which the sensing element is operating.

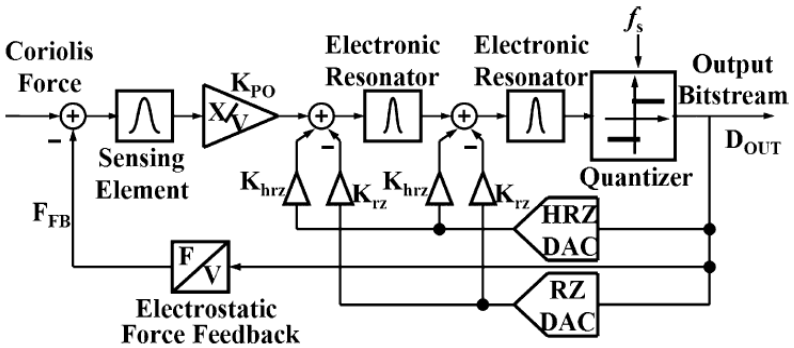

Figure 3.7: Control loop for the sense mode of a micro-machined gyroscope sensing element. In this interface the sense mode is embedded in a 6th order band-pass EMSDM by replacing the first second order loop filter with the sense mode of a sensing element (reproduced from [25]).

Furthermore, in 2008 D. Chinwuba et al. presented a gyroscope that exploited mode matching and boxcar sampling [59] to reduce power dissipation. The interface ensures mode matching over tolerances of MEMS and IC fabrication and ambient variations using background calibration, and addresses the bandwidth and gain-stability challenges raised by the high-Q sensing element using a force-feedback architecture that is robust against spurious mechanical resonances. A brief system diagram of this system with emphasis on deploying of EMSDM for the sense mode is shown in Figure 3.8.

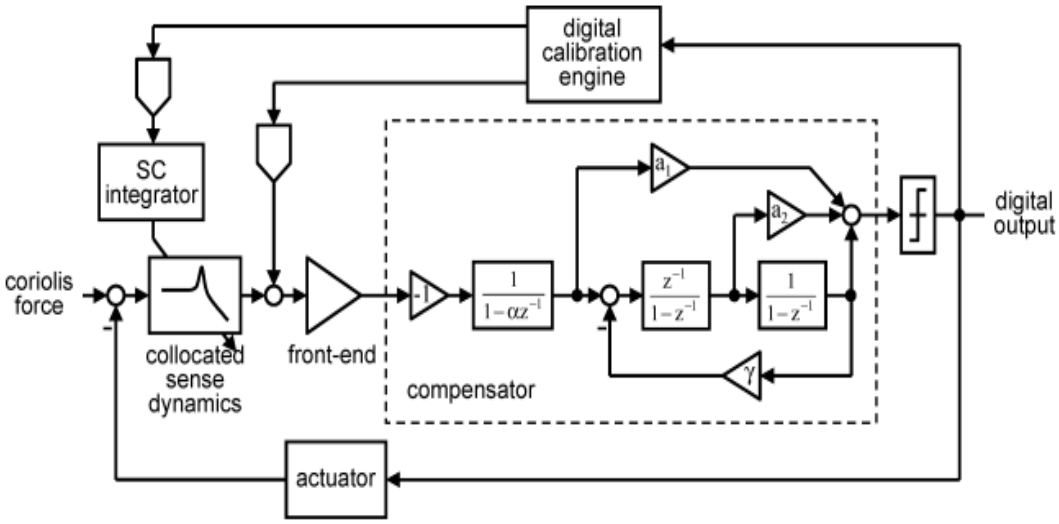

Figure 3.8: Force feedback loop using low-pass modulator. Also quadrature error compensation is presented (reproduced from [60])

In this design, a noise floor of 0.004 $°/s/\sqrt{Hz}$ at the bandwidth of 50 Hz was measured. Measurements also showed about one order of magnitude reduction in level of quadrature and offset error. The paper also shows that due to the use of boxcar sampling and mode-matching technique the power dissipation has significantly reduced [60].

Later in 2012, F. Chen et al. reported an implementation of band-pass EMSDM architecture where the resonators and pick-off of the system (shown in Figure 3.7) are built by using analogue operational amplifiers and sampling signal, half return zero (HRZ) and return zero (RZ) and feedback signals where generated by using micro-controller and FPGA as shown in Figure 3.9. This implementation, showed improvements in band-width and bias stability in comparison to open loop gyroscope with the same sensing element. These improvements are achieved in terms of scale factor, bias stability and band-width. In this work, scale factor increased from 14.3 mV/°/s to 22 mV/°/s, bias stability decreased from 89°/h to 34.15°/h and bandwidth increased from 50Hz to 110Hz [61].

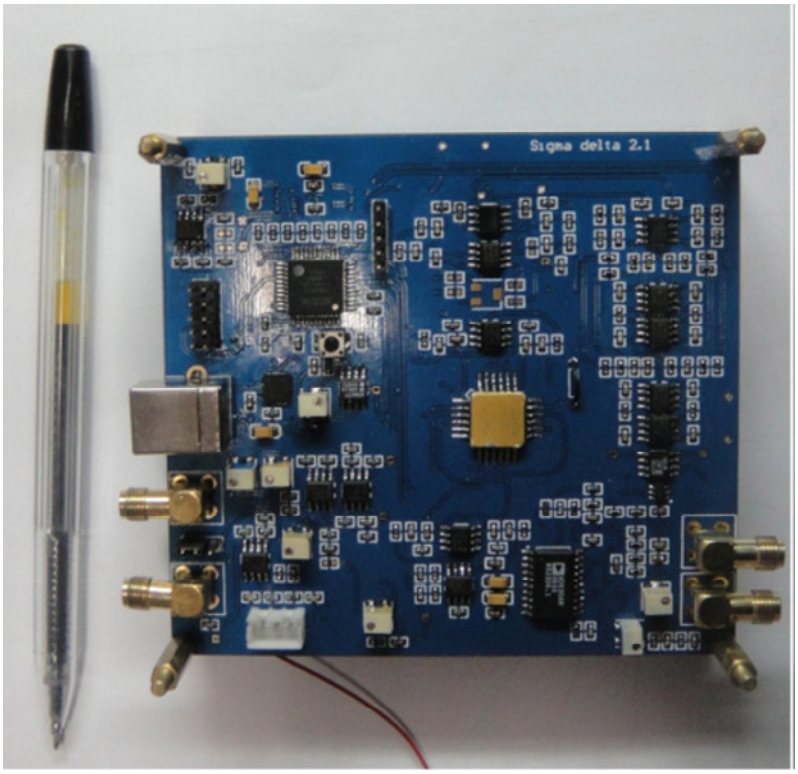

Figure 3.9: Sixth order band-pass EMSDM interface circuit that is implemented on a PCB (reproduced from [61]).

3.4. Read-out circuits for sensing element

As was shown in chapter 2, the displacement against induced Coriolis force is realized as proof mass displacement, hence a change in capacitance between proof mass and finger combs. This block in the Simulink model in chapter 4 is shown as simple gain; however, in practical circuits (real world), a mechanism is needed to read the changes of proof mass location as an electric signal. In other words, the variation of charge in the sense mode of the micro-gyroscope needs to be read out. There are two methods considered for implementing the readout circuit:

- Circuits based on switched capacitors [62] [63] [64]: In a switched capacitor circuit the sense and reference capacitors are charged with voltages of opposing polarity and a packet of charge proportional to the capacitance difference is integrated on the input feedback capacitor (C_{int}) [64]. This type of circuit is implemented as an ASIC structure because it is impossible to find symmetrical discrete transistors. A conceptual diagram of this circuit is shown in Figure 3.10.
- Circuits that use modulation and demodulation technique: For demonstrating this type of circuit, a capacitance to voltage converter (CVC) circuit that is described in details is presented here. The basic circuit of the differential capacitance to voltage converter is shown in Figure 3.11. The CVC is completely symmetrical and consists of two frequency- independent half ac-bridges which act as AM modulators, two AM

demodulators, and an instrumentation amplifier which rejects common mode signals. In Figure 3.11, one of the electrodes of the variable sensor capacitance is connected to a voltage source providing an excitation voltage $V_{excitation}$ with a carrier frequency of $F_{carrier}$[Hz] and a $V_{carrier}$ amplitude [V], and the other one to the input of a current detector (which is at virtual ground potential) with a very low input impedance.

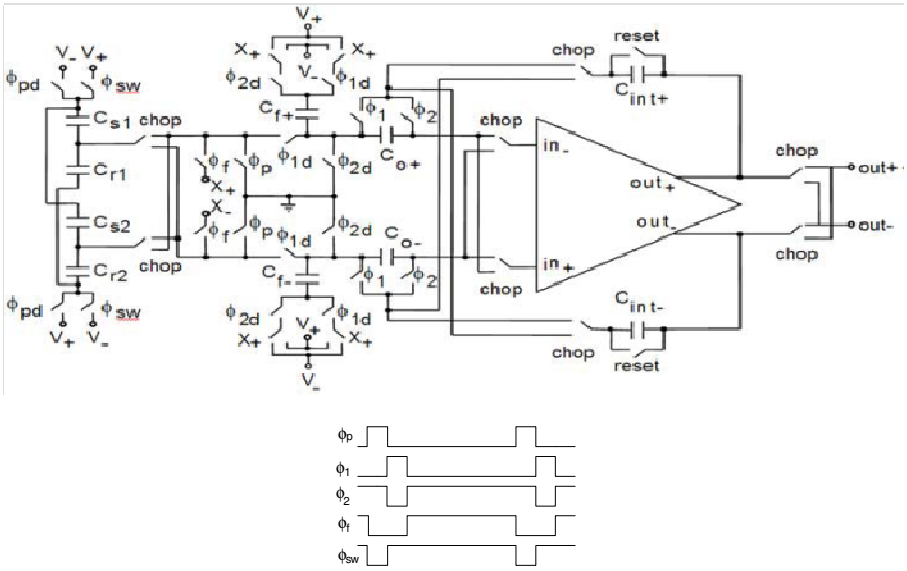

Figure 3.10: A readout circuit for capacitive accelerometers based on switching capacitors. The main clock phases are ϕ_p: pre-charge; ϕ_1: readout phase; ϕ_2: Offset sampling for CDS; ϕ_f : Feedback phase for closed-loop operation mode; ϕ_{sw}: Sense electrode in readout & feedback phases. Reset phase (reset) and ϕ_2 are the same (reproduced from [64]).

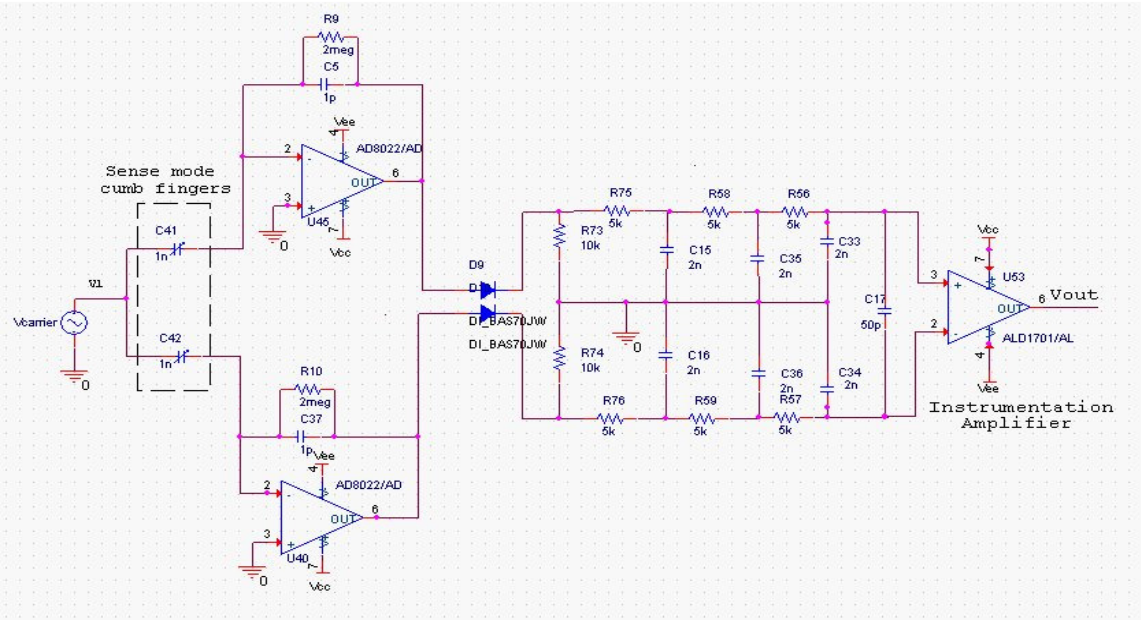

Figure 3.11: Capacitance to voltage convertor circuit based on concepts of ac-bridge and amplitude modulation and demodulation (adopted from [63]).

Considering the fact that it is impossible to have 100% symmetric discrete transistors and on the other hand it is less time consuming and more cost effective for this project to implement the ac-bridge circuit, this has been chosen as the pick-off circuit for our interface despite the fact that switched capacitors readout circuits can be more accurate. However, increasing the carrier frequency can compensates this shortage to a significant extend. Also, the advanced technology of operational amplifiers makes it possible to increase the carrier frequency significantly (beyond 1 MHz).

3.5. Quadrature error cancellation techniques

As discussed in section 2.4, quadrature error is one of the main challenges that confront the accuracy and specially the dynamic range of micro-machined gyroscopes [37]. Hence, several quadrature error compensation techniques have been introduced. In this section, previous works on compensating quadrature error which have been deployed in both open-loop and closed-loop micro-gyroscopes are presented with a critical review.

In 1996 Clark et al. proposed applying a balancing force to the proof mass. As quadrature error is a signal which is directly proportional to the position of the proof mass, a balancing force is applied to the proof mass which is exactly proportional to the position of the proof mass. As the proof mass oscillates, the position sense capacitors change proportionately. Applying slightly different V_{DC} voltage to sense mode comb fingers results in a net force directly proportional to position of the proof mass as given by equation (***3.1*** [39]:

$$F_y = \frac{2C_{overlap}}{y_0} V_{DC} \Delta V . x(t) \tag{3.1}$$

In this equation, F_y is the balancing force, $C_{overlap}$ is the capacitance between sense mode comb fingers and proof mass fingers, y_0 is the displacement in sense mode due to quadrature error and *x(t)* is the displacement of proof mass due to the oscillation of drive mode.

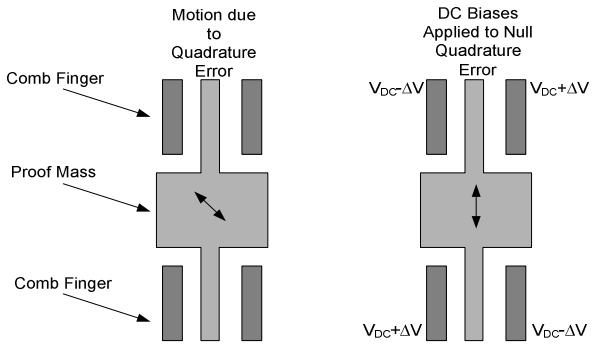

Figure 3.12: The figure on the left shows the displacement of the proof mass due to the presence of quadrature error and the figure on the right shows the movement after the effect of quadrature error is eliminated by applying an asymmetric DC bias to sense fingers (reproduced from [39]).

In 2006, Saukoski et al presented a technique in which the quadrature error is detected and extracted by using coherent demodulation of the output signal of band-pass SDM (in digital format). Then the extracted digital signal is fed into a high-voltage digital to analogue converter (HV- DAC) in order to generate a voltage level that is proportional to the displacement which is due to quadrature error. Ultimately the HV DAC output is applied to feedback nodes on the sense mode of the sensing element as shown in Figure 3.13 [57].

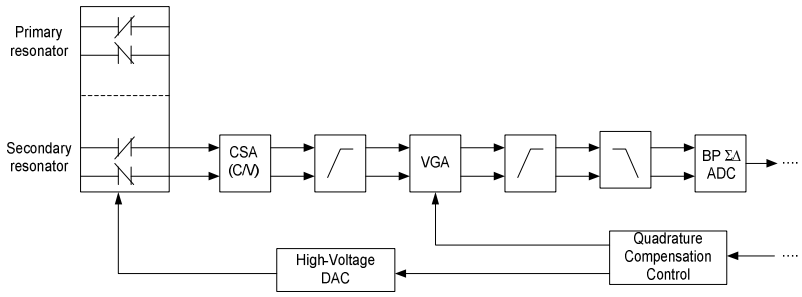

Figure 3.13: Quadrature error compensation is applied as a voltage that is produced from a 7 bit data that is generated produced by coherent demodulation in digital domain of the interface (reproduced from [57]).

It must be noted that in this system, the sensing element is working in open loop mode and only the quadrature error compensation signal is fed to the feedback comb finger set of the sense mode.

In 2008, Bo Yang et al, published a quadrature and offset error correction, which deploys a phase sensitive detection mechanism to detect and extract these errors. The detected quadrature error and offset error are separately restructured electronically and an electrostatic force which is proportional to quadrature error and an electrostatic force which is proportional to the offset error is applied to the sense mode of the sensing element as shown in Figure 3.14 [65].

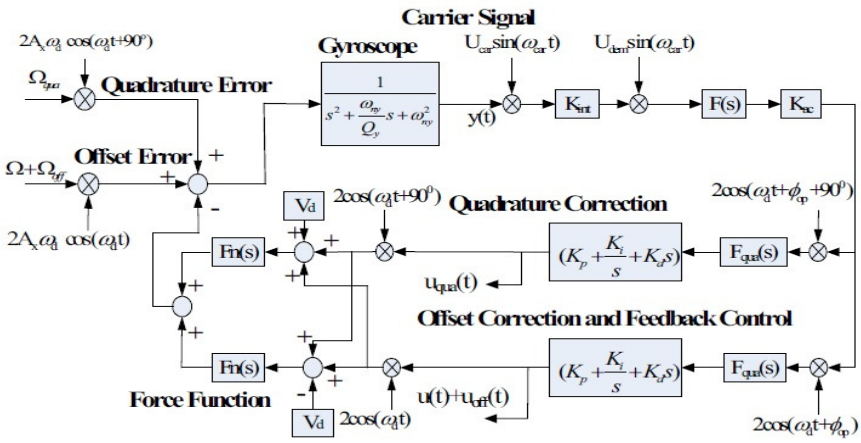

Figure 3.14: Schematic of the closed-loop feedback control with quadrature error. The two compensation signals are extracted by a phase sensitive demodulation method and the equivalent magnitudes of both errors are fed back to the sensing element as electrostatic forces (reproduced from [65]).

Ezekwe et al. proposed the injection of calibration, dither and offset compensation signal as a method of compensation for offset and quadrature error (collectively). This method was deployed for the low-pass EMSDM gyroscope. In this method, a slow regulation loop is used to force the average output of the quantizer to zero, which ensures that the average input of the quantizer is also zero. In this method, the compensation signal is injected before the from-end circuit to reuse the already available systems blocks. A conceptual schematic of this method is shown in Figure 3.15 [60].

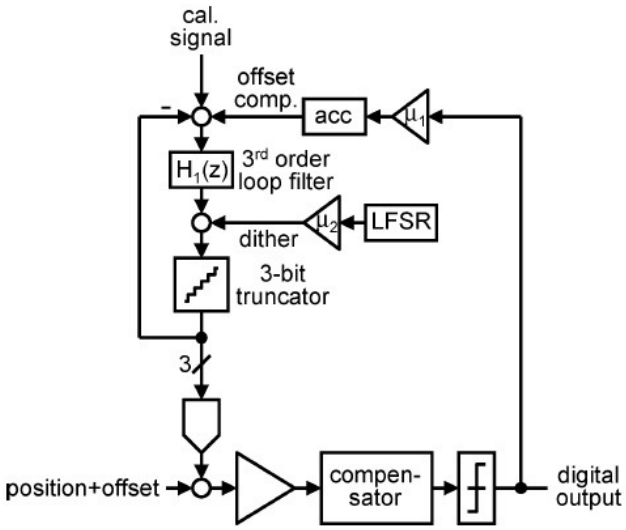

Figure 3.15: Conceptual schematic of the offset & quadrature error compensation signal injection (reproduced from [60]).

In 2009, Antonello et al, proposed the use of two banks of capacitors between the sense mode nodes and the read-out circuit. As shown in Figure 3.16, in this scheme two banks of capacitors $C_{s,+}$ and $C_{s,-}$ (as the sense mode output is differential) are placed in parallel with the capacitance of the sense mode in the sensing element $C_{c,+}$ and $C_{c,-}$. These capacitors perform the quadrature error compensation directly on the measured displacement of the proof mass. This mechanism effectively avoids the saturation of the following read-out circuit. The effect of deploying quadrature error compensation at the output of read-out circuit is presented as:

$$V_{\circ}(t) = -\frac{C_{s,+}(t) - C_{s,-}(t)}{C_I} V_s - \frac{C_{c,+}(t) - C_{c,-}(t)}{C_I} V_s \tag{3.2}$$

In this equation, C_I is the integration capacitor of the charge amplifier in Figure 3.16 and V_s the amplitude of carrier voltage source. In this implementation, due to symmetry in the mechanical structure, the sensing capacitors can be written as:

$$C_{s,+}(t) = C_s + \frac{\delta C_s(t)}{2}, C_{s,-}(t) = C_s - \frac{\delta C_s(t)}{2} \tag{3.3}$$

where $\delta C_s(t)$ is the sense mode capacitance variation and it is proportional to the motion of the proof mass due angular motion and quadrature error. Therefore, the output $V_o(t)$ is derived as:

$$V_o(t) = -\frac{V_s}{C_I}[\delta C_s(t) + \delta C_c(t)] \tag{3.4}$$

Hence the compensation capacitance (C_c) must be built in a way that it satisfies the following condition:

$$\delta C_c(t) = -\delta C_q(t) \tag{3.5}$$

Where $\delta C_c(t)$ is the variation of the compensation capacitor and $\delta C_q(t)$ is the variation of the sense mode capacitance due to quadrature error. In other words, by adjusting the capacitance of compensation capacitors, the variation of compensation capacitance equals the variation of the proof mass due to quadrature error. This method is realized as part of the electromechanical micro-structure which is fabricated as a part of ASIC structure [38].

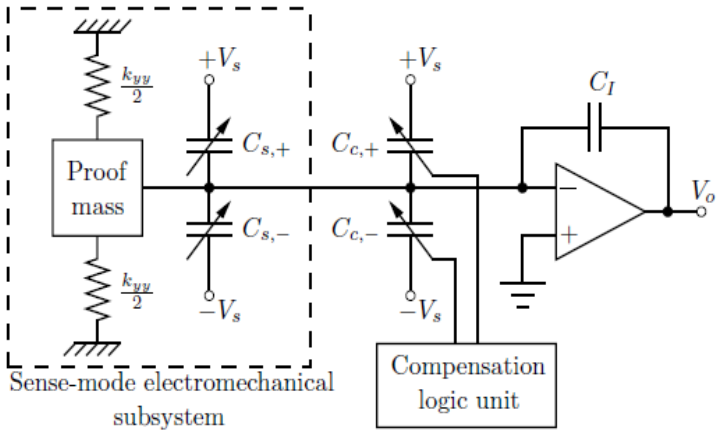

Figure 3.16: Circuit diagram presenting the deployment of quadrature error compensation capacitors (C_{c+},C_{c-})(reproduced from [38]).

In 2010, Descharles et al proposed a quadrature error compensation that is based on the PID (proportional–integral–derivative) control. Firstly, a passive quadrature error compensation was implemented by re-injecting the driving charges (which are in quadrature with charges due to Coriolis force) in the sense channel through the same drive impedance as that shown in Figure 3.17a. Furthermore, an active architecture which is based on the same principle was proposed in the same work. In active architecture, a demodulator extracts the quadrature error and the amplitude of

this signal commands a FET transistor through a PI (proportional-integrator) corrector to adjust the compensation gain. It was proved that compensating quadrature error improves bias stability by three times. The conceptual presentation of this method is shown in Figure 3.17b [66].

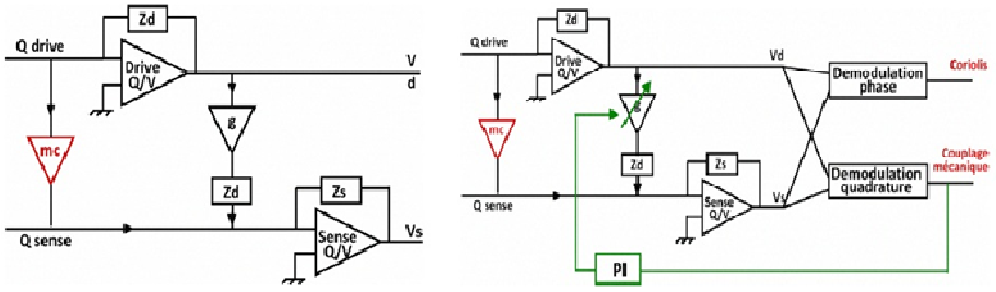

(a) (b)

Figure 3.17: Schematic of (a) passive and (b) active quadrature error compensation by re-injecting drive charges in the sense channel (reproduced from [66]).

In 2011, Tatar et al, proposed the idea of adding quadrature error compensation electrodes to the proof mass frame of the sensing element Fig. 3.14. A DC potential is applied to these electrodes while AC phase information is directly picked from the drive displacement itself.

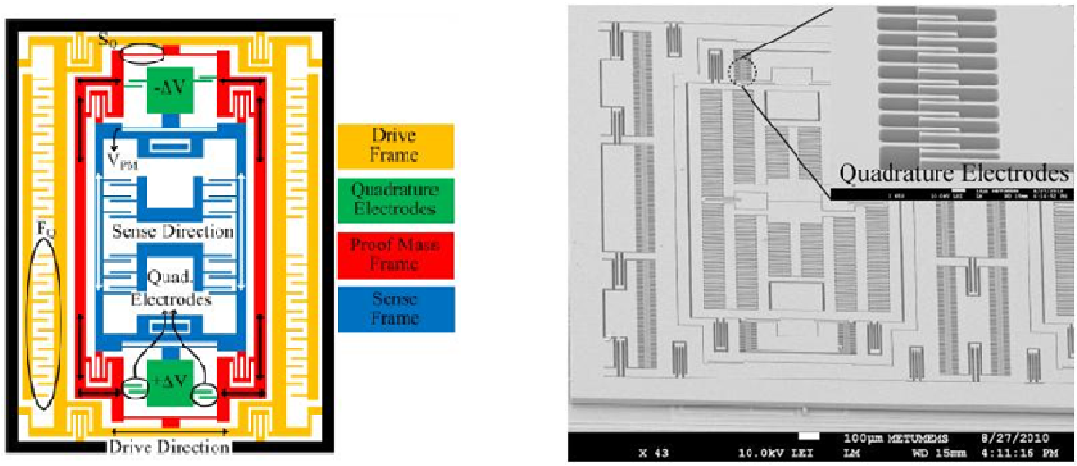

(a) (b)

Figure 3.18: Implementation of a mechanical structure for quadrature error compensation (a) simplified structure (b) SEM photograph (reproduced from [67]).

Table 3.1: Experimental demonstration of zero rate output improvement with the quadrature error cancellation (reproduced from [67]).

Performance Parameters		Gyro #1	Gyro #2
Zero rate output (mV)	With quad. cancellation	0.25	2.5
	Without quad. cancellation	-207	235
	Factor of improvement	828	89

Table 3.2: Experimental demonstration of bias stability improvement with quadrature error cancellation (reproduced from [67]).

Performance Parameters		Gyro #1	Gyro #2
Bias (°/h)	With quad. cancellation	0.91	3.1
	Without quad. cancellation	7.1	12
	Factor of improvement	7.8	3.9

Table 3.3: Experimental demonstration of angle random walk improvement with quadrature error cancellation (reproduced from [67]).

Performance Parameters		Gyro #1	Gyro #2
Angel random walk (°/√h)	With quad. cancellation	0.034	0.07
	Without quad. cancellation	0.36	0.49
	Factor of improvement	10.6	7

Moreover, it was shown how quadrature cancellation can affect bias stability and angle random walk. Implementing the quadrature nulling method has proved to improve these two parameters by up to 10 times. The improvement on two sample gyroscope sensing elements is shown in Table 3.1, Table 3.2 and Table 3.3 [67].

3.6. Discussion and conclusion

In this chapter, contributions towards improving the performance of micro-machined gyroscopes were presented. As reviewed in section 3.2, attempts were made to improve the sensitivity, accuracy and bandwidth by improving the fabrication process and proposing different mechanical structures. Moreover, as closed-loop systems have advantages such as improved bias stability, increased dynamic-range and improved bandwidth, in section 3.3 some contributions towards improving the functionality and reducing the design complexity were presented and the latest interfaces that deploy band-pass EMSDM were presented and discussed in more detail [30] [25]. In addition, a number of methods for compensating quadrature error were presented and the effect of cancelling quadrature error was shown. In order to summarize the literature review, a summary of the achievements on compensating quadrature error and the level of implementation (device/circuit) is presented in Table 3.4.

Table 3.4: Summary of contribution towards and achievements with regards to quadrature error compensation.

Year	Method	Implementation level	Measured compensation
1996	Applying DC voltage to drive nodes [39]	Circuit level	N/A
2006	Applying a high voltage DC levels proportional to the quadrature error to feedback nodes at the sense mode [68]	Circuit level	N/A
2008	Injection of calibration, dither, and offset compensation signals [60].	Circuit level	≈ 80 °/s (Quadrature error + offset error)
2009	Placement of capacitor banks between sensing elements and read-out circuit [38].	Circuit level	≈ 100 °/s (Quadrature error + offset error)
2009	Applying dynamic quadrature error compensation to dedicated comb finger for quadrature trimming [69].	Structure level/Circuit level	Maximum residual error ≈ 0.09 °/s
2011	Inclusion of quadrature error compensation comb fingers in the sensing element structure [67].	Structure level	Up to 828v/v attenuation

However, there is a group of micro-gyroscopes that cannot take advantage from the methods and techniques presented in section 3.4. These micro-gyroscopes bear the following characteristics:

1- Already fabricated and packed with a defined fabrication process. For instance, the method introduced in [70] cannot be deployed, as it would require alterations to the layout that can be expensive and hence not cost effective.
2- Firstly, one set of comb fingers are built for the sense mode, and secondly it is coupled with a closed-loop control system that uses this set of comb fingers for feeding the feedback signal. For this group of sensors, the methods that are introduced in [71] [68] [72] cannot be used because these finger combs are used to only compensate quadrature error and hence no space is available for feedback signal from the output bit stream. More over if a solution could be proposed that does not need high-voltage DAC unlike the one introduced in [58], it can make the design simpler and potentially reduce the power dissipation. Ultimately, an interface that was proposed in [73], which can be implemented as a discrete circuit and is suitable for fabricated and packed sensors and can be exploited for improving their dynamic range and fabrication tolerance, doesn't have a quadrature error elimination scheme. This problem limits the dynamic range despite the feedback system. In other words, although the dynamic range will

increase regardless, compensating the quadrature error brings further increase to the dynamic range as well as improving bias stability and angle random walk as shown in [67].

Chapter 4 Quadrature error cancellation method for band-pass EMSDM

4.1. Introduction

It was concluded in the literature review that a novel solution is required to fulfill the requirement for an interface for either stand alone gyroscopes sensing elements or the interfaces which lacks the required performance due to the short comings which was stated in chapter 3. In this chapter a new solution for elimination of quadrature error in closed loop systems is proposed. However, prior to introducing the new solution, a new design software package (Matlab code) is introduced. It has proved to speed up the process of designing complex solutions (i.e. low/band pass interface). Also, the design of a band-pass EMSDM (the base of the new solution) by this software is presented. Afterwards, theoretical bases of the new solution is presented and it is followed by presenting the system level simulation and the simulation results. The new design is verified at system level for both low quality factor and high quality factor. In addition, the stability of new solution is verified by using leaner approximation models and applying linear time invariant control theory. In summary, the idea of this design is formed by inspiration from a mature technique known as quadrature amplitude modulation and demodulation [42] and the structure of band-pass EMSMD for vibratory micro-gyroscope. This design approach is presented in detail in this chapter. In addition, there is some notes on the necessity of deploying excess loop compensation for band-pass EMSMD.

4.2. Automated design method for EMSDM

4.2.1. Introduction

As it was discussed in section 2.3.3, the linear approximating and transforming from pure electronic ΣΔ modulator to electromechanical ΣΔ modulator are quite time consuming and can be inaccurate. As an alternative, an automated design method has been designed and introduced by Dr. Reuben Wilcock [74] that produces optimized solutions in terms of both performance and robustness while avoiding all the time consuming manual iteration. In this section, this design package is introduced, and examples are presented. Also it is used in designing the novel micro-gyroscope closed-loop system. However, first it is used to design a 6th order micro-gyroscope system, in order to demonstrate how it work for designing existing systems.

4.2.2. Matlab genetic algorithm optimization

GA (genetic algorithm) and DST (direct search toolbox) extends the optimization capabilities in MATLAB and optimization toolbox by including tools for using genetic algorithms, simulated annealing, and direct search [75] [74] . These algorithms are used for problems that are

difficult to solve with traditional optimization techniques, including problems that are not well defined or are difficult to model mathematically (e.g. ΣΔ modulator). Genetic algorithm and direct search toolbox complements other optimization methods to help with finding good starting points. Traditional optimization techniques can be used as an extension to further optimize the final solution. GA starts by setting out some starting values for parameters of a sample system from a range that is defined by the user for each parameter. At the first step, a population of solution (set of values for parameters) is created with a size defined by the user. A fitness function is executed, and the performances are examined by GA to see which solutions are heading towards the minimum value of the function. The fitness function in the case of GA is any function which is executed to generate a number or performance parameters from a number of design parameters. This function can include commands to run a Simulink model at different sets of conditions (different sets of coefficients). This method is basically the operating principle of the automatic design package for closed-loop electro-mechanical inertial sensors systems (i.e.: gyroscope) [74].

4.2.3. Automatic EMSDM optimizer

As mentioned in the previous section, this system uses GA (genetic algorithm) to find the optimum solution. The figures of merit for an optimized system (in case of closed-loop inertial sensors) are the maximum signal to noise ratio and minimum displacement of the proof mass. The system uses three files to obtain the necessary information and structure to deliver the optimum solution for interface architecture. These files are listed as follow:

1- Simulink model: This file contains the Simulink model of the required system which is formed by function blocks (e.g. mathematical block). As an example, a 6^{th} order band-pass gyroscope closed-loop system is used here, and its structure is shown in Figure 4.1. This structure was originally proposed by Y. Dong [32], and it was designed for quality factor of 100. However, for the gyroscope in this experiment it was essential to add a phase compensator as the high-quality factor sensing element (as shown in Table 4.1) has got a sharp phase-shift around the resonant frequency. In addition, this model has ports to pass produced values to the Matlab workspace for further processing.

Table 4.1: Parameters of running the Simulink model in GA process

Parameters for sense mode of the gyroscope used in this example	
Drive and sense mode frequency	$\omega_d = \omega_s = (2\pi * 4000)$ rad/s
Proof Mass	$m = 2\times10^{-9}$ Kg
Quality factor	Q = 100
Input signal (angular rate) magnitude	Ω = 100 °/s
Input signal (angular rate) frequency	F_Ω = 32 Hz

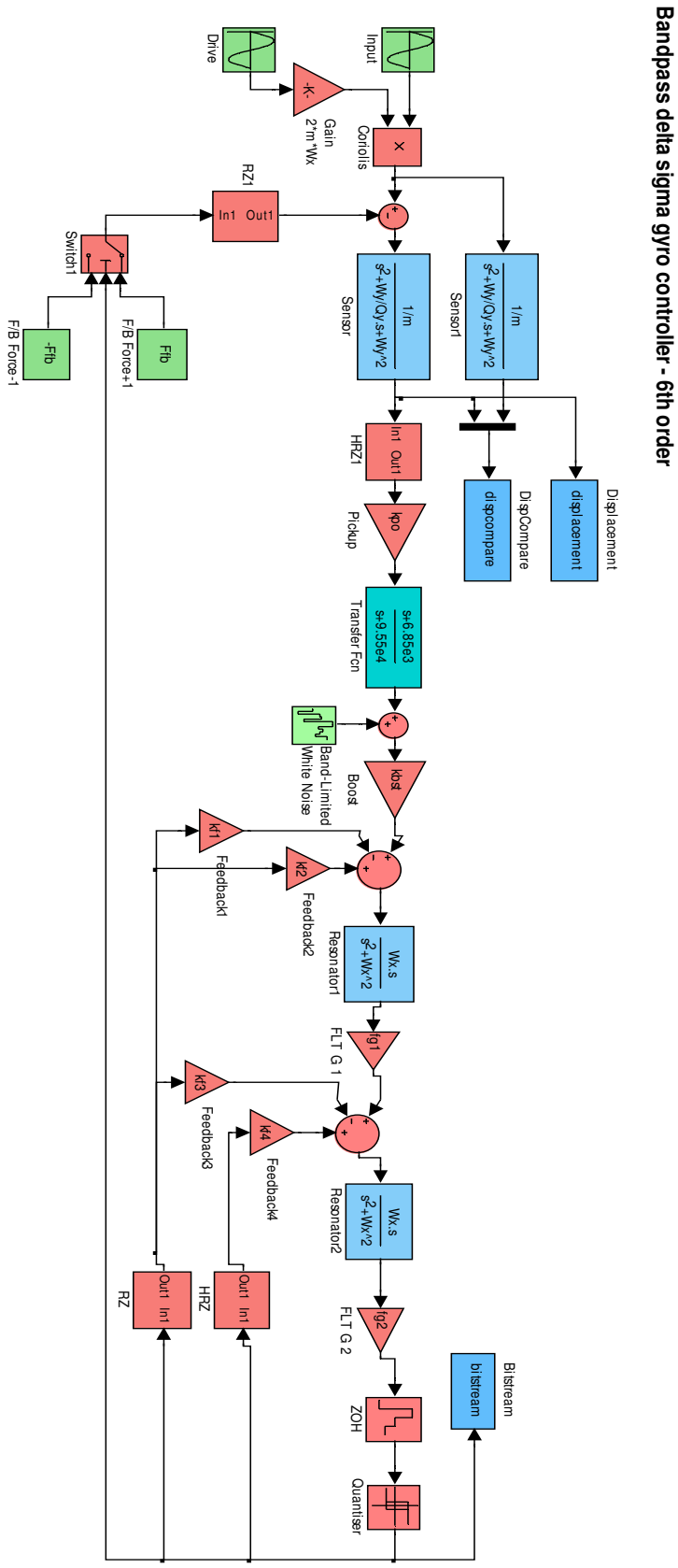

Figure 4.1: Simulink model of a 6th order band-pass micro-machined gyroscope closed-loop control system that is used in GA system (reproduced from [73]).

2- System file: this is a .m file (Matlab code file as shown in appendix A) which defines the condition in which the design process must be executed. These conditions include the number of variables, acceptable output (in this case minimum acceptable -SNR), position of the variables in the output metrics, upper limit and lower limit of each variable and standard variation for each value (for Monte Carlo robustness simulations). To be precise, in addition to limits and standard deviations all static values for the model are also defined. These parameters include drive ad sense mode frequency, input angular rate magnitude, input angular rate frequency and sensing element quality factor.

3- Fitness function file: this is a .m file (as shown in appendix A) which defines a function that returns SNR and displacement against each set of generated parameters (also known as solution). This function, runs the Simulink model for a defined period of time (in system file). Then two data sets as results of simulation (in this case quantized output bit stream and displacement data) is passed to Matlab space to calculate SNR and RMS (root mean square) of displacements of proof mass.

In order to explain the design process, it is beneficial to follow the design of an example system like a 6th order band-pass EMSDM. At the first step, the system file is loaded and run in Matlab work space. This file clears all existing variables in Matlab space and defines the conditions for the optimization process. Then a file called "run_gaoptimization" is executed and it prompts the user to enter a name for the design process. Once the name is entered this code starts the GA and a list of different solutions (parameters for the model) appears on the screen along with expected SNR and RMS of displacement as shown in Figure 4.2.

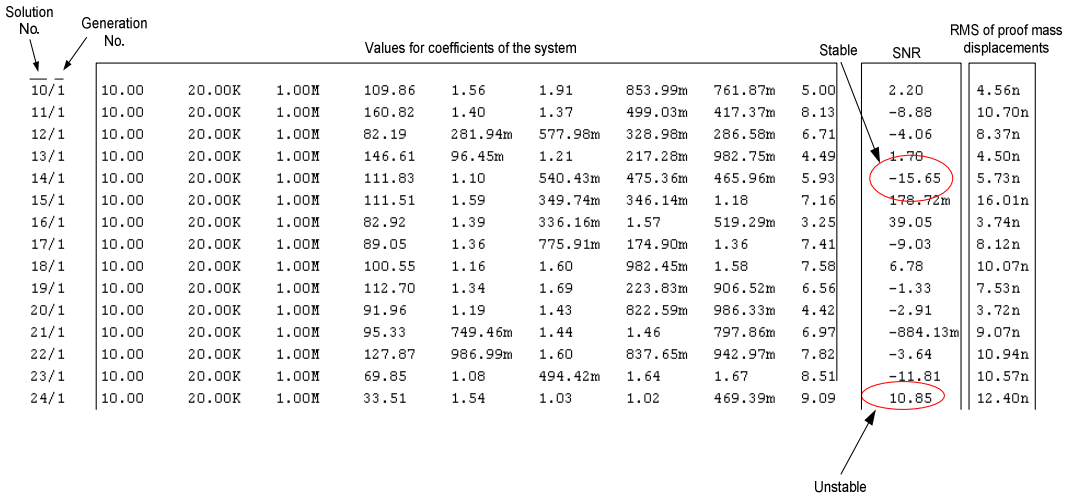

10/1	10.00	20.00K	1.00M	109.86	1.56	1.91	853.99m	761.87m	5.00	2.20	4.56n
11/1	10.00	20.00K	1.00M	160.82	1.40	1.37	499.03m	417.37m	8.13	-8.88	10.70n
12/1	10.00	20.00K	1.00M	82.19	281.94m	577.98m	328.98m	286.58m	6.71	-4.06	8.37n
13/1	10.00	20.00K	1.00M	146.61	96.45m	1.21	217.28m	982.75m	4.49	1.70	4.50n
14/1	10.00	20.00K	1.00M	111.83	1.10	540.43m	475.36m	465.96m	5.93	-15.65	5.73n
15/1	10.00	20.00K	1.00M	111.51	1.59	349.74m	346.14m	1.18	7.16	178.72m	16.01n
16/1	10.00	20.00K	1.00M	82.92	1.39	336.16m	1.57	519.29m	3.25	39.05	3.74n
17/1	10.00	20.00K	1.00M	89.05	1.36	775.91m	174.90m	1.36	7.41	-9.03	8.12n
18/1	10.00	20.00K	1.00M	100.55	1.16	1.60	982.45m	1.58	7.58	6.78	10.07n
19/1	10.00	20.00K	1.00M	112.70	1.34	1.69	223.83m	906.52m	6.56	-1.33	7.53n
20/1	10.00	20.00K	1.00M	91.96	1.19	1.43	822.59m	986.33m	4.42	-2.91	3.72n
21/1	10.00	20.00K	1.00M	95.33	749.46m	1.44	1.46	797.86m	6.97	-884.13m	9.07n
22/1	10.00	20.00K	1.00M	127.87	986.99m	1.60	837.65m	942.97m	7.82	-3.64	10.94n
23/1	10.00	20.00K	1.00M	69.85	1.08	494.42m	1.64	1.67	8.51	-11.81	10.57n
24/1	10.00	20.00K	1.00M	33.51	1.54	1.03	1.02	469.39m	9.09	10.85	12.40n

Figure 4.2: Screen-shot of series of possible solutions generated by GA-optimization fitness function. As shown for each solution a SNR and displacement are calculated. Negative SNR denotes that the system is stable.

As GA is designed to find the minimum of a function, the output of the fitness function is the negative of SNR. Therefore, for stable solutions the SNR output will be a negative number with the aim to find the most negative value denoting a system with the maximum ratio between power of input signal and power of quantization noise. Once the GA process has completed by simulating all populations for all generations, a file containing all solutions is available for further data processing. This involves filtering out unstable solutions and any solution below acceptable specification in terms of SNR and RMS of displacement (which is defined in system specification file) at the first stage and then thinning out similar solutions at the next stage. Monte Carlo simulation can then be executed to find out which solutions are most robust considering variations in all the design parameters as set by the user in the system file. Eventually, a graphic presentation of frequency response of the most stable system can be generated, and for band pass system it will be similar to the one shown in Fig. 4.3.

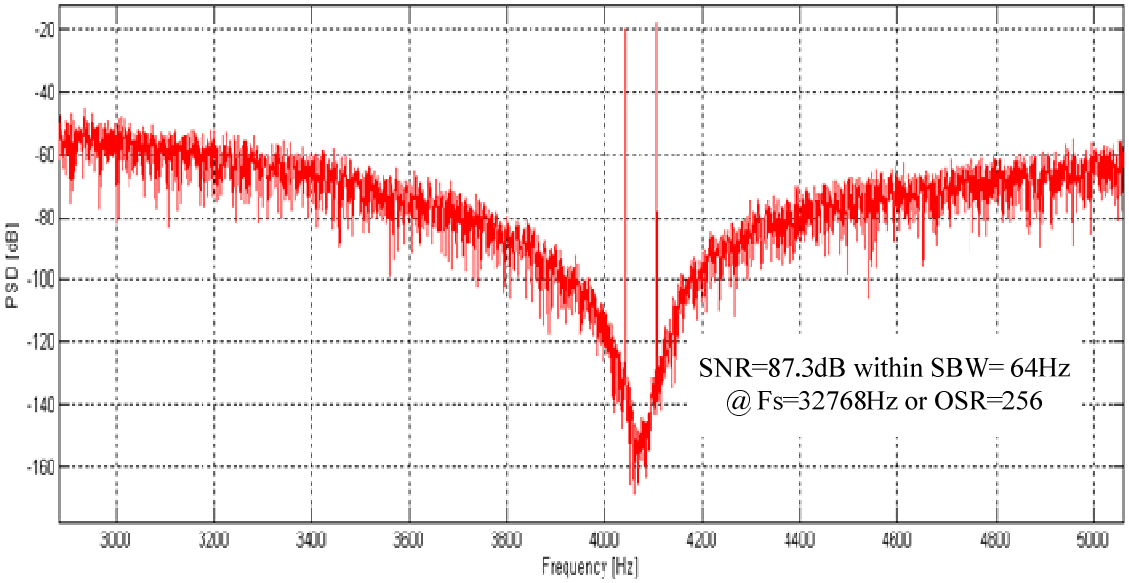

Figure 4.3: Power spectral density for a sample 6th order band-pass closed-loop micro-gyroscope system generated by GA optimization system with parameters in table 1. The sampling frequency of this system is F_s=32768Hz and oversampling ratio (OSR) is 256.

As shown in Fig. 4.3, GA optimization method, has built a 6th order band-pass EMSDM system with full-scale signal to noise ratio (SNR) of above 85dB at over sampling ration (OSR) of 256. In other words, as it was previously introduced in section 2.2.5 the sampling frequency can be only 4 times of the drive mode resonance frequency. However, using OSR of 256 (8 times) has given a higher performance comparing with OSR of 128. It must be noted that this package only changes the coefficient for a predefined structure. This package is not able to alter the given structure or built a new structure.

4.2.4. Verifying the automatically designed system by a linear model

In the previous section it was explained how GA system generates a set of solution for a given closed-loop system architecture. However, it should not be neglected that the core of the package runs some random number generation to ultimately concludes the most stable solution. Hence there should be a method to prove that the system is mathematically (as a linear system) feasible. A method to verify this aspect of the inertial sensor closed-loop system (gyroscope/accelerometer) , is to use bode plots and apply linear control theory. On the other hand, EMSDM is a nonlinear system due to deployment of a quantiser and therefore, a linear approximate model is made for it. Although some inaccurate assumptions are made when approximating a nonlinear system to a linear model, it helps to use bode diagram to determine the behavior of the system against input signals and different types of noise [76]. Figure 4.4 shows the linear approximation model for 6th order band-pass EMSDM for gyroscope whose non-linear Simulink model is shown in Figure 4.1**.** In order to derive STF (Signal Transfer Function), ENTF (Electronic Noise Transfer Function) and QNTF (Quantisation Noise Transfer Function) the linear approximation model (Figure 4.4) is used. In order to do this, similat to what is shown Figure 2.20 the angular input signal, electronic noise source and quantizer are replaced by three input ports that are marked In1, In2 and In3 and the output signal is marked Out1.

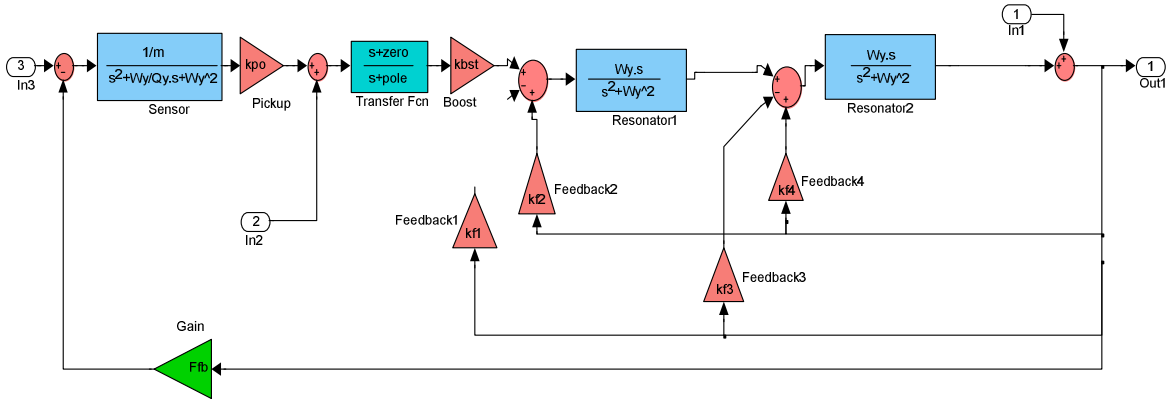

Figure 4.4: Linear approximation model of the Simulink model of the closed-loop 6th order band-pass gyroscope which was shown in Figure 4.1. In this figure "In1" is used to extract quantization noise transfer function in relation to "Out1". "In2" is used to extract electronic noise transfer function in relation to "Out1" and "In3" is used to extract signal transfer function in relation to "Out1".

The parameters for this system is obtained from the GA system (as final solution) and subsequently by using Matlab code (Appendix B) , transfer functions for signal, electronic noise and quantization noise is derived from the linear Simulink model which is shown in Figure 4.4 and the following bode plots that are shown in Figure 4.5 have been generated. These graphs represent the approximate behavior of the system that is shown above. As it is shown in this figure, the linear approximation frequency responses of STF, QNTF and ENTF prove that the system design (in

which its parameters are obtained from GA automation software package) demonstrates an expected behavior. As shown in Figure 4.5, QNTF attenuates the quantization noise around the resonance frequency and STF and ENTF both have their highest gain around the resonance frequency.

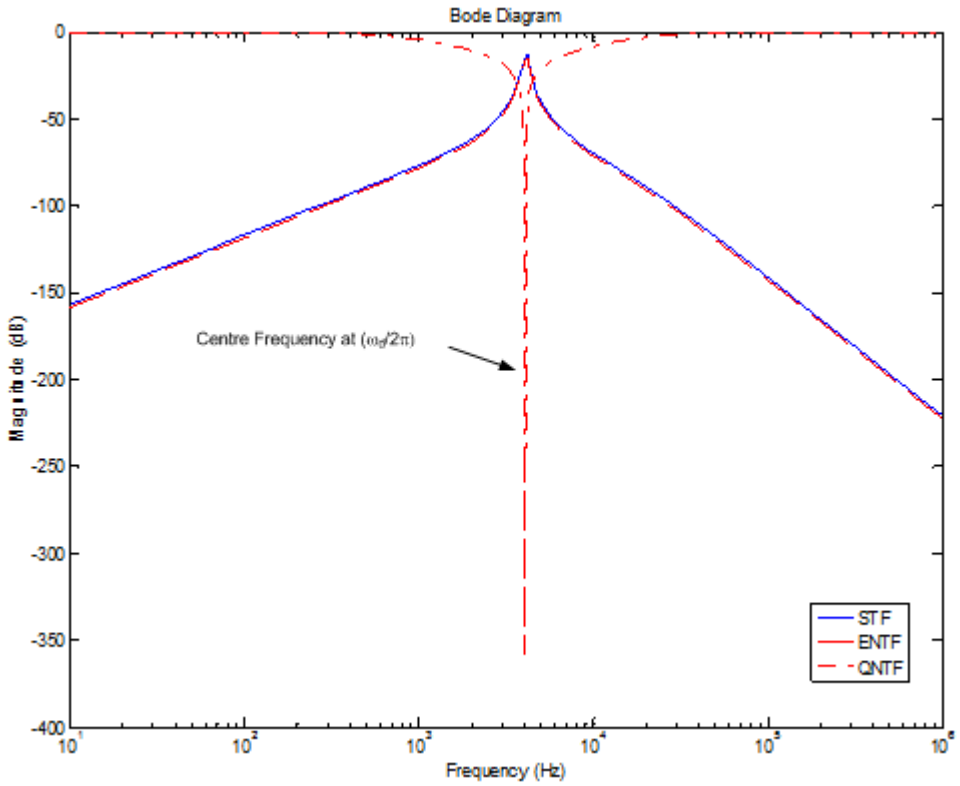

Figure 4.5: Frequency responses of STF, ENTF, QNTF for the 6th order band-pass gyroscope linear model shown in Figure 4.4 operating around the drive mode frequency (ω_d).

Up to this stage in this chapter, a new method of for designing closed-loop inertial sensors is introduced which does reduce the design over head and the correctness of its ultimate output proved to be verifiable by linear approximation model. In the following part the fundamental idea of the novel interface is presented and how the automated GA software package is used to design it, is explained.

4.3. System design theory

In order to design this interface, a band-pass EMSDM was adopted. The advantage of this interface is that it operates at significantly lower sampling frequency than the low-pass one. Hence, it is simpler in the circuit design to deal with the frequency response of some active components (i.e. operational amplifiers). In addition, as it was mentioned in the literature review, this closed-loop interface extends the dynamic range, and generates a feedback signal as a bit stream; this is

quite useful for digital domain signal processing, and in the case of this interface, this advantage is exploited and it is discussed in detail later in this chapter.

As presented in Chapter Two, the information (angular rate) and quadrature error are combined whilst being applied to the mass of the sense mode. The total force that is applied to the proof mass of the sense mode can be shown as follow:

$$F_{Coriolis} = 2 \times m \times \Omega \times \omega_d \times \mathrm{A} \times \sin(\omega_d t) \quad (4.1)$$

$$F_{Quadrature} = \varepsilon \times A \times \omega_d^2 \times m \times \cos(\omega_d t) \quad (4.2)$$

$$F_{Total} = F_{Coriolis} + F_{Quadrature} = mA\omega_d(2 \times \Omega \times \sin(\omega_d t) + \varepsilon\omega_d \times \cos(\omega_d t)) \quad (4.3)$$

Prior to discussing further the signal processing of the novel system, it is useful to remember how EMDSM works. In this architecture, the goal is to bring the proof mass back to its rest position during its operation; this is achieved by using the force feedback pulse stream which is pulse density modulated pulse train. From the point of view of the mechanical operations, this control means that any displacements that are caused by quadrature error and Coriolis force are constantly monitored and compensated. However, when the control bit stream contains both Coriolis force and quadrature error, it means that just as with the open loop sensor the dynamic range is still limited although due to the use of EMSDM control the overall dynamic range is increased in comparison to the same sensor in an open loop operation. Therefore, it is essential to add a process which extracts the quadrature error and returns a compensation signal (in this case, a bit stream) back to the sense mode of the micro-gyroscope sensing element

As the first step, the quadrature error and the angular rate (Coriolis) signal must be separated from each other. From the mechanical point of view, equations (4.1) and (4.2) show the mechanical amplitude modulation of information and error signals. To carry out the separation of the two signals, both the quadrature amplitude modulation and the quadrature amplitude demodulation from communication systems [42] are deployed and adopted as shown below:

- First each part of F_{Total} is multiplied by $\sin(\omega_d t)$ and $\cos(\omega_d t)$; these are 90 degrees out of phase. The following two trigonometric identities show that:
  - $2\cos(\omega_d t)\cos(\omega_d t) = 1 + \cos(2\omega_d t)$
  - $2\sin(\omega_d t)\sin(\omega_d t) = 1 - \cos(2\omega_d t)$

After multiplying the F_{Total} once $\cos(\omega_d t)$ and once by $\sin(\omega_d t)$, by applying the above equations the following equations are derived for Coriolis force and quadrature error respectively:

- $mA\omega_d(2\Omega\sin(\omega_d t)\sin(\omega_d t) + \varepsilon\omega_d\cos(\omega_d t)\sin(\omega_d t)) =$
  $mA\omega_d\,(2\Omega(1 - \cos(2\omega_d t)) + \frac{1}{2}\varepsilon\omega_d\sin(2\omega_d t))$

- $mA\omega_d(2\Omega\sin(\omega_d t)\cos(\omega_d t) + \varepsilon\omega_d\cos(\omega_d t)\cos(\omega_d t)) =$
  $mA\omega_d\,(2\Omega\sin\,(2\omega_d t)) + {}^1/_2\varepsilon\omega_d(1+\cos\,(2\omega_d t))$

- Then by passing these two signals through low-pass filters the following terms remain from the above equations:
  - $2mA\omega_d\Omega$
  - $\frac{1}{2}\varepsilon mA\omega_d^2$

As is shown in the above, the first term contains angular rate information (Ω) and the second term contains the quadrature error component. Also, it must be noted that once the signals are demodulated, both parts are moved to their base band frequency while the interface is operating at the frequency of drive mode (for band-pass EMSDM). This means that a signal reconstruction process is required to take the frequency band of both signals to the operating frequency of the sensor and the frequency band of the modulator [25]. This process can be undertaken by following the way that the micro-gyroscope sensing element performs a mechanical amplitude modulation on the angular rate information at the resonant frequency of drive mode [35]. In other words, the same process is performed but this time in electronic domain. A diagram of the separation process of the two signals and their reconstruction at the micro gyroscope sensing element resonance frequency is shown in Figure 4.6.

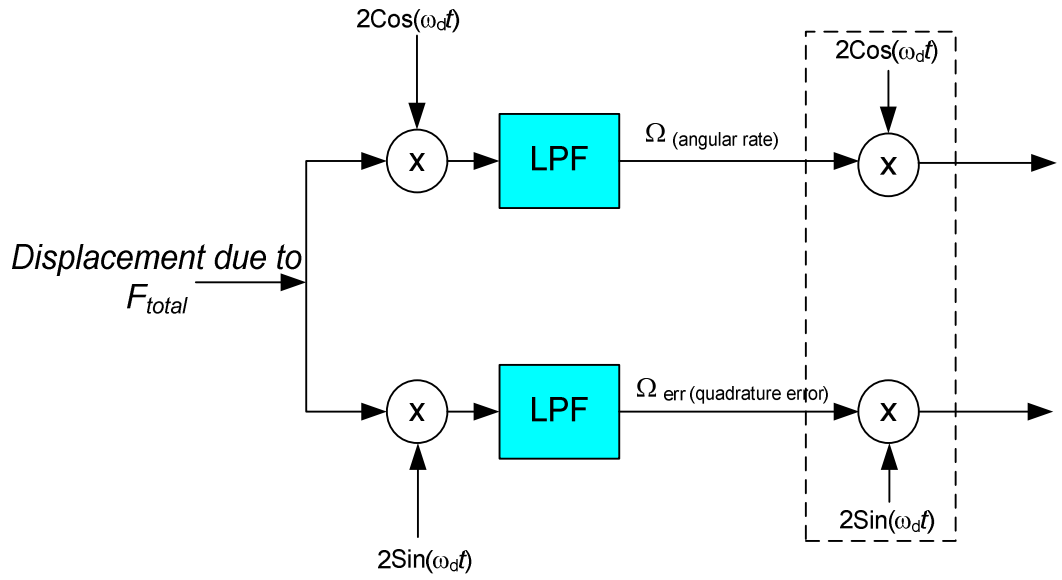

Figure 4.6: System diagram of the method for separating the angular rate information and quadrature error and reconstructing them at the sensing element drive mode resonance frequency.

So far, breaking down the read-out signal into the angular rate information signal and quadrature error signal, as well as subsequently reconstructing them to the drive mode resonance

frequency has been exemplified. The next step is to integrate this process into the closed loop band-pass SDM.

For the novel system, the basic principle of EMSDM [31] is used to integrate the separation mechanism into an electromechanical sigma delta architecture. This means that, in this design, both the information signal and quadrature error are fed into two sets of band-pass loop filters and quantizers. In this way, the quadrature error at the output node is attenuated, but at the same time the displacement due to both the angular rate and quadrature error are equally monitored. The sine and cosine wave (which are taken from the drive signal source) are used for electronic demodulation and modulation. These two signals must have a phase delay (ϕ in Figure 4.7) in relation to the local oscillator for the drive mode. The calculation for this phase shift described in [65].

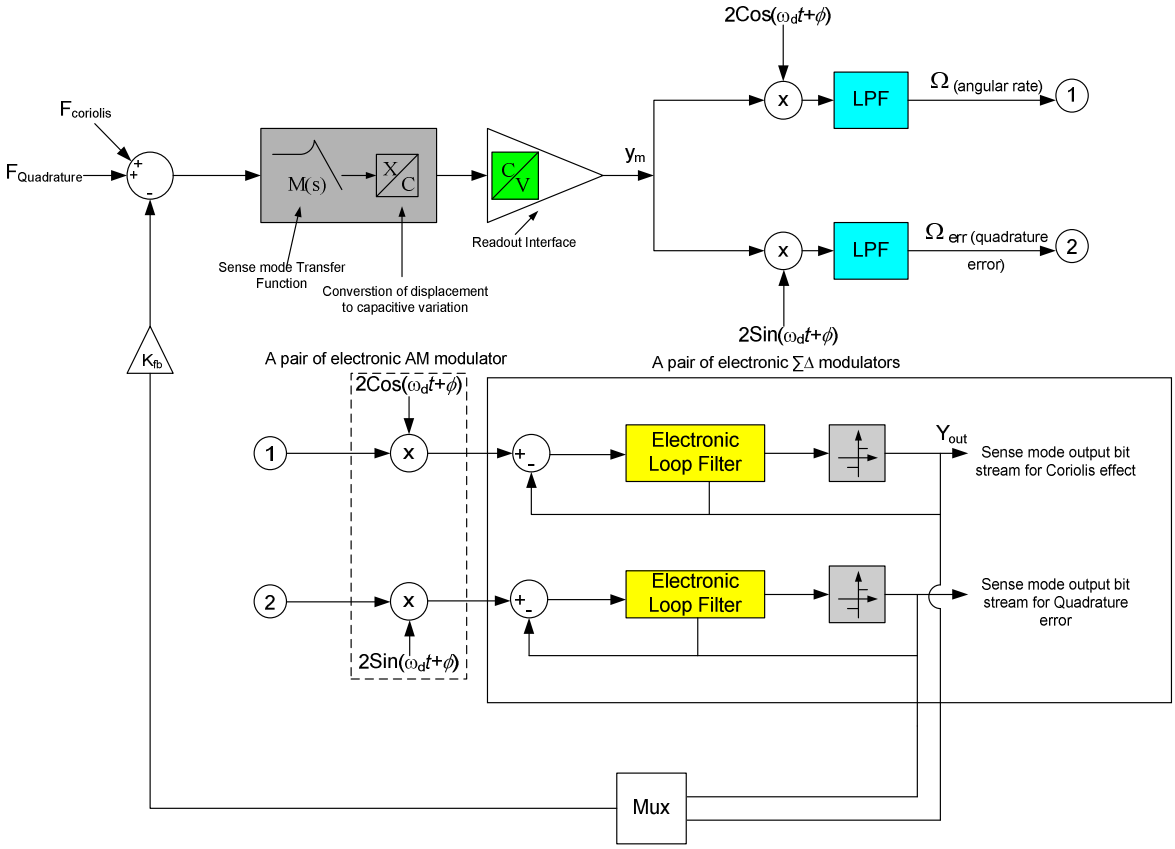

Figure 4.7: A conceptual diagram of the novel gyroscope sense mode closed loop interface with quadrature error elimination system. As is shown each components of the read-out signal is separately fed into two sets of electronics loop filter and the output of the two quantizers are sent to a multiplexer. Ultimately, the multiplexer output is converted to electrostatic force and is applied to feedback electrodes.

As discussed in the literature review, in the new design it should be taken into account that the targeted sensors have only one set of sense mode comb fingers for the feedback signal. This means

that both the quadrature compensation signal and the force feedback signal must be combined to be fed through one channel. In order to meet this requirement, a multiplexer, operating at four times of the sampling frequency, is used in this design. This technique is similar to time division multiplexing (TDM) which is normally used in communication system. TDM takes frames of (for example) voice signals and multiplexes them into a TDM frame which runs at a frequency higher than the maximum frequency of each input channel. For example, if the TDM frame consists of *n* voice frames, the bandwidth will be *n**64 Kbit/s when the voice is sampled at 64 Kbit/s [77]. Later in this chapter it is shown how this principle is used to feed the force feedback signal to the feedback nodes on the sensing element.

It must also be noted that, for the loop filters in this system, a 6^{th} order SDM is used. As shown in the literature review, the band-pass architecture works at a much lower sampling frequency than the low-pass one. Hence, for simplifying the design with regard to frequency compensation, the band-pass system is preferable. Also, another benefit of a band-pass system is that band-pass filters can be used before and after multiplayer blocks in order to avoid the injection of unwanted signals to the multipliers. Moreover, the order of the system is set to 6, as lower order systems (e.g. 4^{th} order) achieved lower signal to noise ratios of around 60dB. In addition, higher order system (e.g. 8^{th} order) were found not to be necessary as it was verified that quantization noise is not the dominant source of noise. The comparison was achieved by using Simulink models and a summary of this comparison is presented in Table 4.2.

Table 4.2: Comparison of different orders of band-pass EMSDM systems

System order and condition	Signal to noise ratio
4^{th} order band-pass EMSDM with electronics noise source	60dB
6^{th} order band-pass EMSDM with electronics noise source	93dB
6^{th} order band-pass EMSDM without electronics noise source	97dB

In conclusion, the 6th order band-pass EMSDM was chosen as the optimum architecture for the novel interface.

Linear system approximation can be used as a method to show the correct operation of this system (as described in section 2.2.3). In order to use this method, the system must first be simplified into two 6^{th} order band-pass EMSDM. This method of simplifying is feasible as the two input forces (Coriolis force and quadrature error) are independent of each other hence allow a linear model to be extracted for each input. This way, one of the outputs of the signal separator in

the system can be ignored when the corresponding input is assumed to be zero. Consequently, two 6th order band-pass EMSDM are derived as shown in Figure 4.8 Figure 4.9.

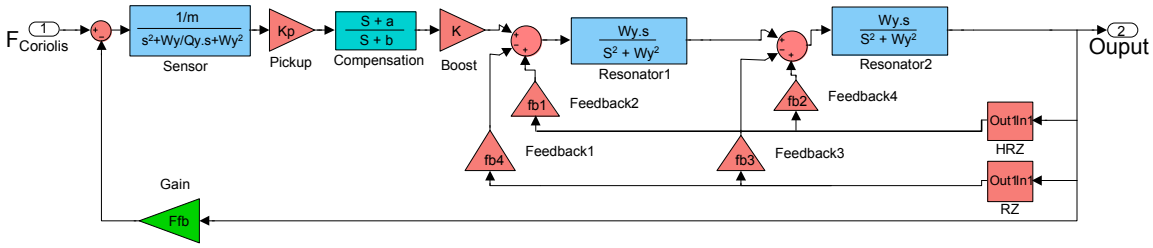

Figure 4.8: Linear approximation model for Coriolis force part of the system.

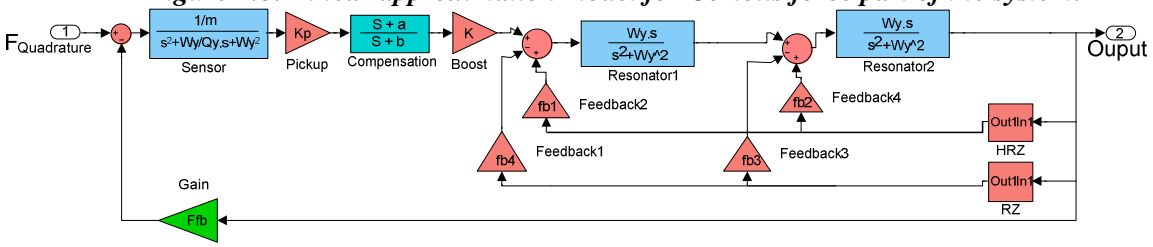

Figure 4.9: Linear approximation model for the quadrature error part of the system.

For designing the system, GA design automation was used, as the first step of the design process in order to verify the feasibility of the idea. Also, as described in Section 4.2, the manual design can be quite time consuming as this system is even more complex in comparison to its predecessor [73]. Hence, an automatic system design method that deploys generic algorithm (as described in Section 4.2) was used to produce a system with a maximum signal to noise ratio and with the optimum control of the displacement of the sense mode proof mass. The Simulink model used by this package is shown in Figure 4.10 and the specific codes for this design can be found in Appendix B. As shown in Fig. 4.9, both Coriolis force and the quadrature error are modeled and the sense mode transfer function is placed in the model to compare the controlled and open loop displacements in the resulting system.

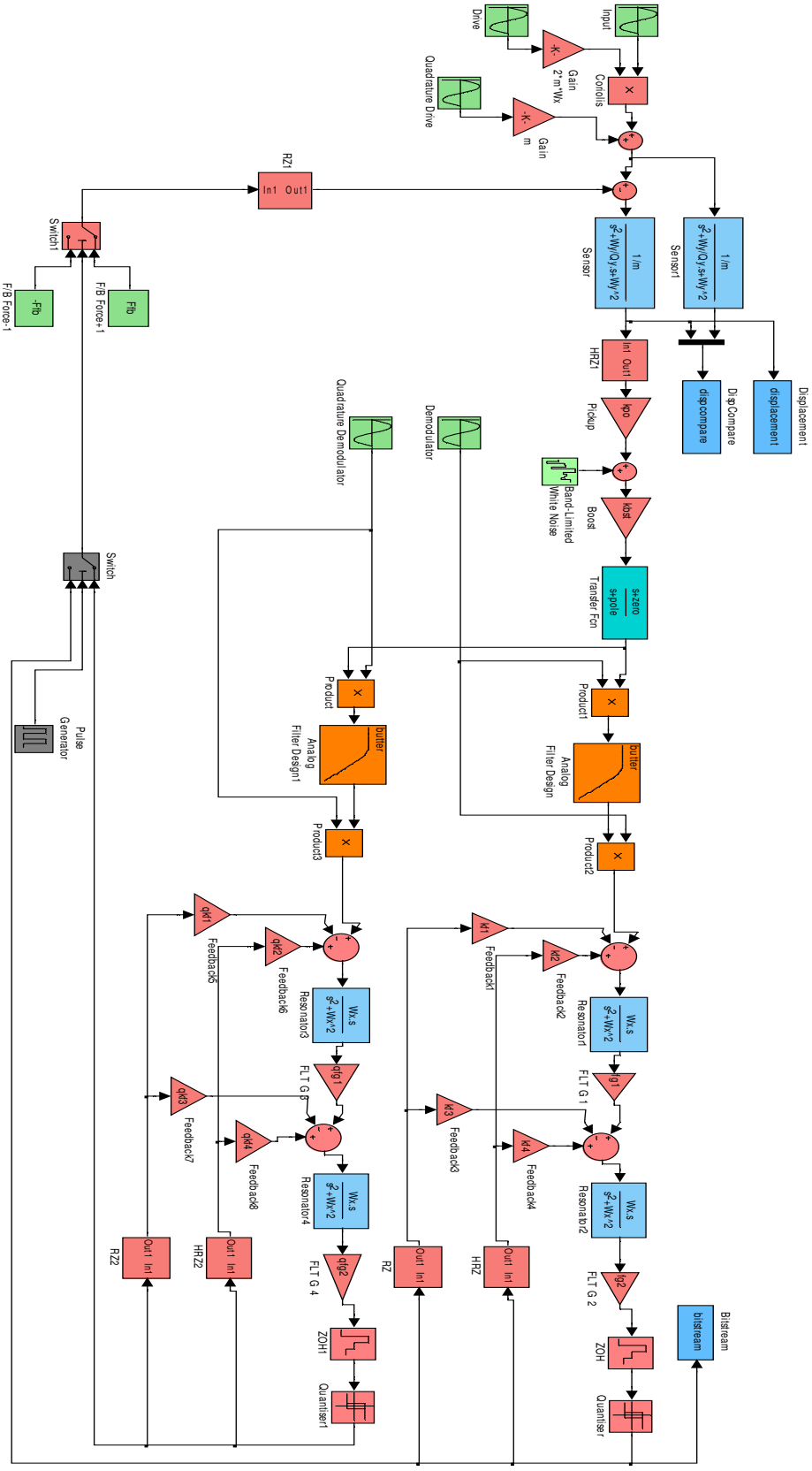

Figure 4.10: System level structure of the novel micro-machined gyroscope system with quadrature error elimination capability.

In this model, the conversion of displacement to voltage is modeled as a capacitance to voltage (V/C) gain and the electronic referred input noise is added before the booster gain block in order to model the added noise in the real world in electronic parts of the circuit. After the amplifier, the signal arrives at a compensator which is deployed to compensate for the phase-lag that is caused by the sense mode of the sample sensing element; this consequently makes the control loop stable. After the compensator, a multiplier and a second order low-pass filter and then another multiplier form the extracting mechanism for information and quadrature error. Then amplitude modulation is performed for these two signals at drive mode resonance (operation) frequency. These two signals are then fed into two electronic loop filters that are part of the EMSDM. The quantized outputs of the two independent electronic loop-filters are fed to the multiplexer model (three input switch) and multiplexed at four times the sampling frequency. Ultimately the output of this multiplexer arrives at a set actuator which converts the multiplexer output to appropriate feedback pulses for the feedback nodes of the sensing element.

4.4. Simulation results

4.4.1. Sensing elements

This simulation was run for a low Q factor sample sensing element and a high Q factor sample sensing element. The specifications of these sensors are listed in Table 4.3 and Table 4.4.

Table 4.3: Sensing element specification for the low Q factor type

Parameter	***Value***
Proof mass (m)	$2e^{-6}$ Kg
Sense mode (Q)	100
Drive mode (Q)	200
Drive mode resonance frequency (ω_d)	$2\pi \times 4100$
Sense mode resonance frequency (ω_s)	$2\pi \times 4120$

Table 4.4: Sensing element specification for the high Q factor type

Parameter	***Value***
Proof mass (m)	$2e^{-6}$ Kg
Sense mode (Q)	100
Drive mode (Q)	200
Drive mode resonance frequency (ω_d)	$2\pi \times 4100$
Sense mode resonance frequency (ω_s)	$2\pi \times 4120$

4.4.2. System design for the low Q factor sensing element.

After running the GA design automation, for designing the system whose structure is described in Section 4.3, the following performance was obtained in terms of signal to noise ratio and control of the proof mass displacement in the sample micro-gyroscope sensing element.

In a match-mode micro-gyroscopes system, where both the drive and sense modes have the same frequency, a displacement gain of Q is expected. As shown in Fig.4.10, the best displacement against any induced force (Coriolis force in this case) is achieved, when the sense mode oscillates at its resonance frequency.

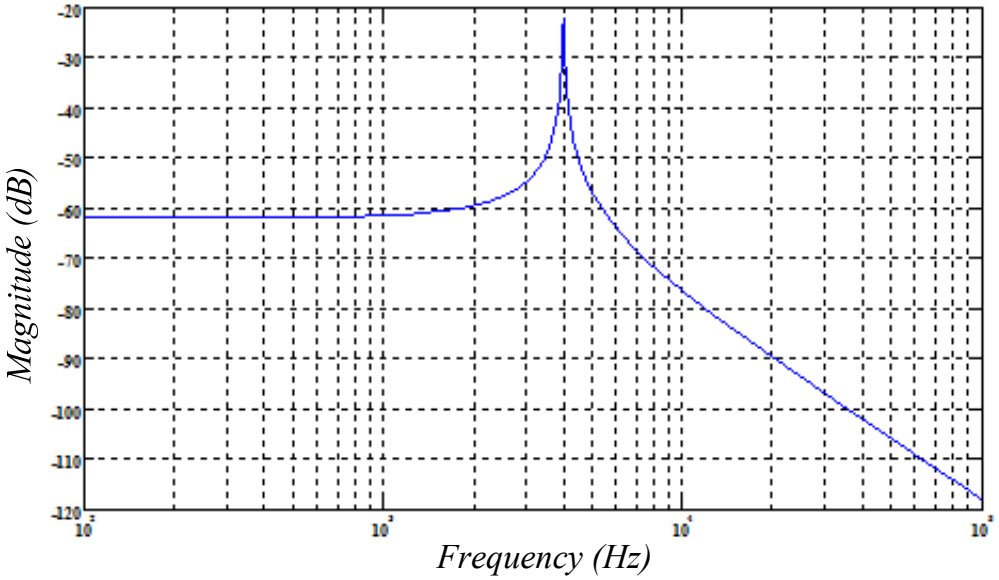

Figure 4.11: Bode plot (magnitude) of a sense mode (of a sample sensing element) transfer function with a low Q (quality factor) of 100.

Table 4.5: Simulation parameters for the sense mode of the gyroscope

Parameter	***Value***
Drive and sense mode frequency	$F_d = F_s =$ 4100 Hz
Proof Mass	$m = 2\times10^{-6}$ Kg
Quality factor	Q = 100
Input signal (angular rate) magnitude	Ω = 300 °/s
Input signal (angular rate) frequency	F_Ω = 32 Hz
Sampling frequency	$F_s = 8*F_d$ = 32000 Hz
multiplexer switching frequency	$F_{mux} = 4*F_s$ = 128000 Hz

A set of parameters was generated for the novel architecture with the simulation conditions as presented in the above table. The performance of this system is shown in the power spectral density

diagram and in the displacement variation figure as shown in Figure 4.12 and Figure 4.13 respectively.

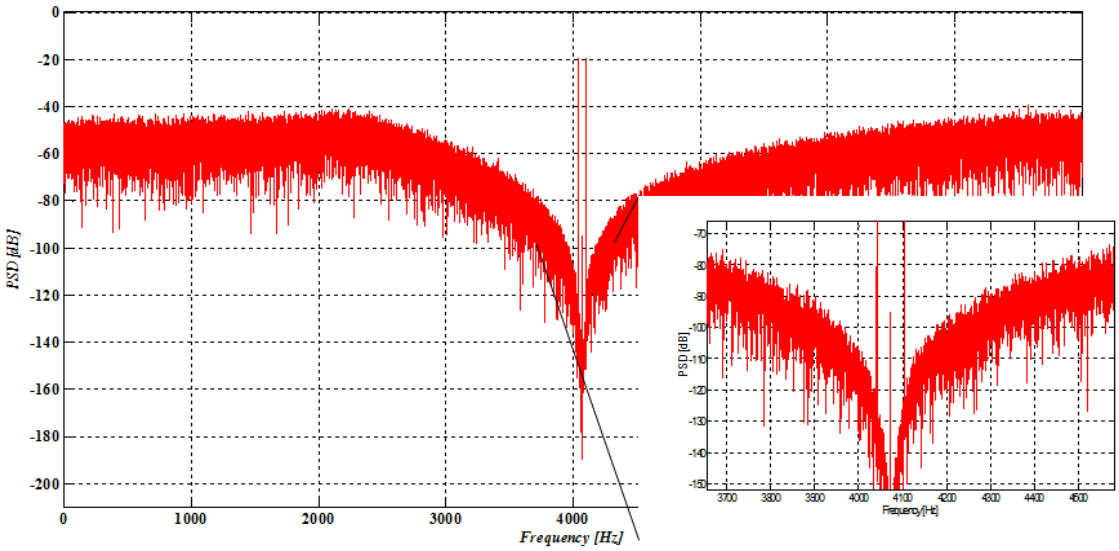

Figure 4.12: Power spectral density of the output bit-stream of the novel system architecture for a low Q factor (~100) sensing element. As shown, the power spectral density of the quadrature error is significantly attenuated (by around 8 orders of magnitude) in comparison to its predecessor.

As shown in Figure 4.12, for the same amount of quadrature error presented in Figure 2.28 , as seen in Chapter 2, the new system offers about 80dB reduction in quadrature error, and signal to noise ratio has risen from -6.5dB in section 2.4.2, to about 72dB in this system. In addition, it is expected that when the sense mode of the gyro sensor is in the control loop, the displacement of the sense mode of the sensing element is reduced. In this simulation, the displacement of the sense mode in both open and closed loop was simulated. It has been proved that, for this sample micro-gyroscope sensing element, the displacement is reduced to a third of the value of that for the open-loop system. This is shown in Figure 4.13.

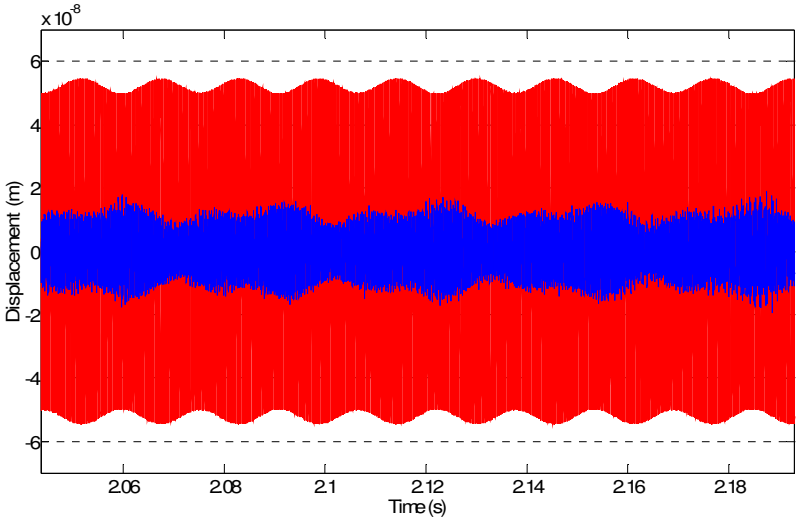

Figure 4.13: Proof mass displacement comparison between the closed-loop (blue) and open-loop (red) system.

The sensitivity of the gyroscope system is determined by increasing the input angular rate from zero with 0.1 °/s steps. For this system the minimum detectable input was calculated to be 0.17 °/s. The same method was used to obtain the dynamic range but steps of 30 °/s were used due to simulation time constraints and dynamic range of more than 950 °/s was calculated. The estimate of SNR vs. the angular rate that was used to determine the sensitivity is shown in Figure 4.14.

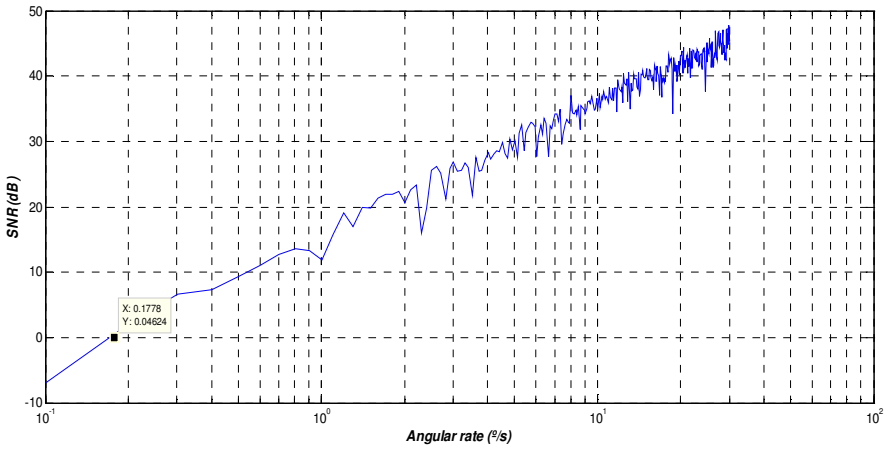

Figure 4.14: SNR vs. angular rate diagram for estimating the minimum detectable angular rate. As is shown the minimum detectable rate is around 0.17 °/s.

4.5. Linear analysis

One method to verify the stability and consistency of a system is to use control theory. However, a linear time invariant control theory can only be applied to a linear system. In contrast, there is a non linear component in the system that is called the quantizer. Hence, a method is required to project this non-linear system as a linear system in linear control domain.

4.5.1. Linear system approximation for the novel system

The linear approximation of the information is shown in Figure 4.15 and Figure 4.16. Using the STF (signal transfer function) shown in (4.4) and the QNTF (quantization noise transfer function) shown in (4.5),the stability of the system and the expected signal to noise ratio can be calculated. An explanation of each parameter in the two equations is listed in Table 4.6.

Table 4.6: Parameters for the linear approximation models

Parameter	***Description***
A	Proof mass displacement at resonance frequency (m)
Q_y	Quality factor of sense mode
ω_y	Resonance frequency of sense mode (rad/s)
m	Weight of proof mass (Kg)
K_{po}	Pick-off gain (C/V)
K_{bst}	Booster gain (V/V)
Comp	Compensation circuit transfer function
F_{fb}	Electrostatic feedback force (N)

The linear approximation of QNTF is written as follow:

$$QNTF = \frac{AQ_y^2\omega_y 2K_{po}K_{bst}m\left(s^4 + 2s^2\omega_y^2 + \omega_y^2\right)}{L} \tag{4.4}$$

where the denominator L is:

$$\begin{aligned} L = \left(Q_y.\omega_y^2 + \omega_y.s + Q_y.s^2\right)\left(Q_y.\omega_y^4.m + Q_y.ms^4 + 2Q_y.\omega_y^2.m.s^2 + Q_y.\omega_y^2.Kf_1.m.s^2\right. \\ + Q_y.\omega_y.Kf_3.m.s^3 + Q_y.\omega_y^3.Kf_3.m.s + Ffb.\omega_y^3.comp.K_{bst}.K_{po}.s^3 \\ \left. + Ffb.Q_y.\omega_y^2.comp.K_{bst}.K_{po}.s^4 + Ffb.Q_y.\omega_y.comp.K_{bst}.K_{po}.s^2\right) \end{aligned}$$

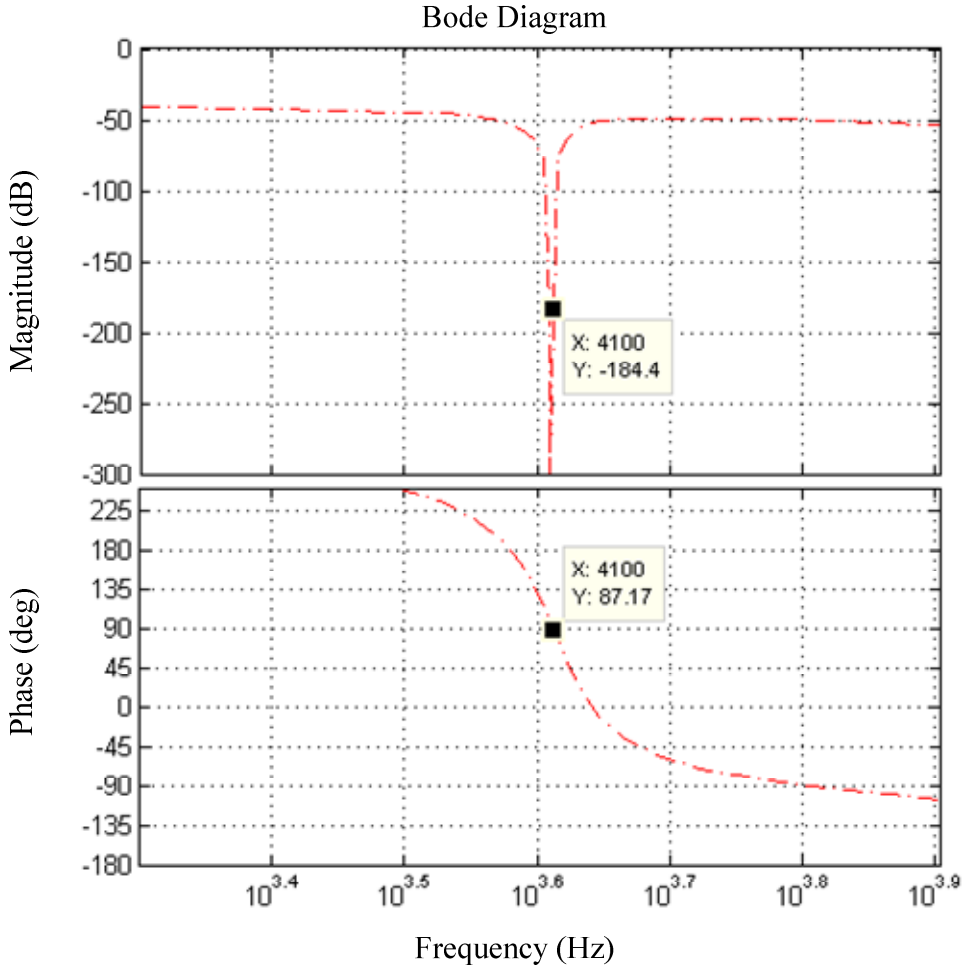

Figure 4.15: Diagram of the noise transfer function at information channel shown in Figure 4.8.The bode diagram indicates that the system is stable within the simulated band-width.

Also, the linear approximation for the signal transfer function is written as follows:

$$STF = \frac{AQ_y.\omega_y^3.b.comp.Kbst.Kpo.m.s^2}{L} \tag{4.5}$$

where L is:

$$L = 2.\omega_y^3.m.s^3 + Q_y.\omega_y^6.m + Q_y.m.s^6 + \omega_y.m.s^5 + \omega_y^5.m.s + 3.Q_y.\omega_y^2.m.s^4 + 3.Q_y.\omega_y^4.m.s^2 + \omega_y^3.kf1.m.s^3 + \omega_y^2.kf3.m.s^4 + \omega_y^4.kf3.m.s^2 + Q_y.\omega_y^2.kf1.m.s^4 + Q_y.\omega_y^4.kf1.m.s^2 + 2.Q_y.\omega_y^3.kf3.m.s^3 + Q_y.\omega_y.kf3.m.s^5 + Q_y.\omega_y^5.kf3.m.s + Ffb.Q_y.\omega_y^2.comp.kbst.kpo.s^2$$

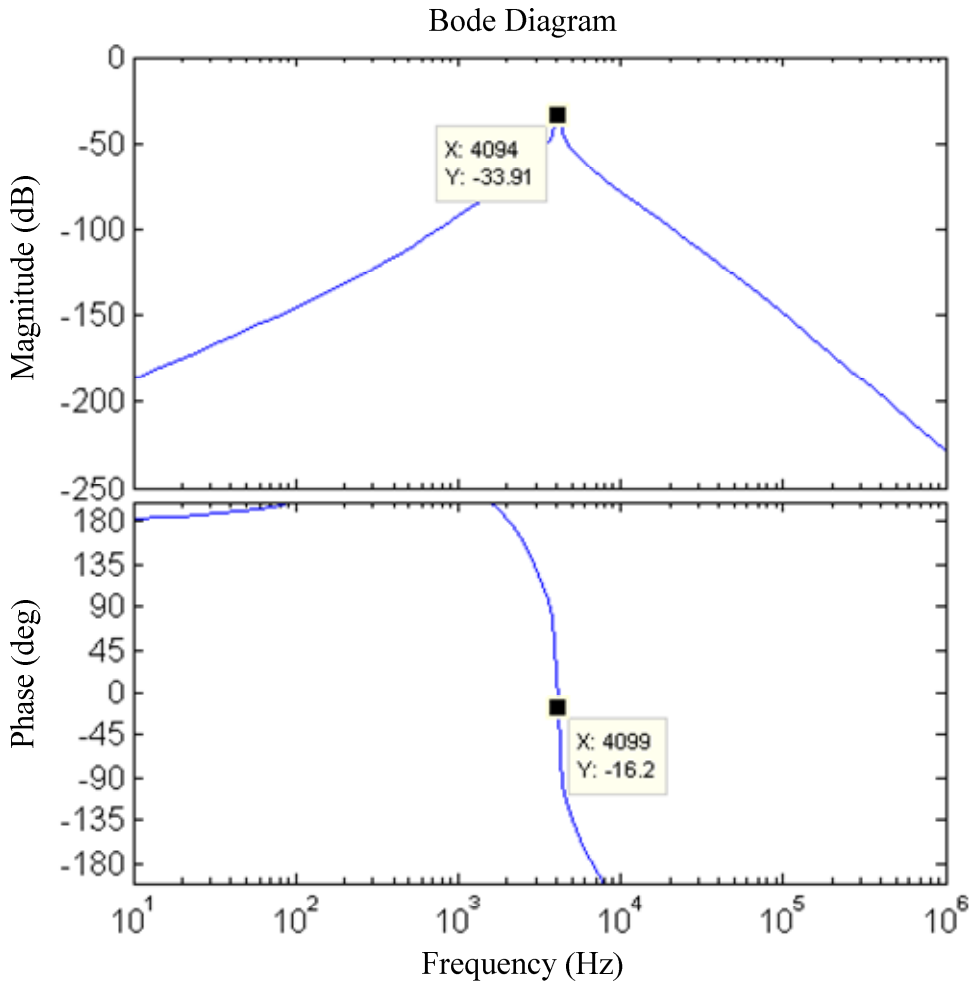

Figure 4.16: Bode diagram of the signal transfer function at the information channel shown in Figure 4.8. The bode diagram indicates that the system is stable within the simulated band-width in the Simulink model.

Moreover, the dynamic range of this system can be approximately calculated with the use of root-locus diagram. By using the root-locus (for quantizer variation) of the signal transfers function, the dynamic range of the interface can be determined. A root-locus for the quantization error transfer function as shown in Figure 4.17. The gain of a quantizer is variable, as the output of quantizer has only two level of voltage but the input is an analogue signal which can be any value limited by a maximum and minimum (that is defined by circuit design). Therefore, that part of the root-locus diagram which falls in the right plane indicated that for some values of this gain (and subsequently the level of the quantizer input), the system becomes unstable.

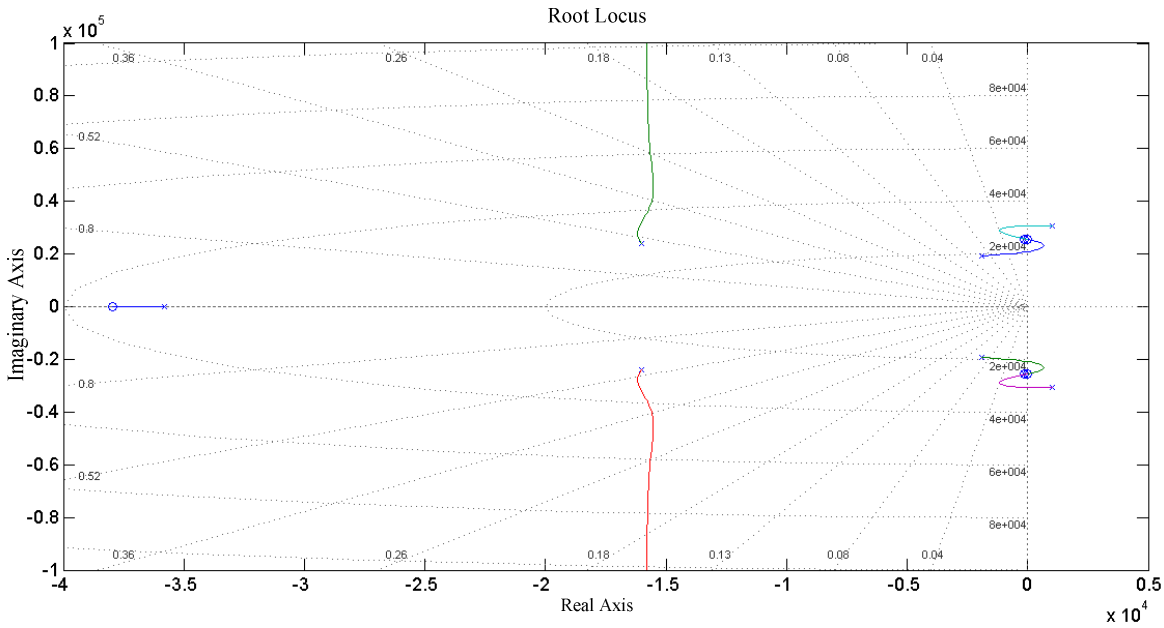

Figure 4.17: A root-locus diagram for the quantization noise transfer function (QNTF). As is shown the system is stable for a limited magnitude of gain; this determines the dynamic range of the system.

4.5.2. Calculating the signal to noise ratio by the linear transfer function

Another use of the linear transfer function is to estimate the signal to noise ratio at the output of the system. For this purpose, the power of quantization noise at the output (bit-stream) node is calculated, in addition to the power of the electronic noise. Then, the power of the angular rate signal is calculated at the output node. For this sample system, the signal to noise ratio was calculated in terms of the presence and absence of electronic noise. This is shown in Table 4.7.

Table 4.7: Conditions and results of SNR calculation

Condition	***Value***
With electronic noise	79.87dB
Without electronic noise	101.67dB

It must be noted that this calculation is carried out only on the information channel of the novel system. It is useful to determine what bit-resolution can be expected from the output of this interface for a specific parametric design.

4.6. System design for micro-gyroscopes with a high quality factor

The same process was followed to simulate the closed loop system for a sample sensing element with a high sense mode quality factor (Q≈10000). A high quality factor means that at the resonant frequency the mechanical gain (displacement of the proof mass) is quite high. This is an advantage since it improves the sensitivity of the micro gyroscope by offering greater displacement against any given angular rate as shown in Figure 4.18.

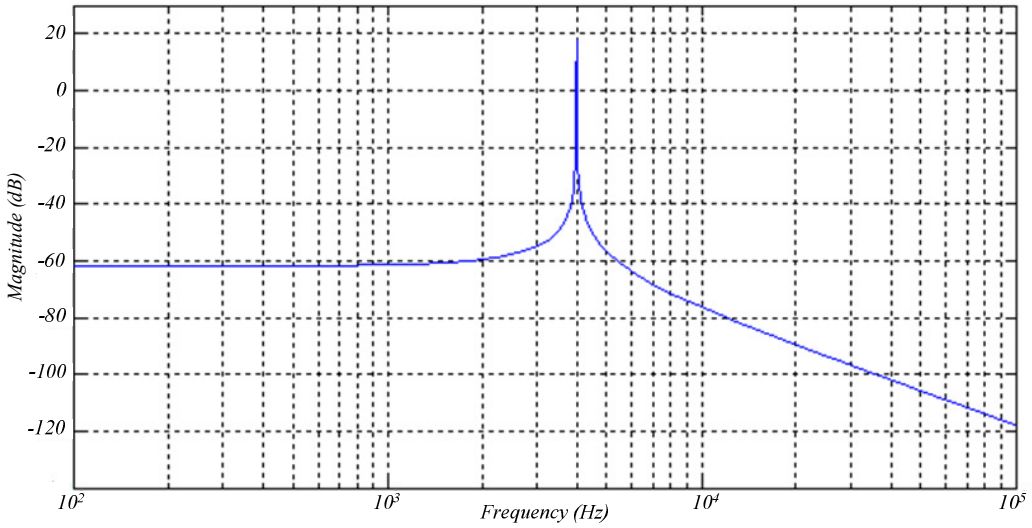

Figure 4.18: Bode plot of a sense mode transfer function with high a Q (quality factor) of about 10000.

The specifications of the sample high quality factor sensing element which was used for this simulation, are listed in Table 4.8.

Table 4.8: Parameters for the sense mode of the gyroscope used in this example

Drive and sense mode frequency	$F_d = F_s =$ 4000 Hz
Proof mass	$m = 2\times10^{-6}$ Kg
Quality factor	Q = 10000
Input signal (angular rate) magnitude	Ω = 300 °/s
Input signal (angular rate) frequency	F_Ω = 32 Hz
Sampling frequency	$F_s = 8*F_d$ = 32000 Hz
Feedback switching frequency	$F_{fd} = 4*F_s$ = 128000 Hz

The simulation results for the system with the above specifications, and the architecture that is presented in Figure 4.7 were produced as shown in Figure 4.19 and Figure 4.20.

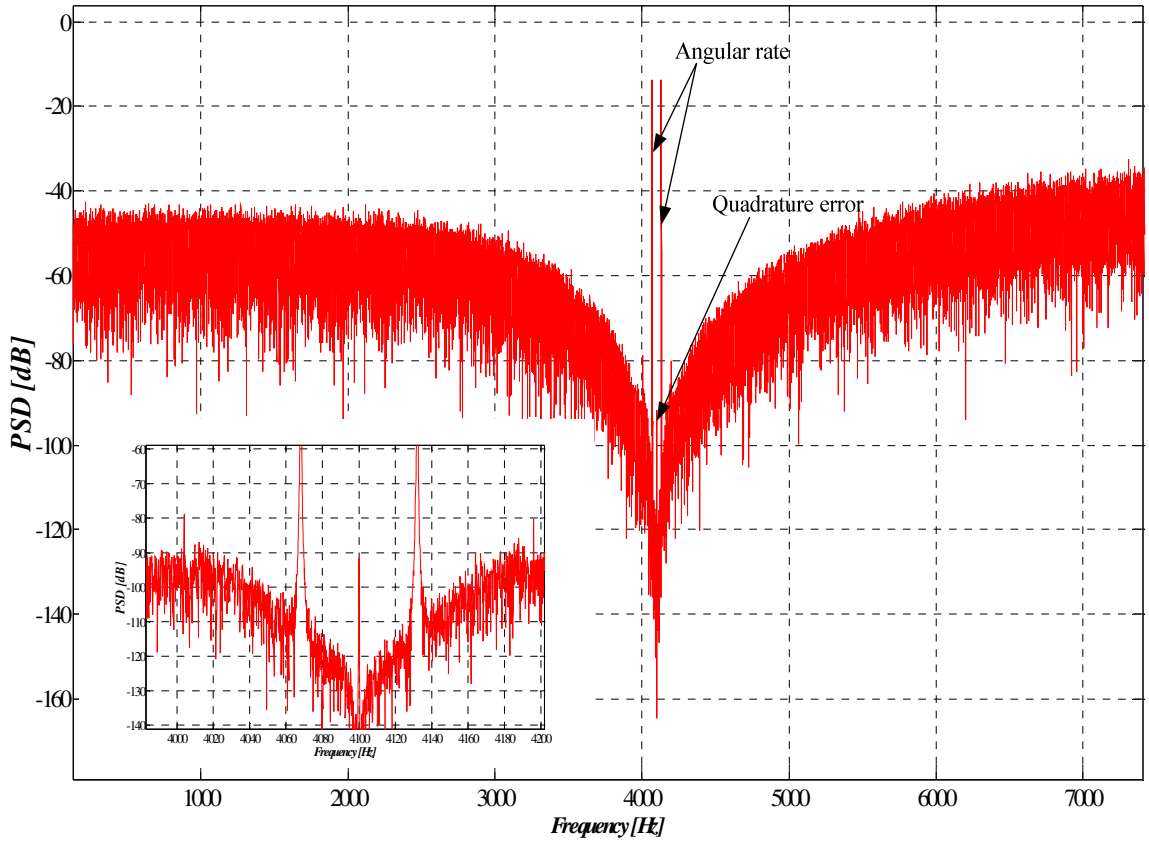

Figure 4.19: Power spectral density for the novel gyroscope system with high quality factor. Attenuation of more than 70dB (for quadrature error) is achieved in this simulation model.

As shown in Figure 4.19, for the same amount of quadrature error that was presented in Figure 2.28 in Chapter 2, the new system gave more than 70dB reduction in quadrature error and as a result, signal to noise ratio rose from -6.5dB shown in Section 2.4 to 68dB in this system. It must be noted that none of these signal to noise ratios illustrate the performance of the interface. This is a figure to show how much the power of the unwanted signal (in this case quadrature error) is reduced within the band of interest. In addition, just like simulation results for the sample low Q sensing element, it is shown that when the sense mode of the sensing element is in control loop, the displacement of the proof mass in the sensing element is reduced. As shown in Figure 4.20 the displacement of the proof mass has been significantly reduced comparing to the one in an open loop system. As shown, the displacement in the open loop mode for a sensing element with high quality factor sensing elements, is in excess of resonating space (in this case about 1um). This indicates that any high quality factor sensing element needs a closed-loop control system to control

the displacement of the proof mass and in order to prevent it from reaching any extreme distance from rest position.

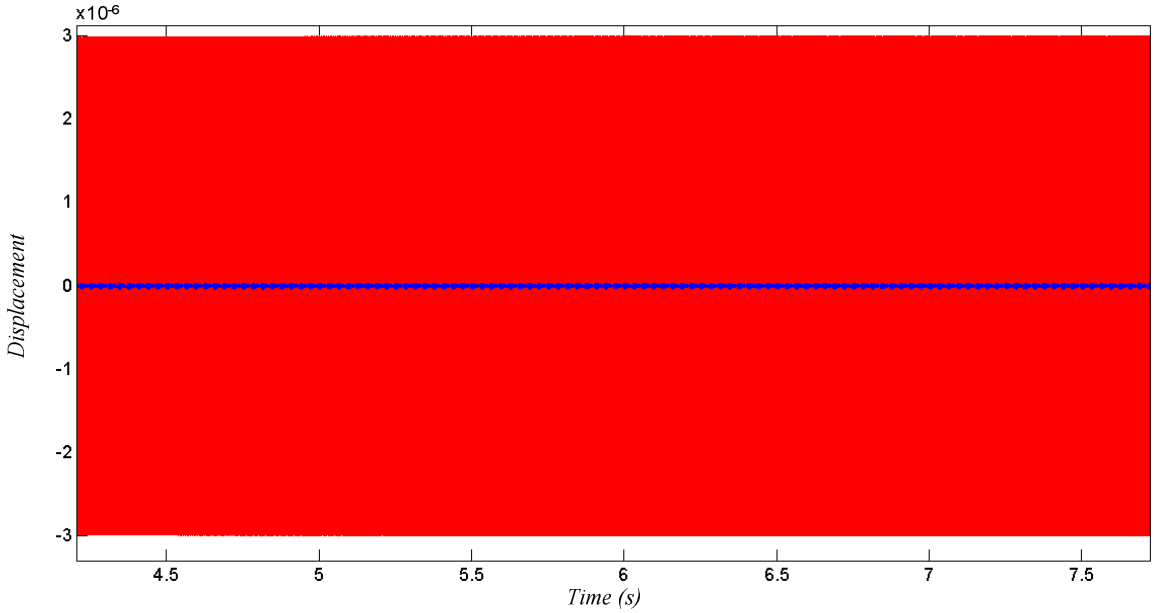

Figure 4.20: Comparison between the displacement of the proof mass in a high Q sense mode of the sample sensing element. It shows the displacement in open loop condition (red) and closed loop condition (blue).

This system controlled the displacement and reduced it to an RMS (root mean square) of 16nm. Thus this simulation verifies the claims about increasing the dynamic range and linearity of the change in capacitance [31]. Moreover, the sensitivity of the interface is determined by increasing the input angular rate from zero with 0.001 °/s steps; for this system, the minimum detectable input is calculated to be 0.03 °/s. The same method was used to obtain the dynamic range, but with steps of 30 °/s due to time constraints; a dynamic range of more than 1250 °/s was calculated. A summary of the achievements using this interface is shown in Table 4.9.

Table 4.9: Summary of achievements of the novel system for a high Q sensing element

Parameter	***Value***
Bandwidth	64 Hz
Minimum detectable angular rate	0.03 (°/s)
Dynamic range	1250 (°/s)

In addition, as shown in Figure 4.18, due to the extremely narrow pass band of the sense mode transfer function (around the resonance frequency), angular rates with frequencies above DC may not be sensed at the same level as angular rates with close to DC frequencies. As it is shown in

Figure 4.21, a point-to-point SNR vs. frequency of this system proves that angular rate input with frequencies up to 60 Hz can be monitored, and signal to noise ratio stays approximately at the same level.

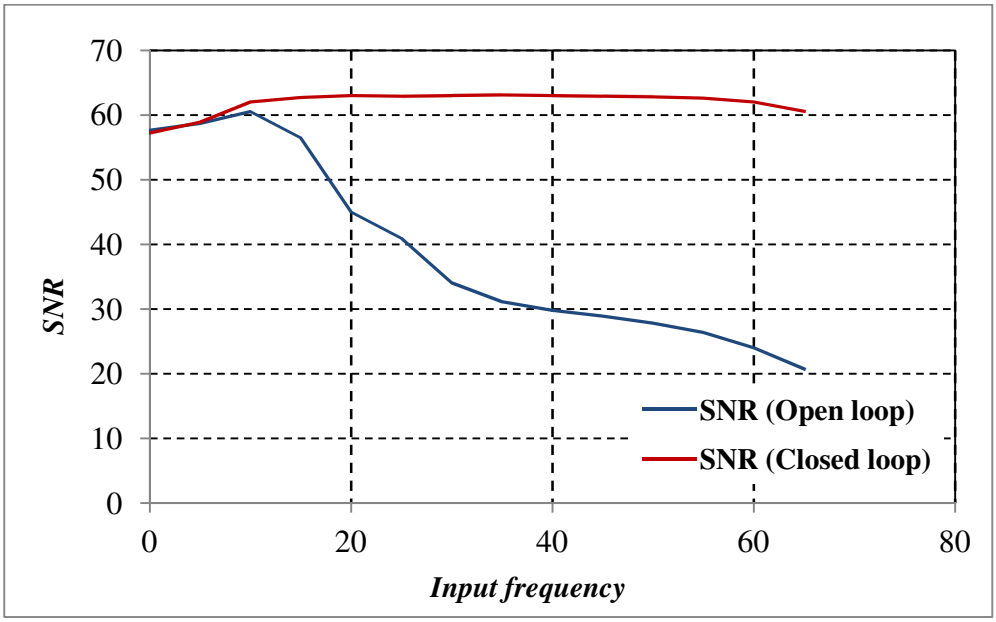

Figure 4.21: Comparison between the signal to noise ratio versus the angular rate frequency for an open-loop system and the novel closed- loop system for a sample sensing element with high quality factor for both sense mode and drive.

As can be seen in Figure 4.21, the SNR drops slightly around DC, despite the expectation of a gain from using a band-pass loop filter. This reduction is due to a lack of precise data points between quadrature error and the input signal (using Matlab modelling). This conclusion is based on the fact that signal levels did not change, and displacement of mass stayed at the same level. However, at below a frequency of 5Hz, there was an obvious lack of data points from the information signal to error signal in SNR graph. This indicates that the number of data points or the resolution of the frequency was not high enough to keep the accuracy of the calculations constant.

4.7. Removal of excess loop delay compensation

As this work is a continuation of the 6th order EMSDM for gyroscopes introduced in [76], excess loop delay compensation which was originally introduced in [30] was deployed. However, further investigations shows that the implementation of this technique is not necessary for the present system. This is because the delay generated by the quantizers in this loop is significantly smaller than the sampling period (about 600 times smaller). This technique was originally used in electronic sigma delta modulator, where the input signal frequency is quite close to quantizer propagation delay [78] [79]. Since this is not the case in this design, the feedback paths were

changed as shown in Figure 4.22. This change showed no degradation in term of the performance of the novel gyroscope system.

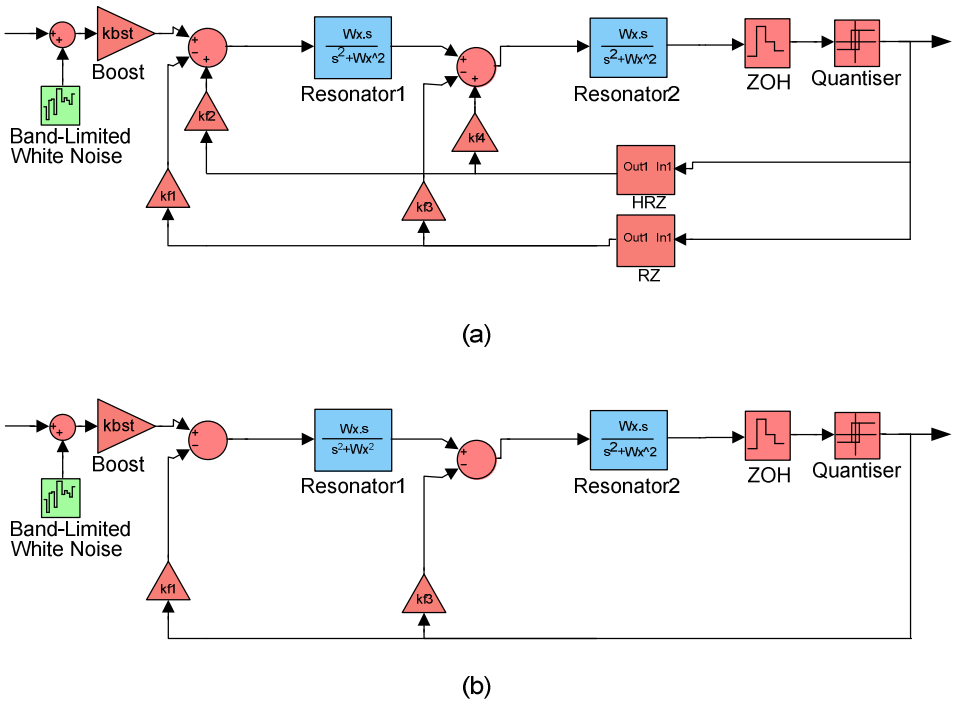

Figure 4.22: Removal of excess delay compensation for the band-pass EMSDM by removing the return-zero(RZ) and the half return-zero (HRZ) in (a) and changing it two the arrangement that is in (b).

4.8. Summary

In this chapter, a new method for designing closed-loop EMSDM for a micro-machined gyroscope was introduced and its reliability was verified by using a linear model approximation method. Then, the idea behind the design of a novel interface with quadrature elimination was introduced and presented in detail. A GA automatic system designer was used to optimize the given architecture. The simulations from Simulink models clearly showed the effectiveness of this novel approach in eliminating the quadrature error. In addition, the displacement figures show how the closed-loop interface keeps the operating point around the linear region. At this stage, the achievement and operation of this novel interface is proved at the system level. In the next two chapters the circuit level simulation and the realization of the novel system are presented.

Chapter 5 Circuit level simulation

5.1. Introduction

The feasibility and effectiveness of the novel system has been proved and verified at the system level as shown in the previous chapter. As a further step towards the possible realization of the novel system, it is essential to carry out a circuit level simulation as this gives an insight into possible problems with regard to the realization of the novel system. For this purpose, in this chapter, the realization of each part of the system is described and simulated. This is shown in the diagram that is depicted in Figure 4.7 and includes the readout circuit, booster, compensator and electronic loop filter. In the circuit, the behavioral model of the sense mode of the sensing element is used because a Pspice model for micro-gyroscope sensing element was not available. Each sub-circuit in this system, (i.e. in the electronic part), takes its input as a differential signal from the sensing element (the sense mode nodes of the micro-gyroscope) and all the way throughout the circuit blocks. This technique is regularly used in instrumentation circuits to minimize the common input/output noise [80] [81].

Moreover, in this work, the circuit, which was designed and introduced in [61], is used as sub-circuits which carry out the loop-filtering role. This decision speeds up the process of reaching the project goal as this sub-circuit has been proven to be a working prototype. In this way more time could be spent on making the rest of the novel system (e.g. the modulator/demodulator) operational.

5.2. Circuit simulation model of the sub-system blocks

Most parts of the novel system are modeled as electronic circuits which were made from Pspice libraries. However, the sense mode is modeled as a variable capacitor whose capacitance is proportional to a voltage that is the projection of the proof mass displacement in the sensing element behavioral model. In other words, Coriolis force, the feedback force and the displacement of proof mass are projected as voltage variations. The sense mode of the gyroscope sensing element is modeled as shown in Figure 5.1.

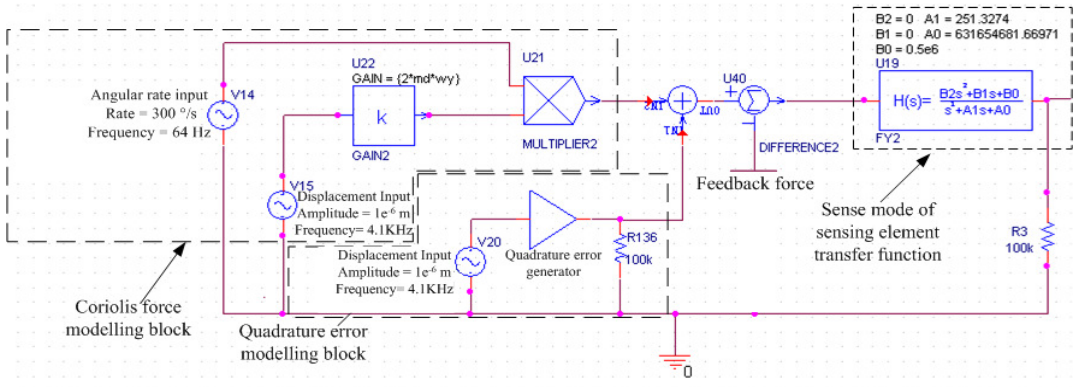

Figure 5.1: Behavioral model of sense mode of a sample micro-gyroscope.

As shown above, in this sub-system block, the behavioral model of adders, multipliers and mathematical models are used to simulate the generation of Coriolis force and quadrature error. Also, a transfer function mathematical block is used to model the sense mode of the sensing element. In addition, a sigma (adding) block is used to model the addition of the feedback force to Corilis force prior to exertion on the sense mode proof mass. Subsequently, the output of the transfer function block is fed to a block which converts the displacements of the proof mass into capacitance variation as shown in Figure 5.2.

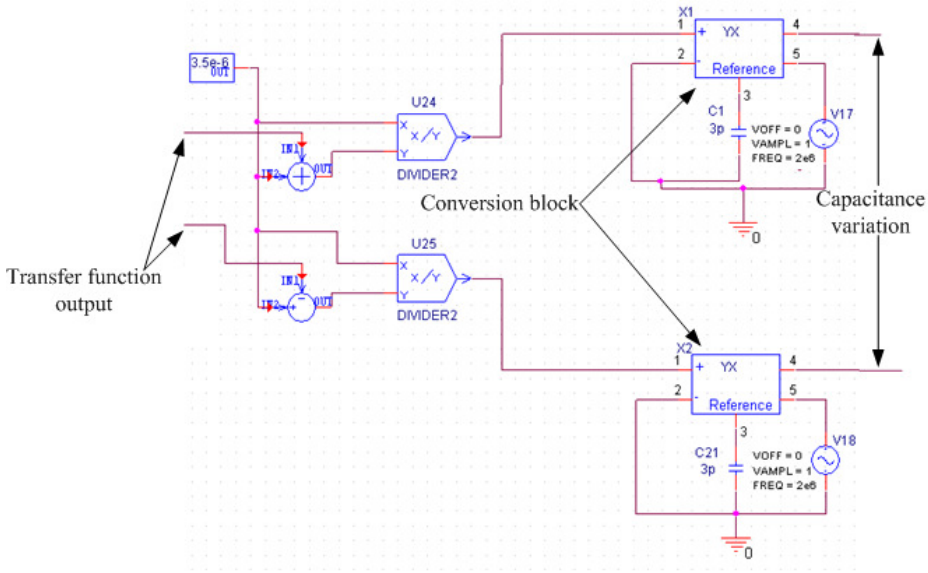

Figure 5.2: Sub-circuit for conversion the voltage (projected displacement) variation to capacitance variation. The input to this circuit is the output of transfer function block shown in Figure 5.1.

In the Pspice circuit model for the novel system, the readout circuit which was introduced in [82] is used and modeled. Considering time and cost constraints, to implement (in terms of hardware) the ac-bridge circuit shown in Figure 5.3, is the preferred choice for reading the displacements of proof mass in the sample sensing element. The output of this readout circuit is differential as shown in Figure 5.4 and the two output nodes are connected to the inputs of a fully differential instrumentation amplifier [83]. As shown, the two output signals are complementary to each other. The resulting signal (the output of the amplifier) is shown in Figure 5.5. It must be noted that in order to improve the consistency of the system level simulation (the Simulink model) and the Pspice model, the gain of the readout circuit was calculated by using the behavioral model of the sensing element in conjunction with the circuit model of the readout circuit. As shown in Figure 4.10, the readout circuit was modeled as a gain in system level simulation and the open-loop interface Pspice model of the sense mode of a sample gyroscope was used to calculate the magnitude of this gain. Moreover, while the simulation of entire novel system was executed, it was noted that due to the existence of a high frequency sub-circuit (in this case the readout circuit

which was operating at 1.5 MHz), the time steps generated by Pspice to calculate the state of the entire circuit model, were quite small (approximately 10^{-12} s). On the other hand, the minimum simulation time to determine the permanent state of the circuit model was about 250ms. Considering the very small time steps, it is impossible to reach a permanent state with regard to the circuit without a software crash occurring due to the excessive amount of data points. Hence, the readout circuit was replaced with its equivalent gain behavioral model. This decision resulted in increasing the simulation time steps to approximately 10^{-6} and the simulation can be carried out without any concern for a software crash.

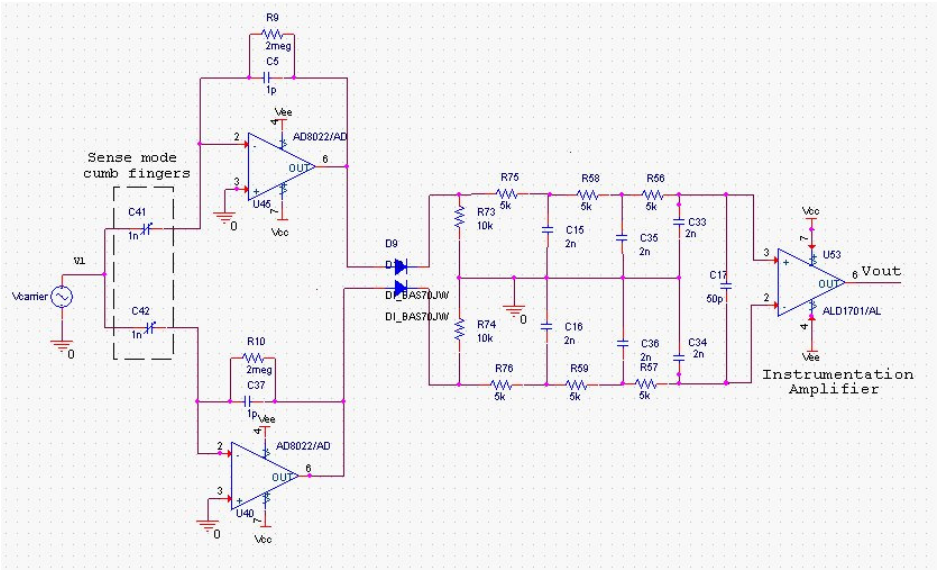

Figure 5.3: Capacitance to voltage convertor circuit. This circuit uses ac-bridge and AM demodulation (reproduced from [82]). The output of sense mode of the sensing element is differential which is a contributory factor in improving accuracy and removing common input noise.

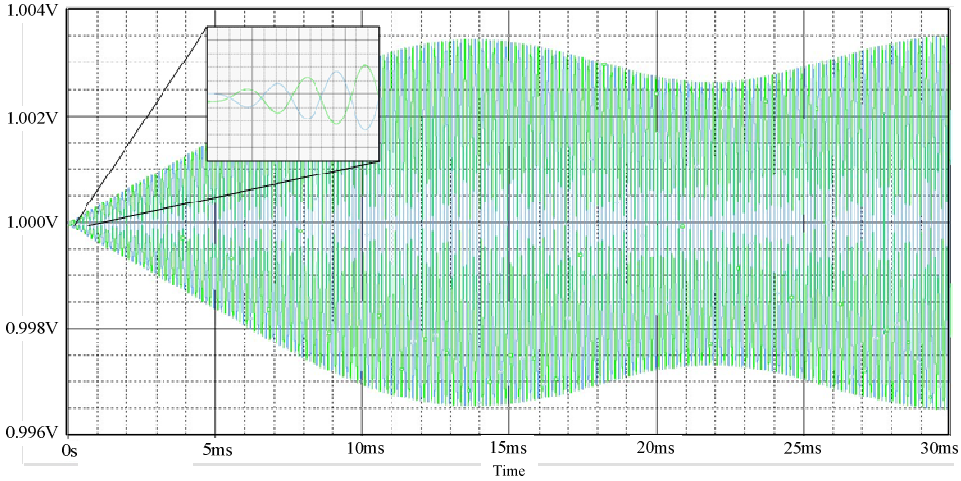

Figure 5.4: The differential output of the instrumentation amplifier. As shown, the output of each side of the sense mode (in the sensing element) is complementary to the other.

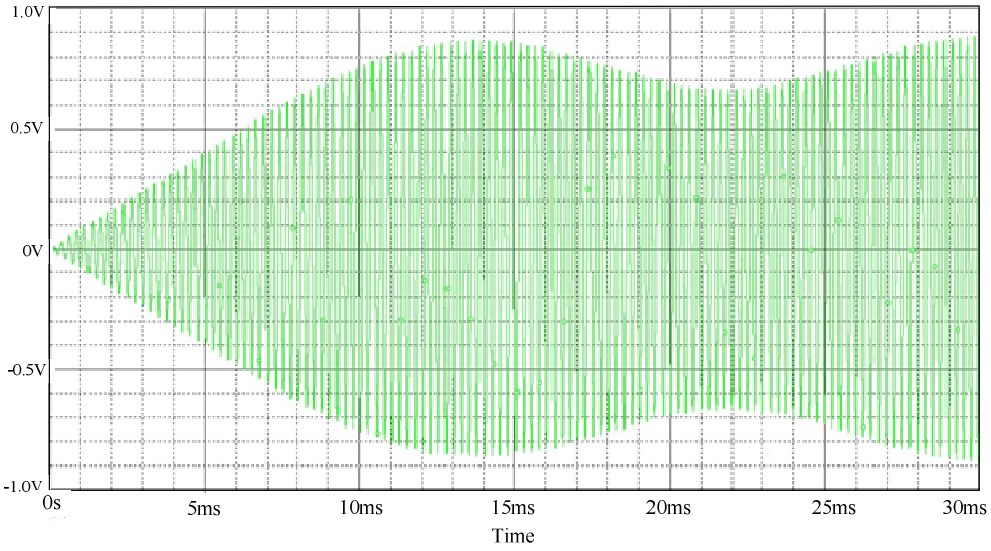

Figure 5.5: The output of the instrumentation amplifier for a sample angular rate of 300 %s at 64Hz.

The next stage in the development of the novel system is the phase compensation system. As discussed in Chapter 4, this is required in order to generate phase lagging compensation due to loop-filtering. In Figure 5.6 the transfer function block (in Simulink) for a phase lead compensation is shown and in Figure 5.7 the realization of this compensation and an all-pass/phase-shifting is presented.

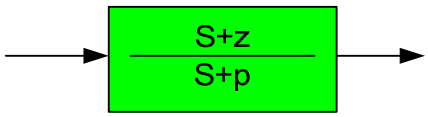

Figure 5.6: Compensation transfer function block in the Simulink model with zero z and pole p. To make this transfer function a phase lag compensation, zero in this circuit must be smaller than the pole in this circuit.

To make a phase lag compensating circuit the zero (z) must be greater than the pole (p) of this transfer function. Consequently, in the circuit realization, the following conditions, must be met for resistors and capacitors, which are shown in Figure 5.7.

$$R25.C11 < R22.C9$$

$$\&$$

$$R24.C12 < R23.C10$$

The output signal versus the input signal of this circuit is shown in Figure 5.8. Although it was planned to have an all pass/phase shifting circuit with unity gain, however, the design required a

level of phase shift which would lead to some loss of gain. However, this gain loss is compensated for by increasing the gain of the instrumentation amplifier.

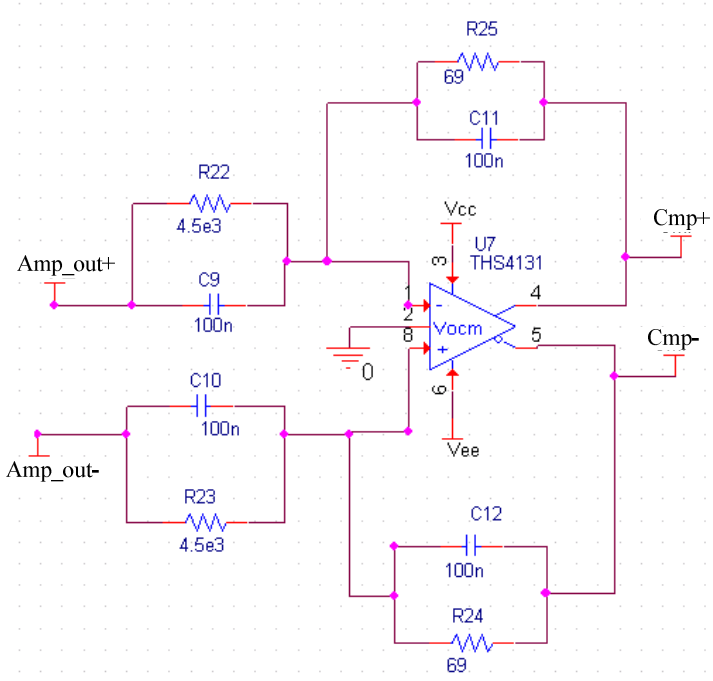

Figure 5.7: Realization of the compensation transfer function. The function is realized as an all pass/phase shift circuit. Amp_out+ and Amp_out- denote the differential input of the circuit from the instrumentation amplifier while Cmp+ and Cmp- denote the differential output from the circuit.

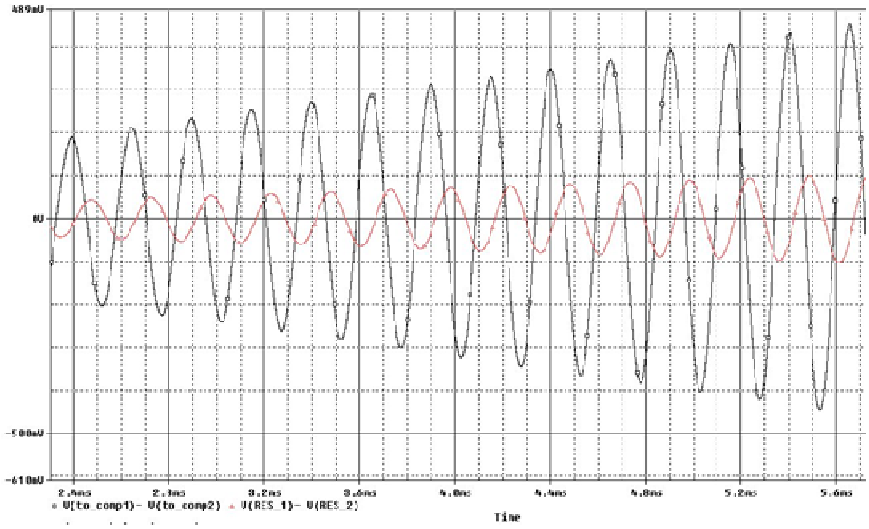

Figure 5.8: Input (black) and output (red) signals of the phase compensation circuit shown in Figure 5.7.

After this block, the next sub-circuit breaks down the compensation output signal into information and quadrature error signals at base-band (for this system from DC to 64Hz). Then, each component is taken back to the frequency of the drive mode resonance frequency as described in Section 4.3. In this sub-circuit, the behavioral model of a multiplier block is used and the low-

pass filters are made using a THS4131 operational amplifier as shown in Figure 5.9. The results of this sub-circuit are shown in Figure 5.10 where both the information (300°/s at 64Hz) and the quadrature error are at drive mode resonant frequency separately. As shown in this circuit, this part takes the signal from the output of the compensator circuit (Cmp+, Cmp-) and sends the two signals (i.e. the information signal and the quadrature error signal) to the following electronic loop filters.

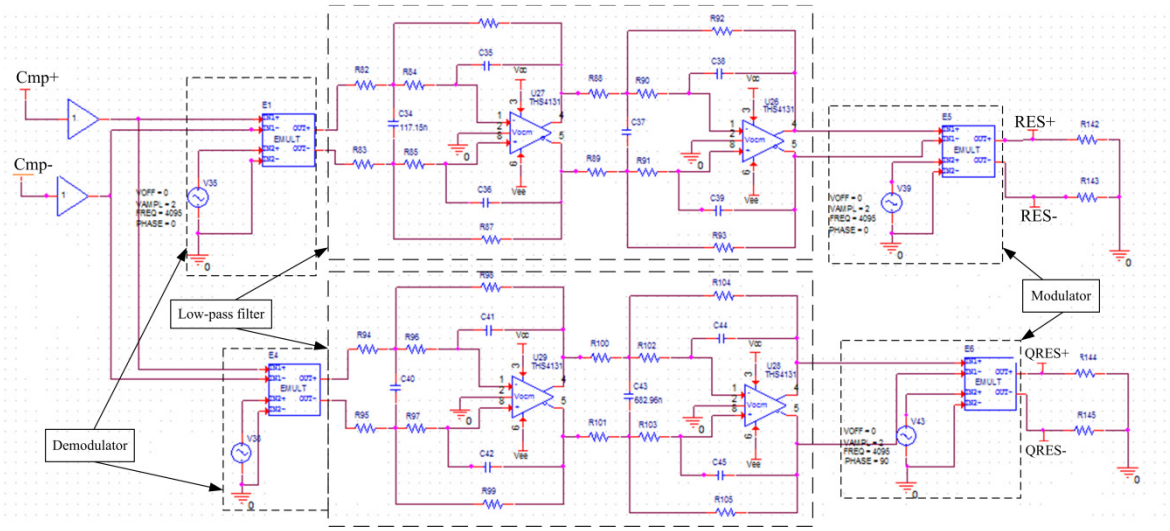

Figure 5.9: Demodulator and modulator block for the separation of the information signal from quadrature error. Cmp+ and Cmp- nodes denote the inputs from the compensation circuit, RES+ and RES- denote the outputs to the information electronic loop filter and QRES+ and QRES- denote the outputs to the quadrature error electronic loop filter.

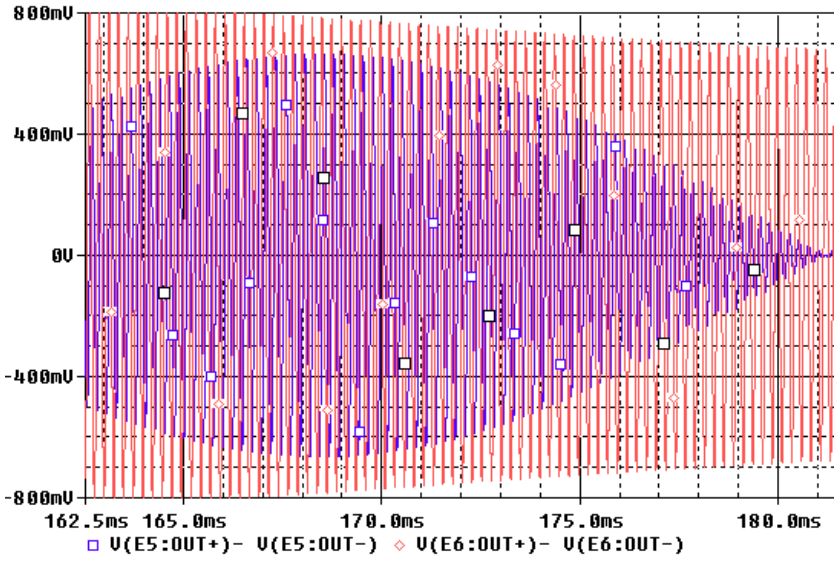

Figure 5.10: The output signal from the two outputs of the sub-circuit block shown in Figure 5.9. The red signal is the quadrature error and the blue signal is the information signal at 300 °/s at 64Hz.

As can be seen in Figure 5.10 the signal is broken down into the information signal and the quadrature error signal. However, although the quadrature error was expected to have a constant amplitude, there was a variation in amplitude. This is due to cross talk between the two channels which is caused by demodulation with an imperfect phase-match. However, as the primary objective in this work is to prove that the novel system works at a circuit simulation level, this status of the outputs is acceptable.

The part of this novel interface which plays the key role in shaping the quantization noise around the resonance frequency is the electronic loop filter. As shown in Figure 4.7 this system uses two sets of 4th order band-pass filters. The electronic circuit model uses the sub-circuit (shown in Figure 5.11) as the resonator component in the loop. The frequency response of this circuit is shown in Figure 5.12.

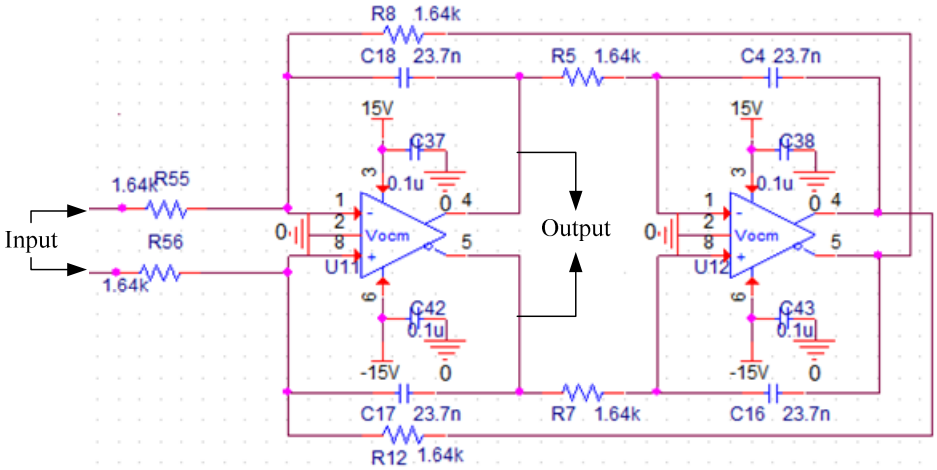

Figure 5.11: Circuit model of the resonator element in the band-pass loop filter.

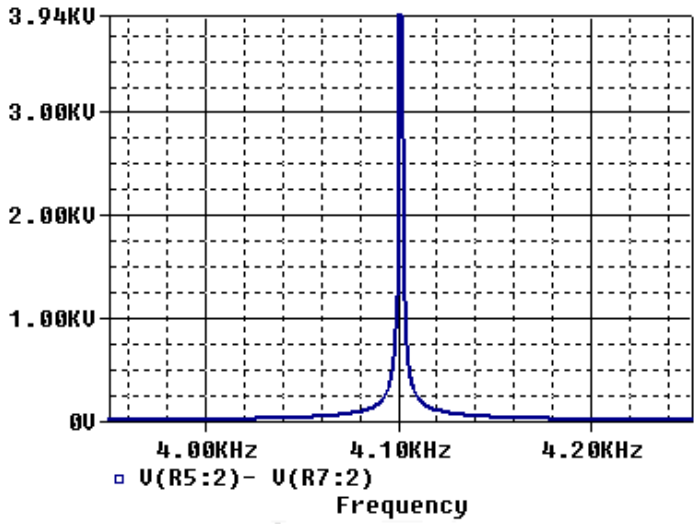

Figure 5.12: Fast Fourier transform (FFT) for the output of the resonator shown in Figure 5.11. For this resonator, the resonance frequency was about 4.10KHz.

As shown in Figure 5.12, the resonator has got a very high gain around its resonance frequency. As depicted in Figure 4.7, the output of the electronic loop filter is fed to a quantizer which is modeled as a zero crossing circuit as shown in Figure 5.13. This circuit is formed by an analogue comparator and the output of this comparator is fed into a D type flip flop to convert it to a digital format bit-stream. The output of the flip flop in the qauntizer is shown in Figure 5.14. This bit-stream is a snap shot of the bit-stream from the operations of the entire circuit model and the variation in the pulse duty cycle is due to a pulse density modulation which is deployed in each EMSDM stage of the novel system.

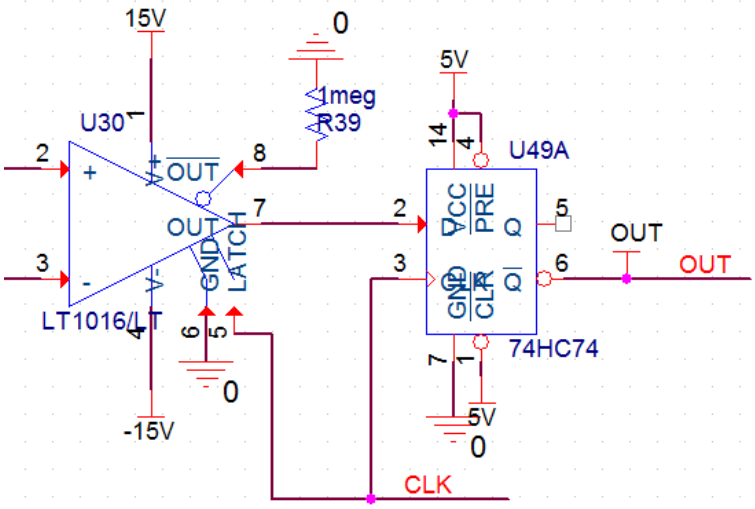

Figure 5.13: Pspice circuit model for the quantizer. An analogue comparator switches between a positive DC voltage and a negative DC voltage. This quantized signal is then transformed into a digitally compatible format by using a D-flip flop.

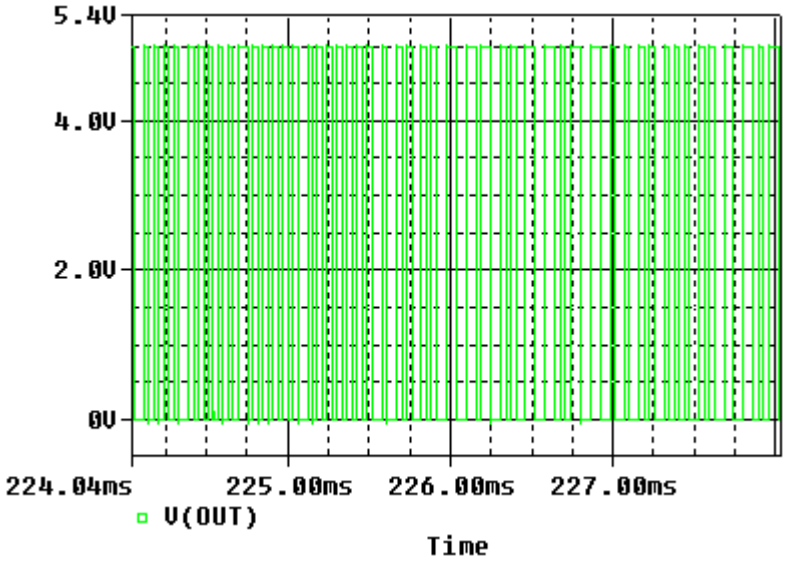

Figure 5.14: The output of the D type flip flop. The variation in the width of each pulse, denotes the pulse density modulation which is deployed by each EMSDM stage in the novel system.

Another sub-system block which was modeled in this simulation is a multiplexer block. This is the fundamental block that allows the generation of force feedback according to both angular rate information and quadrature error, in spite of the fact that the two signal are separated at an earlier stages of the system. As shown in Chapter 4, the outputs of the two electronic loop filters are multiplexed at a frequency which is twice as the sampling frequency. In this block the multiplexing frequency is twice the sampling frequency. The circuit model for this sub-system block is shown in Figure 5.15.

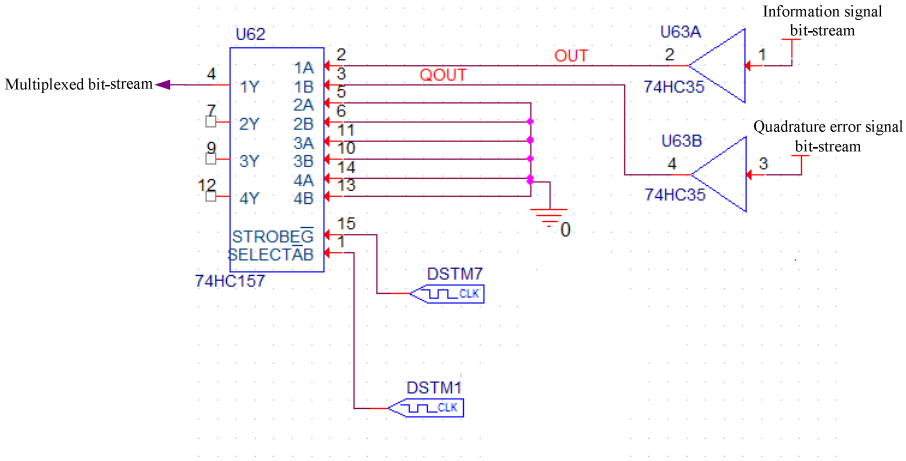

Figure 5.15: Time division multiplexer block for multiplexing the information signal bit-stream and the quadrature error bit-stream. The multiplexer chip switches between the channels at a frequency which is twice the sampling frequency.

Ultimately, the output of the multiplexer is fed to an analogue switch with a single-pole double-terminal (SPST) arrangement. This analogue switch shifts the signal (i.e. multiplexer

output) levels from 0V and 5V to $-V_{fb}$ and $+V_{fb}$. V_{fb} is an adjustable voltage which is used to manipulate the magnitude of electrostatic feedback force. The circuit model for the analogue switch is shown in Figure 5.16.

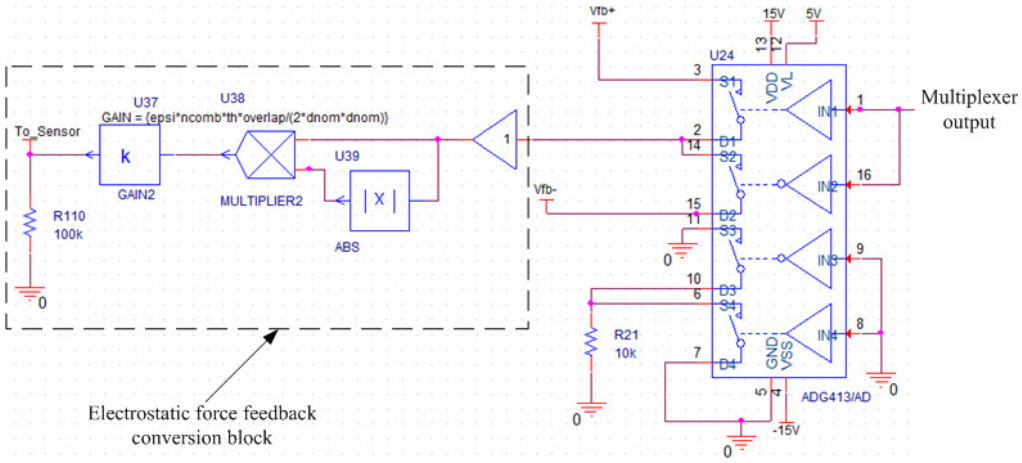

Figure 5.16: Circuit model for an analogue switch with SPDT configuration.

Also, as shown in Figure 5.16, a behavioral model for a sub-system block that converts the analogue pulse train to electrostatic force is used to model the application of the pulse train with amplitudes altering between $+V_{fb}$ and $-V_{fb}$. It must be noted that, in reality, two sets of complimentary pulses are generated and each set is applied to the feedback comb fingers of each side of the sensing element. This physical function of the feedback force and feedback comb finger was adopted here so the feedback for both sides could be applied to the "To_Sensor" node shown in Figure 5.16.

In this section, all the fundamental blocks which play key roles in making the entire novel system, are presented. A complete Pspice circuit model of the novel system can be found in Appendix C.

5.3. Circuit simulation results

To run the simulation for this model, a combination of a sample angular rate and quadrature error was set at the input of the behavioral model of the sense mode of the sensing element. The simulation parameters are listed in Table 5.1.

Table 5.1: Circuit level simulation parameter for the novel gyroscope system

Parameter	*Value*
Drive mode quality factor (Q_d)	100
Sense mode resonance frequency ($_s$)	4100 Hz
Sense mode quality factor (Q_s)	200

Mass (m)	2e-6 Kg
Input angular rate	300 °/s
Angular rate frequency	64Hz
Quadrature error (equivalent angular rate)	250 °/s

It must be noted that, the parameters of the circuit model simulation were obtained from the system level (Simulink) simulation. In this simulation, all parameters were held constant while the feedback force voltage (V_{fb}) was changed for three different simulation runs. The objective of this variation is to determine the maximum feedback voltage at which the displacement of the proof mass is most reduced without the control-loop becoming unstable. If this variation is proved to hold the control loop stable, it can be concluded that, in this architecture a designer will have the freedom to make a trade-off between proof-mass displacement control and power consumption. This simulation was run for three feedback voltages (V_{fb}) of 5V, 8V and 9V.

As shown in Figure 5.17, the circuit level simulation of the novel system indicates that the quadrature error at the output point is reduced by about two orders of magnitude. It must be noted that in the previous chapter, showed the power spectral density; in this section however, the figure is in volts and the fast Fourier transform (FFT) of the information channel output bit-stream is depicted. It is also demonstrated that the interface extracts the quadrature error as shown in Figure 5.18. In contrast, in the quadrature error channel, the information signal is attenuated.

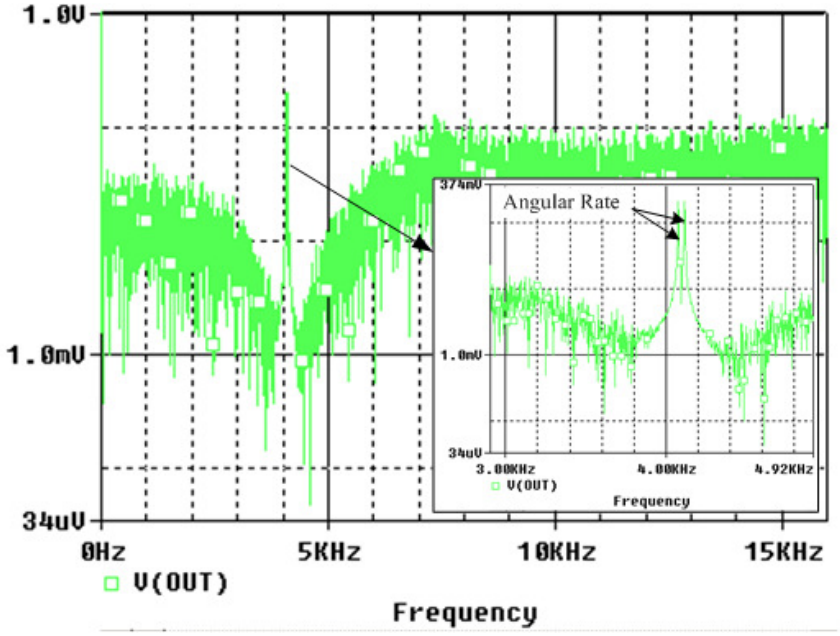

Figure 5.17: FFT of the information channel bit-stream. As shown, the quadrature error is attenuated by about two orders of magnitude.

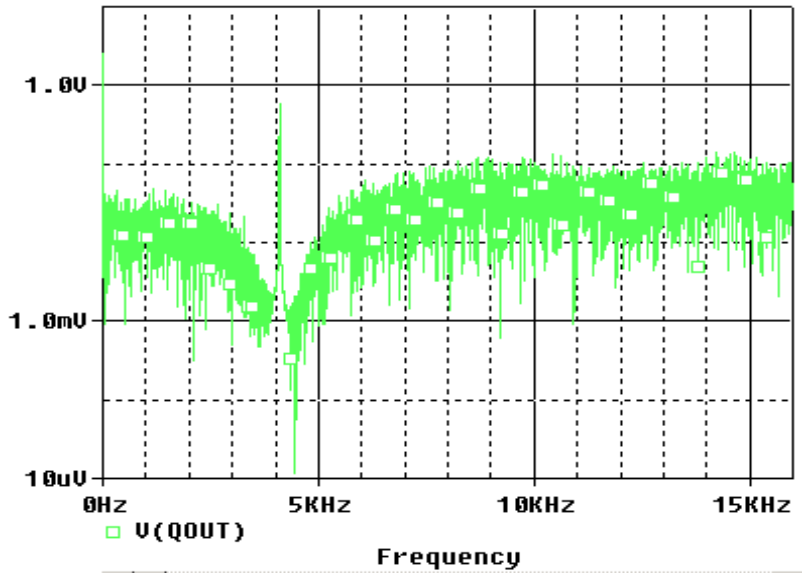

Figure 5.18: FFT of the quadrature error channel bit-stream. As shown, the quadrature error is extracted and fed through this channel.

In addition, as stated in the previous chapter, another objective is to control and reduce the displacement of the proof mass. In order to compare the displacement of the proof mass in both open-loop and closed-loop conditions, a combination of the Coriolis force and quadrature error is applied to a sense mode transfer function block which is outside of the control loop. The feed of the combined signal is carried simultaneously to the two blocks as shown in Figure 5.19.

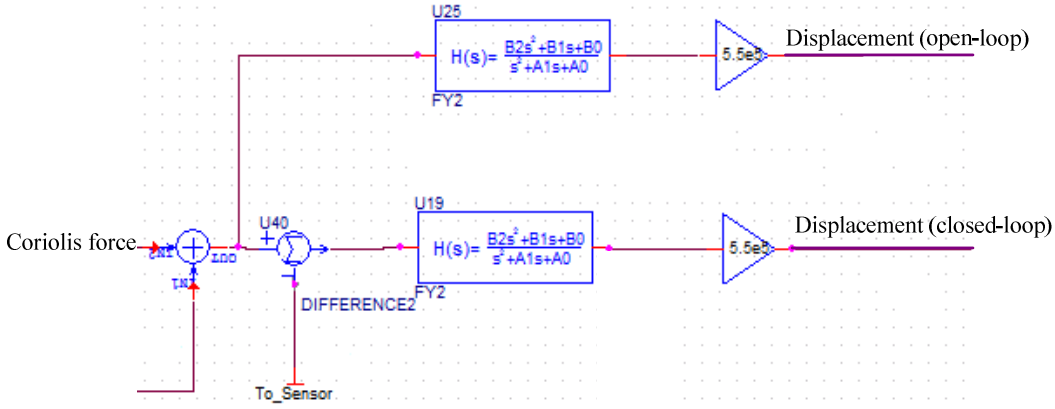

Figure 5.19: Two sense mode transfer function blocks. One is in the control loop and one is in open-loop mode. The one in the control loop recieves the feedback signal via the "To_Sensor" node.

As shown in all of the following figures, it is clearly proven that the proof mass displacement is controlled at any of the applied feedback voltage levels. It must be noted that in all these scenarios half of the displacement compensation is compensating for the movements which are

generated by quadrature error. This is because the duty cycle of the multiplexer selection signal is set at 50%.

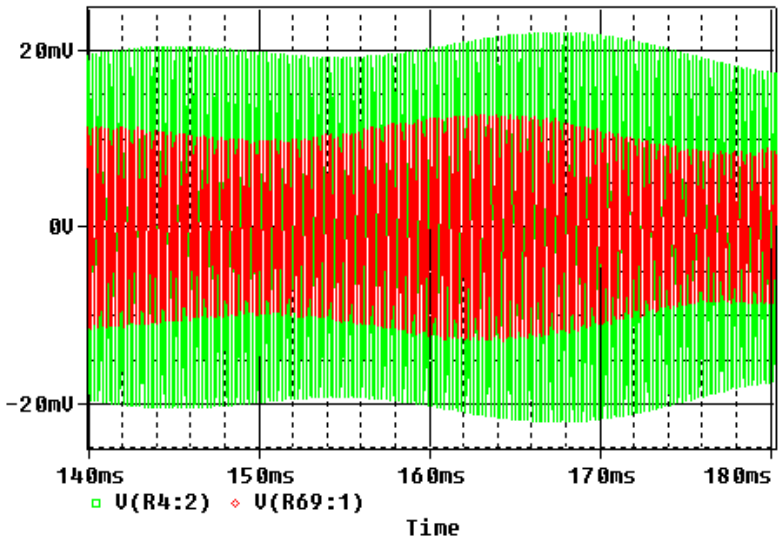

Figure 5.20: Comparison between proof mass displacement (readout circuit output) in open-loop (green) and closed-loop (red) modes. The feedback voltage is set to 5V.

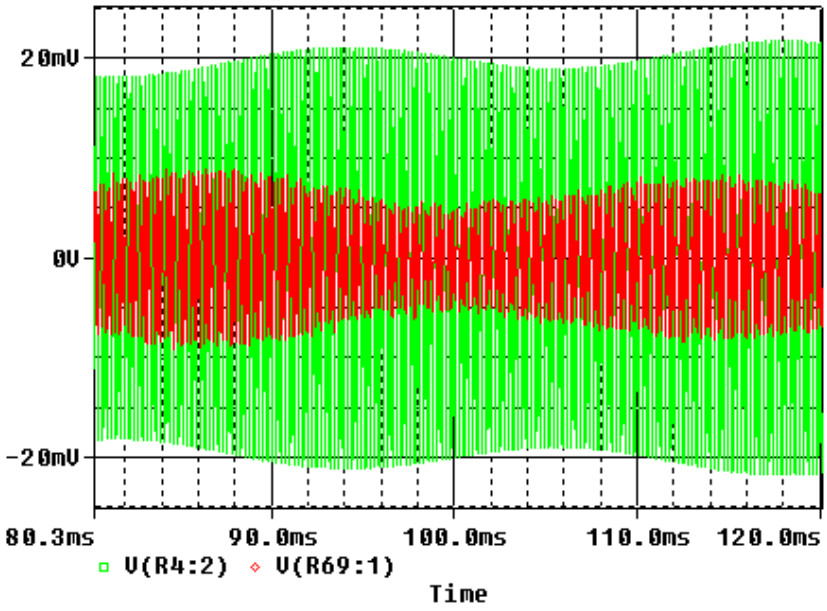

Figure 5.21: Comparison between proof mass displacement (readout circuit output) in open-loop (green) and closed-loop (red) modes. The feedback voltage is set to 8V.

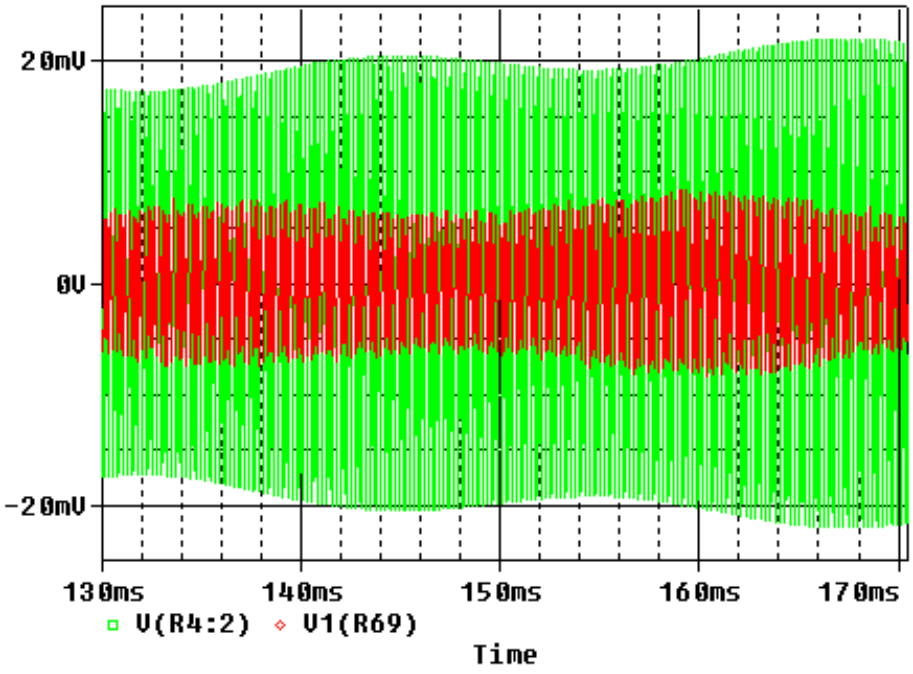

Figure 5.22: Comparison between proof mass displacement (readout circuit output) in open-loop (green) and closed-loop (red) modes. The feedback voltage is set to 9V.

As shown in the figures above, there is a significant decrease in the magnitude of the displacement for the feedback voltage at 8V (Figure 5.21) compared to the one at 5V (Figure 5.20). However, there is no decrease in the displacement when the feedback voltage is changed from 8V to 9V; This is shown in Figure 5.22. To have a more accurate understanding of this measurement the root mean square (RMS) of the proof mass movements are presented in Table 5.2. It must be noted that values are taken from the output of the readout circuit and not the sense mode transfer function. Hence, the unit of this measurement is voltage; it is not a projection of any other units.

Table 5.2: RMS of proof mass displacement versus feedback voltage

Feedback voltage	*RMS of readout circuit output*
0V	13.8mV
5V	7.8mV
8V	4.8mV
9V	4.7mV

5.4. Conclusion

In this chapter a circuit level simulation of the novel system was implemented. For the mechanical part (the sense mode of the sensing element), a behavioral model was used and the rest of system was modeled using the Pspice model of components which are available in the market. It

has been shown that quadrature error can be attenuated by about two orders of magnitude at the information signal output; at the same time, both information originated displacement and quadrature error originated displacements can be monitored and fed back to the sensing element. In addition, it was proven that the displacement of the proof mass could be reduced to about 30% of that an open-loop system for the same micro-gyroscope sensing element. Also, all electronic components can be integrated on one single chip as an application specific integrated circuit (ASIC) design.

Chapter 6 Experiment results

6.1. Introduction

In this chapter, a hardware implementation of the novel quadrature error cancellation scheme is examined, in order to determine if the results which were obtained at the system/circuit simulation level can be reproduced in practice. It must be noted that some parts in the hardware implementation did not exist in the simulation models and were therefore presented as a source (e.g. voltage source). For instance, a driver for the drive mode of the sensing element is one of the circuits presented in this chapter. Also, the deployment of some additional sub-circuits is explained. It is crucial to use these sub-circuits due to the existence of non-idealities in the real world; these did not matter in the system and circuit level simulations. These sub-circuits were deployed to overcome the existence of non-idealities (which are discussed in detail later in this chapter) that were encountered while the circuit was built.

In the first step, the function of the sub-circuits of the novel system (which were previously modeled and simulated) is explained; the outputs of the circuits are presented to verify their correct function. Afterwards, the operation of the complete circuit is presented and discussed. Ultimately, the results obtained are compared with those achieved from the system level and circuit level simulations. The complete circuit schematic can be found in Appendix C.

6.2. Sub-circuits deployed in the implementation of the novel system

The primary objective of EMDSM is to embed an inertial sensing element in a closed-loop control system. Hence, first of all, the sensing element and the readout circuit are explained. For this experiment, the gyroscope sensing element depicted in Figure 6.1 was used. This was provided by South China University.

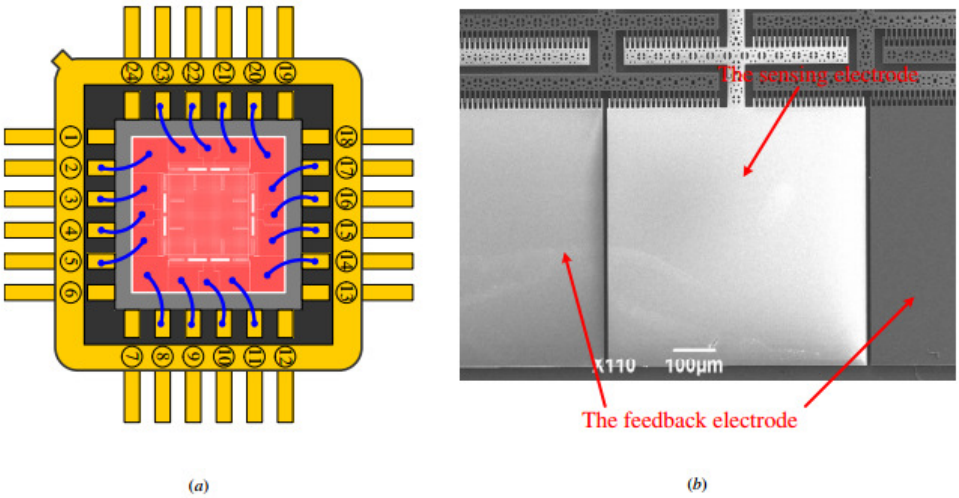

Figure 6.1: (a) Diagram of the packaged and wire bonded MEMS gyroscope; (b) a SEM view of the sensing and feedback electrodes (reproduced from [61]).

Each side of this sensing element has two sets of comb fingers. Each pair of opposite sides is appointed to play either the sense mode or the drive mode. The fact that there are two separated sets of comb fingers at each side provides the facility to monitor the displacement of the proof mass in the drive mode. The drive signal is applied to opposite sides (with opposite polarity) and at the same time the displacement of the proof mass is read via a readout circuit which are connected to two sets of comb finger (for instance via nodes 15,17 and 3,5 in Figure 6.1 (a)). This structure is deployed to implement a closed-loop circuit by applying the feedback signal to one set of comb fingers on one side of the sense mode while the sense mode movements are read out via the other set on the same side.

As discussed in Section 3.4, the half-bridge readout circuit is deployed to read the displacements of the proof mass [82]. As this circuit uses a high frequency (more than 1MHz), the proof mass is connected to a high frequency sine wave source. For this design, the best output was obtained at around 1.5MHz. It must be noted that, due to the existence of parasitic capacitors between the drive mode and the sense mode, the drive mode voltage leaks into the electrodes of the sense mode and, if this is not filtered out, it will appear at the output as an unwanted signal. The fact that the coupled drive voltage is at drive frequency and is much lower than the frequency of the carrier (at around 1 MHz) justifies the use of high pass filters right after the charge amplifiers where the capacitance changes are translated into voltage level variations. This is shown in Figure 6.2.

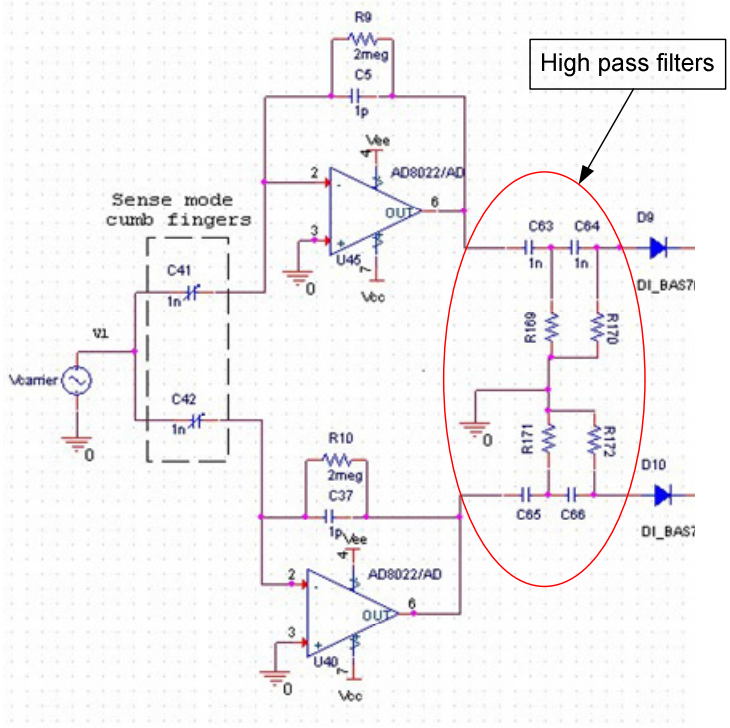

Figure 6.2: Placement of the passive high-pass filter, in order to filter the coupled voltage from the drive mode. The cut-off frequency for this filter is set to 1.4MHz.

The output of the readout circuit is passed through some further band-pass filters (the pass-band is around the drive mode frequency) in order to filter out any induced noise. Then, the signal is fed to an instrumentation amplifier (here AD8221) to amplify further the signal while keeping the noise as low as possible. The combination of AD8221 and AD8676 make it possible to convert the single-ended output of the amplifier into a differential output, as shown in Figure 6.3.

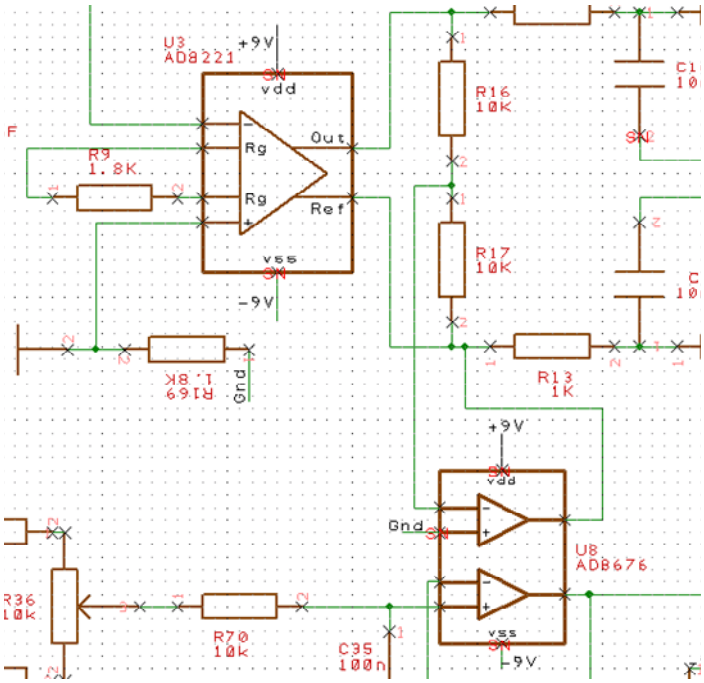

Figure 6.3: Instrumentation amplifier with its output converted from single ended to differential output. This arrangement contributes towards conserving space and lowering power.

At the next stage, a differential amplifier which has a differential output (THS4131) is deployed to amplify the signal further. After this stage, the phase compensation circuit is put in place to provide phase compensation and subsequently stabilize the control loop.

The next point in the circuit is the stage where the readout signal is broken down into the information (angular rate) signal and quadrature error at sense mode resonance frequency. The circuit is exactly the same as it is described in Section 5.2. Here, a quadrature demodulator is implemented by using analogue multiplayer chips (i.e. AD633) and a second-order active low-pass filter. The multiplayer is deployed in such a way that the output is scalable and this is done to compensate the 0.1 factor that is applied to the output by the internal circuit of the chip, as shown in [84]. The active low-pass filter is built as a fully differential filter by using THS4131. The two components of the readout circuit are extracted, by using the second stage of multipliers to modulate them electronically at the sense mode resonance frequency. At this stage, the scalable circuit arrangement is used again as well as the demodulation stage. Oscilloscope snap-shots from the output of the sub-circuit for zero-rate input and non-zero-input are shown in Figure 6.4 and

Figure 6.5 respectively. As shown in Figure 6.5, at zero-rate input, there are some cross talks and some surrounding vibrations which appears in the output of both the quadrature error channel and the information (angular rate) channel. The cross talk can be further reduced with further signal processing on the output bit-stream from the output channel.

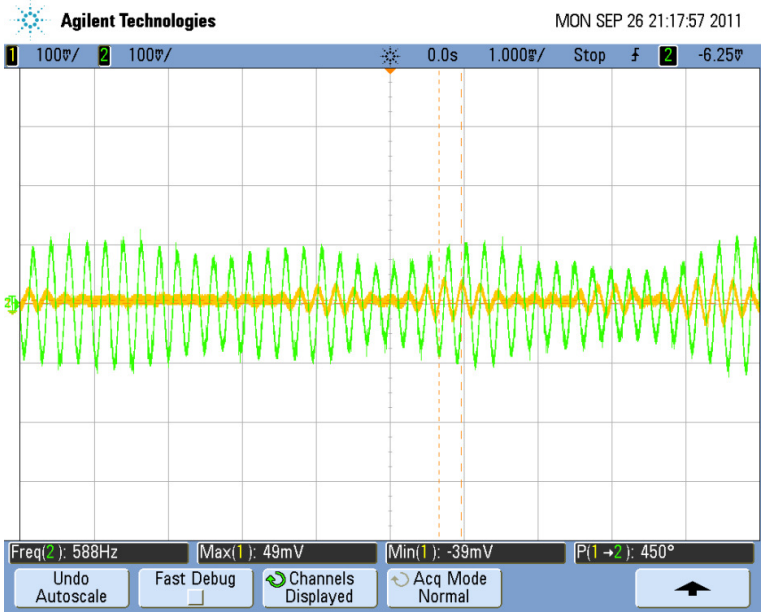

Figure 6.4: The two outputs of the quadrature demodulator against a zero angular rate input. One output extracts quadrature error (green) and the other one extracts angular rate (yellow).

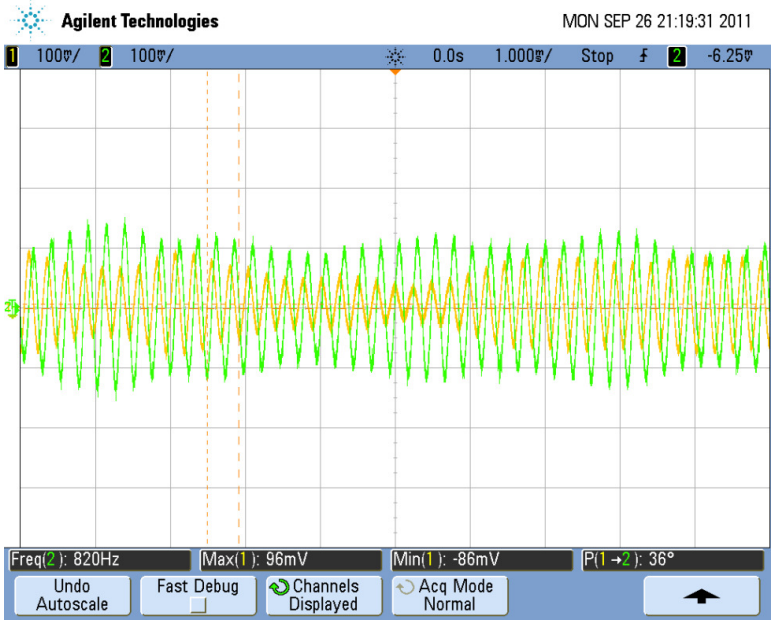

Figure 6.5: The output signals from the quadrature demodulator again a non-zero angular rate input. One output extracts quadrature error (green) and the other one extracts angular rate (yellow).

Also, as shown in Figure 6.5, for a non-zero angular rate, the amplitude of the output in the quadrature error channel stays approximately the same. On the other hand, the amplitude of the signal in the angular rate channel is increased significantly as expected. At this point it is confirmed that the quadrature demodulator/modulator circuit functions appropriately in separating angular rate information from quadrature error.

At the next point, each component is fed into a band-pass 4^{th} order pure electronic SDM (sigma delta modulator). In order to test that these two SDMs work correctly on their own (and not as a part of closed-loop system), the output of the previous stage (demodulator/modulator) is fed into these sub-circuits. As shown in Figure 6.6 it is proved that the two sets of electronic SDMs shape quantization noise around the sense mode resonance frequency. It must be noted that, in order to avoid as much as possible the effect of noise sources in the circuit, both modulators are based in a fully differential operational amplifier (i.e. THS4131).

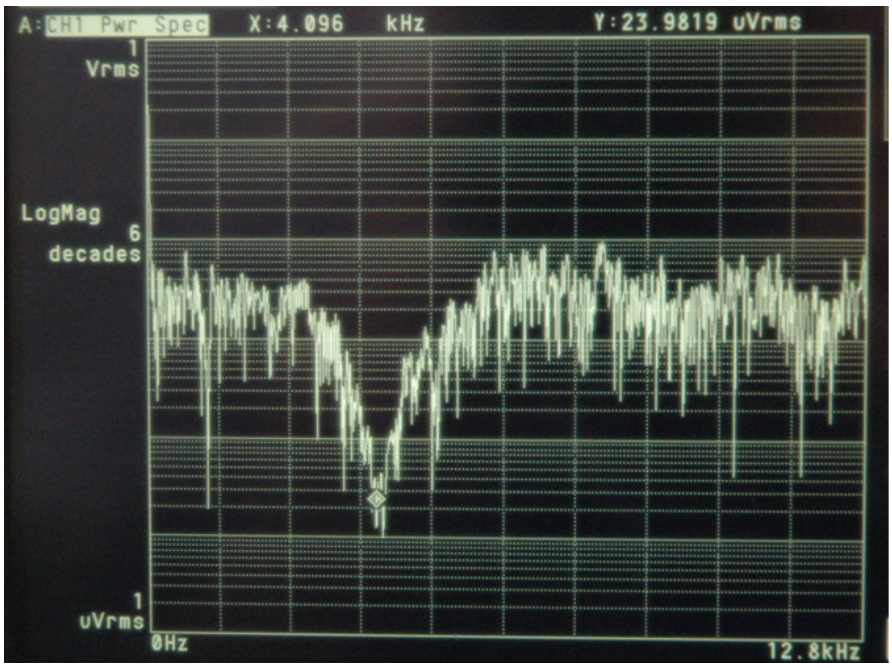

Figure 6.6: The frequency response spectrum for the 4^{th} order pure electronic SDM output bit-stream for zero-input. As shown, the quantization noise is shaped away around 4.1KHz which is the resonant frequency of the sense mode in the sensing element.

As illustrated in the previous two chapters, at this point, the output bit-stream from both the information and quadrature error channels are multiplexed at a frequency which is twice the sampling frequency. This action is carried out by deploying a two channel to one channel multiplexer (i.e. SN74LVC2G157). The output of the multiplexer is fed to a buffer and an inverter for two reasons: firstly, to drive the analogue switch which applies the feedback voltage to the feedback nodes on the sensing element; secondly, to generate two complementary bit-streams for the opposite sides of the sensing element (in the sense mode). The clocking for this multiplexer and

quantizers is formed from a programmable oscillator and a D-type flip flop as shown in Appendix D. The role of analogue switches (i.e. MAX333A) in this design is to shift the level of feedback bit-stream from logic level (0V-5V) to $-V_{fb}$ and $+V_{fb}$ where V_{fb} is the feedback bit-stream. A picture of the complete system is presented in Figure 6.7.

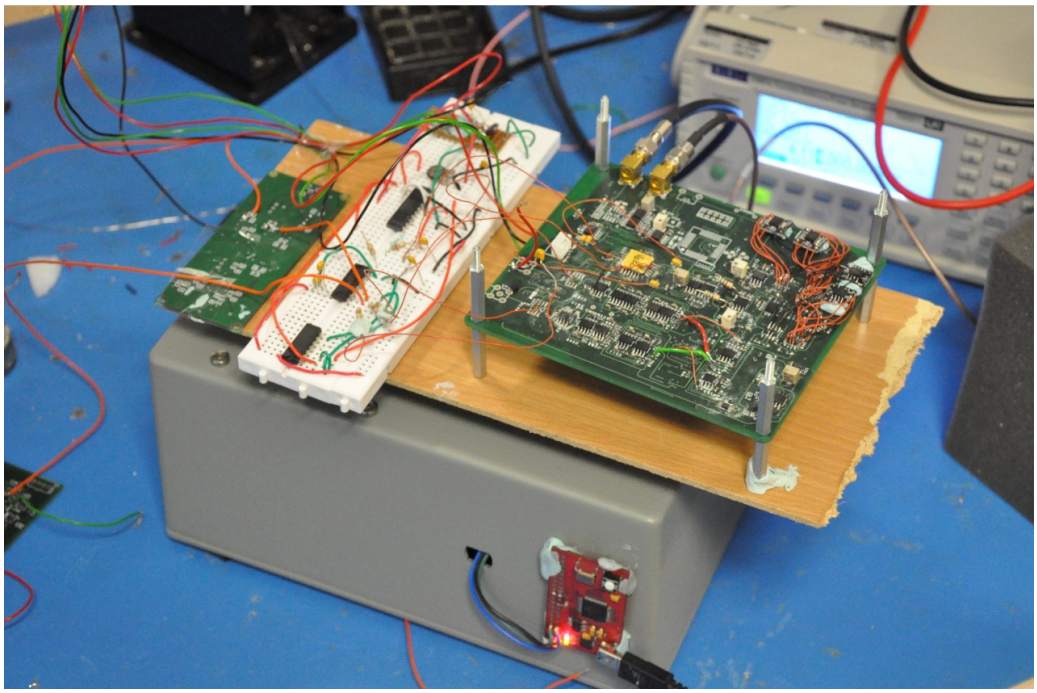

Figure 6.7: The complete circuit for a 6th order band-pass EMDSM with the capability of eliminating quadrature error.

6.3. Experiment results

The structure of the prototype circuit for the novel interface was explained in the previous section. In this section, the results of experiments which were carried out for a sample gyroscope sensing element are presented and discussed. For this experiment, a gyroscope sensing element with the following specifications was used.

Table 6.1: Specifications for the sample gyroscope sensing element

Parameter	*Value*
Proof mass (Kg)	1.99e-6
Sense mode quality factor	200
Drive mode quality factor	100
Sense mode resonance frequency (Hz)	4120
Drive mode resonance frequency (Hz)	4100

The parameters for the circuit (e.g. gains and feedback co-efficient) are all taken from the Simulink system level design. In the first step, the parameters from the system level simulation are

interpreted into circuit parameters (e.g. resistor values). This is the first attempt to determine if the Simulink simulation model can be a suitable starting point to realize a design. In this experiment, the system was first directly implemented from the parameters which were produced by the GA design automation system. Before closing the control loop, all sub-circuits worked as expected and the extracted quadrature error was seen the spectrum diagram of the bit-stream from the 4th order SDM as shown in Figure 6.8.

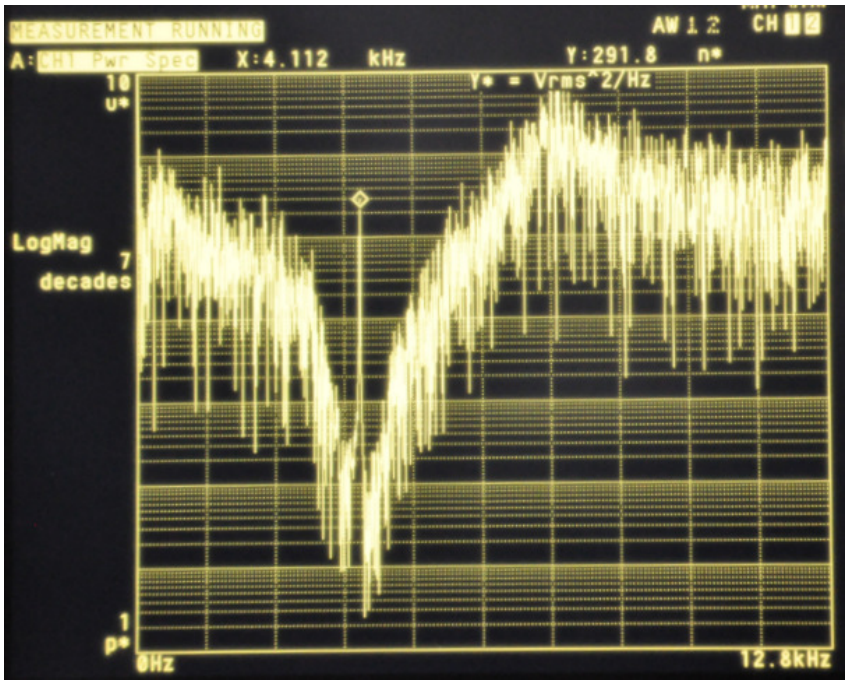

Figure 6.8: Power spectrum for the bit-stream from the quadrature error channel in open loop mode.

However, once the feedback voltage (V_{fb}) starts increasing from 0V, the performance of the quadrature channel starts to decay and a number of unknown tones appear at the power spectrum, as shown in Figure 6.9. The reason for such a fault in the circuit arises from the fact that the feedback voltage is fed to the feedback nodes on the gyroscope sensing element in the form of pulse trains. Considering that a pulse train with a frequency of ω_0 can be written as:

$$x(t) = \frac{4}{\pi}\sin(\omega_0 t) + \frac{4}{3\pi}\sin(3\omega_0 t) + \frac{4}{5\pi}\sin(5\omega_0 t) + \frac{4}{7\pi}\sin(7\omega_0 t) \ldots. \quad (6.1)$$

Then this shows that a pulse train at ω_0 frequencies contains some very high frequency components, in addition to the main frequency and they are all multiples of ω_0. On the other hand, the structure of the gyroscope sensing element is a capacitive one, as shown in chapter 2. From basic rules considering electricity, it is known that the impedance of a capacitor is in reverse relation to the frequency of the exerting signal. Hence, it can be concluded that the high frequency components

from the feedback pulse train lower the impedance of the feedback capacitive structure to a level that a high level of current is drawn from the circuit which affects the function of the modulators. Using a first order low-pass RC filter with cut-off frequency of 5KHz, rectified the problem as shown in Figure 6.10.

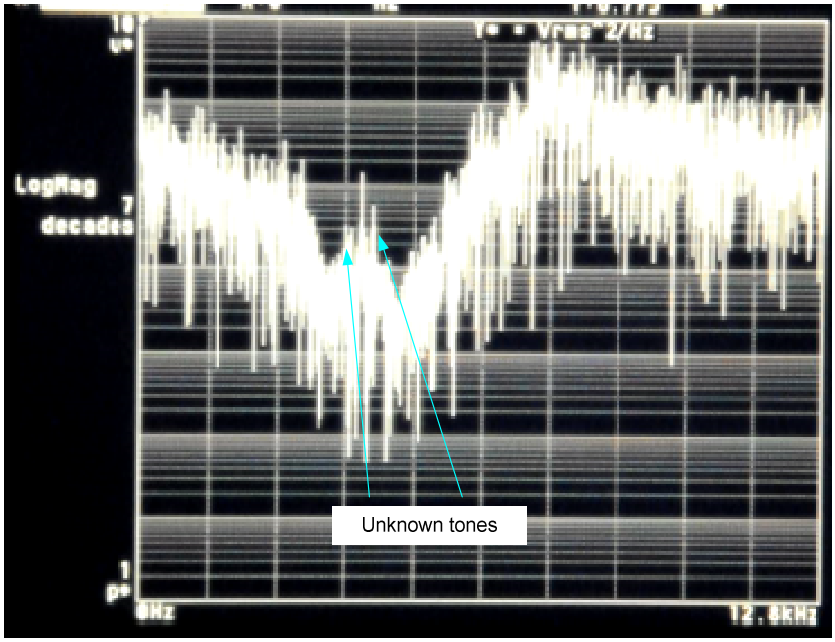

Figure 6.9: Power spectrum for the output bit-stream from the quadrature error channel when feedback voltage was increased to greater than 1V.

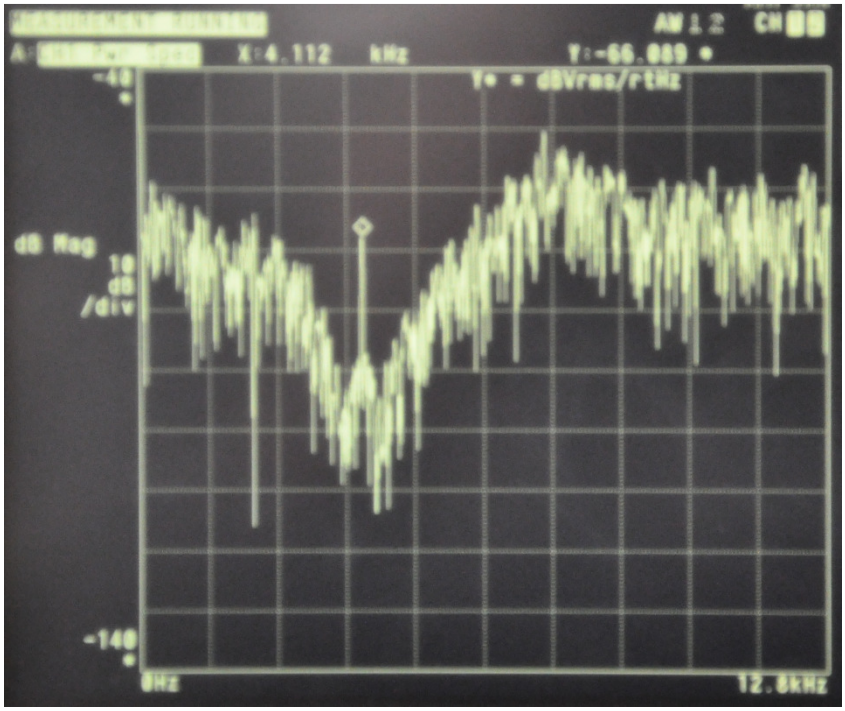

Figure 6.10: Power spectrum from the quadrature error channel bit-stream when the feedback voltage was set at 5V.

At this point, it is established that the closed-loop system works as expected since the input signals (i.e. Coriolis force and quadrature error) appear at the output of the novel interface. The next step is to determine how much the novel system attenuates quadrature error and how much it controls (reduces) the displacement of the proof mass in the sample micro gyroscope sensing element. For running the experiment from the by adjusting the phase shift on the carrier signal, the effort was made to maximize the quadrature error power in quadrature error channel and minimize it in information signal channel as shown in Figure 6.11 and Figure 6.12.

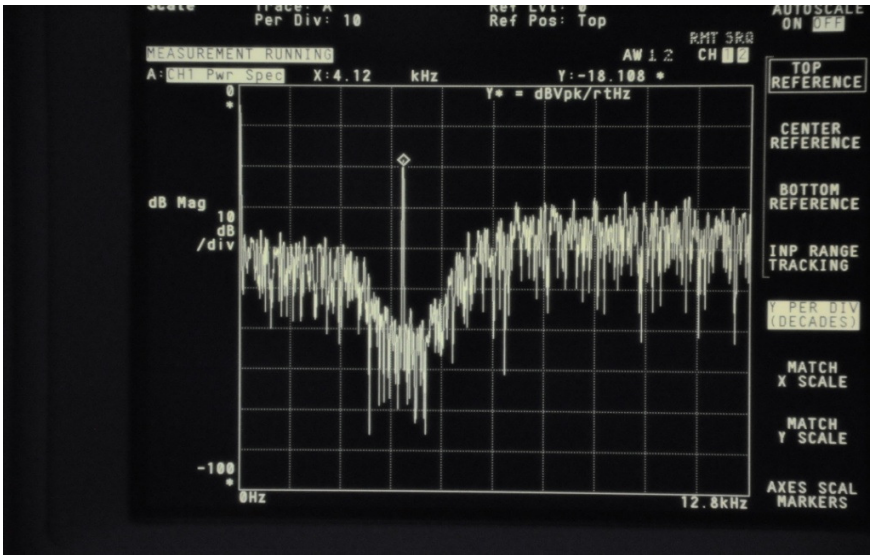

Figure 6.11: Power spectral density of the bit-stream from the quadrature error channel after adjustments where mad to maximize the quadrature error power in the channel.

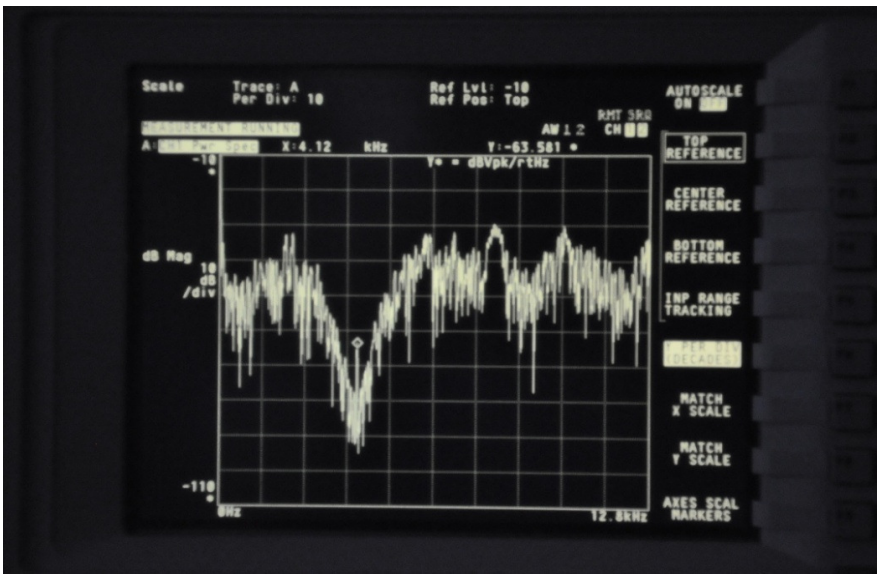

Figure 6.12: Power spectral density of the bit-stream from the angular rate channel, after adjustments was made to minimize the quadrature error power in the channel.

In the power spectral density figures above, the feedback voltage was at 0V. Also, the displacement of the proof mass must be monitored under this condition (as shown in Figure 6.13) so there is a way of comparing the displacement when the feedback voltage increases. Once the phase adjustment was accomplished the feedback voltage was increased first to 3V and then to 5V. For a feedback voltage of 3V, the following results were obtained.

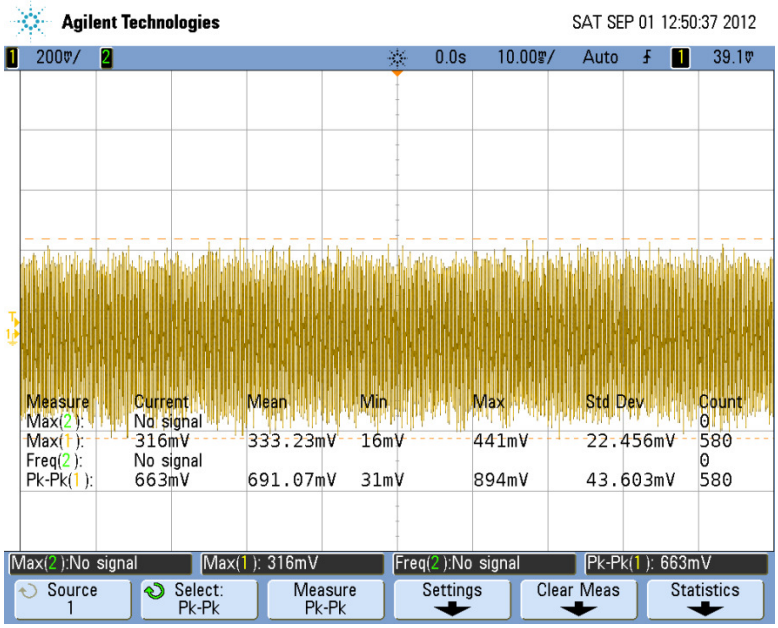

Figure 6.13: The output from the instrumentation amplifier for a feedback voltage of 0V. This diagram projects the displacement of the proof mass.

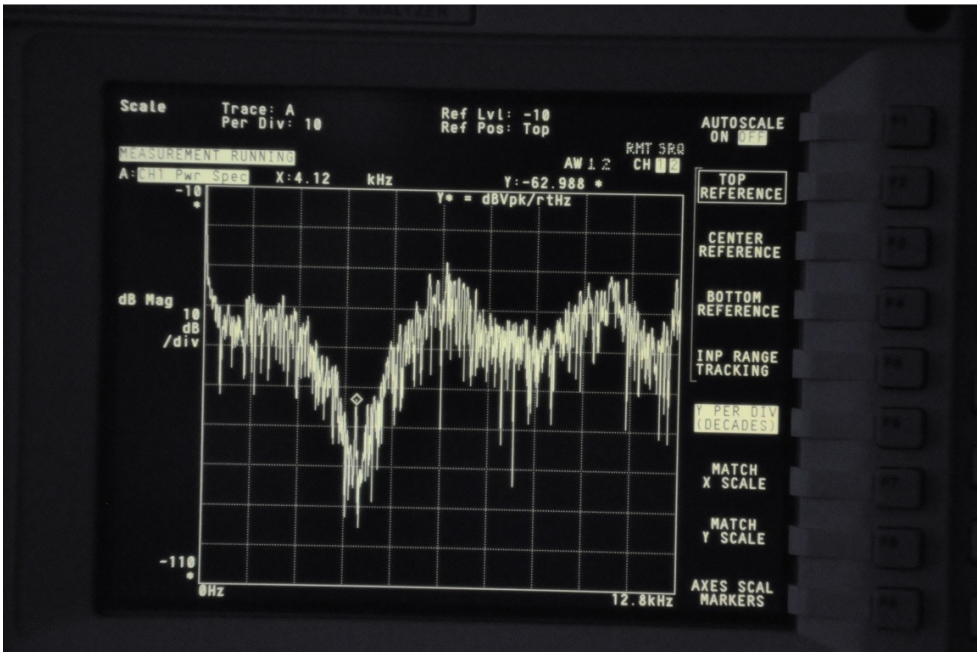

Figure 6.14: Power spectral density of the information (angular rate) channel at a zero angular rate with 3V feedback voltage. There is some cross talk from the quadrature error channel into this channel.

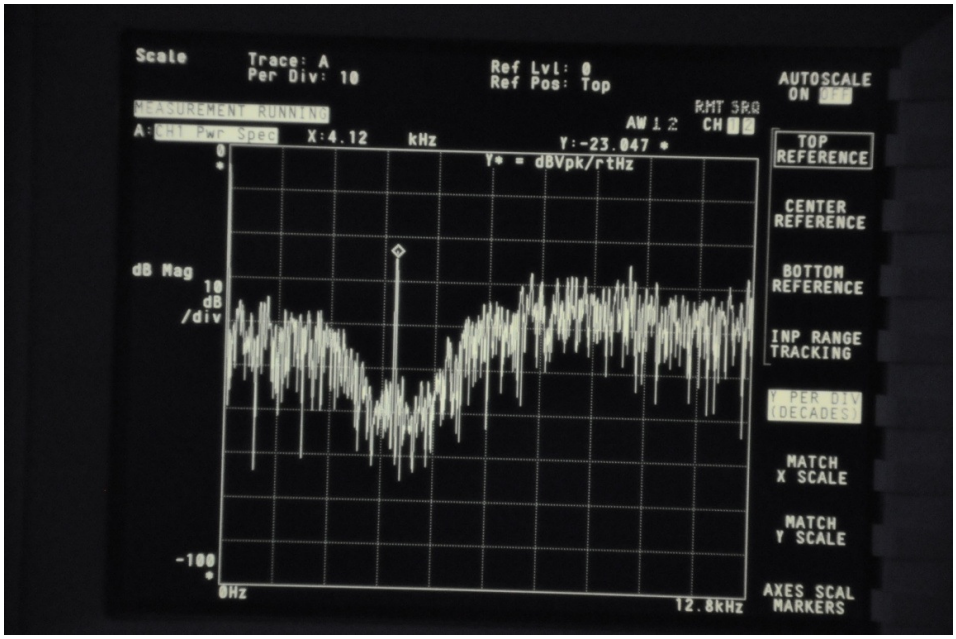

Figure 6.15: Power spectral density of the bit-stream from the quadrature error channel at a feedback voltage of 3V. In contrast to the one with a feedback voltage of 0V the power has decreased by about 5dB.

In order to verify that, while the new system attenuates the quadrature error in the output, the proof is mass fully controlled, the changes in the amount of displacement were also monitored and it is confirmed that the new system can successfully control the displacement of the proof mass, as shown in Figure 6.16.

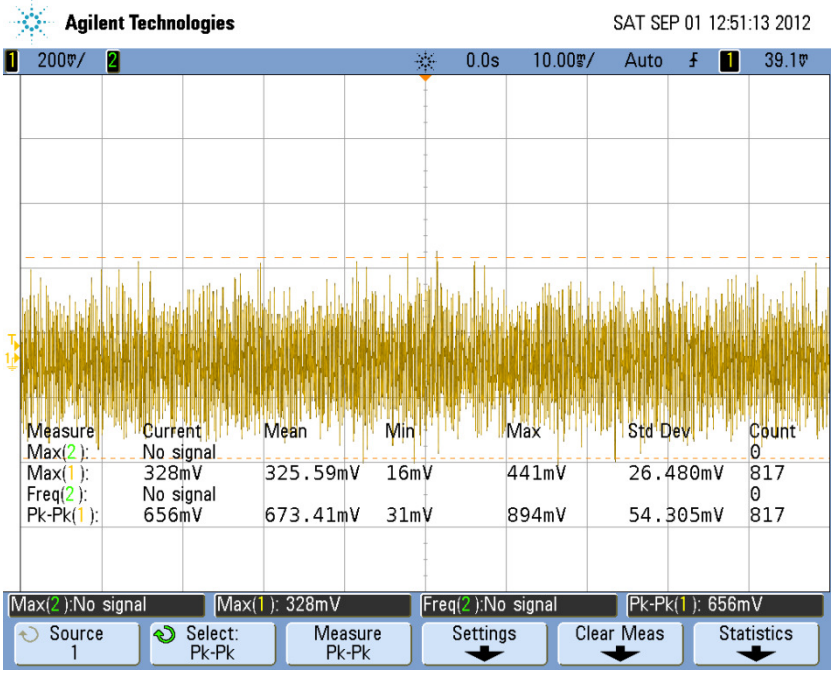

Figure 6.16: The displacement of the proof mass (amplifier output) at a feedback voltage of 3V.

Furthermore, when the feedback voltage was increased to 5V, a further decrease in the displacement of the proof mass was achieved, as shown in Figure 6.17. In the meantime, the performance of the system stayed intact as shown in Figure 6.17 and Figure 6.18.

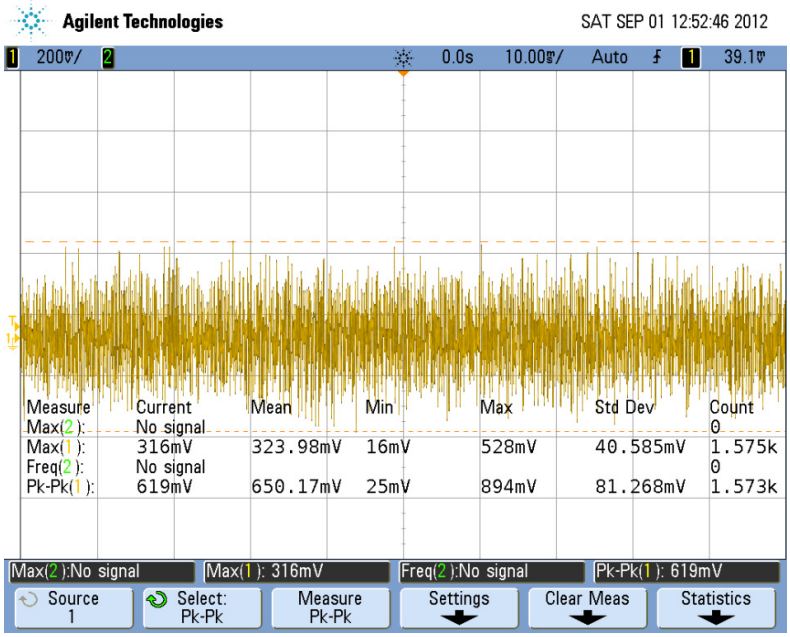

Figure 6.17: The displacement of the proof mass (amplifier output) at a feedback voltage of 5V.

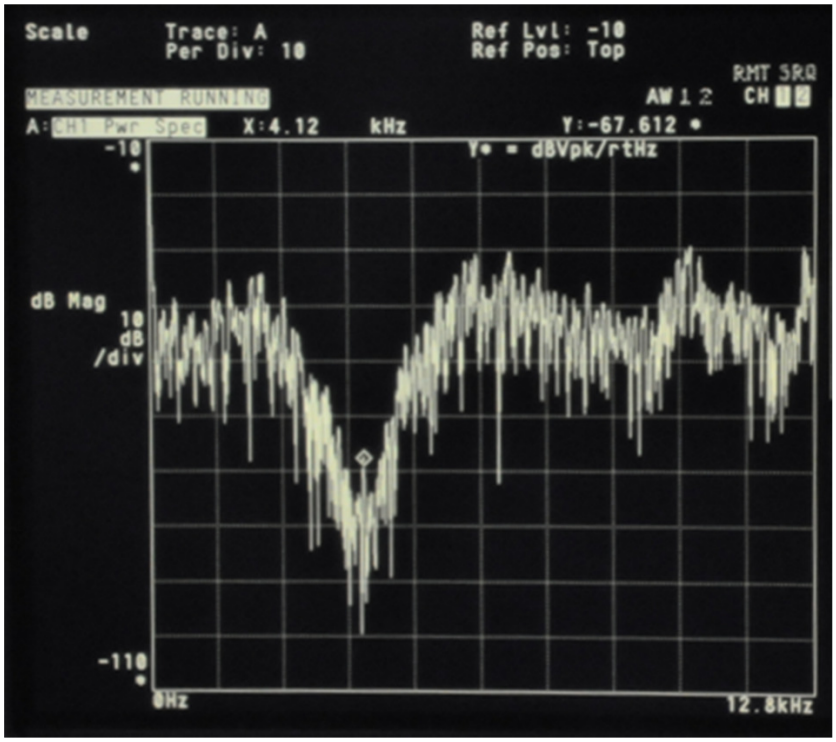

Figure 6.18: Power spectral density of the information (angular rate) channel at a zero angular rate with a 5V feedback voltage. There is some cross talk from the quadrature error channel into this channel. There is about a 5dB decrease in the amount of cross talk in comparison to the one with a feedback voltage of 3V.

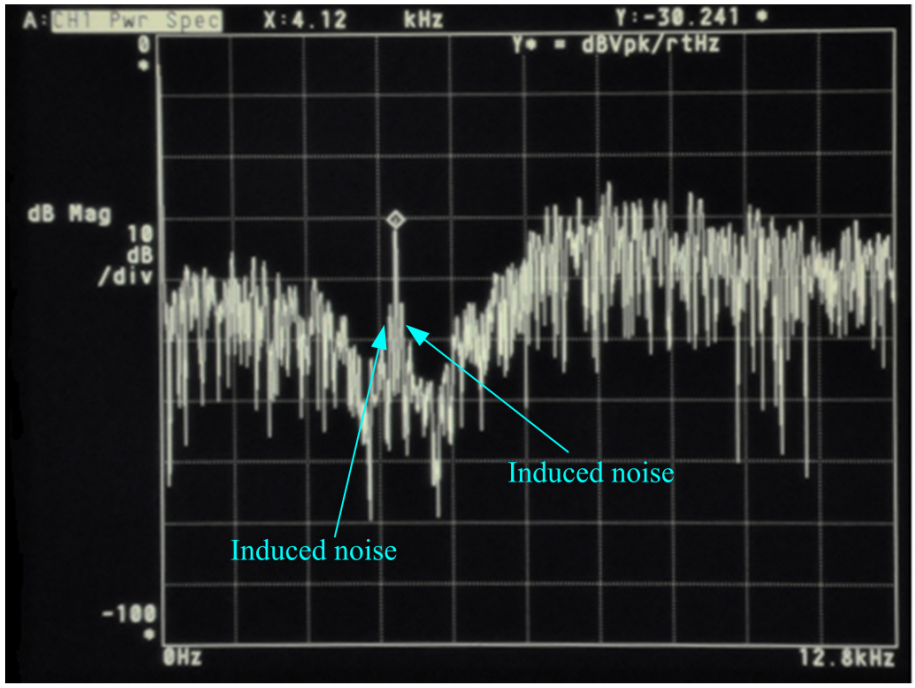

Figure 6.19: Power spectral density of the bit-stream from the quadrature error channel at a feedback voltage of 5V. In comparison with the one with a feedback voltage of 0V the power has decreased by about 7dB.

As can be observed, there is a slight decrease in the displacement of the proof mass in comparison with the one with a feedback voltage of 3V. Failing to achieve more significant control is due to the induced noise which appears in the quadrature error channel power spectrum, as shown in Figure 6.19. In other words, because of the existence of this noise, the system cannot precisely track the movement of the proof mass in the micro-gyroscope sensing element.

6.4. Discussion

The hardware implementation of the system shows an acceptable correspondence to the system level simulation of the design which was presented in Chapter 4 (shown in Figure 4.12). The quadrature error power spectral density is attenuated by about 70dB which is equivalent to more than 3 orders of magnitude attenuation. This achievement is shown in Figure 6.14 and Figure 6.18 with feedback voltage of 3V and 5V respectively.

Table 6.2: Feedback voltage versus root mean square of proof mass displacement

Feedback voltage(V)	*Displacement (mV)*
0	320
3	213
5	198

Moreover the measurements from the output of the pick-off circuit (capacitance to voltage converter followed by an amplifier) shows that increasing the feedback voltage decreases the displacement of the proof-mass as presented in Table 6.2. This observation proves that the hardware implementation controls the movement of the proof mass in the sensing element of the gyroscope as expected. A comparison between displacement control achievements in the simulation (shown in Figure 4.13) in Chapter 2 and hardware implementation (presented in Table 6.2) shows that the same level of decrease is not achieved. As mentioned earlier in this section, it is due to existence of noise and also the fact that the behavioral model of the sensing element sense mode (in this case a second order transfer function), does not reflect the absolute real world behavior of the sensors. This issue could be addressed in a future implementation of the system by using noise reduction techniques such as those described in [85] [86].

6.5. Conclusion

In this chapter a hardware implementation of the novel band-pass EMSDM with quadrature error cancellation capability, has been presented and it has been verified that the novel design can be successfully implemented using discreet passive components and operational amplifiers. The quadrature error power spectral density is attenuated by about 70dB which is equivalent to more than 3 orders of magnitude attenuation. The experimental values of quadrature error attenuation are in good agreement with the system level simulations. In addition, in this chapter, some practical imperfections which were encountered during the process of implementation (effect of capacitive structure of the sensing element) were discussed and a solution was proposed and implemented as presented in the work best result.

Chapter 7 Conclusion and future work

7.1. Conclusion

In this work, a novel approach for attenuating quadrature error in EMSMD for micro-machined gyroscopes was proposed in which it was aimed to retain the advantages of the band-pass single loop EMSDM. The novel system has been designed and for generating the system parameters, the GA design automation Matlab package was used. Subsequently the system was simulated in system level (Simulink) and circuit simulation level (Pspice). At this stage the functionality of novel system is verified by simulation at two different (system and circuit) levels. Ultimately, a hardware implementation of the novel control system has been built and it is proven that the results of hardware implementation are similar to the one of system and circuit level simulation.

In conclusion, it is shown that by using this technique, the effect of quadrature error can be significantly reduced while the advantages of the band-pass EMSDM for micro-gyroscopes can be retained. Moreover, the deployment of this interface can relax the fabrication process in the sense that even produced gyroscope sensing elements with relatively high amount of quadrature error, can be used marketable.

7.2. Future works

7.2.1. Deploying MESH technique in the novel system

For improving quantization noise there is an alternative method to increasing the order of the modulator. This method is knows as multi stage noise shaping (MASH) [18] [87]. Primarily, it was proposed in an investigation for improving accuracy, overloading and sensitivity without increasing the order of the modulator.

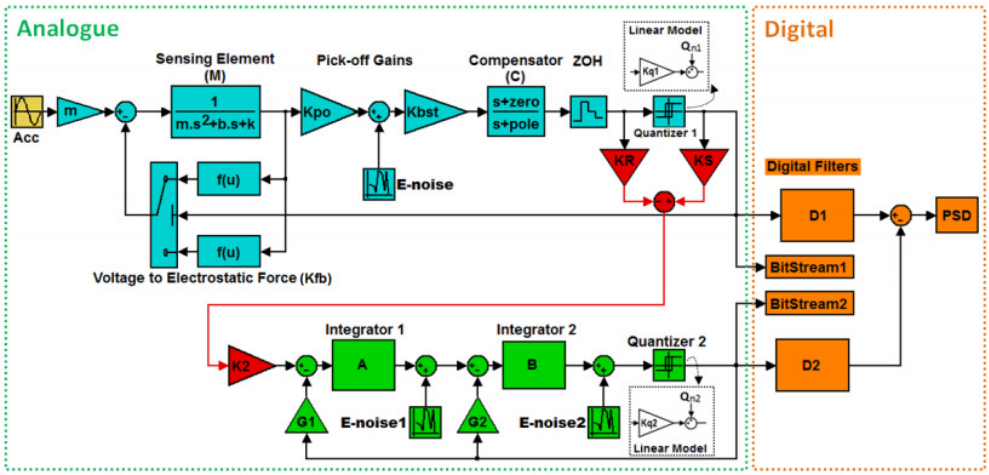

Figure 7.1: Electromechanical 4th order MASH22 SDM. The sensing element is embedded within the first loop, whereas the second loop is purely electronic SDM. The output bit-streams of the two loops are combined by digital filters (reproduced from [88]).

Recently, this concept was presented as an alternative to higher order EMSDM for accelerometer [88]. In this approach a second order closed-loop accelerometer is cascaded with a pure electronic second order SDM as shown in Figure 7.1. It was concluded that the MASH architecture is unconditionally stable (against component variation). Also, the level of noise shaping was same as 5th order single loop EMSDM for accelerometer. Hence, same approach can be examined for the novel band-pass EMSDM. In this approach each 6th order loop is replaced with a second order loop with a matching pure electronic band-pass second order SDM.

7.3. Deploying a 4th order complex SDM

In 1997, Stephen A. Jantzi et. al. proposed a quadrature SDM as an alternative to deploying two real 4th order SDM in an IF two channel communication system. The implementation of this modulator is shown as an ASIC structure [89]. The idea of designing a complex SDM along with a sample implementation of its core component is shown in Figure 7.2. An implementation of the novel system can be conducted by replacing the two discrete sigma delta modulators with a chip implementation of the complex SDM as shown in Figure 7.2 and Figure 7.3.

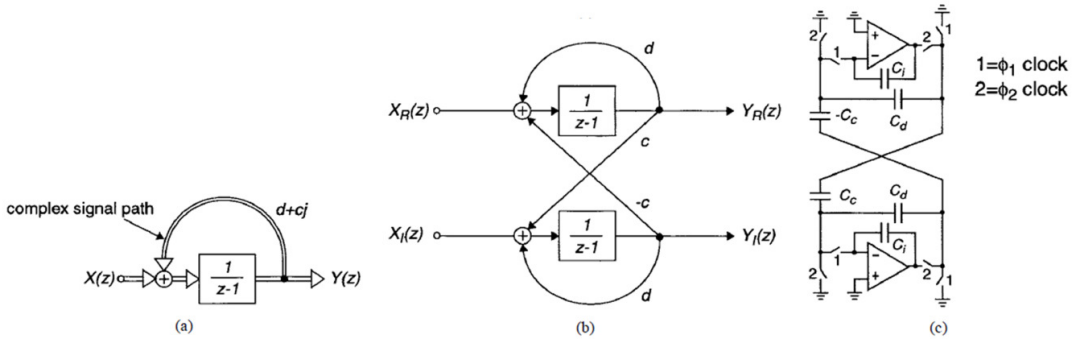

Figure 7.2: Creating a z-plane complex pole: (a) complex signal flow graph, (b) two-path signal flow graph, and (c) single-ended circuit realization.(reproduced from [89]).

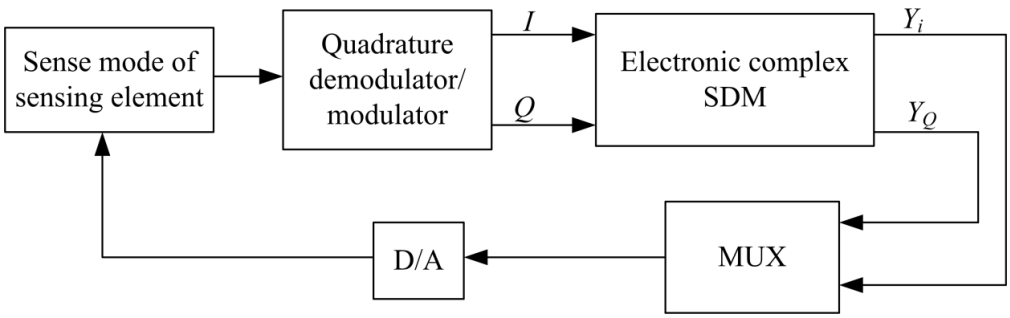

Figure 7.3: A conceptual flow graph of deploying a complex pure electronic SDM in implementation of the novel gyroscope system.

7.4. Extending GA design automation to hardware implementation

The motivation for designing and using this Matlab package was the time conservation is the design process for a non-linear system (e.g. EMSDM). Considering all the non idealities in implementation of a design, suggest that there is a potential for extending the use of this design automation package directly into hardware design. A conceptual presentation of the design flow for this idea is shown in Figure 7.4.

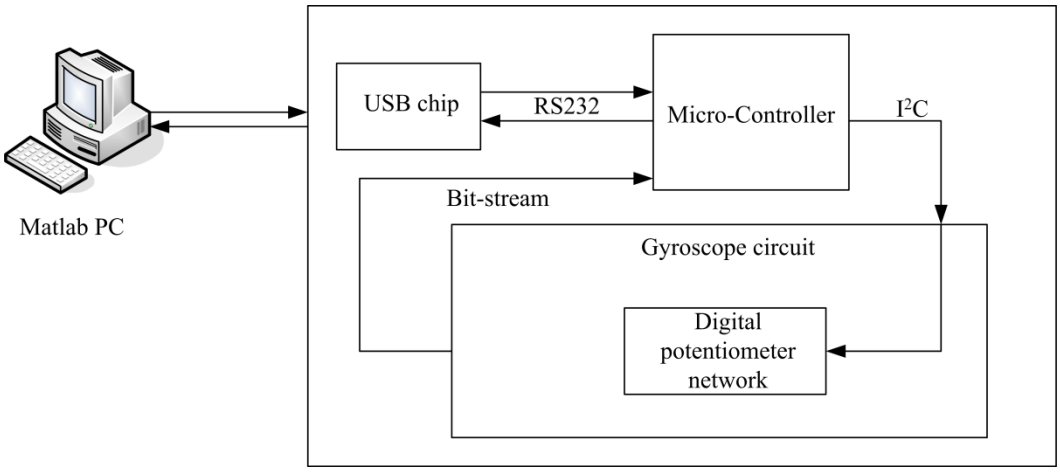

Figure 7.4: Conceptual presentation of deploying GA system for direct hardware implementation. In this method a network of digital potentiometers change some circuit parameters to reach an optimum hardware design.

In this method, some of the fixed value resistors in the circuit is replaced by programmable digital potentiometer (i.e. AD5252). For example, the resistor that adjusts the gain of the instrumentation amplifier can be replaced so this gain can be modified by the micro-controller via I2C interface. As an starting point, a set of coefficients is generated by the GA system and sent to the micro-controller on the gyroscope board via a USB connection. Then, the micro-controller interprets these values into a code for the digital potentiometers on the circuit. Subsequently, as the new values for potentiometers emerge, a sample of output bit-stream is sent to the PC via the USB connection (exactly like the current GA system) for performance examination. This loop is repeated for set number of times during (exactly like the one for system level) and ultimately a practically optimized solution can be concluded. Finally the best solution will be stored on the EEPROM of the microcontroller.

Appendix A

The MatLab code for defining the limits for each parameter in genetic automation for designing a micro-gyroscope sensing element. Also, the numbers of trials in each generation, number of generations and number of Monte Carlo trials for the best solution are defined here.

```
% ******************************************************************
% Parameter file
% This file contains all the parameters for all the subsequent analysis.
% Make sure all the parameters are set, expecially those for the
% analysis you intend to run.
% ******************************************************************

startup_initialisation          % dont remove this line

% ******************************************************************
% General parameters
% ******************************************************************
system_name = 'BP_GYR_6_SM_RES_Quad_staticosc_singlefb_singlecomp';
num_params = 36;
print_set = [1 2 3 4 5 6 7 8 9];% the parameters to print during
simulation
scatter_set = [1 2 3 4 5 6 7 8 9];         % set of scatter parameters
which you want to plot
quick_sim = 256;% how many times the input frquency to simluate for a
quick sim
long_sim = 4096;% how many times the input frquency to simluate for a
long sim

%
**********************************************************************
% Specification parameters
%
**********************************************************************
snr_pass = 66;           % pass for SNR
snr_pos = 37;            % index for SNR in the solution set
snr_pos_scores = 1;      % index for the SNR in the score set
rms_pass = 6e-8;        % pass for rms displacement
rms_pos = 39;            % index for rms displacement in the solution set
specs = [rms_pass -snr_pass];   % the specification list
spec_pos = [rms_pos snr_pos];   % the specification indexes

%
**********************************************************************
% Variation Specification parameters
%
**********************************************************************
var_snr_pass = 50;        % pass for SNR
var_snr_pos = 40;         % index for SNR in the solution set
var_rms_pass = 6e-8;      % pass for rms displacement
var_rms_pos = 42;         % index for rms displacement in the solution set
var_specs = [var_rms_pass -var_snr_pass];   % the specification list
var_spec_pos = [var_rms_pos var_snr_pos];   % the specification indexes
```

```
% ************************************************************************
% Amplitude analysis parameters
% ************************************************************************
amp_min = 1;     % the minimum amplitude for the sweep
amp_max = 300;   % the maximum amplitude for the sweep
amp_steps = 50;  % the number of steps to use
amp_pos = 20;    % the index of the amplitude value in the parameter sets

% ************************************************************************
% Noise parameters
% ************************************************************************
enoise_pos = 21;        % enoise position in the parameter set
enoise_val = 7e-9;      % enoise value

% ************************************************************************
% GA parameters
% ************************************************************************
pop_size = 200;         % GA population size
gen_num = 40;           % GA number of generations

% ************************************************************************
% Genetic optimisation upper and lower parameter bounds:
% ************************************************************************
lb(1) = 2;      ub(1) = 30;         % ratio of pole to zero frequency
lb(2) = 1e3;    ub(2) = 6e3;        % frequency between the pole and zero
lb(3) = 1e6;    ub(3) = 1e6;        % pickoff gain
lb(4) = 10;     ub(4) = 200;        % boost gain
lb(5) = 0;     ub(5) = 5;           % RZ feedback 1 kf1
lb(6) = 0;     ub(6) = 5;           % HRZ feedback 1 kf2
lb(7) = 0;     ub(7) = 5;           % RZ feedback 2 kf3
lb(8) = 0;     ub(8) = 5;           % HRZ feedback 2 kf4
lb(9) = 5;      ub(9) = 40;         % Feedback voltage
lb(10) = 1.99e-6; ub(10) = 1.99e-6; %mass of proof mass in kg
lb(11) = 4073;    ub(11) = 4073; % Resonant frequency of drive mode in Hz
lb(12) = 0;        ub(12) = 0 % Difference between drive and sense
frequency (sense - drive)
lb(13) = 216;    ub(13) = 216;      % Q factor of drive mode
lb(14) = 10000;        ub(14) = 10000; % Q factor of sense mode
lb(15) = 80e-6;     ub(15) = 80e-6; % thickness of structure in meters
lb(16) = 5e-6;    ub(16) = 5e-6;% nominal gap of the neighbouring comb
fingers in meters
lb(17) = 168;      ub(17) = 168;% number of comb fingers for feedback
force in sense mode
lb(18) = 64;     ub(18) = 64;        % bandwidth
lb(19) = 256;        ub(19) = 256;   % oversampling ratio
lb(20) = 300;        ub(20) = 300;   % amplitude
lb(21) = 7e-10;        ub(21) = 7e-10;% enoise
lb(22) = 1e-6;        ub(22) = 1e-6;            % drive amplitude
lb(23) = 0.01;        ub(23) = 5;              % Filter gain 1
lb(24) = 0.01;        ub(24) = 5;              % Filter gain 2
lb(25) = 0;       ub(25)=5;          % RZ feedback 1 qkf1
lb(26) = 0;       ub(26)=5;          % RZ feedback 1 qkf2
lb(27) = 0;       ub(27)=5;          % RZ feedback 1 qkf3
lb(28) = 0;       ub(28)=5;          % RZ feedback 1 qkf4
lb(29) = 2;      ub(29) = 30;        % ratio of pole to zero frequency
lb(30) = 1e3;    ub(30) = 6e3;      % frequency between the pole and zero
lb(31) = 0.01;        ub(31) = 5;              % Filter gain 1
lb(32) = 0.01;        ub(32) = 5;              % Filter gain 2
lb(33) = 0;      ub(33) = pi;           % phase for demodulation osc1
lb(34) = 0;      ub(34) = pi;           % phase for demodulation osc2
lb(35) = 0;      ub(35) = 0;        % Filter Gain 1
```

```
lb(36) = 0;      ub(36) = 0;        % Filter Gain 2
% ************************************************************************
% MC parameters
% ************************************************************************
max_filtered = 25;      % the filtered census will be thinned to approx
this number of solutions
yield_accept = 100;     % above this yield value (%) the variation
algorithm will stop
num_mc = 100;           % number of monte carlo runs for each solution
num_mc_single = 1000;   % number of monte carlo runs for the final design
type = 'gaussian';      % type of distribution

% ************************************************************************
% Standard deviations (% of mean) for all statistical analysis
% MUST set for any value which ga has control over
% ************************************************************************
sd(1) = 2; % ratio of pole to zero frequency
sd(2) = 2; % frequency between the pole and zero
sd(3) = 2; % pickoff gain
sd(4) = 2; % boost gain
sd(5) = 2; % RZ feedback 1 kf1
sd(6) = 2; % HRZ feedback 1 kf2
sd(7) = 2; % RZ feedback 2 kf3
sd(8) = 2; % HRZ feedback 2 kf4
sd(9) = 2; % Feedback voltage
sd(10) = 1; % sensor mass of proof mass in kg
sd(11) = 20; % Resonant frequency of drive mode in Hz
sd(12) = 5; % Difference between drive and sense frequency (sense -
drive)
sd(13) = 0; % Q factor of drive mode
sd(14) = 0; % Q factor of sense mode
sd(15) = 1; % sensor thickness of structure in meters
sd(16) = 2; % sensor nominal gap of the neighbouring comb fingers in
meters
sd(17) = 0; % sensor number of comb fingers for feedback force in sense
mode
sd(18) = 0; % bw
sd(19) = 0; % osr
sd(20) = 0; % amplitude
sd(21) = 0; % Enoise
sd(22) = 0; % drive emplitude
sd(25) = 2;
sd(26) = 2;
sd(27) = 2;
sd(28) = 2;
sd(29) = 2;
sd(30) = 2;
sd(31) = 2;
sd(32) = 2;
sd(33) = 2;
sd(34) = 2;
sd(35) = 2;
sd(36) = 2;
-------------------------------------------------------------------------
```

In addition, there is a file which defined the function that is used to find the optimized solution.

```
---------------------------------------------------------------------------------------------------------
function [scores] =
   BP_GYR_6_SM_RES_Quad_2ndordflt_singlefb_singlecomp_Fitness(x,simr,plt)
% ************************************************************************
% Fitness function
% x(1) = ratio of pole to zero frequency
% x(2) = frequency between the pole and zero
% x(3) = pickoff gain
% x(4) = boost gain
% x(5) = RZ feedback 1 kf1
% x(6) = HRZ feedback 1 kf2
% x(7) = RZ feedback 2 kf3
% x(8) = HRZ feedback 2 kf4
% x(9) = Feedback voltage
% x(10) = sensor mass of proof mass in kg
% x(11) = Resonant frequency of drive mode in Hz
% x(12) = Difference between drive and sense frequency (sense - drive)
% x(13) = Q factor of drive mode
% x(14) = Q factor of sense mode
% x(15) = sensor thickness of structure in meters
% x(16) = sensor nominal gap of the neighbouring comb fingers in meters
% x(17) = sensor number of comb fingers for feedback force in sense mode
% x(18) = bw
% x(19) = osr
% x(20) = amplitude
% x(21) = Enoise
% x(22) = Drive ampltiude
% x(23) = Filter Gain 1
% x(24) = Filter Gain 2
% score1 = returned ratio of passband to stopband
% ************************************************************************

% ************************************************************************
% Process the sensor values
% ************************************************************************
m = x(10);        % mass of proof mass in kg
Fx = x(11);       % frequency of drive oscillation in Hz
Fy = Fx + x(12); % frequency of sense oscillation in Hz
Qx = x(13);       % Q factor in the drive direction
Qy = x(14);       % Q factor in the sense direction
th = x(15);       % thickness of structure in meters
dnom = x(16);     % nominal gap of the neighbouring comb fingers in meters
ncomb = x(17);   % number of comb fingers for feedback force in sense mode
Wx=2*pi*Fx;       % angular frequency of drive oscillation
Wy=2*pi*Fy;      % angular frequnecy of sense oscillation

% ************************************************************************
% Process the system parameters
% ************************************************************************
bw = x(18);
osr = x(19);
fs = osr*2*bw;                    % sampling frequency
ts = 1/fs;                          % sampling period
```

```
% ************************************************************************
% Define the simulation setup
% ************************************************************************
simn = bw*simr;                 % calculate the number of samples
simt = simn/fs;                 % calculate simulation time

% ************************************************************************
% Define the input
% ************************************************************************
sf = 2;                         % input as fraction of bw
in_f = bw/sf;                   % input frequency
in_a = x(20);                   % input amplitude
in_aw = in_a*pi/180;            % input amplitude (rad)
in_w = in_f*2*pi;               % input frequency (rad)
din_f = Fx;                     % drive frequency (drive at resonant freq)
din_w = din_f*2*pi;             % drive frequency in radians
din_a = x(22);                  % drive amplitude

% ************************************************************************
% Define the compensator for signal part
% ************************************************************************
rat = x(1);                     % ratio of pole to zero
ccf = x(2);                     % mid point between pole and zero
zero_f = ccf/rat;               % zero frequency
pole_f = ccf*rat;               % pole frequency
zero = 2*pi*zero_f;             % zero frequency (rad)
pole = 2*pi*pole_f;             % pole frequency (rad)

% ************************************************************************
% Define the compensator Quadrature error part
% ************************************************************************
qrat = x(29);                     % ratio of pole to zero
qccf = x(30);                     % mid point between pole and zero
qzero_f = qccf/qrat;               % zero frequency
qpole_f = qccf*qrat;               % pole frequency
qzero = 2*pi*qzero_f;             % zero frequency (rad)
qpole = 2*pi*qpole_f;             % pole frequency (rad)

% ************************************************************************
% Define the system parameters
% ************************************************************************
kpo = x(3);                     % pickoff amp
kbst = x(4);                    % boost amp
kf1 = x(5);
kf2 = x(6);
kf3 = x(7);
kf4 = x(8);
fg1 = x(23);
fg2 = x(24);
qkf1 = x(25);
qkf2 = x(26);
qkf3 = x(27);
qkf4 = x(28);
qfg1 = x(31);
qfg2 = x(32);
osc_phase1 = x(33);
osc_phase2 = x(34);
flgain1 = x(35);
flgain2 = x(36);
fbdc=50;                        % feedback duty cycle
```

```
sdc=50;                          % sense duty cycle
enoise = x(21);

% ************************************************************************
% Define the feedback force
% ************************************************************************
vfb = x(9);
epsi=8.85e-12;                   % permitivity of vacuum
overlap = 22e-6;
Ffb=epsi*ncomb*th*overlap*(vfb^2)/(2*(dnom^2)); % feedback force

% ************************************************************************
% Update the workspace variables
% ************************************************************************
assignin('base', 'm', m);
assignin('base', 'Wx', Wx);
assignin('base', 'Wy', Wy);
assignin('base', 'Qy', Qy);
assignin('base', 'kpo', kpo);
assignin('base', 'zero', zero);
assignin('base', 'pole', pole);
assignin('base', 'kbst', kbst);
assignin('base', 'kf1', kf1);
assignin('base', 'kf2', kf2);
assignin('base', 'kf3', kf3);
assignin('base', 'kf4', kf4);
assignin('base', 'fg1', fg1);
assignin('base', 'fg2', fg2);
assignin('base', 'ts', ts);
assignin('base', 'Ffb', Ffb);
assignin('base', 'fbdc', fbdc);
assignin('base', 'sdc', sdc);
assignin('base', 'din_a', din_a);
assignin('base', 'in_aw', in_aw);
assignin('base', 'din_w', din_w);
assignin('base', 'in_w', in_w);
assignin('base', 'enoise', enoise);
assignin('base', 'qzero', qzero);
assignin('base', 'qpole', qpole);
assignin('base', 'qkf1', qkf1);
assignin('base', 'qkf2', qkf2);
assignin('base', 'qkf3', qkf3);
assignin('base', 'qkf4', qkf4);
assignin('base', 'qfg1', qfg1);
assignin('base', 'qfg2', qfg2);
assignin('base', 'osc_phase1', osc_phase1);
assignin('base', 'osc_phase2', osc_phase2);
assignin('base', 'flgain1', flgain1);
assignin('base', 'flgain2', flgain2);

options = simset('Solver', 'ode45','MaxStep', ts/10);
sim('BP_GYR_6_SM_RES_Quad_2ndordflt_singlefb_singlecomp',simt,options);
% simulate the design

% ************************************************************************
% Plot the psd and find the snr and rmsroot
% ************************************************************************
[snr rmstot peak] =
plotpsd(simn,in_f,fs,bw,Fx,bitstream,displacement,osr,plt);
if (plt==1)
```

```
    plotwaveforms(dispcompare, simt);
end
score1 = -snr;
score2 = peak;
score3 = rmstot;

scores = [score1 score3]';

% ************************************************************************
% Display the design point
% ************************************************************************
if (plt==0)
    displaygeneration();
    displaysolutionset(x,scores);
end

% ************************************************************************
% Record the census
% ************************************************************************
if (plt==0)
    storecensus(x, [score1 score2 score3]);
    savecensus();
end
```

Appendix B

The code for generating a linear approximation model and plotting a bode diagram. A Simulink model whose quantizer is replaced with a linear noise source.

```
% ************************************************************************
% Defining the values for sensing element (mass, Q factor,
% resonant frequency), feedback co-efficients, resonator co-efficient
% and  linear model.
% ************************************************************************
Wy = 2.559e4;     % Sense mode resonant frequency
Q = 10000;        % Sense mode quality factor
m = 2e-6          % Sense mode proof mass (Kg)
th=80e-6;         % Thinkness of structure
epsi=8.85e-12;    % Boltzman constant
overlap = 22e-6; % Comb finger overlap
vfb=2.4823;       % Feedback voltage
dnom=5e-6;        % Nominal gap
ncomb=168;        % Number of comb fingers
Ffb=epsi*ncomb*th*overlap*(vfb^2)/(2*(dnom^2)); % Electrostatic feedback
force

% Generating transfer function from simulink models
[A,B,C,D] = Linmodv5('BP_GYR_6_SM_RES_lieanmodel_sg');
BP6gyr_ln_sg_tf=ss(A,B,C,D);
[A,B,C,D] = Linmodv5('BP_GYR_6_SM_RES_lieanmodel_en');
BP6gyr_ln_en_tf=ss(A,B,C,D);
[A,B,C,D] = Linmodv5('BP_GYR_6_SM_RES_lieanmodel_qn');
BP6gyr_ln_qn_tf=ss(A,B,C,D);
bodemag(BP6gyr_ln_sg_tf)
hold
bodemag(BP6gyr_ln_en_tf/1.2,'r--')
bodemag(BP6gyr_ln_qn_tf,'r-.')
```

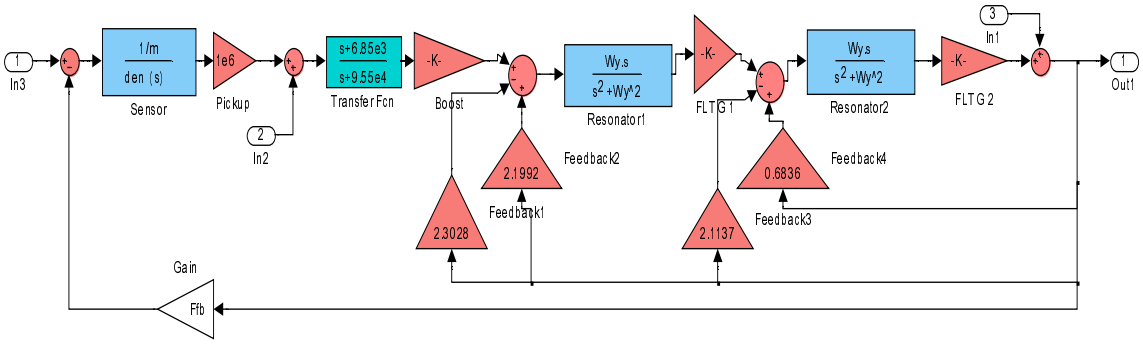

Figure B.1: Linear approximation model for a band-pass electromechanical micro-gyroscope system.

Appendix C

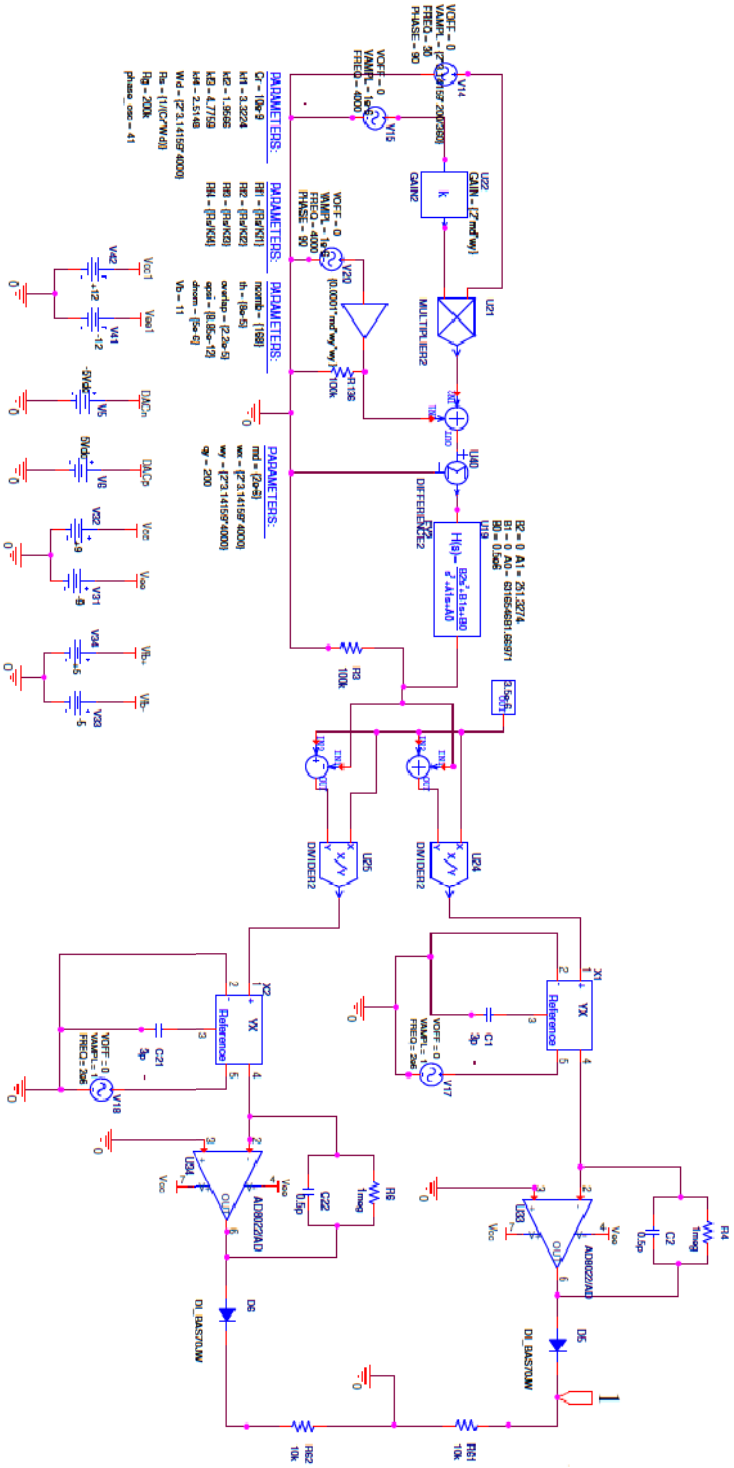

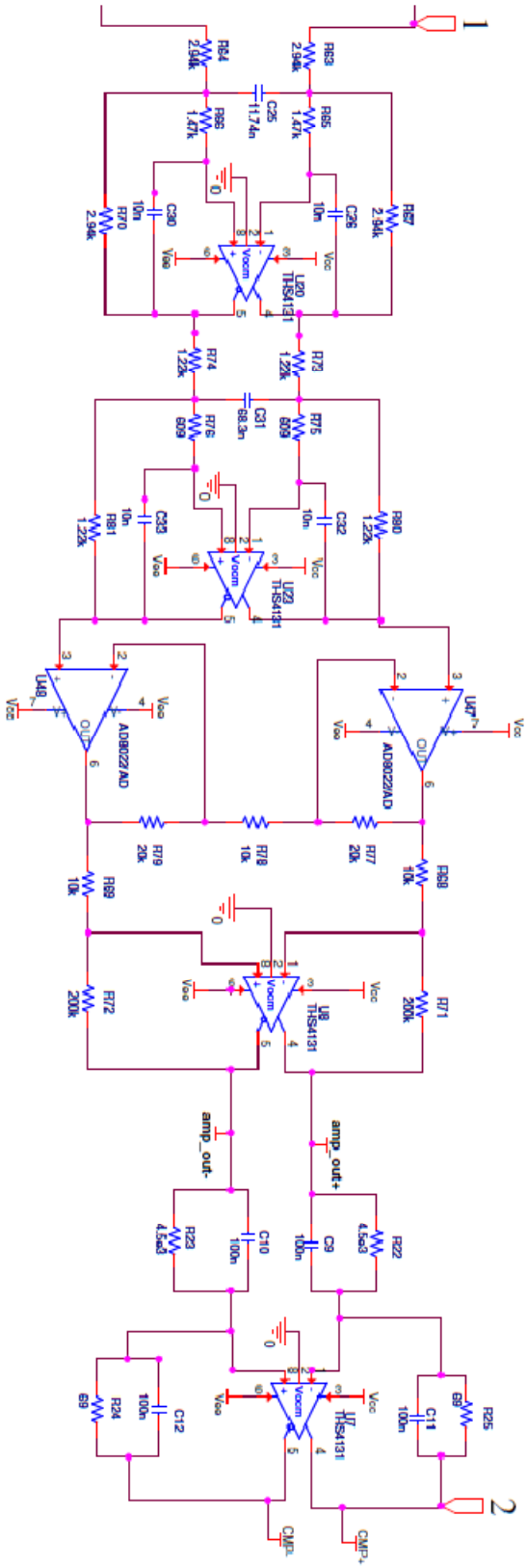
1
2
R84
2.94k
R83
2.94k
C25
11.74n
R86
1.47k
R85
1.47k
R70
2.94k
C30
10n
C26
10n
R87
2.94k
U20
THS4131
R74
1.22k
R73
1.22k
C31
68.3n
R76
609
R75
609
R81
1.22k
C35
10n
C32
10n
R80
1.22k
U23
THS4131
U48
AD8022AD
U47
AD8022AD
R79
20k
R78
10k
R77
20k
R69
10k
R89
10k
U8
THS4131
R72
200k
R71
200k
amp_out-
amp_out+
R23
4.5e3
C10
100n
C9
100n
R22
4.5e3
R24
69
C12
100n
U7
THS4131
C11
100n
R25
69
CMP-
CMP+

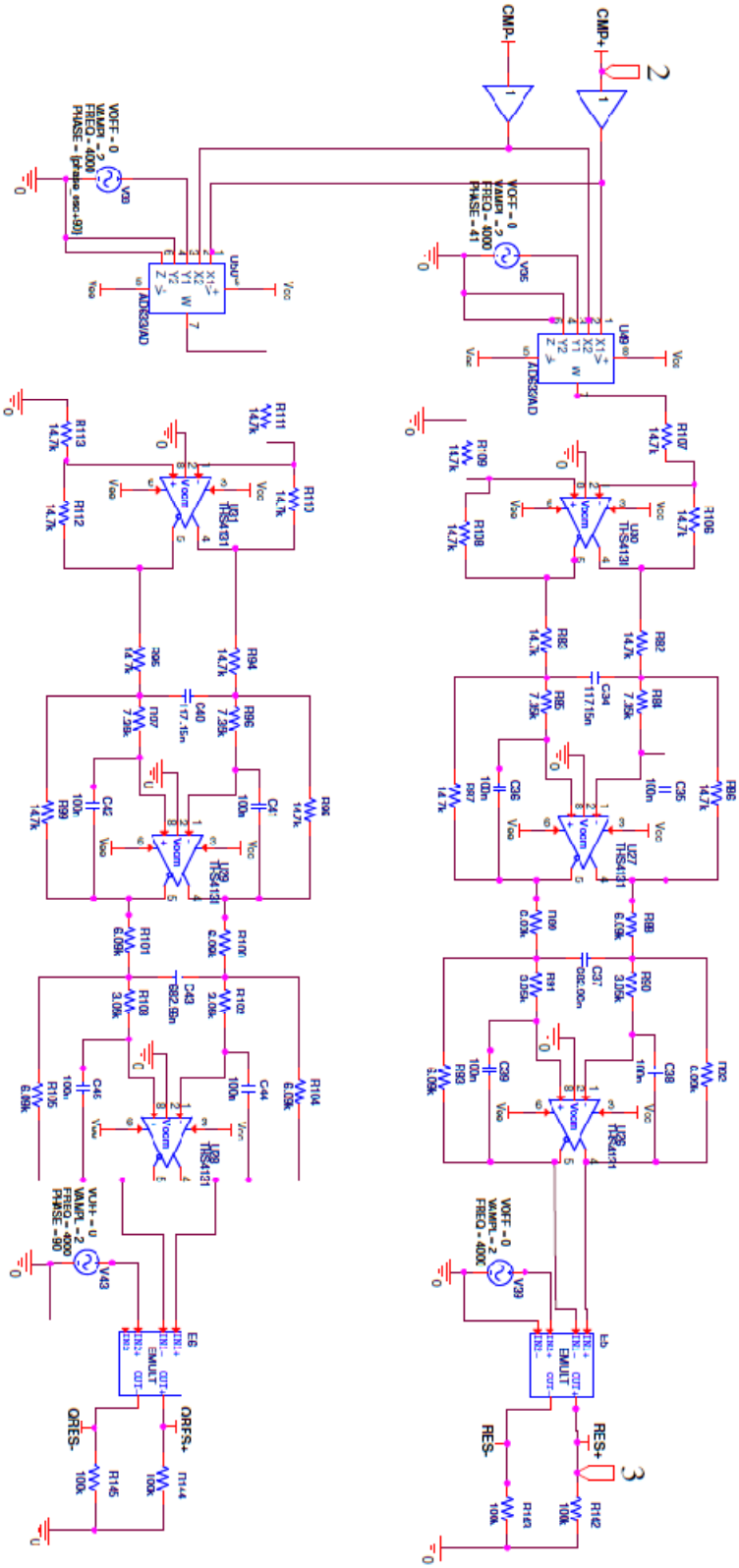
CMP-
CMP+
2
VOFF = 0
VAMPL = 2
FREQ = 400k
PHASE = 41
V35
VOFF = 0
VAMPL = 2
FREQ = 400k
PHASE = {phase_esc+90}
V28
U49
ADS8324AD
U50
THS4131
U27
THS4131
U28
THS4131
U29
THS4131
R107
14.7k
R109
14.7k
R108
14.7k
R106
14.7k
R86
14.7k
R82
14.7k
R85
7.35k
R84
7.35k
C34
117.15n
R87
14.7k
C36
10n
C35
10n
R88
6.04k
R89
6.04k
R91
3.09k
R90
3.09k
C37
882.95n
C39
100n
C38
100n
R93
6.09k
R92
6.09k
R111
14.7k
R113
14.7k
R112
14.7k
R110
14.7k
R94
14.7k
R96
7.35k
C40
117.15n
R97
7.35k
C41
100n
R95
14.7k
C42
100n
R99
14.7k
R98
14.7k
R101
6.09k
R107
6.09k
R100
3.09k
C43
882.95n
R102
3.09k
C45
100n
C44
100n
R105
6.09k
R104
6.09k
V43
VOFF = 0
VAMPL = 2
FREQ = 400k
PHASE = -90
V39
E6
E5
EMULT
OUT+
OUT-
IN1+
IN1-
IN2+
IN2-
ORES-
ORES+
R145
100k
R144
100k
RES-
RES+
3
R163
10k
R162
10k

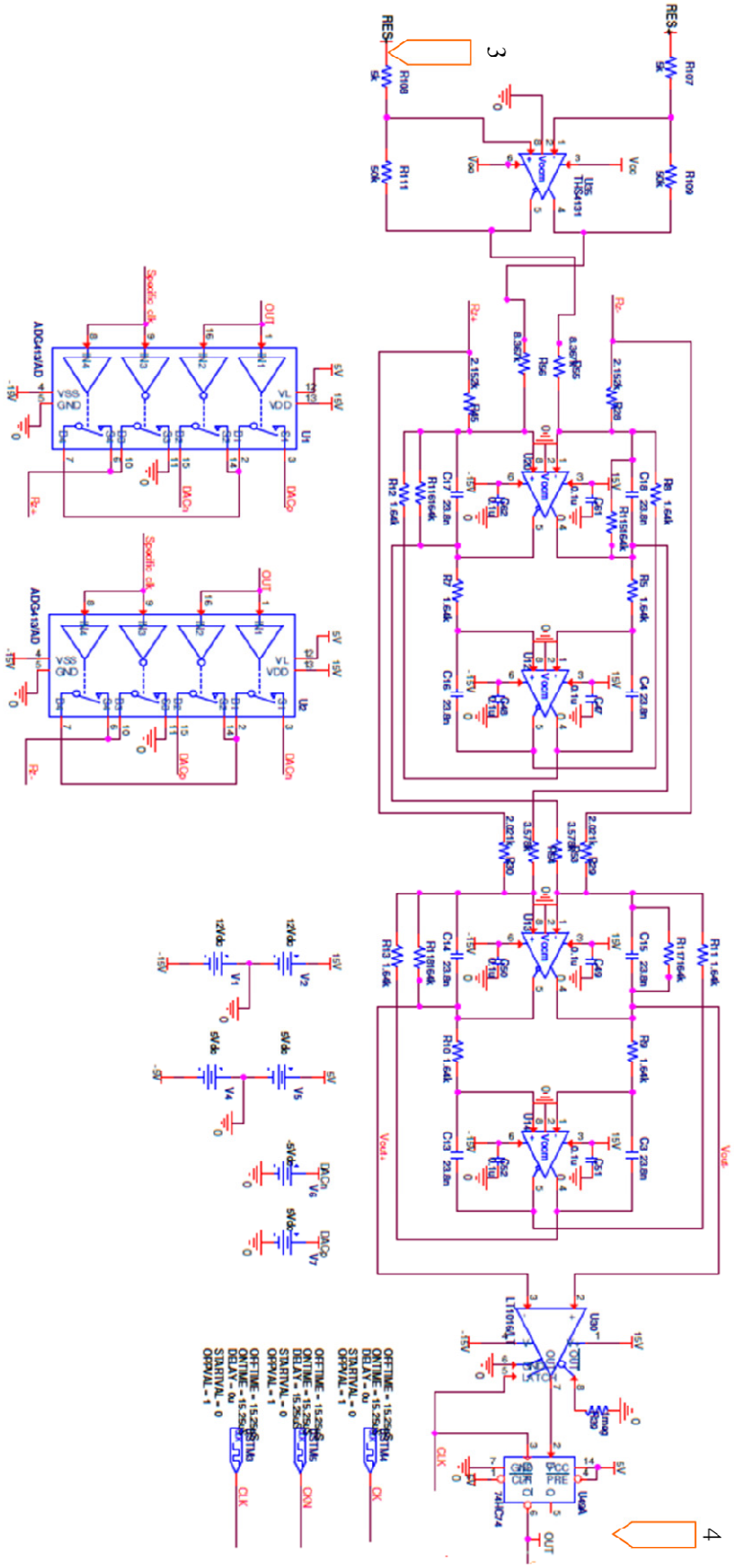

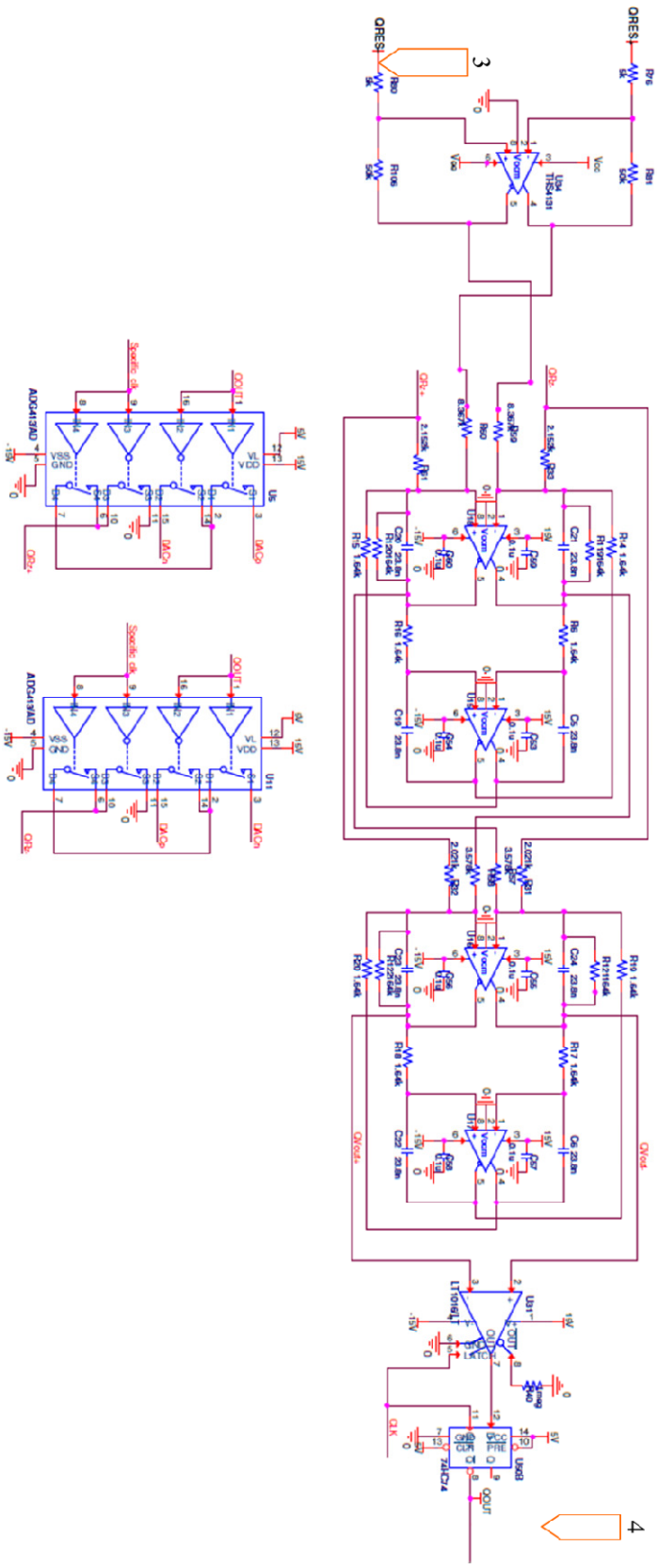

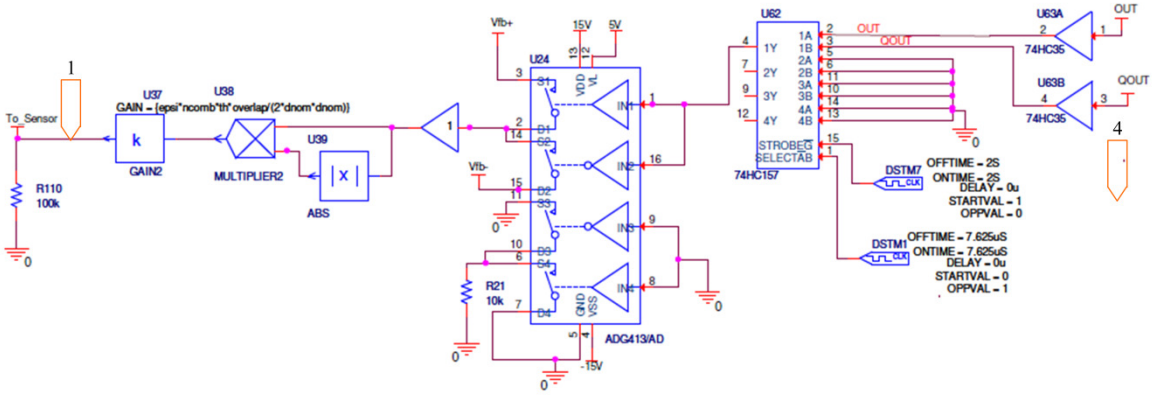
1
To_Sensor
R110
100k
U37
GAIN = {epsi*ncomb*tf*overlap/(2*dnom*dnom)}
k
GAIN2
U38
MULTIPLIER2
U39
|X|
ABS
1
Vfb+
Vfb-
15V
5V
U24
VDD
VL
GND
VSS
IN1
IN2
IN3
IN4
S1
S2
S3
S4
D1
D2
D3
D4
R21
10k
ADG413/AD
-15V
U62
1A
1B
2A
2B
3A
3B
4A
4B
1Y
2Y
3Y
4Y
STROBE
SELECTAB
74HC157
OUT
QOUT
U63A
U63B
74HC35
OUT
QOUT
4
DSTM7
OFFTIME = 2S
ONTIME = 2S
DELAY = 0u
STARTVAL = 1
OPPVAL = 0
DSTM1
OFFTIME = 7.625uS
ONTIME = 7.625uS
DELAY = 0u
STARTVAL = 0
OPPVAL = 1

Appendix D

In this section the schematic and PCB lauyout of hardware implementation for the 6th order band-pass EMSDM for micro-gyroscope, is shown. It must be noted that supply smooting capacitors are not shown here.

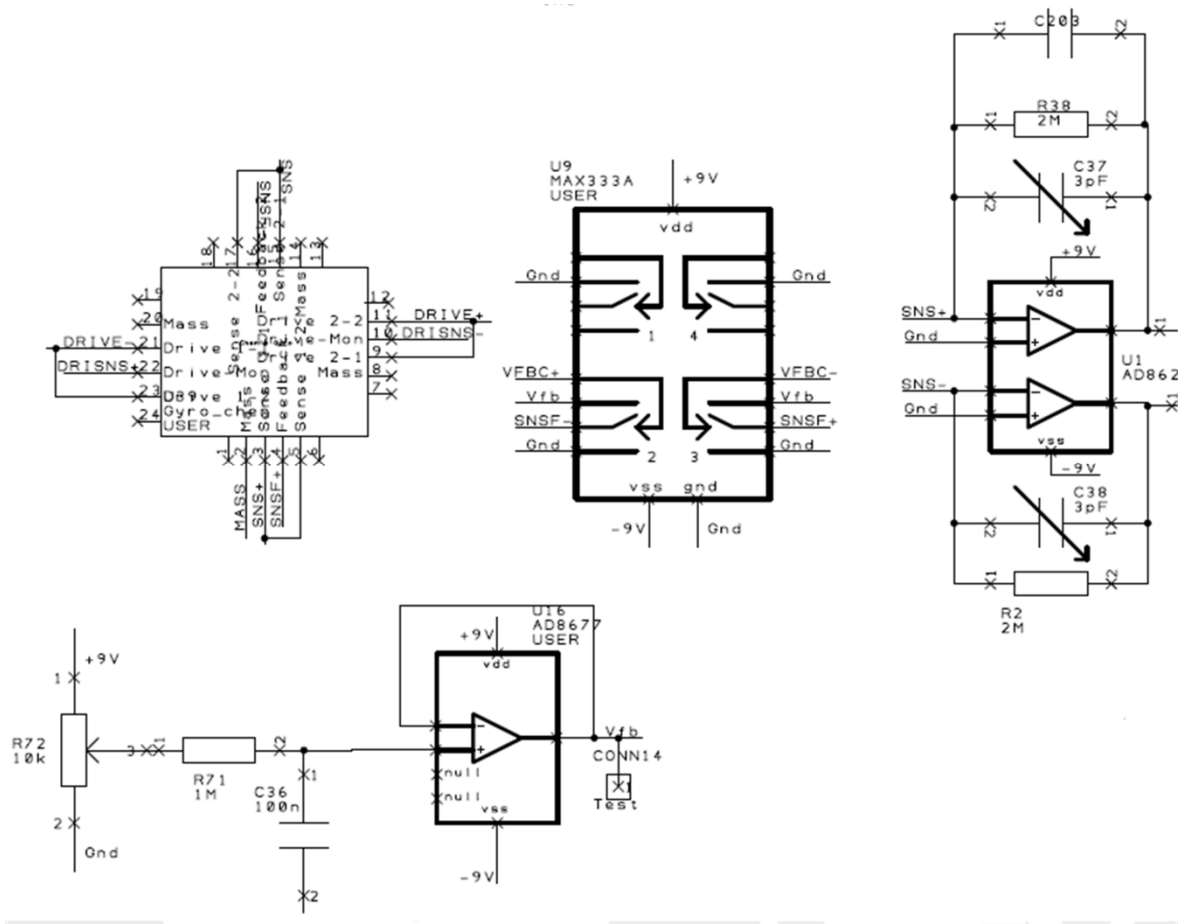

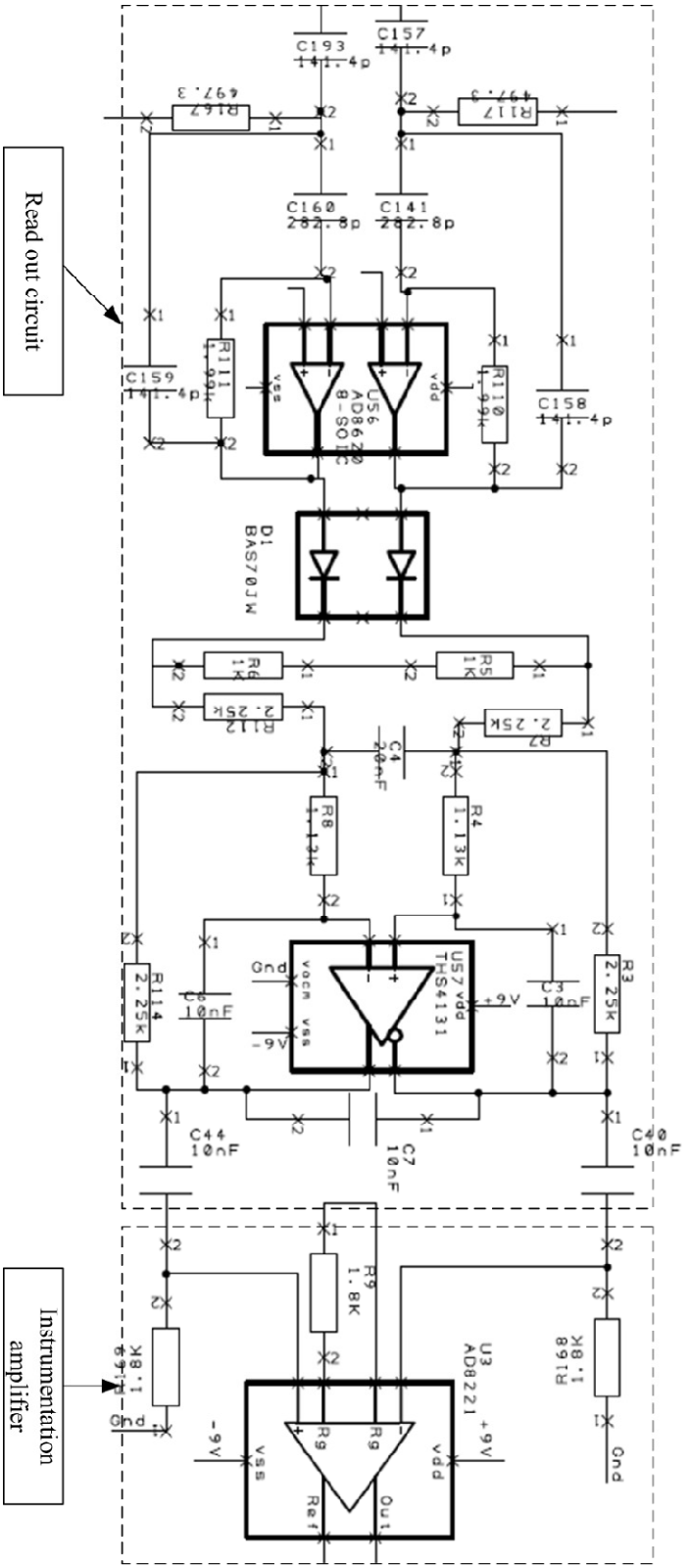
Read out circuit
Instrumentation amplifier
C193
C157
C160
C141
C159
C158
R117
R116
R111
R110
C56
AD8620
8-SOIC
D1
BAS70JW
R6
R5
R112
R7
C4
R8
R4
R114
R3
U57
THS4131
C44
C7
C40
R9
1.8K
U3
AD8221
R168
Gnd
vdd
vss
Ref
Out
Rg

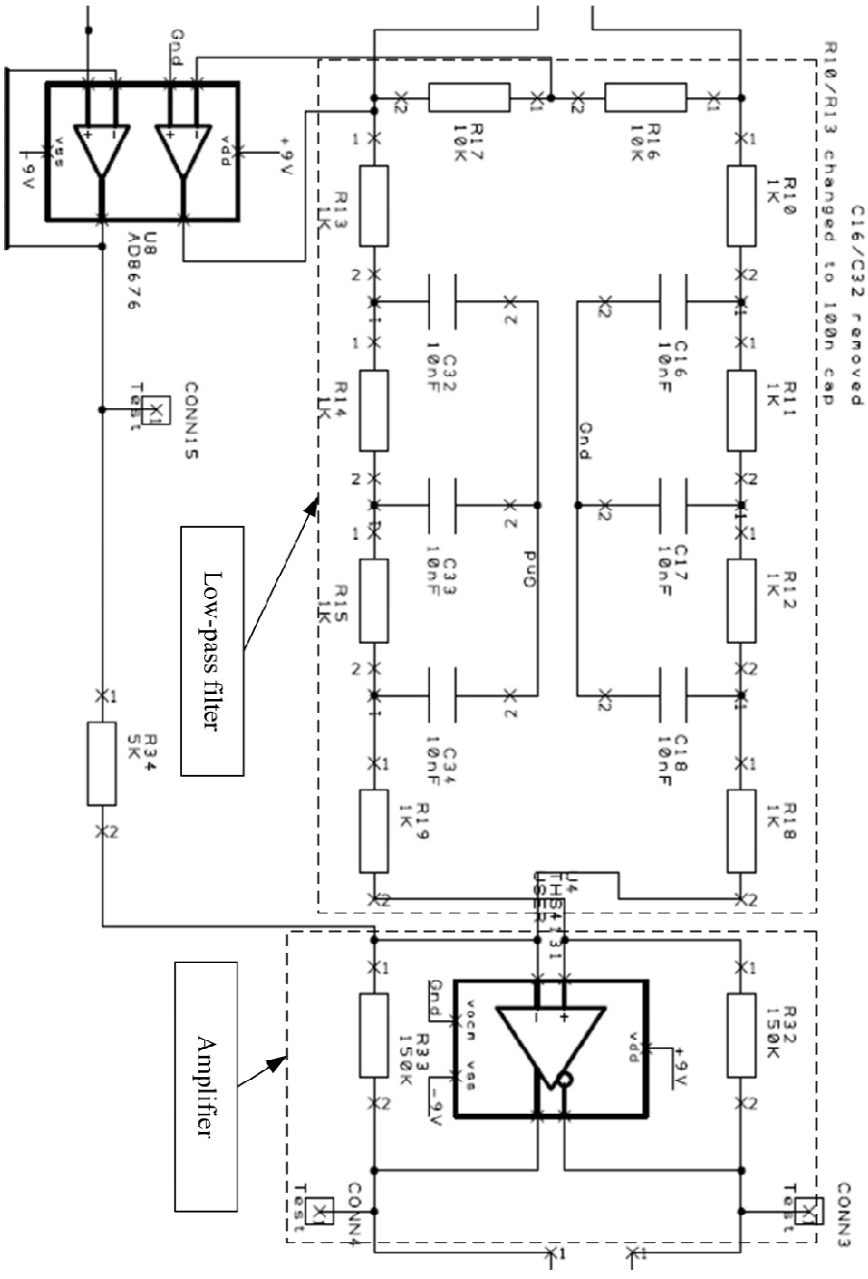
C16/C32 removed
R10/R13 changed to 100n cap
Low-pass filter
Amplifier
U8
AD8676
CONN15
CONN4
CONN3
R17
10K
R16
10K
R10
1K
R11
1K
R12
1K
R18
1K
R13
1K
R14
1K
R15
1K
R19
1K
C32
10nF
C33
10nF
C34
10nF
C16
10nF
C17
10nF
C18
10nF
R34
5K
R33
150K
R32
150K
+9V
-9V
Gnd
vdd
vss
vocm
Test
J4
THS4131
USER

Quadrature Demodulation

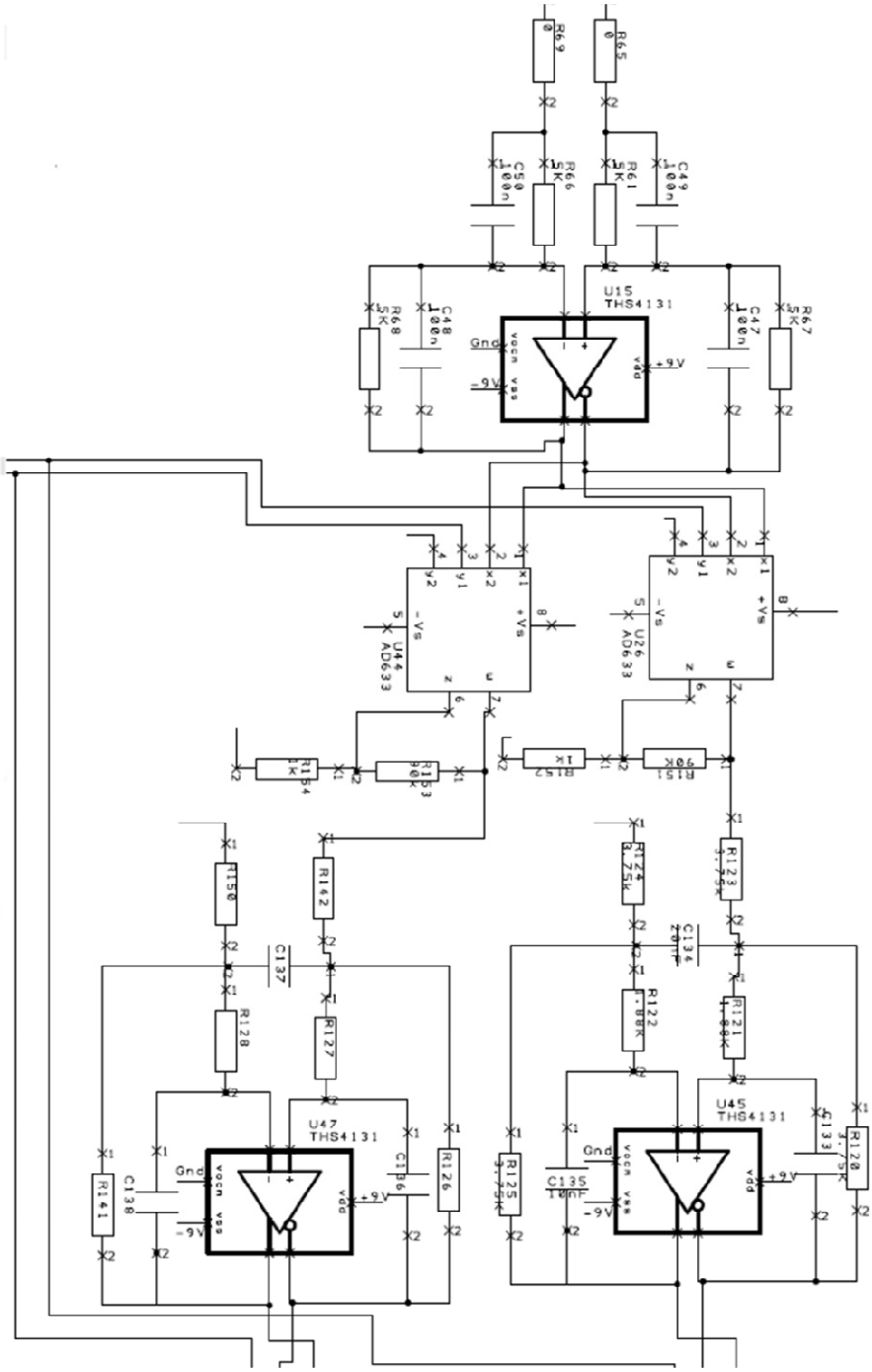

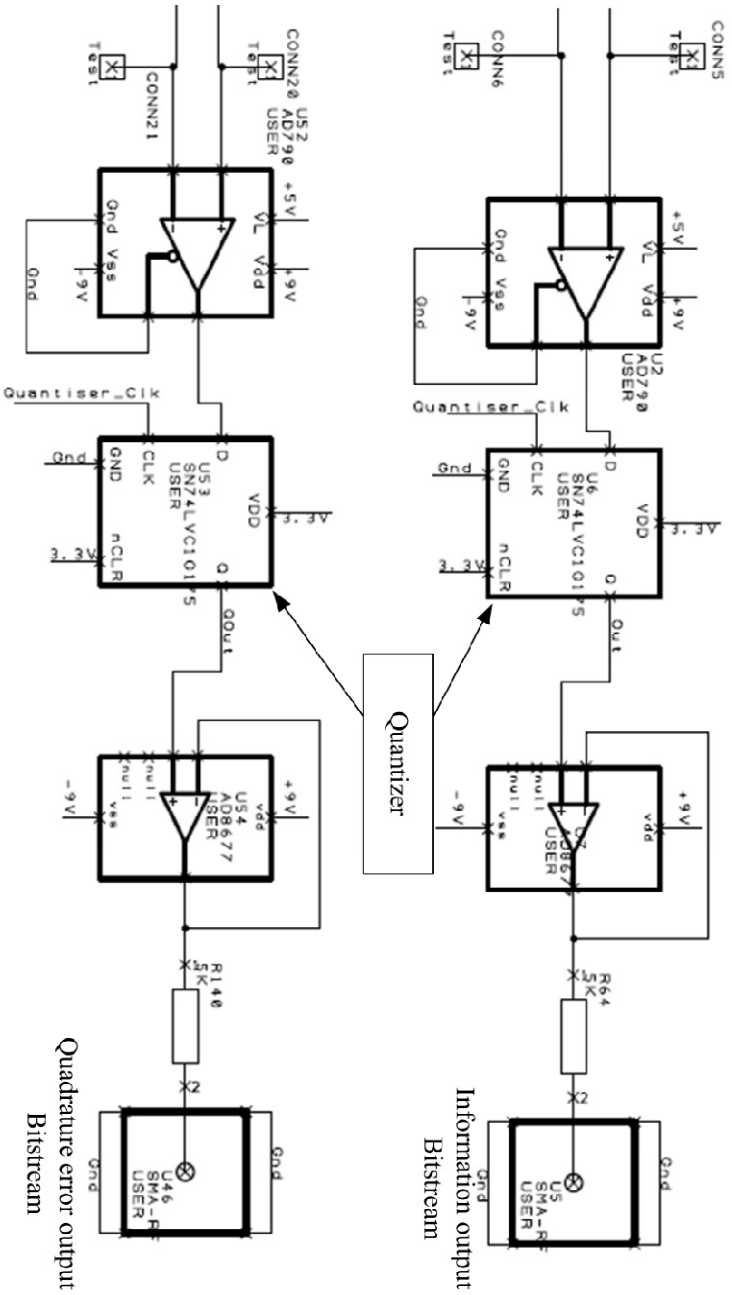
Quantiser_Clk
Quantiser_Clk
Quantizer
Quadrature error output
Bitstream
Information output
Bitstream

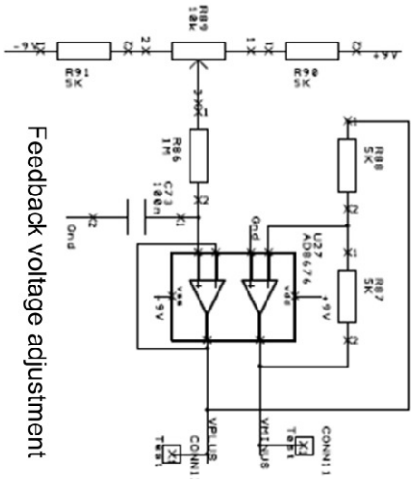

Feedback voltage adjustment

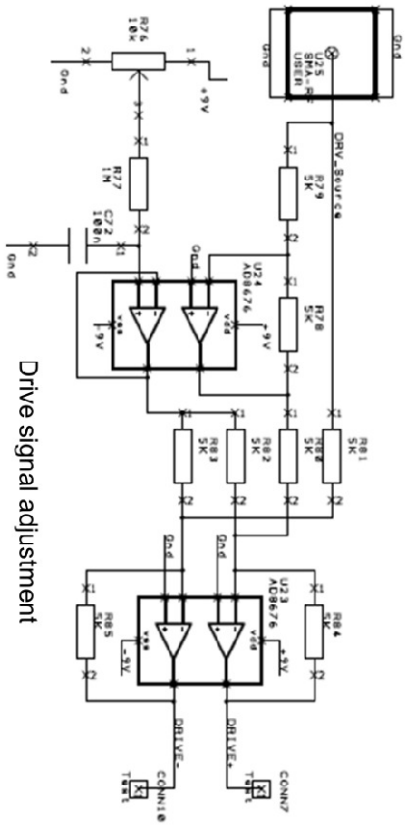

Drive signal adjustment

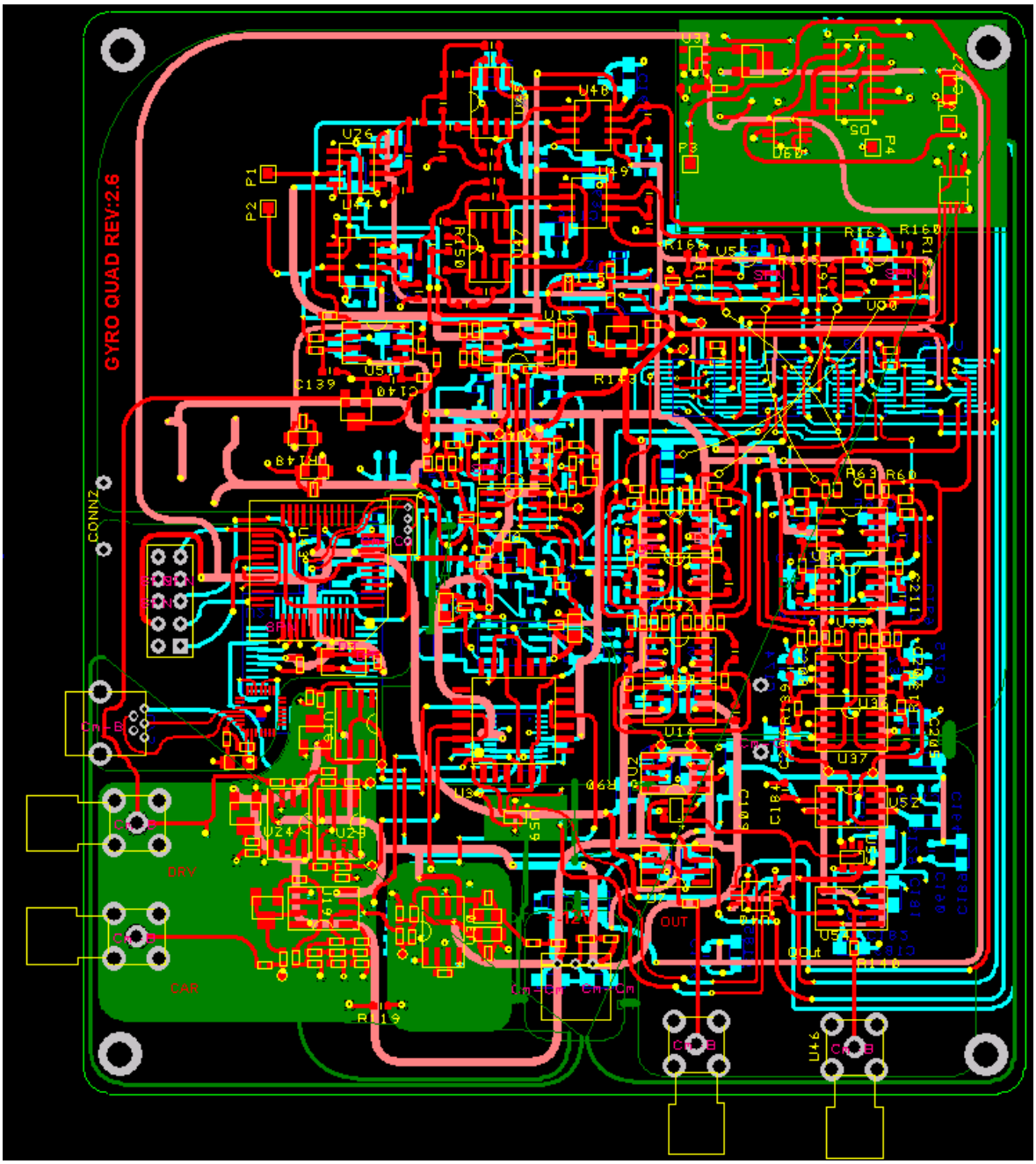
GYRO QUAD REV:2.6
CONN2
P1
P2
P3
DRV
CAR
OUT

References

[1] J. W. Judy, "Microelectromechanical systems (MEMS): fabrication, design and applications," *INSTITUTE OF PHYSICS PUBLISHING,* vol. 10, no. 6, p. 21, 2001.

[2] P. Dario, M. C. Carrozza, A. Benvenuto and A. Menciassi, "Micro-systems in biomedical applications," *Journal of Micromechanics and Microengineering,* vol. 10, no. 2, 1999.

[3] N. Barbour and G. Schmidt, "Inertial Sensor Technology Trends," *IEEE Sensors Journal,* vol. 1, no. 4, pp. 332-340, 2001.

[4] N. Yazdi, F. Ayazi and K. Najafi, "Micromachined inertial sensors," *IEEE,* vol. 86, no. 8, August 1998.

[5] J. Diad and J. Lobo, "Vision and inertial sensor cooperation using gravity as a vertical reference," *Computer Society-IEEE,* vol. 25, no. 12, December 2003.

[6] J. Alves, J. Lobo and J. Dias, "Camera-Inertial Sensor Modeling and Alignment for Visual Navigation," *Machine Intelligence & Robotic Control,* vol. 5, no. 3, pp. 103-111, 2003.

[7] J. Leclerc, "MEMs for Aerospace Navigation," *IEEE A&E SYSTEMS MAgazine,* October 2007.

[8] S. J. Posser, "Automotive sensors: past, present and future," *Journal of Physics: Conference Series 76,* 2007.

[9] F. E. H. Tay, X. Jun, Y. Liang, V. J. Logeeswaran and Y. Yufeng, "The Effects of non-parallel plates in a differential capacitive microaccelerometer," *J. Micromech. Microeng,* 1999.

[10] L. Dong, L. Che, L. Sun and Y. Wang, "Effects of non-parallel combs on reliable operation conditions of capacitive inertial sensor for step and shock signals," *Sensors and Actuators A physical,* vol. 121, no. 2, pp. 395-404, 2005.

[11] Y. Mochida, M. Tamura and K. Ohwada, "A micromachined vibrating rate gyroscope with independent beams for the drive and detection modes," *International Conference on Micro Electro Mechanical Systems, 1999. MEMS '99. Twelfth IEEE,* pp. 618-623, 17-21 Jan 1999.

[12] G. K. Fedder and X. H., "Integrated Microelectromechanical Gyroscope," *Journal of aerospce engineering,* pp. 65-75, 2003.

[13] Y. Mochida, M. Tamura and K. Ohwada, "A micromachined vibrating rate gyroscope with independent beams for the drive and detection modes," in *Micro Electro Mechanical Systems, 1999. MEMS '99. Twelfth IEEE*, Yokohama, 1999.

[14] Y. Hong, S. Kim and H. Lee, "Modeling of angular-rate bandwidth for a vibrating microgyroscope," *Microsystem Technologies,* vol. 9, pp. 441-448, 2003.

[15] A. Noureldin, H. Tabler and M. P. Mintchev, "New technique for reducing the angle random walk at the output of fiber optic gyroscopes during alignment processes of inertial navigation systems," *Society of Photo-Optical Instrumentation Engineers,* vol. 40, no. 10, 2001.

[16] A. Lawrence, Modern inertial technology: navigation, guidance, and control, Springer, 2001.

[17] O. J. Woodman, "An introduction to inertial navigation," University of Cambridge, 2007.

[18] R. Schreier and G. Temes, Understading delta-sigma data converters, IEEE Press, 2005.

[19] S. Park, Principles of sigma-delta modulation for analog-to-digital converters, Motorola.

[20] M. Kozak and I. Kale, Oversampled delta-sigma modulator, Boston: Kluwer Academic Publishers, 2003.

[21] E. Janssen and A. van Roermund, Look-Ahead Based Sigma-Delta Modulation, Springer, 2011.

[22] F. Francesconi, V. Liberali and F. Maloberti, "A band-pass sigma-delta modulator architecture for digital radio," *Midwest Symposium on Circuits and Systems,* August 1995.

[23] J. M. De La Rosa, B. Perez Verdu, F. Medeiro and A. Rodriguez-Vazquez, "A fourth-order bandpass sigma delta modulator using current-mode analogue/digital circuit," *IEEE instrumentation and measurement technology conference,* 1996.

[24] B. Borovic, A. Q. Liu, D. Popa, H. Cai and F. L. Lewis, "Open-loop versus closed-loop control of MEMS devicees: choises and issues," *Journal of Micromechanics and Microengineering,* no. 15, pp. 1917-1924, 2005.

[25] Y. Dong, M. Kraft and W. Redman-White, "Microgyroscope control system using a high-order band-pass continues-time sigma-delta modulator," 2007.

[26] M. Lemkin and B. E. Boser, "A three-axis micromachined accelerometer with a CMOS position-sence interface and digital offset-trim electronics," *IEEE Journal of solid-state circuits,* vol. 34, no. 4, 1999.

[27] R. Kepenek, I. E. Ocak, H. Kulah and T. Akin, "A ug resolution microaccelerometer system with a second-order sigma-delta readout circuitry," *IEEE,* 2008.

[28] V. P. Petkov and B. E. Boser, "High-order electromechanical sigma delta modulation in micromachined inertial sensors," *IEEE TRANSACTIONS ON CIRCUITS AND SYSTEMS,* vol. 53, no. 5, 2006.

[29] Y. Dong, M. Kraft and W. Redman-White, "Higher order noise-shaping filters for high-performance micromachined accelerometers," *IEEE transactions on instrumentation and measurement,* vol. 56, no. 5, pp. 1666 - 1674 , 2007.

[30] T. Northemann, M. Maurer, A. Buhmann, L. He and Y. Manoli, "Excess loop delay compensated electro-mechanical bandpass sigma-delta modulator for gyroscopes," *Procedia*

Chemistry, 2009.

[31] Y. Dong and M. Kraft, "Control systems for capacitive micromachined inertial sensors with high-order sigma-delta modulators," ECS department, University of Southampton, 2006.

[32] Y. Dong and M. Kraft, "Control systems for capacitive micromachined inertial sensors with high-order sigma-delta modulators," ECS department, University of Southampton, 2006.

[33] R. H. M. Veldhoven and A. H. M. Roermund, Robust sigma delta converters, Springer, 2011.

[34] M. Neitola, "A fully automated flowgraph analysis tool for Matlab," 2006. [Online]. Available: http://www.mathworks.com/matlabcentral/fileexchange/loadfile.do?objectId=7224&objecttype=file.

[35] W. A. Clark and R. T. Howe, "Surface micromachined z-axis vibratory rate gyroscope," *IEEE,* 1996.

[36] X. Liang, S. Gao, F. Gao and S. Lv, "Design and simulation of a micro gyroscope with decoupled and high linearity structure," in *The Ninth International Conference on Electronic Measurement & Instruments*, 2009.

[37] B. Y. Yeh, Y. C. Liang and F. E. Tay, "Mathematical modelling on the quadrature error of low-rate microgyroscope for aerospace applications," *Analog integrated citcuits and signal prossecing,* no. 29, pp. 85-94, 2001.

[38] R. Antonello, R. Oboe, L. Prandi, C. Caminada and F. Biganzol, "Open loop compensation of the quarature error in MEMS vibrating gyroscopes," *Industrial Electronics 2009. IECON '09. 35th Annual conference of IEEE,* pp. 4034-4039, 3-5 Nov 2009.

[39] W. A. Clark and R. T. Howe, "Surface micromachined z-axis vibratory rate gyroscope," *IEEE,* 1996.

[40] R. Mounder and L. Yang, "Elec3027 radio communications, background information on amlidute modulation".

[41] A. Gokhale, Introduction to telecommunications, Thomson, 2005.

[42] B. A. Carlson, Communication systems, Mcgraw-Hill, 1986, pp. 515-516.

[43] B. P. Lathi and Z. Ding, Modern digital and analog communication systems, Oxford, 1998, pp. 170-171.

[44] P. Greiff, B. Boxenhom, T. King and L. Niles, "Silicon monolithic micromechanical gyroscope," *Papers, TRANSDUCERS '91., 1991 International Conference on Digest of Technical Solid-State Sensors and Actuators, 1991,* pp. 966 - 968, 1991.

[45] J. Bernstein, S. Cho, A. King, A. Kourepenis, P. Maciel and M. Weinberg, "A micromachined comb-drive tuning fork rate gyroscope," *Micro Electro Mechanical Systems, 1993, MEMS*

'93, Proceedings An Investigation of Micro Structures, Sensors, Actuators, Machines and Systems. IEEE., pp. 143 - 148, 1993.

[46] A. J. Chiou, "Process window of micromachined gyroscopes subjected to vibrational frequencies," *Sensors and Acuators,* no. 125, pp. 519-525, 2006.

[47] K. Tanaka, Y. Mochida, M. Sugimoto and K. Ohwada, "A micromachined vibrating gyroscope," *Sensors and Actuators,* no. 50, pp. 111-115, 1995.

[48] F. E. H. Tay, Y. C. Liang and V. J. Logeeswaran, "Design and fabrication of a micromachined resonant gyroscope," *International journal of electronics,* vol. 86, no. 10, pp. 1179-1191, 1999.

[49] F. Ayazi and K. Najafi, "Design and fabrication of high-performance polysilicon vibrating ring gyroscope," *Micro Electro Mechanical Systems, 1998. MEMS 98. Proceedings., The Eleventh Annual International Workshop on,* pp. 621-626, 25-29 Jan 1998.

[50] M. Palaniapan, R. T. Howe and J. Yasaitis, "Integrated sureface-micromachined z-axis frame microgyroscope," *IEEE,* 2002.

[51] H. Chen, X. Liu, M. Huo and W. Chen, "A Low noise bulk micromachined gyroscope with symmetrical and decoupled structure," in *Nano/Micro Engineered and Molecular Systems, 2006. NEMS '06. 1st IEEE International Conference on*, Zhuhai, 2006.

[52] A. A. Trusov, A. R. Schofield and A. M. Shkel, "Micromachined rate gyroscope architecture with ultra-high quality factor and improved mode ordering," *Sensors and Actuators A: Physical,* vol. 165, no. 1, pp. 26-34, 2011.

[53] H. Ding, X. Liu, L. Lin, X. Chi, J. Cui, M. Kraft, Z. Yang and G. Yan, "A High-Resolution Silicon-on-Glass Z Axis Gyroscope Operating at Atmospheric Pressure," *IEEE Sensors Journal,* vol. 10, no. 6, pp. 1066 - 1074, 2010.

[54] X. Jiang, S. A. Bhave, J. I. Seeger, R. T. Howe and B. E. Boser, "ΣΔ capacitive interface for a vertically-driven X&Y-axis rate gyroscope," in *Solid-State Circuits Conference, 2002. ESSCIRC 2002. Proceedings of the 28th European*, 2002.

[55] H. Kulah, J. Chae, N. Yazdi and K. Najafi, "Noise analysis and characterization of a sigma-delta capacitive microaccelerometer," *IEEE journal of solid-state circuits,* vol. 41, no. 2, pp. 352-361, Febuary 2006.

[56] J. Raman, E. Cretu, P. Rombouts and L. Weyten, "A digitally controlled MEMS gyroscope with unconstrained sigma-delta force-feedback architecture," in *Micro Electro Mechanical Systems, 19th IEEE International Conference*, Istanbul, 2006.

[57] M. Saukoski, L. Aaltonen and K. Halonen, "Integrated readout and control electronics for a microelectromechanical angular velocity sensor," in *Solid-State Circuits Conference.*

ESSCIRC 2006. Proceedings of the 32nd European, Montreux, 2006.

[58] M. Saukoski, L. Aaltonena, S. Teemu and K. A. Halonen, "Interface and control electronics for a bulk micromachined capacitive gyroscope," *Sensors and Actuators A: Physical,* vol. 147, no. 1, pp. 183-193, September 2008.

[59] J. Lee, K. P. Papathanassiou, T. L. Ainsworth, ,. M. R. Grunes and A. Reigber, "A new technique for noise filtering of SAR interferometric phase images," *IEEE transactions on geoscience and remote sensing,* vol. 36, no. 5, pp. 1456 - 1465 , 1998.

[60] C. D. Ezekwe and B. E. Boser, "A Mode-Matching Closed-Loop Vibratory Gyroscope Readout Interface With a 0.004 /s/ Noise Floor Over a 50 Hz Band," *IEEE Journal of Solid-State Circuits,* vol. 43, no. 12, pp. 3039 - 3048, Dec 2008.

[61] F. Chen, H. Chang, W. Yuan, R. Wilcock and M. Kraft, "Parameter optimization for a high-order band-pass continuous-time sigma-delta modulator MEMS gyroscope using a genetic algorithm approach," *Journal of micromechanics and microengineering,* vol. 22, p. 12, 2012.

[62] W. Bracke, P. Merken, R. Puers and C. Van Hoof, "Ultra-low-power interface chip for autonomous capacitive sensor systems," *IEEE transactions on circuits and systems,* vol. 54, no. 1, pp. 130-139, January 2007.

[63] H. Rodjegard and A. Loof, "A differential charge-transfer readout circuit for multiple output capacitive sensors," *Sensors and Actuators A Physical,* vol. 119, no. 2, pp. 309-315, September 2004.

[64] N. Yazdi, H. Kulah and K. Najafi, "Precision readout circuits for capacitive microaccelerometers," *Sensors 2004, Proceedings of IEEE,* vol. 1, pp. 28-31, May 2005.

[65] B. Yang, B. Zhou, S. Wang, L. Huang and Y. Yin, "A quadrature error and offset error supprssion circuitry for silicon micro-gyroscope," *Nano/Micro Engineered and Molecular Systems IEEE,* January 2008.

[66] M. Descharles, J. Guarard and H. Kokabi, "Global modelling and simulation of a Coriolis vibrating micro-gyroscope for quadrature error compensation," Chatillon, France, 2010.

[67] E. Tatar, S. E. Alper and T. Akin, "Effect of quadrature error on the performance of a fully-decoupled mems gyroscope," in *MEMS 2011*, Cancun, 2011.

[68] M. Saukoski, L. Aaltonen and K. Halonen, "Integrated readout and control electronics for a microelectromechanical angular velocity sensor," in *Solid-State Circuits Conference. ESSCIRC 2006. Proceedings of the 32nd European*, Montreux, 2006.

[69] B. Chaumet, B. Leverrier, C. Rougeot and S. Bouyat, "A new tuning fork gyroscope for aerospace," in *Symposium gyro technology 2009*, Karlsruhe, 2009.

[70] R. Antonello, R. Oboe, L. Prandi and C. Caminada, "Open loop compensation of the

quarature error in MEMS vibrating gyroscopes," *Industrial Electronics 2009. IECON '09. 35th Annual conference of IEEE,* pp. 4034-4039, 3-5 Nov 2009.

[71] B. E. Boser and V. P. Petkov, "A Fourth-Order Sigma Delta Interface for Micromachined Inertial Sensors," *IEEE journal of solid-state circuits,* vol. 40, no. 8, August 2005.

[72] M. Saukoski, L. Aaltonen and K. A. Halonen, "Zero-Rate Output and Quadrature Compensation in Vibratory MEMS Gyroscopes," in *Sensors Journal, IEEE*, 2007.

[73] Y. Dong, M. Kraft and W. Redman-White, "Microgyroscope control system using a high-order band-pass continues-time sigma-delta modulator," *Sensors and Actuators A Physical,* 2007.

[74] R. Wilcock and M. Kraft, "Genetic algorithm for the design of electro-mechanical sigma delta modulator MEMS sensors," *MDPI Sensors,* vol. 11, no. 10, 2011.

[75] Matlab, "Genetic algorithm and direct search toolbox 2.4.2," [Online]. Available: www.mathworks.com/products/gads/description1.html.

[76] Y. Dong, M. Kraft and W. Redman-White, "Micromachined vibratory gyroscope controlled by a high-order bandpass sigma-delta modulator," *IEEE sensors journal,* vol. 7, no. 1, January 2007.

[77] W. Y. Yang, T. G. Chang, I. H. Song, Y. S. Cho, J. Heo, W. G. Jeon, J. W. Lee and J. K. Kim, Signals and Systems with MATLAB, Springer, 2009.

[78] W. Gaol, O. Shoaei and W. Snelgrove, "Excess loop delay effects in continuous-time delta-sigma modulators and the compensation solution," in *IEEE International Symposium on Circuits and Systems*, 1997.

[79] V. Singh, N. Krishnapura and S. Pavan, "Compensating for quantizer delay in eExcess of one clock cycle in continuous-time ΔΣ modulators," *IEEE transactions of circuits and systems,* vol. 57, no. 9, 2010.

[80] J. Karki, "Fully-Differential Amplifiers," 2002.

[81] D. Brooks, "Differential signals, rules to live by," 2001.

[82] J. C. Lotters, W. Olthuis, P. H. Veltink and P. Bergveld, "A sensitive differential capacitance to voltage converter for sensor applications," *IEEE TRANSACTIONS ON INSTRUMENTATION AND MEASUREMENT,* vol. 48, no. 1, pp. 89-96, Febuary 1999.

[83] J. Karki, "Fully-Differential Amplifier," 2002.

[84] "AD633 Data Sheet," Analog Devices.

[85] Microchip, "AN1258: Op amp precision design: PCB layout techniques".

[86] R. S. Khandpour, Printed circuit boards, McGraw-Hill, 2008.

[87] Y. Matsuya, K. Uchimura, A. Iwata, T. Kobayashi, M. Ishikawa and T. Yoshitome, "A 16-bit oversampling A-to-D conversion technology using triple - integration noise shaping," *IEEE, Solid-state circuit,* vol. 22, no. 6, pp. 921 - 929, 1987.

[88] B. Almutairi and M. Kraft, "Experimental study of single loop sigma-delta and multi stage noise shaping (MASH) modulators for MEMS accelerometer," *Sensors, IEEE,* pp. 520 - 523, 2011.

[89] S. A. Jantzi, K. W. Martin and A. S. Sedra, "Quadrature bandpass sigma delta modulation for digital radio," *IEEE journal of solid-state circuit,* vol. 32, no. 12, pp. 1935-1950, 1997.

[90] S. An, Y. Oh, S. Lee and C. Song, "Dual-axis microgyroscope with closed-loop detection," *Sensors and Actuators A: Physical,* vol. 73, no. 1-2, pp. 1-6, 1999.

[91] K. Tarlaku, Y. Mochida, S. Sugimoto, K. Moriyo, T. Hasegawa, K. Atsuchi and K. Ohwada, "A micromachined vibratory gyroscope," in *Micro Electro Mechanical Systems, 1995, MEMS '95,* , 1995.

[92] H. Zhou, H. Hu and N. Harris, "Application of wearable inertial sensors in stroke rehabilitation," *Engineering in Medicine and Biology Society-IEEE,* 2005.

[93] [Online]. Available: http://en.wikipedia.org/wiki/List_of_trigonometric_identities.

[94] G. Xia, B. Yang and S. Wang, "Phase correction in digital self-oscillation drive circuit for improve silicon MEMS gyroscope bias stability," *Solid-State and Integrated Circuit Technology (ICSICT),* pp. 1416 - 1418, Nov 2010.

[95] R. Wilcock, "GA Automatic design software".

[96] H. Ding, X. Liu, L. Lin, X. Chi, J. Cui, M. Kraft, Z. Yang and G. Yan, "A high-resolution silicon-on-glass Z axis gyroscope operating at atmospheric pressure," *IEEE sensors journal,* vol. 10, no. 6, pp. 1066-1074, June 2010.

[97] M. Kozak and I. Kale, Oversampled delta-sigma modulators: analysis, applications and novel topologies, Boston: Kluwer Academic Publishers, 2003.

[98] N. Shaohua, G. Shiqiao and L. Haipeng, "A digital control systerm for micro-comb gyroscope," in *Electronic Measurement & Instruments, 2009. ICEMI '09*, Beijing, 2009.